SYNTHESIS, CHARACTERIZATION AND ELECTRON BEAM IRRADIATION STUDIES OF SELECTED NANOCRYSTALLINE TUNGSTATES AND THEIR POLYANILINE COMPOSITES

Thesis submitted to Mahatma Gandhi University
in partial fulfilment of the requirements for the degree of
Doctor of Philosophy in Physics

Under the faculty of Science

By

ALOYSIUS SABU N

Under the guidance of

Dr. THOMAS VARGHESE

LEAD KINDLY LIGHT

Department of Physics
**Newman College Thodupuzha**

August 2017

MAHATMA GANDHI UNIVERSITY CERTIFICATE ON
PLAGIARISM CHECK

1.	Name of the Research Scholar	**ALOYSIUS SABU N**
2.	Title of the Thesis/Dissertation	SYNTHESIS, CHARACTERIZATION AND ELECTRON BEAM IRRADIATION STUDIES OF SELECTED NANOCRYSTALLINE TUNGSTATES AND THEIR POLYANILINE COMPOSITES.
3.	Name of the Supervisor	**Dr. THOMAS VARGHESE**
4.	Department/Institution/ Research Centre	**Department of Physics, Newman College, Thodupuzha**
5.	Similar Content (%) identified	**4% (Four)**
6.	Acceptable Maximum Limit	**25%**
7.	Software Used	**Urkund**
8.	Date of Verification	**14-08-2017**

Report on plagiarism check, items with % of similarity is attached

Checked by (with Name, designation & signature) :
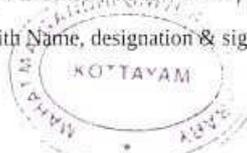
14.8.17

Laila T. Abraham

UNIVERSITY LIBRARIAN-IN-CHARGE

Name & Signature of the Researcher :

Aloysius Sabu N

Name & Signature of the Supervisor :

Dr. Thomas Varghese

Name & Signature of the HoD/HoI(Chairperson of the Doctoral Committee) :

Fr. Dr. Vincent Joseph

URKUND

Urkund Analysis Result

Analysed Document:	A L O Y S I U S S A B U N -SYNTHESIS, CHARACTERIZATION AND ELECTRON BEAM IRRADIATION STUDIES OF SELECTED NANOCRYSTALLINE TUNGSTATES AND THEIR POLYANILINE COMPOSITES.pdf (D30096987)
Submitted:	2017-08-14 07:06:00
Submitted By:	library@mgu.ac.in
Significance:	4 %

Sources included in the report:

https://cyberleninka.ru/article/n/technology-ready-use-for-producing-nanomaterials-in-the-plasma-of-a-low-pressure-pulsed-arc-discharge
https://link.springer.com/article/10.1140/epjp/i2017-11562-1
https://www.terkko.helsinki.fi/feednavigator/?j=204394&c=Physics+and+Astronomy
http://www.oalib.com/references/13903513
http://scholar.google.com/citations?user=r7Vrj9kAAAAJ&hl=en
http://scholar.google.com/citations?user=0u9jqPQAAAAJ&hl=en
http://downloads.hindawi.com/journals/jnt/2013/580308.xml
http://iopscience.iop.org/article/10.1088/1757-899X/73/1/012051/meta
http://adsabs.harvard.edu/abs/2016RaPC..123....1A
https://link.springer.com/article/10.1007/s12648-015-0664-1
http://pubs.rsc.org/en/content/articlelanding/2016/fd/c5fd00191a
https://www.hindawi.com/journals/jnt/2013/580308/
http://nanojournal.ifmo.ru/en/wp-content/uploads/2013/06/NPCM2013-43P357.pdf
http://iopscience.iop.org/article/10.1088/1757-899X/73/1/012051/pdf

Instances where selected sources appear:

72

14.8.17

Laila T. Abraham
UNIVERSITY LIBRARIAN-IN-CHARGE

Dr. Thomas Varghese
Associate Professor
Dept. of Physics
Nirmala College, Muvattupuzha
www.nsrc.in
email:nanoncm@gmail.com

.

Certificate

This is to certify that the thesis entitled SYNTHESIS, CHARACTERIZATION AND ELECTRON BEAM IRRADIATION STUDIES OF SELECTED NANOCRYSTALLINE TUNGSTATES AND THEIR POLYANILINE COMPOSITES is an authentic record of the original research work carried out by **Mr. Aloysius Sabu N**, in the Research Department of Physics, Newman College, Thodupuzha, under my guidance in partial fulfilment of the requirements for the award of the degree of Doctor of Philosophy, under the faculty of Science of Mahatma Gandhi University, Kottayam. The work presented in this thesis has not been submitted for any other degree or diploma earlier. It is also certified that Mr. Aloysius Sabu N has fulfilled the course requirements for the Ph.D degree of the university.

Muvattupuzha

18 August 2017

Dr. Thomas Varghese
(Supervising Teacher)

Declaration

I hereby declare that the work presented in this thesis entitled ***SYNTHESIS, CHARACTERIZATION AND ELECTRON BEAM IRRADIATION STUDIES OF SELECTED NANOCRYSTALLINE TUNGSTATES AND THEIR POLYANILINE COMPOSITES*** *is a record of the original research work carried out by me under the supervision of Dr. Thomas Varghese, in the Department of Physics, Newman College, Thodupuzha, Kerala. The work is original and has not been submitted earlier as a whole or in part for a degree/diploma at this or any other Institution / University.*
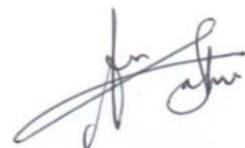
Thodupuzha   ***Aloysius Sabu N***

18 August 2017

Acknowledgements

I would like to express profound gratitude to Dr. Thomas Varghese, my research supervisor, for introducing me to this exciting field of nanomaterials. Under his guidance and invaluable support, I was able to successfully complete this work.

I am grateful to The Manager, Nirmala College, Muvattupuzha for granting permission to pursue my research work while continuing as a teacher in the Department of Physics at Nirmala College.

I thank The University Grants Commission of India for the research fellowship under Faculty Development Programme.

I would like to thank Rev. Dr. Vincent Joseph, Principal, Newman College, Thodupuzha and Dr. T. M. Joseph, Principal, Nirmala College, Muvattupuzha for providing me the laboratory and library facilities during my research work.

I would also like to thank all members of the department, faculty and staff, of the two colleges for their enduring support. My sincere thanks are due to Mr. Jose Karikunnel for his guidance in the administrative details pertaining to the teacher fellowship scheme of UGC. My sincere thanks to Ms. Rajeena Joseph, Head of the Department of Physics, Newman College; Ms. Susan Varghese, Head of the Department of Physics, Nirmala College; and the former Heads and faculty members of the Department Physics for the help and support for the completion of this research work. I am grateful to Dr. Joe Jacob, Research Co-ordinator and Dr. Alex Joseph, Newman College for sharing their expertise in material analysis.

I pay homage to the late Mr. Sunny Joseph, Nirmala College who took initiative to develop the nanomaterial research laboratory in the name Nanoscience Research Centre (NSRC) where I spent most of the time conducting experiments. I wish to

Preface

Metal tungstates are multifunctional materials with novel physical and chemical properties. Nanophase tungstate materials have potential applications in diverse fields. $MnWO_4$ and $CaWO_4$ nanoparticles have attracted much attention due to their interesting properties and micro and optoelectronic applications. The synthesis and characterization of nanocomposites of tungstate with polyaniline can bring out new properties that are useful for potential applications like gas sensing, electromagnetic interference shielding, anti-static coatings, corrosion protection and microwave applications. The studies related to electron beam irradiation effects on materials are interesting. The intrinsic defects produced by the electron beam irradiation offer modification of structural and physical properties of materials, which have technological applications.

Several studies have reported for the synthesis and characterization of $MnWO_4$ and $CaWO_4$ nanoparticles. However, studies based on the influence of electron beam irradiation on the structural, optical and electrical properties of $MnWO_4$, $CaWO_4$ and $PANI\text{-}MnWO_4/CaWO_4$ composite are sparse. It is therefore felt worthwhile to undertake a systematic investigation on the synthesis, characterization and electron beam irradiation studies of nanocrystalline $MnWO_4$, $CaWO_4$ and their polyaniline composites.

In the present investigation, $MnWO_4$ and $CaWO_4$ nanoparticles and their polyaniline composites are synthesized using simple chemical routes and are characterized using various tools for exploring their thermal, structural, optical and electrical properties. The influence of high energy (8

MeV) electron beam irradiation on the structural, optical and electrical properties of $MnWO_4$, $CaWO_4$ and their polyaniline composites is also investigated. The results of these systematic investigations are incorporated in the thesis.

The subject matter of the thesis has been organized into six chapters. Chapter 1 is introduction, which comprises literature survey, statement of the research problem, objectives and scope of the present study. In Chapter 2, the materials and methods used for the synthesis and characterization of the materials are presented. The details of the apparatus, experimental set up and procedure adopted for the various studies are also described in this chapter.

The synthesis and characterization of nanocrystalline manganese tungstate, calcium tungstate and their polyaniline composites are presented in Chapter 3, 4 and 5, respectively. The conclusions drawn on the basis of systematic analysis are summarized in Chapter 6 and the scope for future work in this field is mentioned at the end of this chapter.

PUBLICATIONS

1. **"Enhanced structural and optical properties of the polyaniline-calcium tungstate (PANI-CaWO$_4$ nanocomposite for electronics applications"**. **Aloysius Sabu, N.**, Francis, X., Anjaly, J., Sankararaman, S., & Varghese, Thomas. (2017). *The European Physical Journal Plus, 132*(6), 290. doi: 10.1140/epjp/i2017-11562-1

2. **"Dielectric studies of nanocrystalline calcium tungstate"**. **Aloysius Sabu, N.**, Rintu, M. S., Muhammed, E. M., & Varghese, Thomas. (2016). *Nanosystems: Physics, Chemistry, Mathematics*, 599-603. doi: 10.17586/2220-8054-2016-7-4-599-603.

3. **"Modifications in the structural and optical properties of nanocrystalline CaWO$_4$ induced by 8 MeV electron beam irradiation"**. **Aloysius Sabu, N.**, Priyanka, K. P., Ganesh, S., & Varghese, Thomas. (2016). *Radiation Physics and Chemistry, 123*, 1-5.

   doi: http://dx.doi.org/10.1016/j.radphyschem.2016.02.006.

4. **"Enhancement of electrical properties of manganese tungstate nanoparticles by beam irradiation"**. **Aloysius Sabu, N.**, Priyanka, K. P., Sheena, X., Mohammed, E. M., & Varghese, Thomas. (2015). *IOP Conference Series: Materials Science and Engineering, 73*(1), 012051.

5. **"Dielectric Studies of Nanocrystalline Manganese Tungstate"**. **Aloysius Sabu, N**, Priyanka, K.P., Smitha, T., Anu Tresa. S, Mohammed, E.M., Jaseentha, O.P., & Varghese, Thomas. (2013). *Nanosystems: Physics, Chemistry, Mathematics, 4*(3), 357–362.

6. **"Effect of Electron Beam Irradiation on Optical Properties of Manganese Tungstate Nanoparticles"**. Priyanka, K. P., **Aloysius Sabu, N.**, Anu Tresa. S, Sheena, P. A., & Varghese, Thomas. (2013). *Journal of Nanotechnology, 2013*, 1-6. doi: 10.1155/2013/580308

PRESENTATIONS

1. "Dielectric studies of nanocrystalline calcium tungstate". NANO-15, International Conference on Nanomaterials and Nanotechnology, December 2015, organised by the Centre for Nanoscience and Technology, K.S. Rangasamy College of Technology, K.S.R, Kalvinagar - 637 215, Tiruchengode on 7-10 December 2015.

2. "AC conductivity studies of $CaWO_4$ nanoparticles". National seminar on Advances in Spectroscopic Identification, organised by the Research and Post Graduate Department of Chemistry, Nirmala College, Muvattupuzha on 4th and 5th December 2015.

3. "Structural characterization and photoluminescence properties of $CaWO_4$ nanoparticles prepared by chemical precipitation". 27th Kerala Science Congress, Alapuzha on 27th-29th January 2015.

4. "Structural and optical characterization of $MnWO_4$ nanoparticles prepared by chemical precipitation". National Conference on Recent Advances in Spectroscopy organised by the Department of Chemistry, Mar Athanasius College, Kothamangalam on 31st July and 1st August, 2014.

5. "Synthesis, characterization and optical studies of manganese tungstate nanoparticles". National conference on Nanotechnology's invisible threat: Small science, big consequences, organised by Mahatma Gandhi National Institute of Research and Social Action (MGNIRSA), Hyderabad, India, on 26th-27th September, 2013.

LIST OF FIGURES

LIST OF TABLES

CONTENTS

$\mathbf{C}$hapter - 1
INTRODUCTION

Metal tungstates are multifunctional materials with exciting structural and optical properties. Nanophase tungstate materials have potential applications in various fields, such as luminescence, microwave, scintillation, photocatalysis and humidity sensing [1-3]. Among metal tungstates, $MnWO_4$ and $CaWO_4$ have attracted much attention due to their unique structural, optical, electrical and photocatalytic properties. These novel properties make them suitable materials for potential use in scintillating detectors, lasers, light emitting diodes, optical fibres and humidity sensors [4-7]. The formation of nanocomposites of tungstate with polyaniline is expected to bring out novel properties that are useful for potential applications like gas sensing, electromagnetic interference shielding, anti-static coatings, corrosion protection and microwave applications.

The studies related to electron beam irradiation effects on materials are interesting. The electron beam irradiation introduces small intrinsic defects in samples. The material properties are primarily controlled by

inherent defects or charge carriers, which are produced during irradiation. Hence, electron irradiation technique can be used for the modification of structural and physical properties of materials that have technological applications [8-11].

1.1   Background study

A comprehensive literature survey is conducted on metal tungstates and polyaniline composites. This includes review of nanocrystalline tungstates, polyaniline composites and the effect of electron beam irradiation on materials. Though many different tungstates and polymers are found in the literature, only the reviews of the components relevant to the study are included.

1.1.1   Metal tungstates- Crystal structure

Tungstates having the general formula AWO_4, where A= Mn, Mg, Cd, Ca, Sr, Ba and Pb. In metal tungstates, if A^{2+} has a small ionic radius < 0.77 Å (Mg, Zn), it will form the monoclinic wolframite structure, but larger A^{2+} cations > 0.77 Å (Ca, Ba) form the tetragonal scheelite structure [12,13]. The monoclinic wolframite structure has a space group (SG) of P2/c and contains two formula units (Z=2). But, the tetragonal scheelite structure has a space group of $I4_1/a$, and contains four formula units (Z=4).

In wolframite structure, both A and W cations have octahedral oxygen coordination and each octahedron shares two corners with its neighbours. The WO_6 octahedra are highly distorted, since two of the W–O distances (~2.13 Å) are much larger than the other four W–O distances

($\sim$1.84 Å)[14-16]. In scheelite tetragonal structure, the cation is co-ordinated to eight oxygen atoms in CaO_8 polyhedrons and tungsten atoms are coordinated to four oxygen atoms in WO_4 tetrahedrons [12, 17-20]. The isolated tetrahedron of WO_4 in scheelite is nearly regular with four W-O distances ($\sim$1.79Å) [15]. Fig. 1.1 represents the conventional unit cell of the wolframite and the scheelite structures.
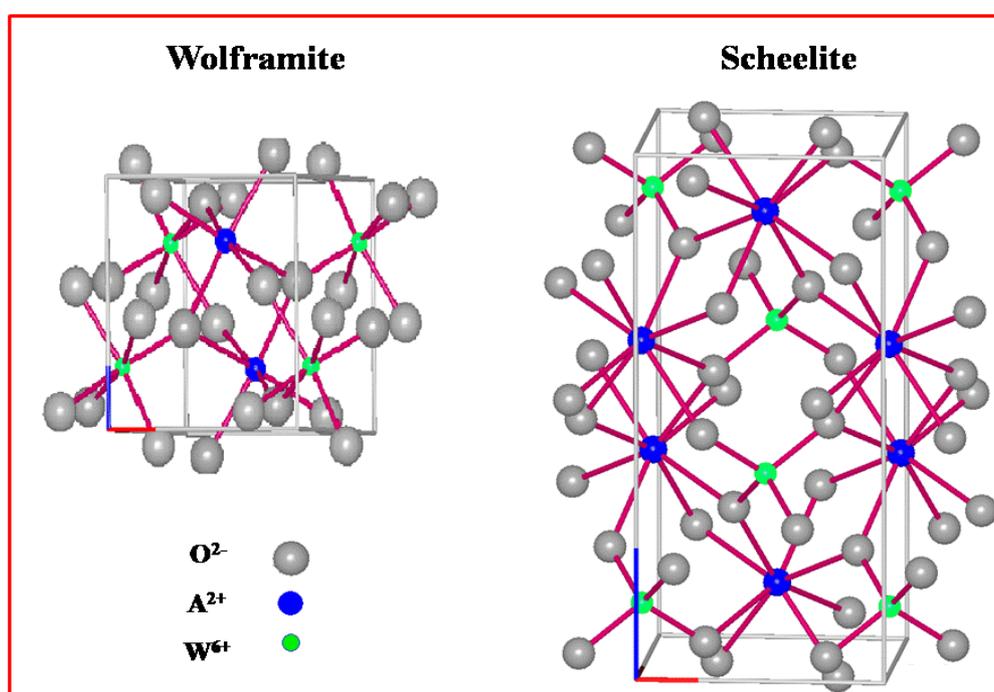
Fig. 1.1 Unit cell for the wolframite and the scheelite structures.

(Adapted from online data base [21])

In the present work, manganese tungstate ($MnWO_4$) and calcium tungstate ($CaWO_4$) nanoparticles are selected for the study. The reason for selecting these materials will be clear from the literature review presented in the following sections and the discussion that follows.

1.1.2 Nanocrystalline MnWO$_4$

The mineral name for MnWO$_4$ is hubnerite [22]. MnWO$_4$ is paraelectric and paramagnetic at room temperature. It possesses spontaneous electric polarization [23-25]. But, at lower specific temperatures 13.5, 12.5 and 8-6.5 K, MnWO$_4$ showed different antiferromagnetic states as reported by Choi *et al.* [26].

The electrical conductivity of MnWO$_4$ is sensitive to changes in humidity. Hence, it can be used as a humidity sensor with potential applications in meteorology, medicine, food production, agriculture, industry and domestic environment [4, 5]. Small variations in the surface adsorbed water plays key role in modulating the electrical conductivity. Also, the porosity of the synthesized material contributes to the sensing property. Zhang *et al.* have reported that MnWO$_4$ nanoplates synthesized by hydrothermal method exhibited ionic conductivity and based on its ionic conductivity they were quite sensitive to water molecules [27]. Excellent varistor behaviour with a negative temperature coefficient of resistance has been reported in lead manganese tungstate ceramics [28]. Saranya *et al.* have measured the conductivity of MnWO$_4$ prepared by ultrasonication method [29]. It was found that conductivity increased with increase in temperature showing a semiconducting behaviour.

It has been reported that the morphology of MnWO$_4$ micro/nanocomposite structures synthesized by microemulsion-based solvothermal approach depended on reaction time and temperature [30].

Ambient template synthesis of multiferroic $MnWO_4$ nanowires and nanowire arrays was reported by Zhou *et al.* [23]. They found that the morphology of nanoparticles depends on the reaction conditions. Wu *et al.* synthesized $MnWO_4$ nanocrystals with different morphologies by controlling pH values using hydrothermal method [31]. It is also reported that the pressure, pH and temperature of the reaction systems played important role in determining the morphologies of $MnWO_4$ [32]. Proper organic surfactants (ethylene glycol, polyethylene glycol-400) added to the reactants can control the growth of the particles. Simple and effective technique of synthesis of $MnWO_4$ nanoparticles seldom happens without using any surfactants. Two such methods are reported by Hu *et al.* and Rahimi-Nasrabadi *et al.* [33, 34]. The first method is hydrothermal and the second method is direct chemical precipitation. Nithiyanantham *et al.* have reported a new route for the aqueous phase synthesis of single crystalline, shape-selective, magnetic $MnWO_4$ nanomaterials on a DNA scaffold [35].

Tungstate nanomaterials are well known for their photoluminescence (PL) properties. It has been reported that the mechanism for the PL properties are the electronic transfer within the $(WO_4)^{-2}$ anion complex. This is true for the scheelite structured tungstate. Since the crystal structures for the monoclinic wolframite is different from the tetragonal scheelite, there must be some difference in the PL property of $MnWO_4$ nanocrystals. $MnWO_4$ monoclinic lattice is formed by interconnected ($...[WO_6]$–$[MnO_6]$–$[WO_6]...$) clusters [22]. In this report the PL emission has been explained on the basis of defects in the lattice and/or between distorted

octahedral [WO_6] clusters. Wu *et al.* have shown that the PL intensity of samples prepared under different pH values were different [31].

Tong *et al.* have observed in their investigation that as particle size reduced from 29 to 8 nm, there existed a 'lattice expansion' followed by lowered lattice symmetry, lattice vibrational variations, and broadened bandgap [2]. Phonon properties of nanosized $MnWO_4$ with different size and morphology have been reported by Mączka *et al.* [36]. In their work they described the particle size dependence on the intensity of the IR and Raman peaks. Eighteen Raman active modes have been observed in the Raman studies of $MnWO_4$ by researchers [37]. So it can be inferred that IR and Raman studies can provide information regarding size changes and disorders occurring to a specimen as a result of heating or treating with energetic radiations.

$MnWO_4$ nanoparticles have strong absorption in the UV-visible region and have potential for the photocatalysis [38]. Contaminants like dye molecules can be removed from water by their photocatalytic degradation by developing such photocatalysts. For this their size and bandgap should be tuned properly. The effect of pH value on the synthesis and photocatalytic performance of $MnWO_4$ nanostructure by hydrothermal method has been reported [31]. In this work photocatalytic degradation of acetone was studied. The possibility of enhancing the photocatalytic activity using $MnWO_4$ encapsulated in mesoporous silica has been claimed by Hoang *et al.* [39]. In their work they obtained nanoparticles of average size 15 nm. When the size of the particles decrease the exposed area

increases which in turn helps in increasing the photocatalytic property. An environment friendly $MnWO_4$ nanocrystalline catalyst has been reported by Khaksar *et al.* [40]. Amina *et al.* have reported antibacterial property of $MnWO_4$ nanoparticles [41].

1.1.3 Nanocrystalline CaWO$_4$

The scheelite calcium tungstate is an important optical material which has found many practical applications. Oishi and Hirao synthesized calcium tungstate whiskers of different sizes grown from KCl flux [42]. This report might be the forerunner to the synthesis of $CaWO_4$ micro and nanocrystals of various morphologies. They obtained 2.5 mm long (5.3 μm diameter) $CaWO_4$ whiskers. Thin films of $CaWO_4$ and $SrWO_4$ prepared on glass plate by spray pyrolysis showed blue and blue-green emissions at 447 and 487 nm, respectively [43]. This is due to the charge transitions within the (WO_4) group. Low-temperature synthesis of metal tungstates nanocrystallite in ethylene glycol was reported by Chen *et al.* [44]. They reported the preparation of several nanosized metal tungstate powders ($CaWO_4$, $SrWO_4$, $BaWO_4$, $CdWO_4$, $ZnWO_4$ and $PbWO_4$) from the reaction between metal chloride and sodium tungstate in the ethylene glycol system at low temperature. In a solvothermal path way, nanocrystalline $CaWO_4$ was fabricated using organic additives ethylene glycol and polyethylene glycol [3]. Nanorods and spherical particles were obtained by this method. The growth in certain plane, for instance (001), results from the favourable interaction between the calcium exposed atoms and the hydroxyl anions

[45]. Mai and Feldmann investigated the influence of cationic and non-ionic surfactants on particle size, shape and photoluminescence of $CaWO_4$ [46].

Mogilevsky *et al.* have reported that the mechanical anisotropy of scheelite ($CaWO_4$) favoured oxidation resistant coatings in high temperature ceramic composites [47]. The bandgap energy of the crystalline thin films was found to be 5.27 eV in $CaWO_4$ and 5.78 eV in $SrWO_4$ [48]. Theoretical study by Cavalcante *et al.* reported that $CaWO_4$ is a direct bandgap material [49] with energy gap of 5.45 eV in nanocrystals. Another study by Vidya *et al.* reported a bandgap of 4.25 eV for the $CaWO_4$ nanocrystals [50].

There are many valid hypotheses regarding the PL properties of $CaWO_4$. The predominant blue emission centred on 420-430 nm is attributed to the charge transfer process taking place within the $(WO_4)^{-2}$ group [51]. The $^1T_2$ to $^1A_1$ transition in the $[WO_4]^{2-}$ excited complexes produce this PL. Also, a blue-green emission may be caused by the WO_3 defect centres produced by the oxygen vacancies [7, 52, 53]. Katelnikovas *et al.* have synthesized $CaWO_4$ particles with size in the range 350- 850 nm by sol-gel process [54]. In this method, the precursor solution was stabilized using citric and tartaric acids. Su *et al.* reported that citric acid and pH played important roles in hydrothermal method to synthesis $CaWO_4$ nanoparticles [55]. They also reported on the systematic lattice expansion, vibrations and electronic absorption bands with size reduction. Parhi *et al.* have reported the synthesis of scheelite-type ABO_4 (A= Ca, Sr, Ba) by solid-state metathetic approach assisted by microwave energy radiation

[12]. Formation of nanoparticles resulted in lattice expansion, and affected the PL behaviour as observed by Li *et al.* [56]. Nanocrystalline $CaWO_4$ of size 12 nm synthesized by microwave irradiation technique [18]. Lin *et al.* reported the synthesis of Eu: $CaWO_4$ with anti-tumour activity [57]. Eu^{3+} doped $CaWO_4$ phosphors showed two peaks in the thermo luminescence at 400 and 500 K [58]. Nanostructured $CaWO_4$ produced by co-precipitation can be applied as a catalyst support for platinum as reported by Farsi and Barzgari [59], and showed better electrochemical activity in oxygen reduction reaction in H_2SO_4. Photocatalytic application of $CaWO_4$ for the degradation of methylene blue has been reported by Farsi *et al.* [60].

Thus by reviewing the literature on nanocrystalline $MnWO_4$ and $CaWO_4$, it can be concluded that no work has been reported on the effect of electron beam irradiation on the structural and physical properties of these metal tungstates.

1.1.4 Conducting polyaniline

Polyaniline is a conducting polymer which was discovered about 153 years ago. It captured much attention by the scientific community since 1980. PANI is an organic semiconductor. It is the most studied among the conducting polymers. PANI was originally known as 'aniline black' [61-63] and was obtained by the polymerization of aniline (C_6H_5-NH_2) under acidic conditions. PANI exists in three different forms: "leucoemeraldine" (fully reduced form with $y = 1$); "emeraldine" (half oxidized form with $y =$

0.5) and "pernigraniline" (fully oxidized form with $y = 0$) derived out of the scheme shown in Fig. 1.1.
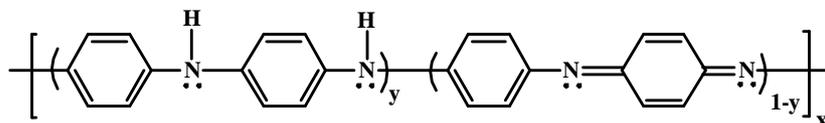
Fig. 1.2 General scheme of representation of PANI

The conducting form of PANI, called the emeraldine salt (PANI-ES), is obtained by protonation of the half oxidized form of PANI called emeraldine base (PANI-EB). When polyaniline is doped with protonic acid its conductivity gets modified from 10^{-10} to 10^{3} Scm^{-1}, depending on protonation.

1.1.5 Polyaniline nanocomposite

Sharma *et al.* have studied the effect of magnetic nanoparticles forming polyaniline composite [64]. They found that the magnetic phase could be retained at higher temperatures in the iron oxide/PANI nanocomposite. Low concentrations of PANI in the composite resulted in antiferromagnetic behaviour and large concentrations of PANI resulted in super paramagnetic behaviour.

Deshpande *et al.* have reported on the ammonia gas sensing property of thin film made from tin oxide-intercalated polyaniline nanocomposite [65]. They have found that while tin oxide remained inactive to the presence of ammonia, tin oxide/PANI nanocomposite could sense its presence. This is due to the modification induced in the electronic

properties of PANI matrix by the presence of tin oxide. The application of graphene/polyaniline nanocomposite as a hydrogen (H_2) gas sensor was reported by Al-Mashat *et al.* [66]. In their experiment, they studied the gas sensing properties of graphene, PANI and their composites separately, and found that the sensing action was highest in the composite. Shi *et al.* have prepared TiO_2/polyaniline nanocomposite from a lyotropic liquid crystalline solution [67]. They found that the presence of inorganic species improved the crystallinity of PANI along a direction perpendicular to the PANI chain.

It is reported that formation of polyaniline composite with carbon nanotube (CNT) resulted improvement in electrical transport [68]. According to Kondawar and his co-workers, PANI formed a layer over the CNT and the conductivity was enhanced by the charge transfer between the quinoid rings of the PANI and the CNT. Similar improvement in conductivity has been reported for PANI/V_2O_5 nanocomposite by Li and Ruckenstein [69]. Synthesis and characterization of polyaniline/zinc oxide (PANI-ZnO) was reported by Mostafaei and Zolriasatein [70]. They observed lower electrical conductivity, changes in thermal and optical properties of the composite. This was due to the adsorption of –NH– group on the surface of ZnO nanorods. Meng *et al.* have developed MnO_2-PANI composite having electrochemical properties with capacitance up to 207 Fg^{-1} [71]. The synergistic effect of MnO_2 and PANI chain is the reason for the high capacitance. Electrochromic and pseudo-capacitive properties of tungsten oxide/PANI (WO_3/PANI) composite have been reported by Nwanya *et al.* [72]. They found that the integration of PANI with WO_3

resulted in the formation of a true electrochemical capacitor. A review article on graphene based polyaniline composites by Wang *et al.* [73] summarizes their applications in supercapacitors, sensing platforms, fuel cells, solar cells, electrochromic devices and lithium ion batteries. Another literature review, conducted by Sen *et al.* have reported on the synthesis and applications of polyaniline nanocomposites [74]. Direct electronic transitions in polyaniline–$NiFe_2O_4$ nanocomposite (PANI–$NiFe_2O_4$) with a bandgap of 1 eV have been reported by Khairy and Gouda [75]. A study on polyaniline–niobium pentoxide (PANI/Nb_2O_5) has reported the dielectric properties and the power law dependence of the AC conductivity [76]. Low frequency AC conduction in polyaniline/zinc tungstate (PANI/$ZnWO_4$) composite was studied by Machappa and Prasad [77].

Microwave absorption properties of Fe_3O_4–polyaniline nanocomposite have been reported by Zhu *et al.* [78]. Lower percentage of PANI in the composite is suitable for anti-static applications where as higher percentage PANI in the composite is suitable for EMI shielding [79]. Large dielectric constant of PANI-TiO_2 nanocomposite provides promising applications in the field of actuators, dynamic random access memory and metal oxide semiconductor devices [80]. Pillalamarri *et al.* have reported polyaniline composites in which both PANI and the metal particles were in the nano regime [81]. PANI–Mn_3O_4 composite prepared by Durmus *et al.* showed higher conductivity and super paramagnetic behaviour [82]. Jianjun *et al.* reported on the γ-MnO_2/polyaniline composite for applications in microwave absorption [83].

Optical spectroscopic studies of composites of conducting PANI with CdSe and ZnO nanocrystals were reported by Bhat and Vivekchand [84]. Banerjee *et al.* in their studies on HCl doped PANI observed that the diameter of the polyaniline nanofibre decreased with increase in the dopant concentration [85]. Sapurina *et al.* showed that presence of sodium tungstate retarded the oxidation of aniline and the presence of sodium tungstate did not much affect the conductivity [86].

Several review articles on the synthesis, characterization and applications of polymer nanocomposites have been published [74, 87-90]. Polyaniline nanocomposite can be easily prepared using *in situ* chemical oxidative polymerization [91-93]. Proper ratio has to be maintained between PANI and the dopant used to achieve optimum synergistic effect [94]. The synthesis of PANI-MnWO$_4$ nanocomposite has been reported [95]. In this study specific capacitance of the composite was measured.

Negative permittivity was observed in polyaniline-barium titanate nanocomposites [96]. Polyaniline-yttrium trioxide (PAni-Y$_2$O$_3$) composites were synthesized by Muhammad and Syed [97]. They succeeded in tuning the microwave absorption property in a wide range of frequencies.

In the present research work, MnWO$_4$ and CaWO$_4$ are selected to form composites with PANI and some property changes are expected in the final products.

1.1.6 Effect of high energy electron beam irradiation

There are few reports on the study of the effect of electron beam irradiation in metal oxides. Using electron beam irradiation the optical, electronic, magnetic and mechanical properties may be tailored for useful applications [98]. Effect of electron beam irradiation on various structural and physical properties of ZnO film [99], gallium zinc oxide thin films [100], CeO_2 nanoparticles [101], nickel oxide nanocubes [102], α-Ag_2WO_4 nanoparticles [103], graphene oxide [104, 105], carbon films [106], anti-ferroelectric materials [107], ZnS nanostructures [8], WS_2 nanotubes [108], InGaAs/GaAs quantum well and quantum dot structures [109], TGA-capped CdTe quantum dots [110], $Bi_2Fe_4O_4$ [111], iron-iron oxide core-shell nanoparticles [112], $LaCoO_3$ [113], $Gd_{0.5}Sr_{0.5}MnO_3$ and $Dy_{0.5}Sr_{0.5}MnO_3$ manganites [114] and AlGaAs/GaAs [115] heterostructure was reported.

There are some reports on the effect of electron beam irradiation of polymer composites. Modifications such as cross-links or chain breaks upon irradiating polyacetyline samples with electron beam results in the decrease of path length of the conjugated chain [116]. Electron beam curing of composites is non-thermal and faster compared to thermal annealing [117]. Nasef *et al.* have observed electron dose dependent changes in chemical structure, thermal characteristics, crystallinity and mechanical properties in ethylene-tetrafluoroethylene copolymer (ETFE) film [118]. Bhadra and Khastgir reported changes in d-spacing, inter-chain separation, and thermal stability in PANI [119]. They also noticed that oxidation level

of PANI was not affected upon electron irradiation. Morphology change in polymer composite was observed due to changes in the polymer network caused by electron beam irradiation [120]. Sangappa *et al.* have reported physical and thermal properties of 8 MeV electron irradiated HPMC Polymer films [121]. Hareesh *et al.* have reported changes in structural and thermal properties of lexan polycarbonate [122].

The detailed literature survey indicates that no adequate studies are reported for polyaniline composites of $MnWO_4$ and $CaWO_4$ nanocrystals. The influence of high energy electron beam irradiation on the structural and physical properties of $MnWO_4$ and $CaWO_4$ nanocrystals and their polyaniline composites is sparse. Electron beam irradiation of PANI-$MnWO_4$/ $CaWO_4$ may help in the curing of these materials so that they can be used for applications like electromagnetic shielding, antistatic coatings and microwave dielectrics.

1.2   Statement of the research problem

Several studies were conducted on the synthesis and characterization of $MnWO_4$ and $CaWO_4$ nanoparticles. To date, no studies have been reported on the structural, optical and electrical properties of polyaniline composites of nanophase $MnWO_4$ and $CaWO_4$. Hence, more extensive and systematic studies on the structural, optical and electrical properties of these nanocomposites are needed. Also, studies on influence of high energy electron beam irradiation on the structural, optical and electrical properties of $MnWO_4$ and $CaWO_4$ nanoparticles are sparse. In order to throw more light on the influence of high energy electron beam irradiation on $MnWO_4$,

$CaWO_4$ and their polyaniline composites, systematic investigation based on various characterization tools are required. The present research is mainly focussed on the synthesis, characterization and electron beam irradiation studies of nanocrystalline $MnWO_4$ and $CaWO_4$, and their polyaniline composites.

1.3   Objectives of the present research

The main objectives of this research work are:

i.   Synthesis of $MnWO_4$ and $CaWO_4$ nanoparticles by simple chemical precipitation method.

ii.   Investigation of structural, optical and electrical properties of the synthesized nanocrystalline $MnWO_4$ and $CaWO_4$.

iii.   Study of the effect of calcination temperature on structural, optical and electrical properties of $MnWO_4$ and $CaWO_4$ tungstate nanoparticles.

iv.   Study of the effect of 8 MeV electron beam irradiation on the structure, optical and electrical properties of nanocrystalline $MnWO_4$ and $CaWO_4$.

v.   Synthesis and characterization of polyaniline composites of nanocrystalline $MnWO_4$ and $CaWO_4$ by *in situ* chemical oxidative polymerization.

vi.   Investigation of the influence of high energy electron beam irradiation on polyaniline composites of nanocrystalline $MnWO_4$ and $CaWO_4$.

References

1   U. M. García-Pérez, A. Martínez-de la Cruz, and J. Peral, Electrochimica Acta **81**, 227 (2012).

2   W. Tong, L. Li, W. Hu, T. Yan, X. Guan, and G. Li, The Journal of Physical Chemistry C **114** (36), 15298 (2010).

3   S.-J. Chen, J. Li, X.-T. Chen, J.-M. Hong, Z. Xue, and X.-Z. You, Journal of Crystal Growth **253** (1-4), 361 (2003).

4   W. Qu, W. Wlodarski, and J.-U. Meyer, Sensors and Actuators B: Chemical **64** (1–3), 76 (2000).

5   A. M. E. Suresh Raj, C. Mallika, O. M. Sreedharan, and K. S. Nagaraja, Materials Letters **53** (4–5), 316 (2002).

6   J. Ninković, G. Angloher, C. Bucci, C. Cozzini, T. Frank, D. Hauff, H. Kraus, B. Majorovits, V. Mikhailik, F. Petricca, F. Pröbst, Y. Ramachers, W. Rau, W. Seidel, and S. Uchaikin, Nuclear Instruments and Methods in Physics Research Section A: Accelerators, Spectrometers, Detectors and Associated Equipment **537** (1-2), 339 (2005).

7   A. B. Campos, A. Z. Simões, E. Longo, J. A. Varela, V. M. Longo, A. T. de Figueiredo, F. S. De Vicente, and A. C. Hernandes, Applied Physics Letters **91** (5), 051923 (2007).

8   Y. Xu, L. Shi, X. Zhang, K. Wong, and Q. Li, Micron **42** (3), 290 (2011).

9   K. Siraj, M. Kanwal, S. Saleem, J. D. Pedarnig, M. S. Rafique, and S. Naseem, Indian Journal of Physics **90** (12), 1431 (2016).

10   S. Tiptipakorn, P. Suwanmala, K. Hemvichian, and Y. Pornputtanakul, Advanced Materials Research **550-553**, 861 (2012).

11   A. T. Ramaprasad, V. Rao, G. Sanjeev, S. P. Ramanani, and S. Sabharwal, Synthetic Metals **159** (19–20), 1983 (2009).

12 P. Parhi, T. N. Karthik, and V. Manivannan, Journal of Alloys and Compounds **465** (1–2), 380 (2008).

13 S. H. Yu, B. Liu, M. S. Mo, J. H. Huang, X. M. Liu, and Y. T. Qian, Advanced Functional Materials **13** (8), 639 (2003).

14 S. López-Moreno, A. H. Romero, P. Rodríguez-Hernández, and A. Muñoz, High Pressure Research **29** (4), 578 (2009).

15 A. Kuzmin and J. Purans, Radiation Measurements **33** (5), 583 (2001).

16 R. Bharati, R. A. Singh, and B. M. Wanklyn, Journal of Physics and Chemistry of Solids **43** (7), 641 (1982).

17 J. T. Kloprogge, M. L. Weier, L. V. Duong, and R. L. Frost, Materials Chemistry and Physics **88** (2–3), 438 (2004).

18 A. Phuruangrat, T. Thongtem, and S. Thongtem, Journal of Experimental Nanoscience **5** (3), 263 (2010).

19 S. Vidya, S. Solomon, and J. K. Thomas, Journal of Materials Science: Materials in Electronics **25** (2), 693 (2013).

20 S. M. M. Zawawi, R. Yahya, A. Hassan, and M. N. Daud, Materials Research Innovations **15** (s2), s100 (2011).

21 T. Mohit, Growth and characterization of Scheelite crystals, ch.1, p. 18 (November, 2010) http://hdl.handle.net/10603/4722

22 M. A. P. Almeida, L. S. Cavalcante, M. Siu Li, J. A. Varela, and E. Longo, Journal of Inorganic and Organometallic Polymers and Materials **22** (1), 264 (2011).

23 H. Zhou, Y. Yiu, M. C. Aronson, and S. S. Wong, Journal of Solid State Chemistry **181** (7), 1539 (2008).

24   S. H. Park, B. Mihailova, B. Pedersen, C. Paulmann, D. Behal, U. Gattermann, and R. Hochleitner, Journal of Magnetism and Magnetic Materials **394**, 160 (2015).

25   T. Möller, P. Becker, L. Bohatý, J. Hemberger, and M. Grüninger, Physical Review B **90** (15), 155105 (2014).

26   W. S. Choi, K. Taniguchi, S. J. Moon, S. S. A. Seo, T. Arima, H. Hoang, I. S. Yang, T. W. Noh, and Y. S. Lee, Physical Review B **81** (20), 205111 (2010).

27   L. Zhang, C. Lu, Y. Wang, and Y. Cheng, Materials Chemistry and Physics **103** (2-3), 433 (2007).

28   R. N. P. Choudhary, R. Palai, and S. Sharma, Journal of Materials Science: Materials in Electronics **11** (9), 685 (2000).

29   S. Saranya, S. T. Senthilkumar, K. V. Sankar, and R. K. Selvan, Journal of Electroceramics **28** (4), 220 (2012).

30   Y. Xing, S. Song, J. Feng, Y. Lei, M. Li, and H. Zhang, Solid State Sciences **10** (10), 1299 (2008).

31   W. Wu, W. Qin, Y. He, Y. Wu, and T. Wu, Journal of Experimental Nanoscience **7** (4), 390 (2012).

32   S.-J. Chen, X.-T. Chen, Z. Xue, J.-H. Zhou, J. Li, J.-M. Hong, and X.-Z. You, Journal of Materials Chemistry **13** (5), 1132 (2003).

33   W. B. Hu, X. L. Nie, and Y. Z. Mi, Materials Characterization **61** (1), 85 (2010).

34   M. Rahimi-Nasrabadi, S. M. Pourmortazavi, M. Khalilian-Shalamzari, S. S. Hajimirsadeghi, and M. M. Zahedi, Central European Journal of Chemistry **11** (8), 1393 (2013).

35   U. Nithiyanantham, S. R. Ede, T. Kesavan, P. Ragupathy, M. D. Mukadam, S. M. Yusuf, and S. Kundu, RSC Advances **4** (72), 38169 (2014).

36   M. Mączka, M. Ptak, M. Kurnatowska, L. Kępiński, P. Tomaszewski, and J. Hanuza, Journal of Solid State Chemistry **184** (9), 2446 (2011).

37   L. Dura, H. Gibhardt, J. Leist, P. Becker, L. Bohatý, and G. Eckold, Journal of Physics: Condensed Matter **24** (33), 335901 (2012).

38   P. Van Hanh, L. Huy Hoang, P. Van Hai, N. Van Minh, X.-B. Chen, and I.-S. Yang, Journal of Physics and Chemistry of Solids **74** (3), 426 (2013).

39   L. H. Hoang, P. V. Hanh, N. D. Phu, X.-B. Chen, and W. C. Chou, Journal of Physics and Chemistry of Solids **77**, 122 (2015).

40   M. Khaksar, D. M. Boghaei, and M. Amini, Comptes Rendus Chimie **18** (2), 199 (2015).

41   M. Amina, T. Amna, M. S. Hassan, N. M. Al Musayeib, S. S. S. Al-Deyab, and M.-S. Khil, Korean Journal of Chemical Engineering **33** (11), 3169 (2016).

42   S. Oishi and M. Hirao, Journal of Materials Science Letters **8** (12), 1397 (1989).

43   Z. Lou and M. Cocivera, Materials Research Bulletin **37** (9), 1573 (2002).

44   D. Chen, G. Shen, K. Tang, H. Zheng, and Y. Qian, Materials Research Bulletin **38** (14), 1783 (2003).

45   V. M. Longo, L. Gracia, D. G. Stroppa, L. S. Cavalcante, M. Orlandi, A. J. Ramirez, E. R. Leite, J. Andrés, A. Beltrán, J. A. Varela, and E. Longo, The Journal of Physical Chemistry C **115** (41), 20113 (2011).

46   M. Mai and C. Feldmann, Journal of Materials Science **47** (3), 1427 (2011).

47   P. Mogilevsky, T. A. Parthasarathy, and M. D. Petry, Acta Materialia **52** (19), 5529 (2004).

48   M. A. M. A. Maurera, A. G. Souza, L. E. B. Soledade, F. M. Pontes, E. Longo, E. R. Leite, and J. A. Varela, Materials Letters **58** (5), 727 (2004).

49   L. S. Cavalcante, V. M. Longo, J. C. Sczancoski, M. A. P. Almeida, A. A. Batista, J. A. Varela, M. O. Orlandi, E. Longo, and M. S. Li, CrystEngComm **14** (3), 853 (2012).

50   S. Vidya, S. Solomon, and J. K. Thomas, Journal of Electronic Materials **42** (1), 129 (2012).

51   X. Lai, Y. Wei, D. Qin, Y. Zhao, Y. Wu, D. Gao, J. Bi, D. Lin, and G. Xu, Integrated Ferroelectrics **142** (1), 7 (2013).

52   Q. Li, Y. Shen, and T. Li, Journal of Chemistry **2013**, 5 (2013).

53   Y. Li, Z. Wang, L. Sun, Z. Wang, S. Wang, X. Liu, and Y. Wang, Materials Research Bulletin **50**, 36 (2014).

54   G. L. Katelnikovas A, Millers D, Pankratov V, and Kareiva A, Lithuanian Journal of Physics **47** (1), 63 (2007).

55   Y. Su, G. Li, Y. Xue, and L. Li, The Journal of Physical Chemistry C **111** (18), 6684 (2007).

56   L. Li, Y. Su, and G. Li, Applied Physics Letters **90** (5), 054105 (2007).

57   C. Lin, C. Jiexin, W. Cong, C. Ping, P. De'an, and A. A. Volinsky, Bulletin of Materials Science **35** (5), 767 (2012).

58   K. Dabre and S. Dhoble, Advanced Materials Letters **4** (12), 921 (2013).

59   H. Farsi and Z. Barzgari, Materials Research Bulletin **59**, 261 (2014).

60   H. Farsi, Z. Barzgari, and S. Z. Askari, Research on Chemical Intermediates **41** (8), 5463 (2014).

61   H. Letheby, Journal of the Chemical Society **15** (0), 161 (1862).

62   J. B. Cohen, Journal of the Society of Dyers and Colourists **3** (7), 104 (1887).

63   A. S. Travis, Technology and Culture **35** (1), 70 (1994).

64   R. Sharma, R. Malik, S. Lamba, and S. Annapoorni, Bulletin of Materials Science **31** (3), 409 (2008).

65   N. G. Deshpande, Y. G. Gudage, R. Sharma, J. C. Vyas, J. B. Kim, and Y. P. Lee, Sensors and Actuators B: Chemical **138** (1), 76 (2009).

66   L. Al-Mashat, K. Shin, K. Kalantar-zadeh, J. D. Plessis, S. H. Han, R. W. Kojima, R. B. Kaner, D. Li, X. Gou, S. J. Ippolito, and W. Wlodarski, The Journal of Physical Chemistry C **114** (39), 16168 (2010).

67   L. Shi, X. Wang, L. Lu, X. Yang, and X. Wu, Synthetic Metals **159** (23–24), 2525 (2009).

68   S. B. Kondawar, M. D. Deshpande, and S. P. Agrawal, International Journal of Composite Materials **2** (3), 32 (2012).

69   Z. F. Li and E. Ruckenstein, Langmuir : the ACS journal of surfaces and colloids **18** (18), 6956 (2002).

70   A. Mostafaei and A. Zolriasatein, Progress in Natural Science: Materials International **22** (4), 273 (2012).

71   F. Meng, X. Yan, Y. Zhu, and P. Si, Nanoscale research letters **8** (1), 179 (2013).

72   A. C. Nwanya, C. J. Jafta, P. M. Ejikeme, P. E. Ugwuoke, M. V. Reddy, R. U. Osuji, K. I. Ozoemena, and F. I. Ezema, Electrochimica Acta **128**, 218 (2014).

73   L. Wang, X. Lu, S. Lei, and Y. Song, J. Mater. Chem. A **2** (13), 4491 (2014).

74   T. Sen, S. Mishra, and N. G. Shimpi, RSC Advances **6** (48), 42196 (2016).

75   M. Khairy and M. E. Gouda, Journal of advanced research **6** (4), 555 (2015).

76   Y. T. Ravikiran, M. T. Lagare, M. Sairam, N. N. Mallikarjuna, B. Sreedhar, S. Manohar, A. G. MacDiarmid, and T. M. Aminabhavi, Synthetic Metals **156** (16–17), 1139 (2006).

77   T. Machappa and M. V. N. A. Prasad, Ferroelectrics **392** (1), 71 (2009).

78   Y. F. Zhu, Q. Q. Ni, Y. Q. Fu, and T. Natsuki, Journal of nanoparticle research : an interdisciplinary forum for nanoscale science and technology **15**, 1988 (2013).

79   S. Koul, R. Chandra, and S. K. Dhawan, Polymer **41** (26), 9305 (2000).

80   D. Ashis, D. Sukanta, D. Amitabha, and S. K. De, Nanotechnology **15** (9), 1277 (2004).

81   S. K. Pillalamarri, F. D. Blum, A. T. Tokuhiro, and M. F. Bertino, Chemistry of Materials **17** (24), 5941 (2005).

82   Z. Durmus, A. Baykal, H. Kavas, and H. Sözeri, Physica B: Condensed Matter **406** (5), 1114 (2011).

83   H. Jianjun, D. Yuping, Z. Jia, J. Hui, L. Shunhua, and L. Weiping, Physica B: Condensed Matter **406** (10), 1950 (2011).

84   S. V. Bhat and S. R. C. Vivekchand, Chemical Physics Letters **433** (1-3), 154 (2006).

85   S. Banerjee, S. Sarmah, and A. Kumar, Journal of Optics **38** (2), 124 (2009).

86   I. Sapurina, S. Fedorova, and J. Stejskal, Langmuir : the ACS journal of surfaces and colloids **19** (18), 7413 (2003).

87   W. R. Caseri, Materials Science and Technology **22** (7), 807 (2006).

88   D. R. Paul and L. M. Robeson, Polymer **49** (15), 3187 (2008).

89   S. Bhadra, D. Khastgir, N. K. Singha, and J. H. Lee, Progress in Polymer Science **34** (8), 783 (2009).

90   W. Guowu, V. Raju, and W. Jin-Ye, Mini-Reviews in Organic Chemistry **14** (1), 56 (2017).

91   A. G. MacDiarmid, Reviews of Modern Physics **73** (3), 701 (2001).

92   N. Gospodinova and L. Terlemezyan, Progress in Polymer Science **23** (8), 1443 (1998).

93   X. Li, D. Wang, G. Cheng, Q. Luo, J. An, and Y. Wang, Applied Catalysis B: Environmental **81** (3–4), 267 (2008).

94   X. Li, Y. Chai, H. Zhang, G. Wang, and X. Feng, Electrochimica Acta **85**, 9 (2012).

95   S. Saranya, R. K. Selvan, and N. Priyadharsini, Applied Surface Science **258** (11), 4881 (2012).

96   X. Zhang, S. Wei, N. Haldolaarachchige, H. A. Colorado, Z. Luo, D. P. Young, and Z. Guo, The Journal of Physical Chemistry C **116** (29), 15731 (2012).

97   F. Muhammad and K. Syed, Bulletin of the Korean Chemical Society **34** (1), 99 (2013).

98   A. V. Krasheninnikov and K. Nordlund, Journal of Applied Physics **107** (7), 071301 (2010).

99   E.-J. Yun, J. W. Jung, Y. H. Han, M.-W. Kim, and B. C. Lee, Journal of Applied Physics **105** (12), 123509 (2009).

100   K. Jeon, S. W. Shin, J. Jo, M. S. Kim, J. C. Shin, C. Jeong, J. H. Lim, J. Song, J. Heo, and J. H. Kim, Current Applied Physics **14** (11), 1591 (2014).

101 K. K. Babitha, K. P. Priyanka, A. Sreedevi, S. Ganesh, and T. Varghese, Materials Characterization **98**, 222 (2014).

102 P. A. Sheena, K. P. Priyanka, S. Aloysius, N., S. Ganesh, and V. Thomas, Bulletin of Materials Science **38** (4), 825 (2015).

103 A. Sreedevi, K. P. Priyanka, K. K. Babitha, S. Ganesh, and V. T, Micron **88**, 1 (2016).

104 L. Chen, Z. Xu, J. Li, C. Min, L. Liu, X. Song, G. Chen, and X. Meng, Materials Letters **65** (8), 1229 (2011).

105 Y. J. Kwon, H. Y. Cho, H. G. Na, B. C. Lee, S. S. Kim, and H. W. Kim, Sensors and Actuators B: Chemical **203**, 143 (2014).

106 K. Siraj, M. Khaleeq-ur-Rahman, M. S. Rafique, and T. Nawaz, Nuclear Instruments and Methods in Physics Research Section B: Beam Interactions with Materials and Atoms **269** (1), 53 (2011).

107 R. Verma, R. Dhar, V. K. Agrawal, I. M. L. Das, M. C. Rath, S. K. Sarkar, V. K. Wadhawan, and R. Dabrowski, Molecular Crystals and Liquid Crystals **547** (1), 18/[1708] (2011).

108 K. Ding, Y. Feng, S. Huang, B. Li, Y. Wang, H. Liu, and G. Qian, Nanotechnology **23** (41), 415703 (2012).

109 A. Aierken, Q. Guo, T. Huhtio, M. Sopanen, C. F. He, Y. D. Li, L. Wen, and D. Y. Ren, Radiation Physics and Chemistry **83**, 42 (2013).

110 S. Chethan Pai, M. P. Joshi, S. Raj Mohan, U. P. Deshpande, T. S. Dhami, J. Khatei, K. S. Koteshwar Rao, and G. Sanjeev, Journal of Physics D: Applied Physics **46** (17), 175304 (2013).

111 P. K. S. Rao, S. Krishnan, M. Pattabi, and G. Sanjeev, Radiation Physics and Chemistry **113**, 36 (2015).

112   J. A. Sundararajan, M. Kaur, and Y. Qiang, The Journal of Physical Chemistry C **119** (15), 8357 (2015).

113   C. J. Benedict, A. Rao, G. Sanjeev, G. S. Okram, and P. D. Babu, Journal of Magnetism and Magnetic Materials **397**, 145 (2016).

114   B. S. Nagaraja, A. Rao, P. D. Babu, G. Sanjeev, and G. S. Okram, Nuclear Instruments and Methods in Physics Research Section B: Beam Interactions with Materials and Atoms **366**, 188 (2016).

115   W. Toshimi, K. Toshihiko, I. Shingo, S. Yoshinobu, and K. Masanori, Japanese Journal of Applied Physics **33** (12S), 7228 (1994).

116   Y. Katsumi, H. Shigenori, and I. Yoshio, Japanese Journal of Applied Physics **21** (9A), L569 (1982).

117   R. E. Norris, C. J. Janke, C. Eberle, and G. E. Wrenn, (SAE International, 2000).

118   M. M. Nasef, H. Saidi, and K. Z. M. Dahlan, Radiation Physics and Chemistry **68** (5), 875 (2003).

119   S. Bhadra and D. Khastgir, Polymer Degradation and Stability **92** (10), 1824 (2007).

120   F. Ziaie, M. Borhani, G. Mirjalili, and M. A. Bolourizadeh, Radiation Physics and Chemistry **76** (11–12), 1684 (2007).

121   Sangappa, T. Demappa, Mahadevaiah, S. Ganesha, S. Divakara, M. Pattabi, and R. Somashekar, Nuclear Instruments and Methods in Physics Research Section B: Beam Interactions with Materials and Atoms **266** (18), 3975 (2008).

122   K. Hareesh and G. Sanjeev, Materials Sciences and Applications **02(11)**, 6 (2011).

****ೲ✪ೞ****

Chapter - 2
MATERIALS AND METHODS

An overview of materials used for the chemical synthesis of samples, experimental methods and various characterization techniques adopted are presented in this chapter along with a brief description about the theory and procedures related to various studies.

2.1 Materials

Chemicals used to synthesize different samples are listed below.

(a) $MnWO_4$ nanocrystals: Manganese chloride ($MnCl_2.4H_2O$, 99.8%, Sigma Aldrich) and sodium tungstate ($Na_2WO_4.2H_2O$, 99.9%, Alfa Aesar).

(b) $CaWO_4$ nanocrystals: Calcium nitrate (Ca $(NO_3)_2.4H_2O$, 99.8%, Sigma Aldrich) and sodium tungstate ($Na_2WO_4.2H_2O$, 99.9%, Alfa Aesar).

(c) Polyaniline nanocomposite: Aniline ($C_6H_5NH_2$, 99%) as monomer, ammonium per sulphate (APS), $(NH_4)_2S_2O_8$, 98.5% from Merck as

oxidant, hydrochloric acid (HCl, 37%, Sigma Aldrich) as dopant and nanocrystalline tungstates obtained by chemical precipitation.

All the chemicals used are of AR grade and distilled water is used to prepare solutions.

2.2   Synthesis methods

The synthesis employs chemical precipitation method [1,2] for the fabrication of nanocrystalline tungstates. Polyaniline nanocomposites of tungstates are prepared *in-situ* by the oxidative polymerization [3-5]. Brief descriptions of each of these methods and the preparation of powder samples are given in the following subsections.

2.2.1   Chemical precipitation

In this method, particles are precipitated from aqueous and ionic solutions of the reactants when they are allowed to react in a controlled manner. When the solution becomes supersaturated, the nucleation begins. The tiny particles grow with time and get precipitated. The size and shape of the particles formed depend on several factors such as pH value, concentration, temperature and pressure. So the chemical kinetics has to be controlled in order to produce nanoparticles required for specific applications.

The precipitate is separated from the supernatant by careful decantation, which is again stirred in distilled water and allowed to settle down. This process is repeated several times to ensure high purity. The

precipitate obtained is then dried in a hot-air oven at 70ºC for 24 h. The dried product is then well powdered using an agate mortar.

2.2.2 Chemical oxidative polymerization

Conventional chemical synthesis of conductive polyaniline is based on the oxidative polymerization of aniline using an oxidant in the presence of a strong acid dopant. Tungstate nanoparticles dispersed in a suitable solvent are added in portions during the polymerization process to synthesize polyaniline nanocomposite. The properties of the final product greatly depend on the type of dopant, temperature, concentration of the reactants and polymerization time. In this work, all the synthesis procedures are performed only at room temperature.

2.3 Characterization techniques

A number of characterization techniques are available to explore various properties of the nanomaterial. The thermal stability of the sample is studied using thermogravimetric analysis (TGA), differential thermal analysis (DTA) and differential scanning calorimetry (DSC). The structural characterizations of the materials are performed using powder X- ray diffraction (XRD), scanning electron microscopy (SEM) and transmission electron microscopy (TEM). The elemental details are obtained from energy dispersive X-ray spectrum (EDS). Fourier transformed infrared (FT-IR) and Raman spectroscopy are used to determine different vibration modes, which in turn reveal different bonds and functional groups in the material synthesized. These methods can also give information about the

purity of the material. The optical properties are studied using UV-Visible (UV) and photoluminescence (PL) spectroscopy. In the subsections, the principle involved in each type of analysis and the details of the instruments used are shortly described.

2.3.1 Thermal studies

Three methods namely TGA, DTA and DSC are generally employed in order to determine the changes occurring to a specimen as a result of heating from room temperature up to certain high temperature [6]. The principle involved in each of these methods is described below.

(a) TGA measures the weight loss occurring to a sample as a function of temperature or time in comparison to an inert reference sample, when both are heated in a furnace. Also, the rate of change of weight in relation to temperature or time can be recorded using derivative thermogravimetry (DTG) [7]. From DTG, it is possible to determine each of the temperatures at which a thermal event becomes prominent. The thermogram helps in drawing conclusions about changes like dehydration, decomposition and crystallization.

(b) DTA detects the temperature difference between the sample and reference as a function of temperature or time due to the evolution or absorption of heat accompanying a thermal event in the sample. In such cases heat energy flows out or into the material under test producing a temperature difference between the sample and

reference. From the nature of the DTA curve, it can be concluded whether physical or chemical change is exothermic or endothermic.

(c) DSC monitors the heat flow into the sample to maintain constant temperature between the sample and reference. The heat flow into the sample peaks at a particular temperature. The area under the time versus heat flow curve gives the enthalpy involved in the process. In a similar manner other thermal effects like dehydration, evaporation, sublimation, chemical decomposition, crystallization and phase changes can be interpreted.

In short, both DTA and DSC are complementary to TGA in the thermal characterization. A simultaneous thermal analyzer STA 6000 (Perkin Elmer) is used for the thermal analysis. The sample is heated from 40 to 900 °C at 10 °C/min. Weight of the sample taken is about 10 to 20 mg.

2.3.2 X-ray diffraction

The interatomic spacing in crystals is of the order of the wavelength of X-rays (0.5-2.5 Å). So, a crystal can act as a three dimensional grating for producing a diffraction pattern. When X-rays are incident on a crystal, their electric field components interact with atomic electrons in different parallel crystal planes and they undergo elastic scattering. X-rays scattered in certain specific directions get superposed to produce a diffraction pattern obeying Bragg's law represented by the relation [8,9],

$$2d\sin\theta = n\lambda, \qquad\qquad\qquad (2.1)$$

where d is the distance between adjacent crystal planes, θ the angle of diffraction, n the order of diffraction and λ the wavelength of incident monochromatic X-ray. The scattered X-rays carry information about the arrangement of atoms within the crystal. Also, the intensity is found to depend on the inter-planar spacing and incident wave angle. The orderly arrangement of atoms produces intense peak. XRD pattern contains information regarding crystal structure and lattice parameters. Any stress or strain occurring to a material's crystal structure will be reflected in the peak position. The stress strain analysis can be performed to draw certain conclusions regarding the material properties. Modern X-ray diffractometer is equipped with computer programs to generate all information pertaining to a crystal.

In powder XRD, the sample is taken in fine powder form, and each powder particle is polycrystalline. The output of the XRD experiment is generally obtained as a plot of 2θ versus intensity of the diffracted beam. Average particle size *D* is calculated from the XRD plot using the Scherrer equation [10, 11],

$$D = \frac{k\lambda}{\beta cos\theta},$$
(2.2)

where k is a constant known as shape factor which is approximately 0.89 for spherical shape, λ= 1.5406 Å is the wavelength of Cu K_α radiation and β the full width at half maximum of the peak at *2θ* value. The crystal phase, crystal planes and unit cell parameters of the samples can be

determined by comparing the XRD pattern obtained with standard data files of the Joint Committee on Powder Diffraction Standards (JCPDS).

In this research work, the powder samples are analysed using the Advance X-ray Spectrometer AXS Bruker D8. The X-ray source is a sealed tube with a copper anode operating at a generator voltage of 40 kV and a current of 35 mA. The Cu K_{α} radiation ($\lambda = 1.5406$ Å) filtered by Ni is incident on the sample. Intensity is measured against 2θ angle in the range of 10-80º.

2.3.3 Scanning electron microscope

In order to investigate the surface features of a material and the distributions of particles on the surface, a scanning electron microscope is used. High magnifications of the order of 10^6 can be attained in SEM which is not possible with an optical system. A SEM consists of an electron gun, a condenser lens and an objective lens to produce an electron probe. A scanning coil scans the electron probe over the surface of the specimen. All these components are situated in a highly evacuated column. The specimen holder is also kept under vacuum. There is a detector system to detect the secondary electron signals coming from the specimen surface. The signals are then fed to the display system as intensity modulating signals [12]. The intensity of signals from different atoms and different topographies are different. The contrast in the final image represents the surface features like the size and shape. It also gives a picture of the distribution of particles on the surface of the material.

There are SEMs with any of the three types of electron guns, namely thermionic emission (TE), field emission (FE) and Schottky emission (SE) guns [13]. Ultra high vacuum of the order of 10^{-8} Pa is needed for FE. The advantage of FE gun over TE gun is that it requires no heating. Hence, FE gun produces only lesser energy spread. Another advantage is that the electron probe is narrow (5-10 nm) compared to that of TE (10-20 μm). For these reasons, a Field Emission SEM (FE SEM) is used to get high resolution image. SE gun requires high electric field as well as heating, hence energy spread is more. But, larger probe current makes it possible to observe properties other than surface features too.

The surface micrographs of the samples are taken using JEOL Model JSM-6390LV scanning electron microscope (resolution-3.0 nm). A double sided carbon tape is lightly covered with fine sample dust. Using a sputtering unit it is coated with a thin layer of gold to avoid charging effect and is then placed on a metal stub. In some cases, where high resolution images are needed, FEI Nova NanoSEM 450 (FESEM: resolution-1.8 nm, high vacuum, 3 kV) is used.

2.3.4 Energy dispersive X-ray spectrum analysis

The X-rays emitted from the sample due to its interaction with high energy electron beams are characteristic of the type of elements producing them. Hence, an energy dispersive X-ray analysis is performed to find out the different elements present in a sample. Often the facility for EDS

analysis accompanies a SEM set up. In this study, a JEOL Model JED – 2300 and BRUKER X Flash 6/10EDS detectors are employed.

2.3.5 Transmission electron microscope

The shapes and size distribution of the particles in a sample can be studied using transmission electron microscope [14]. The crystal lattice and defects can also be analysed when TEM is used in the proper mode.

In a TEM set up, electrons from an electron gun are accelerated by several hundred kilovolts and are controlled by a system of electromagnetic lenses [15]. The whole electron system is kept under high vacuum (10^{-5} Pa). The electron beam is transmitted through a thin layer (~ 500 nm) of the specimen placed between the condenser and objective lenses. Many electrons passing through the sample suffer nearly elastic scattering and emerge in different directions. They carry information regarding the nanostructure and distribution of particles within the sample. TEM images can be obtained from the display unit attached to the detecting system. The extent of details collected depends on the wavelength of the electrons in the incident beam, the beam size and the aberration coefficients of the lenses used. The beam size can be controlled by using apertures at different stages. The wavelength of electrons is given by the equation [16],

$$\lambda = \frac{0.0388}{\sqrt{V}} \text{nm}, \tag{2.3}$$

where V is the accelerating voltage expressed in kV. In a 200 kV TEM this wavelength turns out to be 0.0027 nm.

The electron beam transmitted through the specimen contains both scattered (diffracted) and the direct beams. Depending on the mode of operation, different contrasts can be developed in TEM images. Real space image can be obtained when the TEM is operated in the image mode and diffraction pattern (reciprocal space) in the diffraction mode [17]. In the former case, the diffracted electrons emerging from the specimen are screened from reaching the image plane with the help of an aperture and the image obtained is called bright field image. In the latter case, the direct beam is blocked and the image captured is a dark field image. The bright field imaging method is widely used in analysis.

Crystal lattices can be imaged using high resolution TEM (HRTEM) technique [17]. Unlike bright and dark field imaging, where one electron beam is used, an HRTEM utilizes many beams for imaging. To facilitate this, a very large aperture is selected. In this case imaging is achieved by the phase difference contrast between the direct beam and the scattered beam [17, 18]. The diffracted beams interfere with the direct beam and the phase difference is imaged. It is possible to draw conclusions on lattice spacing, orientation and various types of lattice defects by closely studying the HRTEM image.

Diffraction pattern due to large area of the specimen can be recorded using selected area electron diffraction (SAED). For this, a large area of the specimen is illuminated with a parallel beam and an aperture placed in the first image plane selects an area of interest. Simple pattern of spots corresponds to single crystalline, ring pattern to polycrystalline and highly

diffused to amorphous samples. From the details in the SAED pattern, the structure of the specimen can be confirmed.

In TEM analysis, the powder sample is first suspended in ethanol or water by ultrasonication. It is then coated on carbon coated copper grid by drop casting. In the present study, TEM analyses are done using the JEOL JEM 2100 accelerated by 200 kV. This instrument has a resolution of 0.24 nm.

2.3.6 Fourier transform infrared spectroscopy

A routine test to identify the different functional groups and chemical bonds present in a specimen are carried out using an infrared (IR) spectrometer. Infrared radiations have lesser energy than visible light and their interactions with the specimen can cause excitation of the chemical bonds to various vibrational energy levels that are very close to each other. Only molecules having a net dipole moment are IR active.
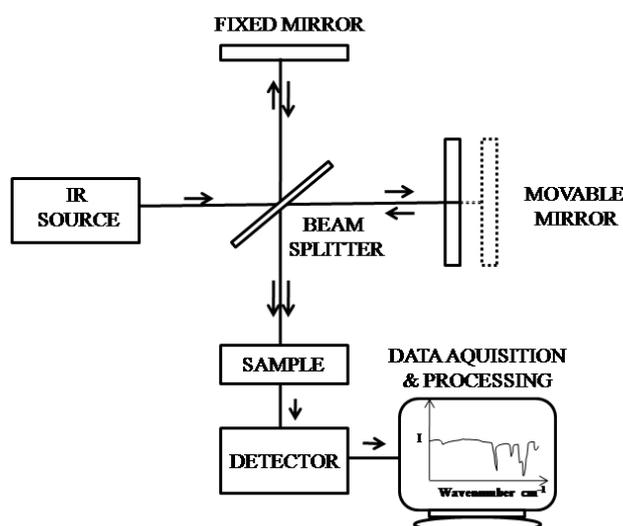
Fig. 2.1 Schematic diagram of FTIR spectrometer

A simplified schematic diagram of a modern IR spectrometer is shown in Fig. 2.1. It makes use of the help of a Michelson's interferometer. A beam of radiations emitted from an infrared source is split into two beams by the beam splitter. Path difference can be introduced between the two beams by adjusting the movable mirror. In the final stages they interfere, pass through the sample and the intensity is detected as electrical signals.

A plot of light intensity versus optical path difference (interferogram) for a mirror moving back and forth once (one scan) from the beam splitter is obtained. Sometimes several such scans are taken and averaged to obtain the final spectrum. To each wavenumber there corresponds a Fourier frequency (F) given by the relation [19],

$$F = 2vW, \tag{2.4}$$

where v is the constant velocity of the moving mirror in cms^{-1} and W the wavenumber in cm^{-1}. In FT-IR spectrometer, interferograms in the time domain are Fourier transformed to frequency domain. Spectrum of the sample is corrected for background radiations. The output of the FTIR analysis is obtained as a plot of percentage transmittance versus wavenumber.

In this research work, FT-IR spectrum is recorded by Thermo Nicolet, Avathar 370 spectrophotometer in the IR wavenumber range (4000-400 cm^{-1}) having a resolution of 4 cm^{-1}.

2.3.7 Raman spectroscopy

Raman spectroscopy is another method by which rotational and vibrational spectra of molecules are studied. The working of a Raman spectrometer is based on the inelastic scattering of monochromatic light by transparent materials, an effect that was discovered by Chandrasekhara Venkata Raman in the year 1928 [20]. According to classical theories, molecules showing variation in polarizability as their vibrations are Raman-active. For this reason, diatomic molecules like H_2 or N_2 become Raman-active. Unlike IR spectroscopy discussed above, where absorption of radiation is utilized, Raman spectroscopy makes use of inelastic scattering of light. The scattered light contains information about the particular bond or functional groups present in a specimen.
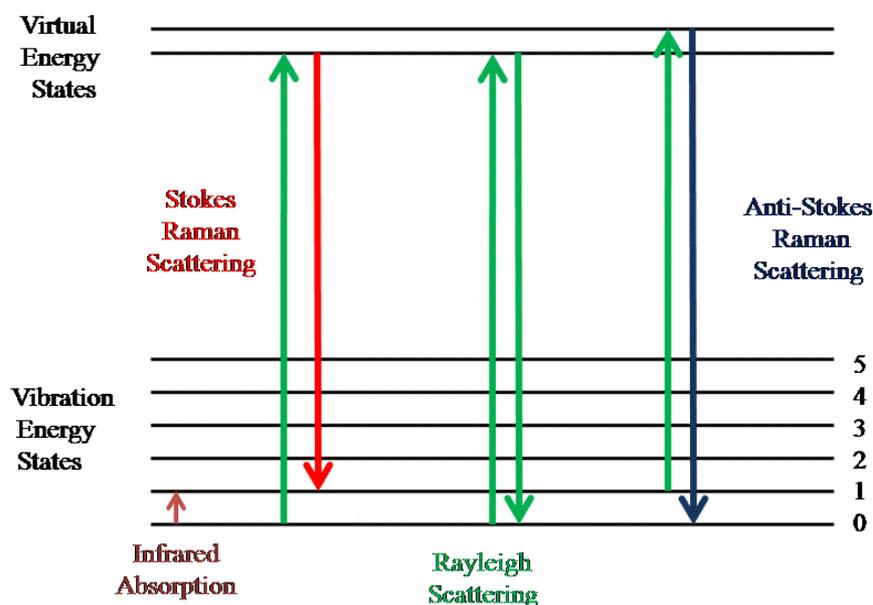
Fig. 2.2 Schematic of different optical processes related to Raman effect

The Raman scattering is represented schematically in Fig. 2.2. The major part of the scattered light is due to elastic (Rayleigh) scattering. The intensity of the Raman scattered light (Stokes and anti-Stokes lines) is very low and is usually detected by suppressing the intense elastic scattered components. Stokes lines are re-emitted light having a frequency lower than the incident radiation. This happens when energy is lost by the incident radiation in the excitation-deexcitation process. The molecule is first excited from a ground state vibration level to a virtual state and then it returns to a vibration level above the original vibration energy level by emitting the Stokes line. The anti-Stokes lines originate when the excitation begins from a level above the ground state. When the excited molecule returns to the ground state, the emitted light has more energy than the Rayleigh scattered light. Since the origin of excitation leading to Stokes line is from a vibration level lower than that for the anti-Stokes line, the occurrence of Stokes line is more probable. Hence, stokes lines are more intense and are easily detected than anti-Stokes line. The difference in energy between the Rayleigh and Raman scattered light happens to be in the infrared region. The corresponding frequency difference is the Raman shift which is usually expressed in wavenumber unit (cm^{-1}).

In this study a BRUKER RFS 27 FT-Raman Spectrometer is used for the Raman studies. It is a multi RAM stand alone model operating in the spectral range from 4000 to 50 cm^{-1} having a resolution of 2 cm^{-1}. The laser source used is Neodymium-doped yttrium aluminium garnet (Nd: YAG) operating at 100 mW power. It is a continuous laser with an output

wavelength of 1064 nm. Powder samples are taken on a metal plate for the analysis.

2.3.8 Ultraviolet-visible spectroscopy

Light having wavelength in the range 200 to 400 nm are called ultraviolet light and those in the range 400 to 800 nm visible light. When ultraviolet-visible (UV-Visible) light is passed through a material, certain wavelengths that are characteristic of the material are absorbed. The working of UV-Visible spectrophotometer is based on the absorption of electromagnetic radiations by the sample in the ultraviolet, visible and near infrared range (200-1000 nm). Along with absorption, a certain part of the incident light gets reflected and another part gets transmitted. Measurements based on absorbance, reflectance and transmittance can be performed by selecting suitable modes of operation of the instrument. In the modern instruments, it is also possible to analyse diffuse reflectance of a powder sample. By measuring absorbance against wavelengths and plotting graph, it is possible to calculate its optical bandgap.

A schematic diagram representing the working of a UV-Visible spectrophotometer is illustrated in Fig. 2.3. Transparent solution of the sample (S) in a suitable solvent and a reference sample (R) are taken in quartz cuvettes. Light from a deuterium lamp and a tungsten filament are paralleled at mirror M_1. After passing through a filter and monochromator the light is divided into two beams by the beam splitter. One beam after reflection at mirror M_2 passes through R and the other through S. The

transmitted beams are detected by photodiodes (PD). The signals are digitized using A to D converters and then finally processed by the computer. The output is obtained as a plot of absorbance versus wavelength in nanometres.
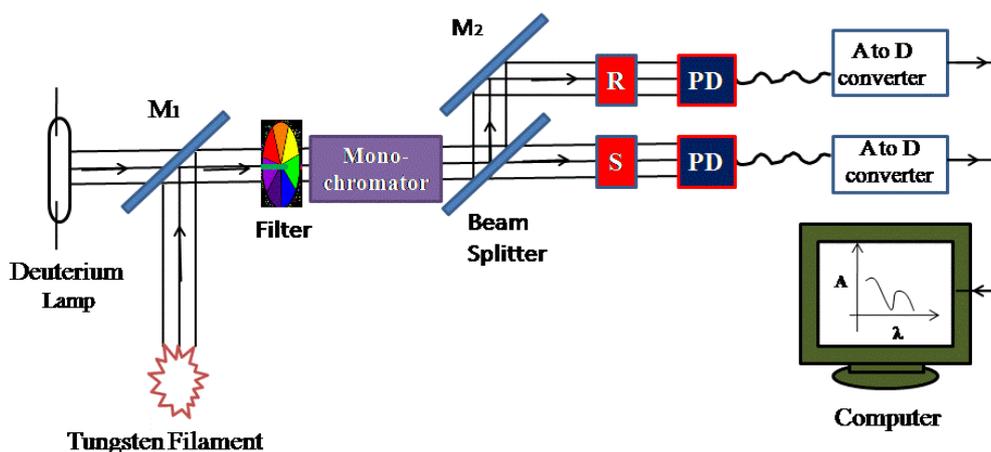
Fig. 2.3 Working scheme of a UV-Visible spectrometer

The optical absorption spectra of the samples are recorded using a Shimadzu UV-2600 in the spectral range 200-1000 nm. In this instrument reflectance of powder samples can be measured and the absorbance can be obtained through Kubelka Monk transformation.

Bandgap determination

Absorption coefficients of powder samples for a given wavelength range can be obtained from the reflectance measurements by the Kubelka Munk transformation [21]. The bandgap of the material is estimated using the Tauc (1974) relation [22],

$$\alpha h\nu = A(h\nu - E_g)^n, \hspace{3cm} (2.5)$$

where A is a constant, h the Planck's constant, ν the frequency, E_g the energy gap and n is a constant associated with the kind of electronic transition ($n = 1/2$ for the direct allowed, $n = 3/2$ for the direct forbidden, $n = 2$ for the allowed indirect transition and $n = 3$ for the indirect forbidden). $(\alpha h\nu)^{1/n}$ versus $h\nu$ curve has a linear region, which when extrapolated to $(\alpha h\nu)^{1/n} = 0$ gives the value corresponding to energy gap.

2.3.9 Photoluminescence spectroscopy

In photoluminescence, materials absorb electromagnetic radiations like X-rays, UV or visible light and re-emit light of a longer wavelength. If the re-emission takes place within 10^{-8} second, the process is called fluorescence and if it takes longer time it is phosphorescence. PL spectrum of a pure sample is the characteristic of that material. It is greatly affected by the presence of defects and impurity levels within the forbidden gap. Various intermediate steps involved during the excitation- deexcitation processes are depicted in the energy level diagram in Fig. 2.4. S_1, S_2, and S_3 are singlet states and T, a triplet state. A molecule absorbing high energy radiation is excited to higher vibrational level in S_2 and from there it suffers few vibrational relaxations followed by internal conversion and reaches the top vibrational level in S_1. Again after a few vibrational relaxations it reaches the lowest state in S_1. Here after there are two possibilities leading to photoluminescence. In the first case, the molecule emits radiation and returns to the ground state. Such overall transitions are sudden and results in

fluorescence. In the second case, the electron may undergo a spin flipping so that the molecule is left in the state T. This process consumes little energy and is called intersystem crossing. A molecule in higher vibrational level of T suffers vibrational relaxations and attains the lowest level. From there the molecule returns to the ground state by emitting radiations of higher wavelengths.
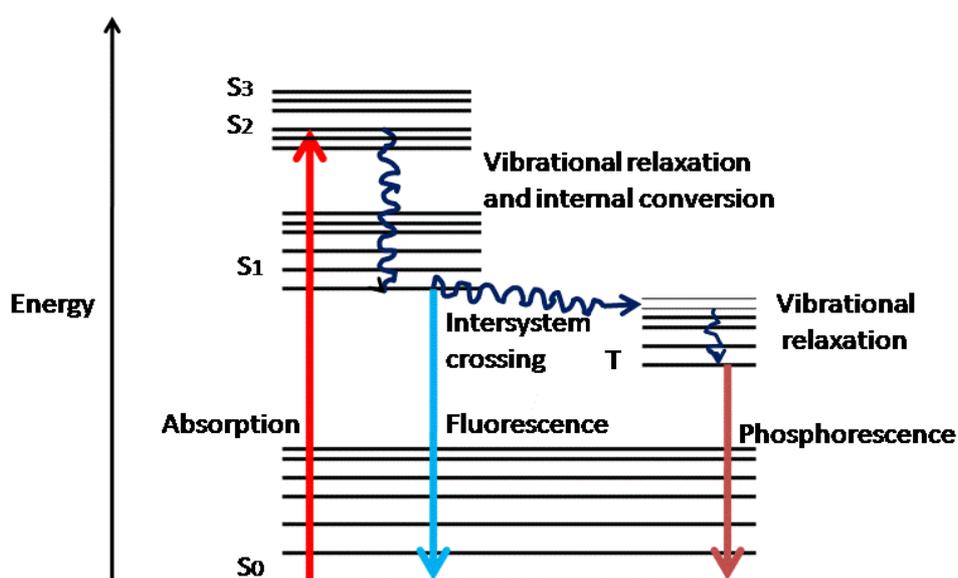
Fig. 2.4 Optical processes associated with photoluminescence

A simplified schematic of a PL spectrophotometer with the major components labelled is shown in Fig. 2.5. The source is a high pressure Xenon arc lamp. Monochromators are used to select the excitation and emission wavelengths. Reflection grating is used in the monochromator to disperse the different wavelength components. The detector used is usually a photomultiplier tube. A computer controls the instrument and helps in data acquisition and processing.
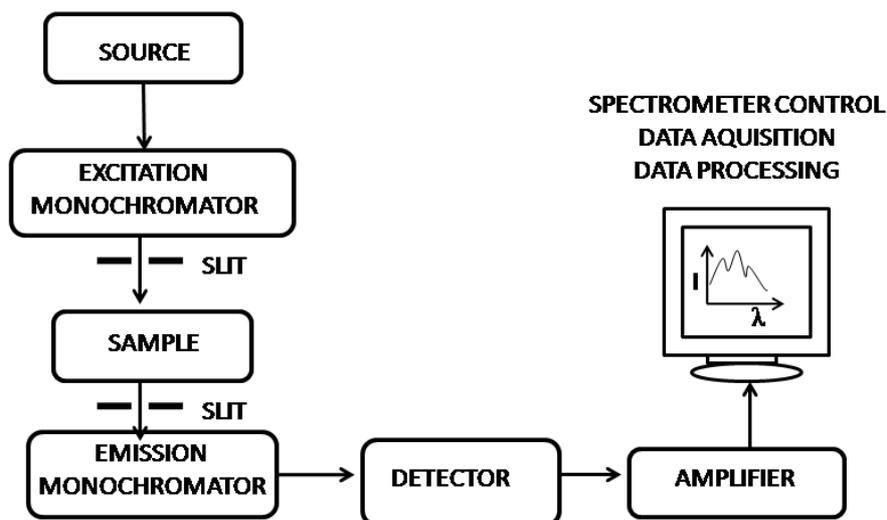
Fig. 2.5 Schematic of a PL spectrophotometer

In the present work, a Horiba Fluoromax-4 is used to carry out the photoluminescence studies. It is a spectrofluorimeter, which can operate in the range 200-950 nm with a scanning speed 80 nm/s.

2.4 Electron beam irradiation

The powder samples are exposed to different doses of electron beam from a variable energy Microton. The properties of the bare and irradiated samples are compared to draw important conclusions on the effects of electron beam irradiation.

In this investigation, powder samples are taken in polyethene covers and irradiated at different electron doses using 8 MeV variable energy Microton facility at the University of Mangalore, Mangalagangotri, India [23]. This Microtron has a maximum pulse current of 50 mA and a pulse rate of 50 Hz. An Image of this Microtron is shown in Fig. 2.6.
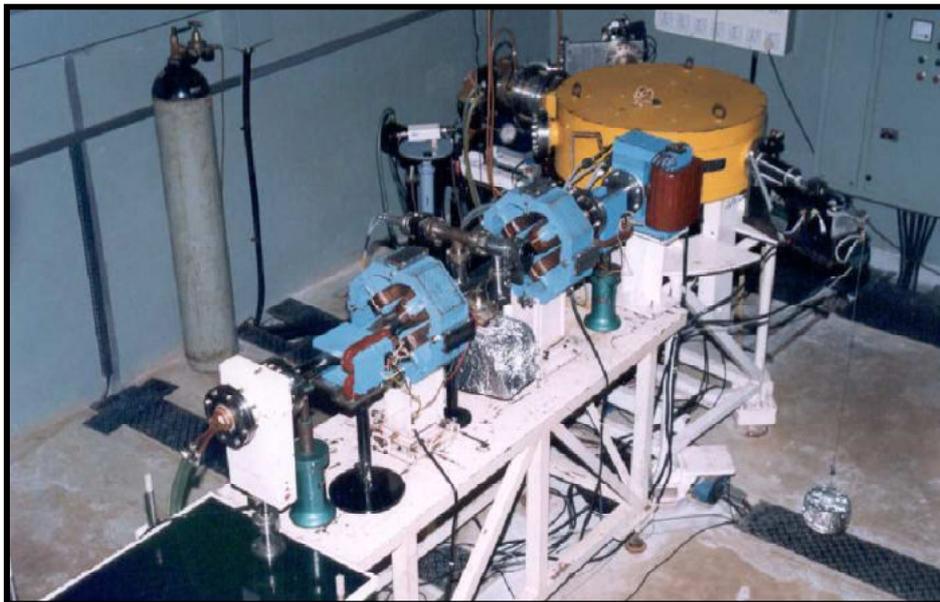
Fig. 2.6   8 MeV Microtron at Mangalore University

The samples are exposed to the electron beam at a distance of 30 cm from the exit port. The dose is uniform over an area of 8 x 8 cm^2, as determined by dosimetry.

2.5   DC electrical studies

In order to carry out the electrical studies, pellets of radius 13 mm are prepared out of the powder samples using a die and a hand operated hydraulic press. A pressure of approximately 8-10 tons is applied in all cases. The thickness of the pellets is chosen to suit the type of electrical measurements.

To determine the DC conductivity of highly resistive samples, a two point probe method is used. For low resistivity samples, the resistance of the probe wires and contact resistance introduce error in the measured value of resistance. Hence, the collinear four point probe method is used in such

cases. The outer probes are used for sourcing the current and the inner ones for measuring the voltage between two points on the sample surface. Here the voltage probes are separate and have direct contacts with the sample only. Since the voltmeter has very high input resistance, only very minute current will be drawn. Hence, errors due to the probe and contact resistances are greatly reduced. The instrument used for the DC electrical studies is Keithley's Model 2450 source meter.
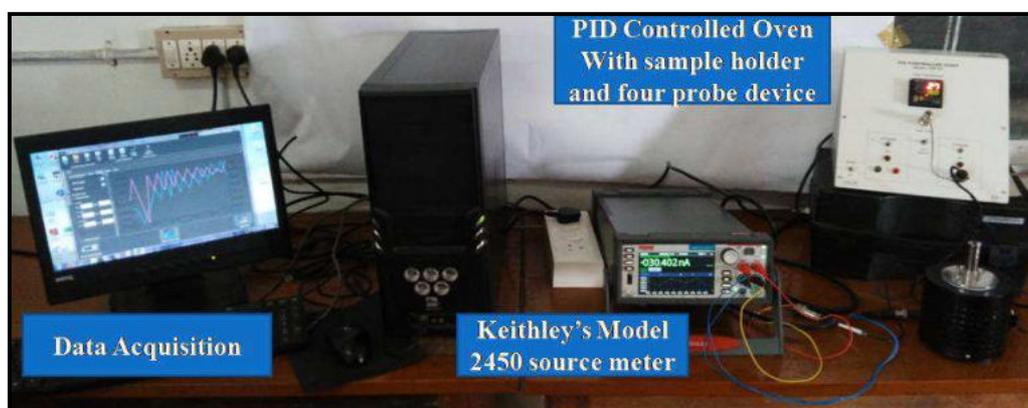
Fig. 2.7 Experimental set up for DC electrical studies

2.5.1 Resistivity equation for two point probe method

In the case of samples having uniform area of cross section, resistivity (ρ) is calculated using the equation,

$$\rho = \frac{RA}{t} \quad \Omega\text{-m,} \tag{2.6}$$

where R is the resistance, A the area of cross section and t the thickness of the pellet. The reciprocal of resistivity gives the DC conductivity (σ_{dc}) represented by the relation,

$$\sigma_{dc} = \frac{1}{\rho} \, \text{mho-m}^{-1} \tag{2.7}$$

2.5.2 Resistivity equation for four point probe method

In the four points probe method ρ is calculated using the equation [24],

$$\rho = \frac{\pi}{ln2} \frac{V}{I} tk \ \Omega\text{-cm,} \qquad (2.8)$$

where V is the voltage, I the current, t the thickness of the pellet in cm and

k the geometric correction factor calculated for the pellet and probes used. The value of k depends on the ratio of thickness of the pellet to the distance between probes and also on the ratio of the diameter of the pellet to the probe separation. Equation 2.8 is simplified as,

$$\rho = 4.532 \ \frac{V}{I} \ tk \ \Omega\text{-cm} \qquad (2.9)$$

$$\sigma_{dc} = \frac{1}{\rho} \ \text{S-cm}^{-1} \qquad (2.10)$$

2.6 Dielectric studies

The circular faces of the pellets used for dielectric studies are coated with silver paste (a conductive coating). When an electric field is applied across a parallel plate capacitor, the medium between the plates gets polarized. As a result of polarization, some of the charges stored in the plates get neutralized so that additional charges can be stored in it. Thus, the capacitance of the capacitor is greater with the presence of a medium between the plates. The polarisable medium between the plates, capable of storing electric energy, is called a dielectric.

Capacitance without dielectric

If a DC voltage is applied between the plates of a parallel plate capacitor, charges will be stored in it and its capacitance without dielectric is given by,

$$C = \varepsilon_0 \frac{A}{t},\qquad(2.11)$$

where A is the area of each plate, t the distance between the plates and $\varepsilon_0 = 8.854 \times 10^{-12}$ Fm^{-1} is a constant called the permittivity of free space.

Capacitance with dielectric

The capacitance with dielectric is given by,

$$C' = \varepsilon_0 \varepsilon_r' \frac{A}{t},\qquad(2.12)$$

where ε_r' is the real dielectric constant or permittivity.

$$C' = \varepsilon_r' C\qquad(2.13)$$

Complex dielectric constant

When an AC voltage V is applied to the capacitor, the total current I will be consisting of two parts- a charging current I_C and a leakage current I_L. The leakage current represents a loss related to the dielectric constant. The total current is given by,

$$I = I_C + I_L\qquad(2.14)$$

$$I = V(j\omega C\varepsilon_r' + \omega C\varepsilon_r'')$$

$$I = V(j\omega C)(\varepsilon_r' - j\varepsilon_r'')$$

$$I = V(j\omega C)\varepsilon_r,\qquad(2.15)$$

where $j\omega C\varepsilon_r''$ is considered as a conductance in parallel with the capacitor representing the dielectric loss, $\omega = 2\pi f$ and $\varepsilon_r = \varepsilon_r' - j\varepsilon_r''$ is the complex dielectric constant. Thus, the complex dielectric constant ε_r consists of a real part ε_r' representing energy storage and an imaginary part ε_r'' representing the energy loss.

The electric displacement is defined by,

$$D = \varepsilon E, \tag{2.16}$$

where $\varepsilon = \varepsilon_0 \varepsilon_r$ is the absolute permittivity that measures the extent of interaction of a material with an electric field E.

Dissipation factor or loss tangent

The imaginary part of the complex dielectric constant is 90° out of phase with the real part. Their resultant makes an angle δ with the real part. This is represented in Fig. 2.8.
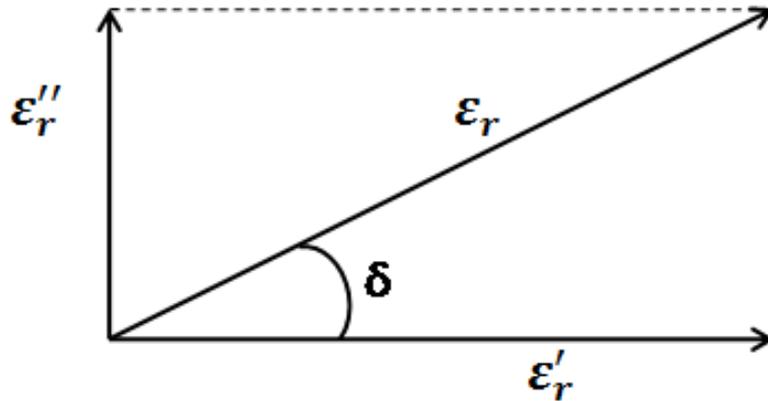
Fig. 2.8 Complex representation of dielectric constant

The dissipation factor D (loss tangent) is defined as the ratio of the imaginary component to the real component of the complex dielectric constant and is expressed as [25],

$$\rule{3cm}{0.4pt} \qquad - \qquad \qquad \text{(2.17)}$$

The AC conductivity of a dielectric sample is given by the relation,

$$, \qquad \qquad \text{(2.18)}$$

In the present work, a circular parallel plate capacitor is made out of the powder sample as described in section 2.5. The experimental set up to perform dielectric measurements are shown in the Fig. 2.9. The capacitance ( ) and the loss tangent ( ) are obtained from the measurements using an impedance analyser (Wayne Kerr 6500B) by two points probe method. Readings are recorded in the frequency range of 100 Hz to 10 MHz at selected temperatures ranging from room temperature to 423 K. Dielectric constant , dielectric loss and the AC conductivity of the samples are calculated using equations 2.12, 2.17 and 2.18, respectively.

Fig. 2.9 Experimental set up for dielectric studies

References

1   C. Burda, X. Chen, R. Narayanan, and M. A. El-Sayed, Chemical Reviews **105** (4), 1025 (2005).

2   R. Viswanatha and D. D. Sarma, in *Nanomaterials Chemistry: Recent Developments and New Directions*, edited by A. M. a. A. K. C. C. N. R. Rao, R. and Sarma, D. D. (Wiley-VCH Verlag GmbH & Co.KGaA, Weinheim, Germany, 2003).

3   S. L. Patil, S. G. Pawar, M. A. Chougule, B. T. Raut, P. R. Godse, S. Sen, and V. B. Patil, International Journal of Polymeric Materials **61** (11), 809 (2012).

4   S. M. Hassan, A. G. Baker, and H. I. Jafaar, International Journal of Basics and Applied Science (2012).

5   R. Sharma, R. Malik, S. Lamba, and S. Annapoorni, Bulletin of Materials Science **31** (3), 409 (2008).

6   P. J. Haines, *Thermal Methods of Analysis*. (Springer Netherlands, 1995).

7   R. Chen and Y. Kirsh, in *The Analysis of Thermally Stimulated Processes* (Pergamon, Amsterdam, 1981), Vol. 15, pp. 82.

8   C. Kittel, *Introduction to solid state physics*. (Wiley, 1976).

9   W. L. Bragg, presented at the Proceedings of the Cambridge Philosophical Society, 1913 (unpublished).

10 T. Varghese and K. Balakrishna, (New Delhi: Atlantic Publishers, 2011).

11 B. D. Cullity, *Elements of X-ray diffraction*, 2nd Edition ed. (Addison-Wesley Publishing Company, California, 1978).

12 S. J. Pennycook, A. R. Lupini, M. Varela, A. Borisevich, Y. Peng, M. P. Oxley, K. Van Benthem, and M. F. Chisholm, in *Scanning Microscopy for*

Nanotechnology: Techniques and Applications, edited by W. Zhou and Z. L. Wang (Springer New York, New York, NY, 2007), pp. 152.

13 JEOL., *SEM Scanning Electron Microscope A to Z: Basic Knowledge for Using the SEM*.

14 *Principles of Analytical Electron Microscopy*. (Plenum Press, New York, 1986).

15 M. v. Heimendahl, *Electron Microscopy of Materials: An Introduction*, 6th ed. (N.Y: Academic Press, New York, 1980).

16 J. Charles P. Poole, and Frank J. Owens, *Introduction to Nanotechnology*. (Hoboken, NJ: John Wiley & Sons, 2003).

17 D. B. Williams and C. B. Carter, *Transmission Electron Microscopy*, 2 ed. (Springer US, 2009).

18 M. v. Heimendahl, (N.Y.: Academic Press, New York, 1980).

19 B. C. Smith, *Fundamentals of Fourier Transform Infrared Spectroscopy* second ed. (CRC Press, Taylor & Francis Group, London, 2011).

20 C. V. Raman and K. S. Krishnan, Nature **121**, 501 (1928).

21 H.-S. Kim, C.-R. Lee, J.-H. Im, K.-B. Lee, T. Moehl, A. Marchioro, S.-J. Moon, R. Humphry-Baker, J.-H. Yum, J. E. Moser, M. Grätzel, and N.-G. Park, Scientific reports **2**, 591 (2012).

22 J. Tauc, *Amorphous and Liquid Semiconductors*, 1 ed. (Plenum Press, New York, 1974).

23 S. Ganesh, Journal of Physics: Conference Series **390** (1), 012005 (2012).

24 http://cp.literature.agilent.com/litweb/pdf/5989-2589EN.pdf.

25 http://academy.cba.mit.edu/classes/input_devices/meas.pdf.

****ॐ✿ॐ****

Chapter - 3
STUDIES ON STRUCTURAL, OPTICAL AND ELECTRICAL PROPERTIES OF NANOCRYSTALLINE MANGANESE TUNGSTATE

Nanostructured manganese has proved to be a multiferroic material and possesses other interesting properties like humidity sensing and photoluminescence. Recently, catalytic, photocatalytic and antibacterial properties of nanostructured $MnWO_4$ have been reported in the literature [1-3]. Many of the synthesis methods mentioned in the literature are performed under harsh reaction conditions [4-9]. Therefore simple and economic preparation routes are needed. The study of the effect of electron beam irradiation on the properties of $MnWO_4$ is not found in the literature. The synthesis, characterization and the effect of 8 MeV electron beam irradiation on the structural, optical and electrical properties of nanocrystalline $MnWO_4$ are presented in this chapter.

3.1   Synthesis of MnWO$_4$ nanoparticles

The morphology and particle size of the nanoparticles depend on the pH value of the reaction medium, reaction temperature and time [4, 10, 11].

Nanocrystalline manganese tungstate samples are prepared by reacting aqueous solutions of manganese chloride and sodium tungstate (0.1M each) at room temperature [12]. In this study the synthesis is performed at room temperature and the pH value is close to 7. The reactants are slowly mixed at the rate of about 10 ml per minute while being stirred well using a magnetic stirrer. The precipitate ($MnWO_4$) formed is collected carefully by decantation of the supernatant liquid that contained NaCl and water. It is again stirred with distilled water. The settled $MnWO_4$ particles are again collected after careful decantation. To ensure the purity of the final product, the overall process is repeated five times, and finally the precipitate collected is dried in an oven at 70 °C for 24 h to get powders of $MnWO_4$. The scheme of preparation of nanocrystalline $MnWO_4$ is shown in Fig. 3.1.

$$MnCl_2 . 4H_2O + Na_2WO_4 . 2H_2O$$
$$\rightarrow MnWO_4 + 2NaCl + 6H_2O$$
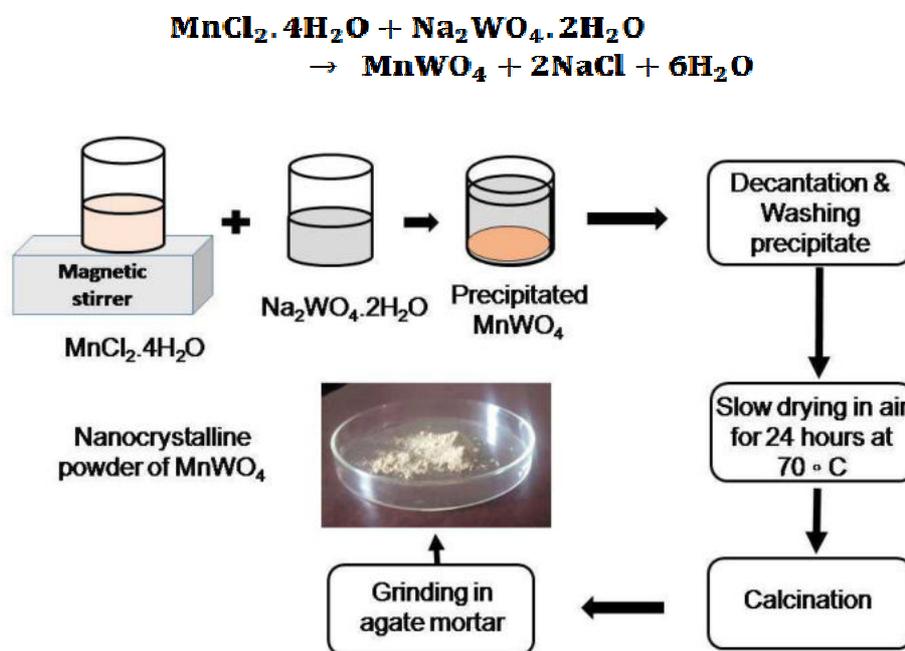
Fig. 3.1 Scheme of preparation of $MnWO_4$

Three powder samples **M₁**, **M₂** and **M₃** are prepared by calcinations for 3 h in a muffle furnace at 450, 600 and 750 °C, respectively. The calcination temperatures are selected after performing the thermal analysis of the precursor discussed in the following section. The calcined samples appear chocolate in colour with a little contrast. The sample M₁ is used for the electron beam irradiation studies. **M₁** is irradiated with electron doses of 5 and 10 kGy, as described in section 2.4 and are designated as **M₁(05)** and **M₁(10)**, respectively.

3.2   Thermal analysis

Thermal stability of the sample is studied using a simultaneous thermal analyzer STA 6000 (Perkin Elmer). The sample is heated from 40 to 850 °C at 10 °C/min. The TGA/DTA and DTG curves of the thermal degradation of the manganese tungstate precursor are shown in Fig. 3.2. They reveal three prominent weight losses centred on 63.01, 235.64 and 390.36 °C with an overall weight loss of ∼8.65 % in the temperature range from 40 to 850 °C.

The first weight loss step (∼1.50 %) represents the physisorbed and interlayer water. The second weight loss (∼4.50 %) attributes to the loss of structural water. Above 390.36°C, the third weight loss of ∼ 2.60 % occurs gradually due to the removal of remaining water molecules that are bound strongly. The DTA pattern shows a prominent endothermic peak centred on 236.64 °C due to the loss of structural water.
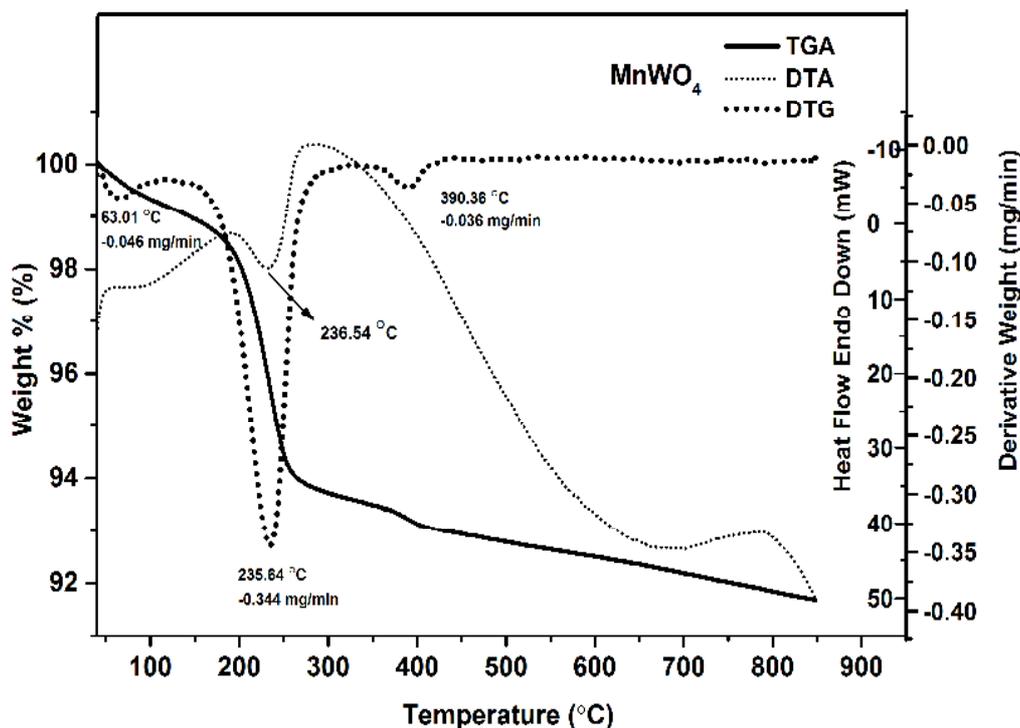
Fig. 3.2 TGA, DTA and DTG curves of MnWO₄ precursor

3.3   Structural characterization of MnWO₄ nanoparticles

3.3.1   XRD patterns of MnWO₄ samples

The   crystal   structure   parameters   of   manganese   tungstate nanoparticles are studied using Bruker D8 Advance X-ray diffractometer (λ=1.5406 Å) with Cu (K$_\alpha$) radiation in the 2θ range from 3 to 70°. Fig. 3.3 shows the powder X-ray diffraction patterns of samples of MnWO₄ nanoparticles calcined at three different temperatures.
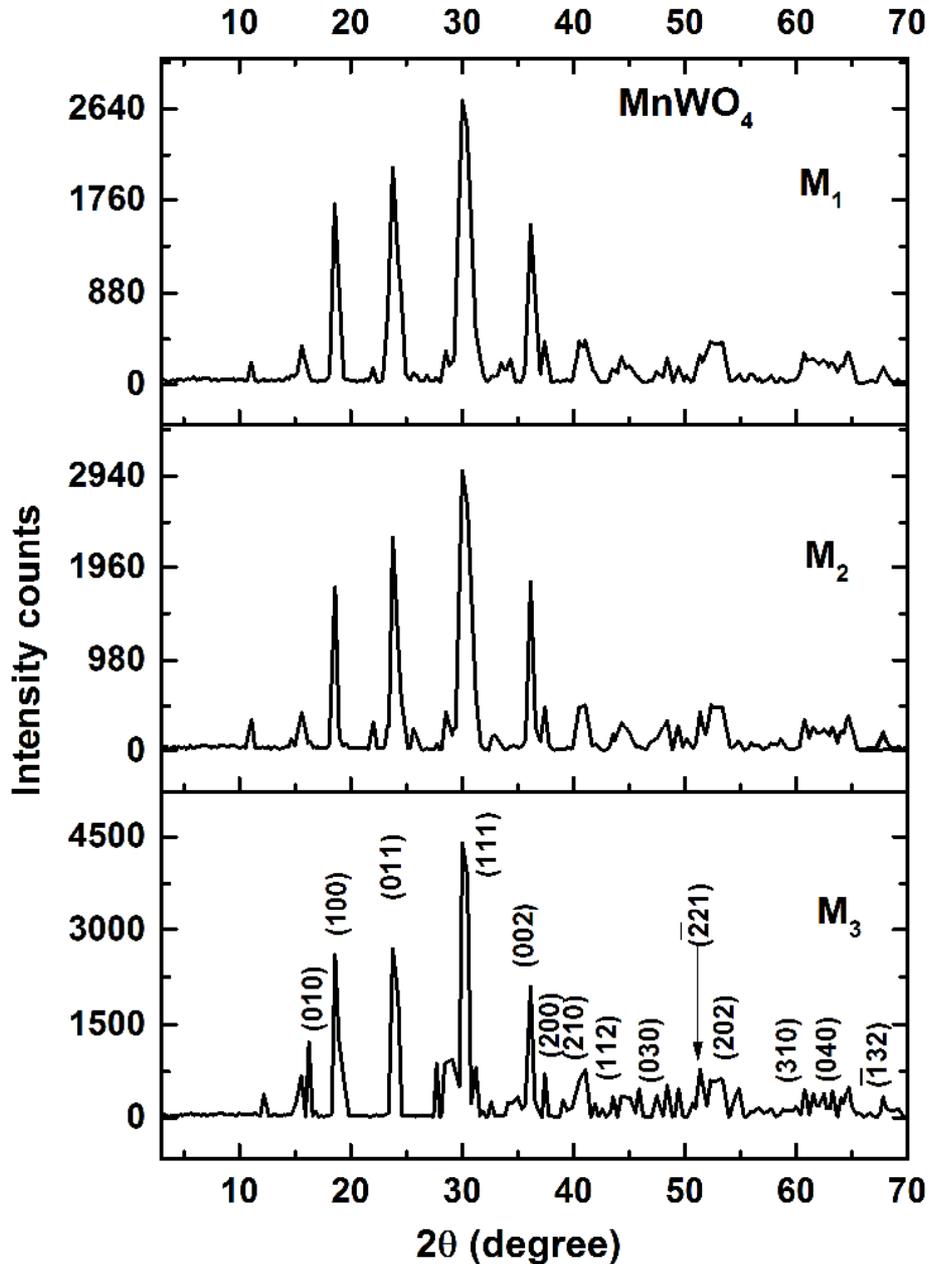
Fig. 3.3 XRD patterns of MnWO$_4$ samples **M$_1$, M$_2$** and **M$_3$**

The XRD patterns confirm that all the peaks of MnWO$_4$ observed are well matched with the X-ray pattern of JCPDS Card No. 80-0135. Also, MnWO$_4$ crystal structure belongs to wolframite type monoclinic structure with *P2/c* space group, C$_{4h}^6$ point group symmetry with two formula units

per unit cell [5, 13-15]. The intense XRD peaks are produced due to the reflections from the (100), (011), (111) and (002) planes located at 2θ values 18.57, 23.57, 30.03 and 36.15°, respectively. These values are found to be almost the same for the prominent peaks of samples **M₁**, **M₂** and **M₃**. These results match well with the values given in the XRD pattern of JCPDS Card No. 80-0135 for MnWO₄. The corresponding d values are 4.78, 3.74, 2.97 and 2.48 (Å); 4.77, 3.74, 2.97 and 2.48 (Å); 4.77, 3.74, 2.96 and 2.48 (Å), for the samples **M₁**, **M₂** and **M₃**, respectively. The particle size is estimated from the Scherrer equation (2.1). The average crystallite sizes obtained are 26.03, 31.74, and 39.72 nm for the samples **M₁**, **M₂** and **M₃**, respectively. At higher calcination temperature, XRD patterns show much sharper peaks because of the increase in size of the particles due to coarsening.

The lattice parameters a, b and c are calculated from the d-spacing for peaks having Miller indices (hkl) using the equation [16],

$$\frac{1}{d^2} = \frac{1}{\sin^2 \beta}\left(\frac{h^2}{a^2} + \frac{k^2 \sin^2 \beta}{b^2} + \frac{l^2}{c^2} - \frac{2hl\cos\beta}{ac}\right), \quad (3.1)$$

for the monoclinic unit cell ($a \neq b \neq c, \beta \neq 90°$). The unit cell volume is calculated using the equation,

$$V = abc \sin \beta, \quad\quad\quad\quad (3.2)$$

The unit cell parameters and volume recorded in the JCPDS file No. 80-0135 for MnWO₄, and the values calculated for the samples **M₁**, **M₂** and **M₃** are given in table 3.1 for comparison.

Table 3.1 Structural parameters of MnWO$_4$ samples

Sample	Unit cell parameters (Å)			β (degree)	Unit cell volume (Å^3)	Crystallite size (nm)
	a	*b*	*c*			
JCPDS Card No. 80-0135	4.7766	5.6810	4.9605	91.19	134.58	--
M$_1$	4.7781	5.6848	4.9660	90.33	134.89	26.03
M$_2$	4.7335	5.6788	4.9652	89.94	133.47	31.74
M$_3$	4.7734	5.4567	4.9626	89.80	129.26	39.72

From the data tabulated, it is seen that the unit cell volume decreases and the particle size increases as the calcination temperature increases. Also, both the lattice constants and the interfacial angle β get slightly reduced upon increasing the calcination temperature. The heat treatment results in the increase of crystallite size, which also results in lattice contraction as well as slight deformation of the lattice. But, the increase in intensity of XRD peaks suggests improvement in the crystalline nature upon increasing the calcination temperature.

3.3.2 XRD patterns of electron beam irradiated MnWO$_4$ samples

XRD patterns of samples **M$_1$**, **M$_1$(05)** and **M$_1$(10)** are shown in Fig. 3.4. Crystallite size and structural parameters are calculated as described in section 3.3.1. The average sizes obtained for samples **M$_1$, M$_1$(05)** and **M$_1$(10)** are 26.03, 23.47 and 24.46 nm, respectively. The major peak corresponding to (111) plane is found to split due to electron beam irradiation. With irradiation, planes have then different distances and cause

different Bragg angles leading to the splitting of the prominent peak. The suppression of peaks below 30º is due to creation of defects affecting them.
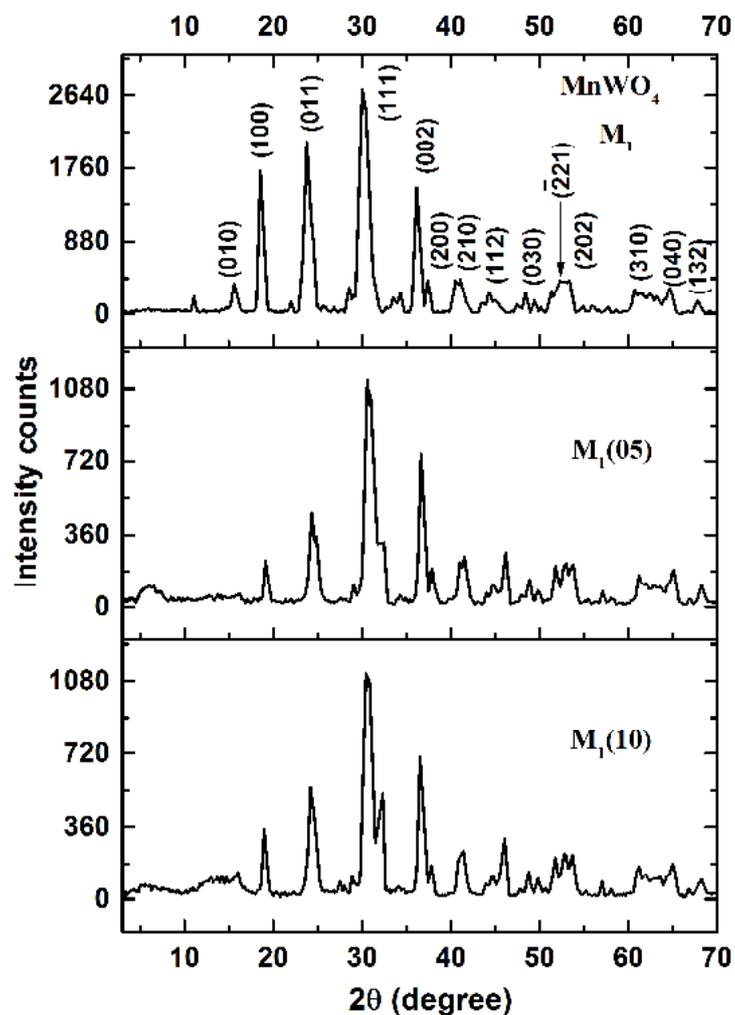
Fig. 3.4 XRD pattern of $MnWO_4$ samples M_1, $M_1(05)$ and $M_1(10)$

Structural parameters calculated for the unirradiated and irradiated samples are given in Table 3.2. It is seen that electron beam irradiation causes slight decrease in the crystallite size. However, the electron irradiation results in lattice expansion for the samples (Table 3.2). The reason for the expansion is inhomogeneity in the lattice strain introduced by

the electron beam irradiation [17]. In short, the electron beam irradiation on the $MnWO_4$ samples causes modifications in the structural parameters.

Table 3.2 Structural parameters of $MnWO_4$ samples M_1, $M_1(05)$ and $M_1(10)$

Sample	Unit cell parameters (Å)			β (degree)	Unit cell volume (Å³)	Crystallite size (nm)
	a	*b*	*c*			
JCPDS Card No. 80-0135	4.7766	5.681	4.9605	91.19	134.58	--
M_1	4.7781	5.6848	4.9660	90.33	134.89	26.03
$M_1(05)$	4.7864	5.7946	4.9706	90.22	137.86	23.47
$M_1(10)$	4.7729	5.7972	4.9740	89.90	137.63	24.46

3.4   Vibration spectroscopy of $MnWO_4$ nanoparticles

The surface chemistry of the samples will affect their lattice parameters and in turn their vibrational properties [11]. Such conclusions are possible by carrying out the FTIR and Raman studies. There are 36 possible modes of vibration in $MnWO_4$ according to the group theory. They are given by the equation [18],

$$\Gamma_{(Raman+Infrared)} = 8A_g + 10B_g + 8A_u + 10B_u \qquad (3.3)$$

Out of these modes, 18 even modes (g) given by the equation,

$$\Gamma_{(Raman)} = 8A_g + 10B_g, \qquad\qquad (3.4)$$

are Raman active [19]. In equation 3.3, fifteen modes ($7A_u$ and $8B_u$) are IR active. The acoustic modes (one A_u and twoB_u) are eliminated [19]. FTIR spectroscopy is used to investigate the formation of $MnWO_4$. While, the

Raman spectroscopy is used for identifying the different modes of molecular vibrations in $MnWO_4$ molecule.

3.4.1 FTIR spectroscopy of $MnWO_4$

The FTIR spectra of the $MnWO_4$ samples **M₁**, **M₂** and **M₃**, are recorded using Perkin Elmer Spectrum 400 (FTIR).
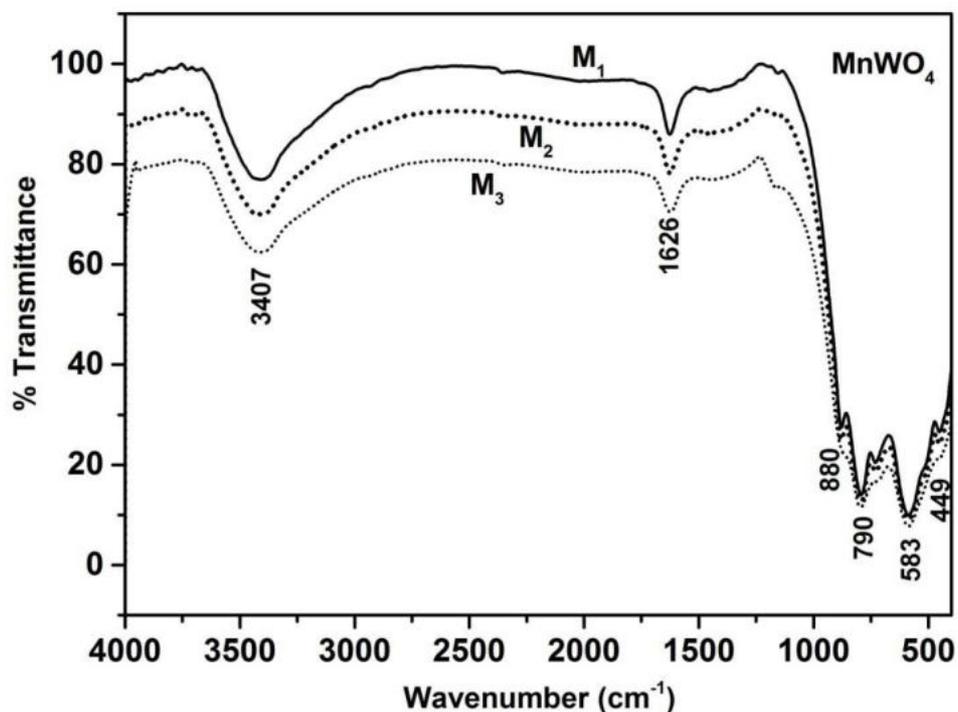
Fig. 3.5 FTIR spectra of $MnWO_4$ samples **M₁**, **M₂** and **M₃**

The Fig. 3.5 shows the FTIR spectra of the $MnWO_4$ nanoparticles prepared. These spectra give information on the characteristic bonds present in the tungstate group. The broad absorption band at 3407 cm^{-1} is a sign of the presence of O-H bond due to the surface hydration of the sample and the band at 1626 cm^{-1} is caused by the H-O-H deformation vibration [8, 20]. The spectrum indicates intense absorption peaks at 449, 583, 790 and 880

cm^{-1} in the range 400-1000 cm^{-1} [5, 21]. The 880 cm^{-1} absorption peak is assigned to the anti-symmetric stretching vibration in the [WO_4] group. The bands at 790 and 583 cm^{-1} are caused by the stretching vibration of W-O bond. It is reported that this band should be formed when the size of the particle formed is small [22]. The band at 449 cm^{-1} can be assigned to the bending vibration of the W-O bond [23]. The small differences in the positions of the absorption peaks are due to the difference in the preparation conditions, and slight variations in the unit cell volumes caused due to strains and distortions in the lattice.

3.4.2 Raman spectroscopy of MnWO₄

Raman spectra for samples **M₁**, **M₂** and **M₃** are shown in Fig. 3.6. Careful observation of the data shows eighteen Raman modes in the range 100-1200 cm^{-1} at room temperature. The most intense Raman band seen at 880 cm^{-1} (A_g^*) originates from the symmetric stretching vibration of a short terminal W-O bond [24]. The bands at 776 cm^{-1} (B_g^*) and 692 cm^{-1} (A_g^*) are due to the asymmetric stretching vibration of a short terminal W-O bond. The modes at 675 cm^{-1} (B_g^*) and 547 cm^{-1} (A_g^*) are due to the asymmetric stretching modes of longer W-O bond. The mode at 394 cm^{-1} (A_g^*) is due to the deformation vibration of short W-O bond. Modes at 547 and 514 cm^{-1} are due to the symmetric stretching vibration of longer W-O bond. Modes at 361, 317 and 297 cm^{-1} are due to the vibrations of Mn-O [12]. Other bands are contributed by inter-chain deformation modes and

lattice modes [11]. Raman modes of $MnWO_4$ samples along with their reported values are presented in Table 3.3.

Fig. 3.6 and Table 3.3 show a shift in wavenumber of the major band from 880 to 869 cm^{-1}, as calcination temperature is increased from 450 to 750 °C. This shift is due the lattice contraction that has occurred due to the increase in the particle size, as is evident from the XRD studies.
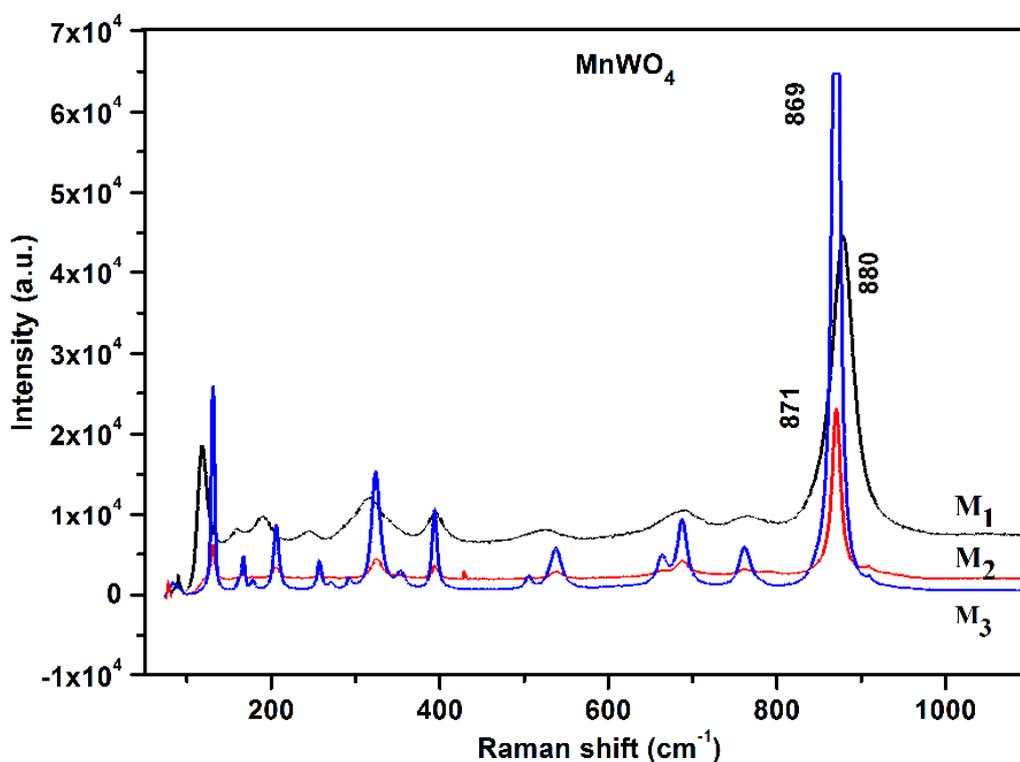
Fig. 3.6 Raman bands of $MnWO_4$ samples **M₁**, **M₂** and **M₃**

It can be seen from Fig. 3.6 that line broadening of the peaks decreases with increase in calcination temperature, indicating a reduction in crystal defects [25]. This observation is in accordance with the XRD results.

Table 3.3 Comparison of Raman modes of $MnWO_4$ with literature values

Vibration modes	Raman shift (cm^{-1})			Literature [18]
	M_1	M_2	M_3	
B_g	90	79	82	89
A_g	117	129	128	129
B_g	159	161	154	160
B_g	168	167	169	166
B_g	172	171	174	177
A_g	190	205	205	206
B_g	262	265	269	272
A_g	247	252	252	258
B_g	297	290	293	294
A_g	317	327	320	327
B_g'	361	369	354	356
A_g^*	394	393	395	397
B_g	514	506	508	512
A_g^*	547	528	535	545
B_g^*	675	653	662	674
A_g^*	692	688	695	698
B_g^*	776	762	769	774
A_g^*	880	871	869	885

3.4.3 Raman spectroscopy of electron beam irradiated MnWO₄ samples

Raman spectra for the bare and irradiated samples of $MnWO_4$ nanoparticles are shown in Fig. 3.7. All the Raman bands obtained are listed in Table 3.4. The Fig. 3.7 shows that intensity and sharpness change upon increasing the dose of electron beam irradiation. For the electron beam irradiated samples **M₁(05)** and **M₁(10),** the peaks are broadened indicating a weak phonon confinement [25]. This broadening is due the creation of a number of defects caused by the electron irradiation. This observation can be related to the small increase in the unit cell volume with increase in the electron dose in the irradiated samples.
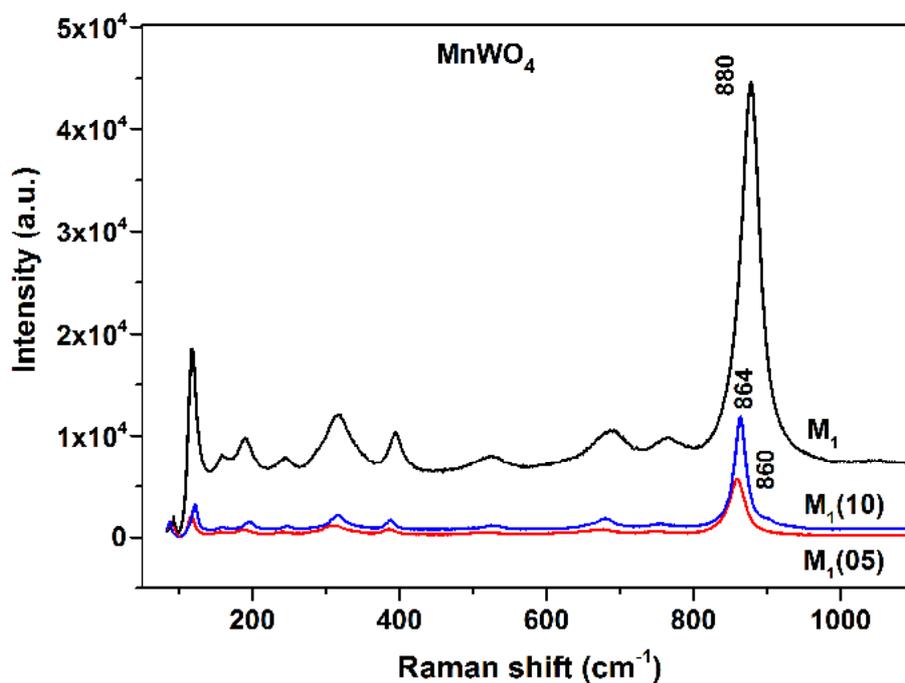
Fig. 3.7 Raman bands of bare and electron beam irradiated MnWO₄ samples The change in intensity of peaks may be due to variation in measurement conditions.

Table 3.4 Raman modes of bare and electron irradiated MnWO$_4$

Vibration modes	Modes observed (cm^{-1}) in samples		
	M$_1$	M$_1$(05)	M$_1$(10)
B_g	90	89	87
A_g	117	116	123
B_g	159	159	159
B_g	168	157	161
B_g	172	171	174
A_g	190	188	194
B_g	262	265	269
A_g	247	246	244
B_g	297	290	293
A_g	317	312	317
B_g'	361	349	354
A_g^*	394	387	386
B_g	514	506	508
A_g^*	547	525	530
B_g^*	675	633	642
A_g^*	692	676	682
B_g^*	776	756	752
A_g^*	880	860	864

3.5 Electron microscopy

Electron microscopy techniques are employed to determine the morphology, shape, distribution and composition of nanoparticles. These studies include SEM, EDS and TEM analyses.

3.5.1 SEM analysis of MnWO$_4$ samples

The SEM image of samples **M$_1$**, **M$_2$** and **M$_3$** are shown in Fig. 3.8. Particles of irregular size and shapes are visible in the image for **M$_1$**. In the SEM image for **M$_2$**, slightly agglomerated clusters are visible. In sample **M$_3$**, clusters of rod shaped structures are formed. From this observation, it is obvious that morphology changes on increasing calcination temperature. Thermal recrystallization and growth in certain directions lead to changes in shape and size [26].

The SEM micrographs of the samples **M$_1$**, **M$_1$(05)** and **M$_1$(10)** are shown Fig. 3.9. Irregular shaped clusters of particles looking like flakes and granules are seen in the SEM micrographs of the unirradiated sample **M$_1$.** The changes in the morphology of samples due to electron irradiation at 5 and 10 kGy doses are clear from the SEM images of **M$_1$(05)** and **M$_1$(10),** respectively (Fig. 3.9). A slight decrease in particle size is observed in the XRD results for electron irradiated samples, as described in section 3.3.2. Though the particle size is reduced, aggregation of particles forms large sized clusters.
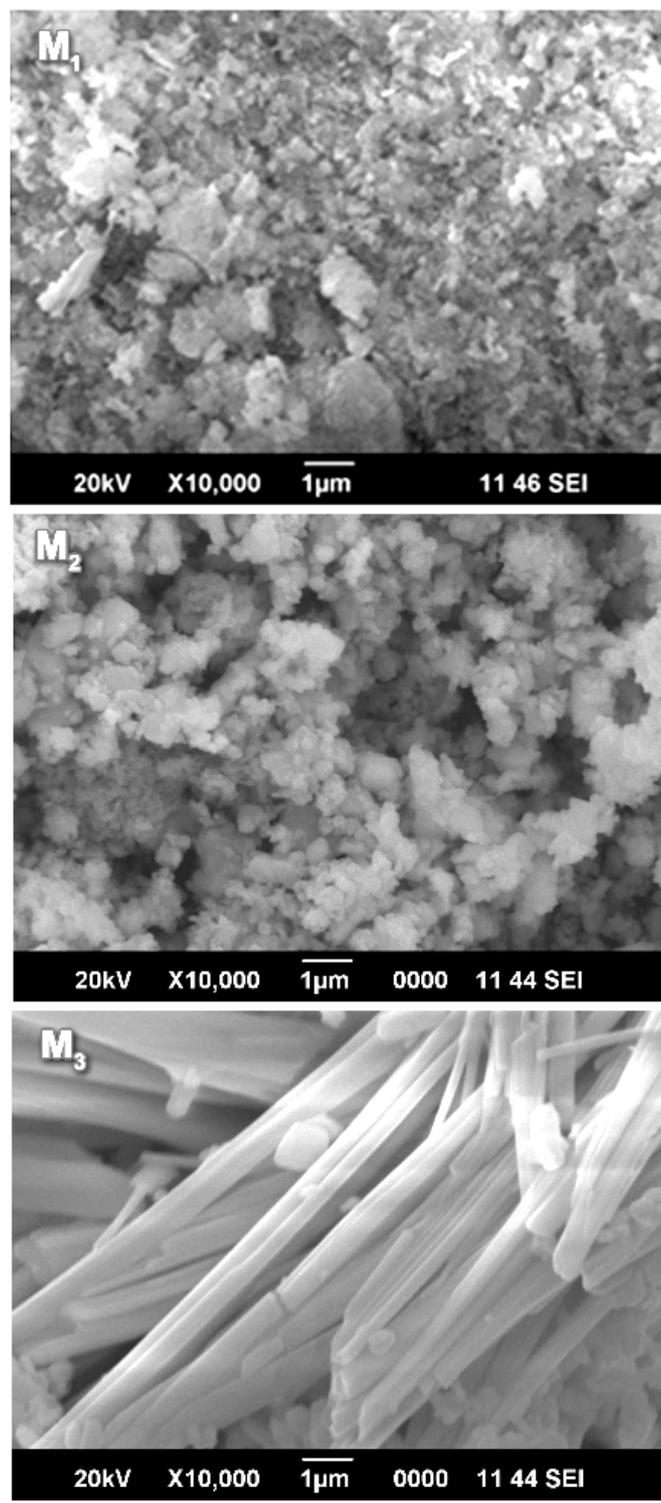
Fig. 3.8 SEM micrographs of MnWO$_4$ samples **M$_1$**, **M$_2$** and **M$_3$**
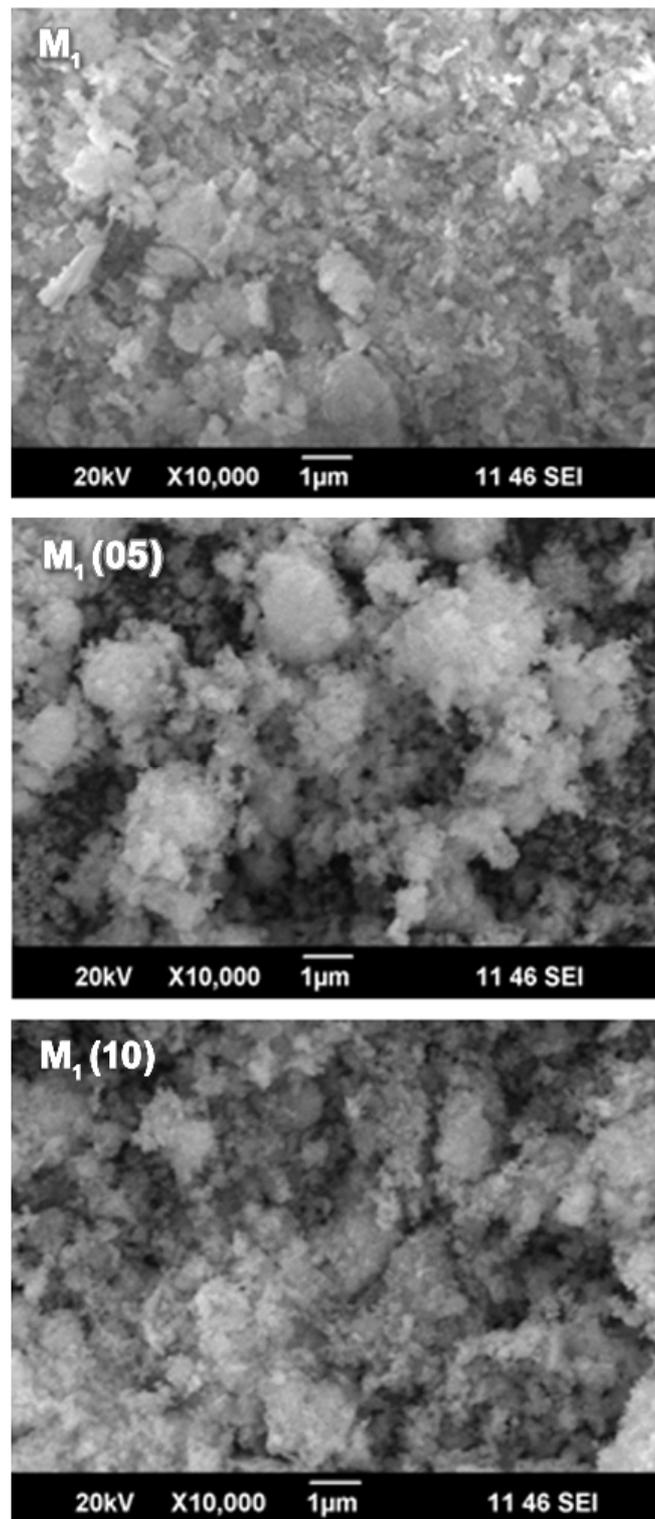
Fig. 3.9 SEM micrographs of MnWO$_4$ samples **M$_1$**, **M$_1$(05)** and **M$_1$(10)**

In Fig. 3.9, the irradiated samples appear to be spongy with lot of pores. After exposing to electron beam, the aggregation of the particles is found to be slightly greater. Thus, the surface morphology is slightly modified in the irradiated samples.

3.5.2 EDS of MnWO₄

The elemental analysis of the sample calcined at 450°C (M_1) is done using a JEOL Model JED – 2300 and BRUKER X Flash 6/10 EDS detector. Fig. 3.10 shows typical EDS pattern of the synthesized MnWO₄ nanoparticles.
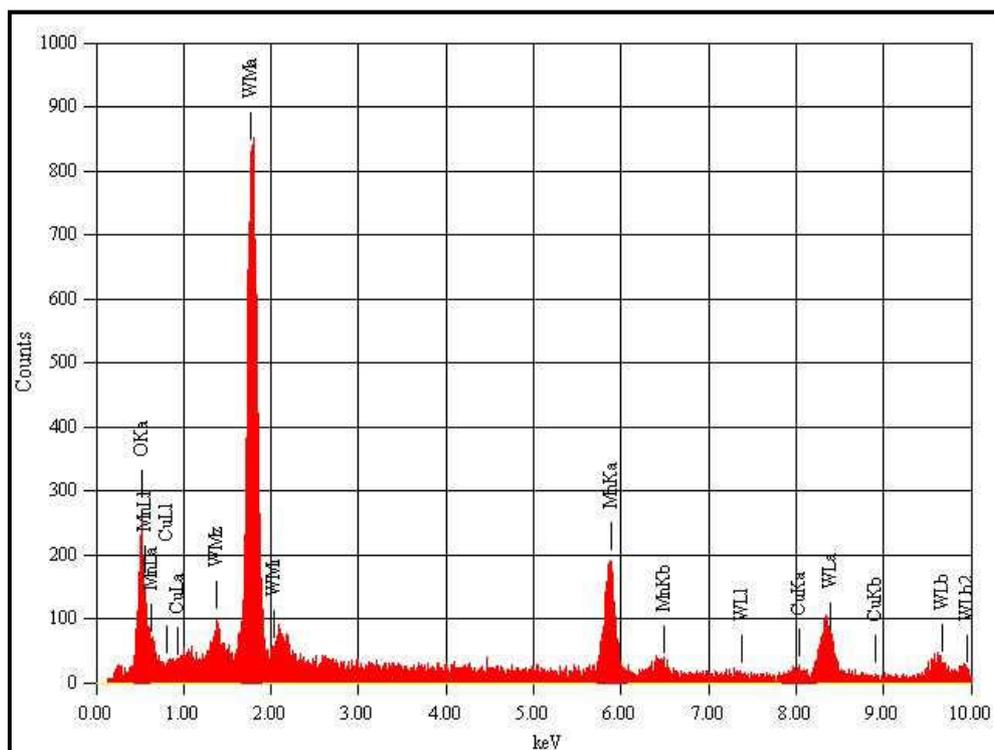
Fig. 3.10 EDS of synthesized MnWO₄ nanoparticles

The peaks in the EDS pattern confirm that the product contains Mn, W and O. Besides, 3.23 mass % of impurity element Cu is observed, which is from the Lacey Cu grid. In no other parts of the experiment, during the

synthesis or the curing thereafter copper related compounds are used. The intense signal near 2 keV indicates that Mn is the major element. The mass percentage and the atom percentages of the sample are given in Table 3.5.

Table 3.5 EDS data of $MnWO_4$ sample M_1

Element	Series	(keV)	Mass%	Atom%
O	K	0.525	7.91	39
Mn	K	5.894	18.78	26.95
Cu	K	8.04	3.23	4.01
W	M	1.774	70.07	30.04
Total			100	100

3.5.3 TEM analysis of $MnWO_4$

TEM images of sample M_1 are shown in Fig. 3.11. TEM images of $MnWO_4$ nanoparticles (Fig. 3.11a & b) show that the particles exhibit bar like shape [12]. The nanobars get arranged in certain directions. In this assembly some of the bars are almost longitudinal, while others are in the transverse direction. Most of the particles are agglomerated. It is reported that such an aggregation occurs due to surface energy by Van der Waal's forces and grow along [100] direction [15]. The average width of the particles is found ~78 nm. HRTEM image of the sample is shown in Fig. 3.11 (c). Average d value obtained from HRTEM is 0.29 nm. The plane corresponds to (111) plane corresponding the peak at 30º in the XRD

spectra. Selected area electron diffraction pattern (Fig. 3.11 d) clearly indicates polycrystalline nature of the $MnWO_4$ nanoparticles [12].
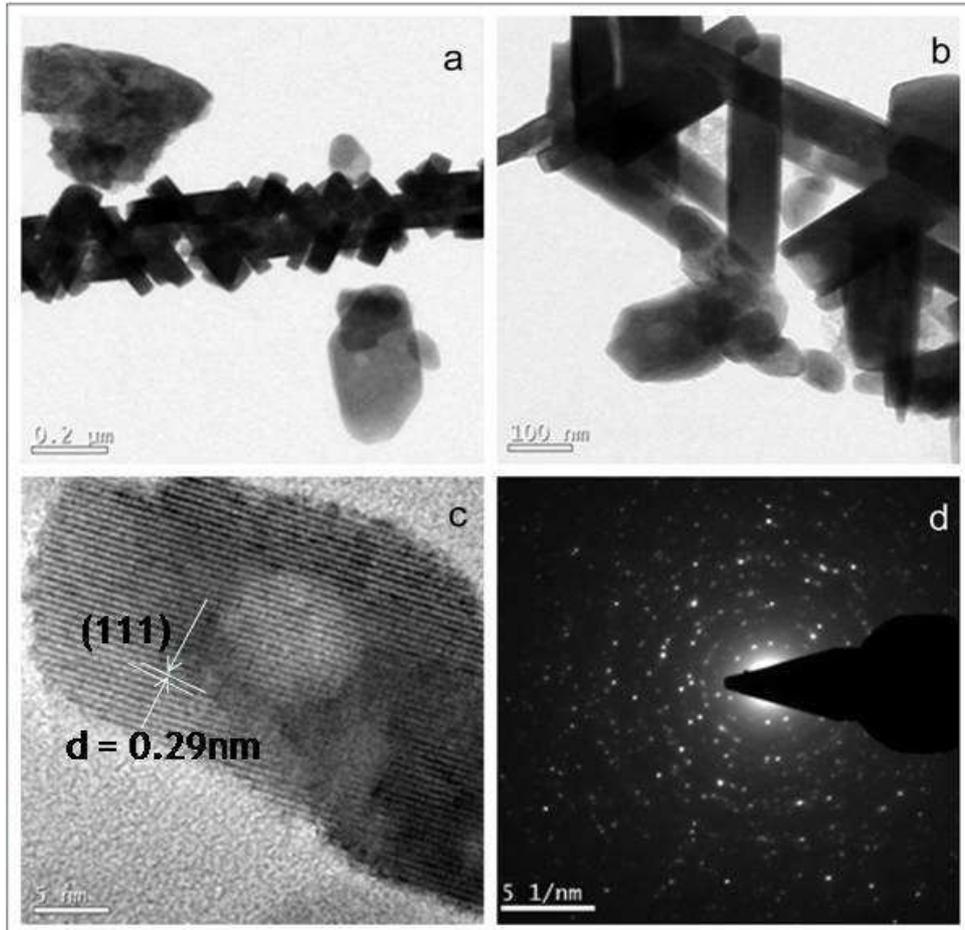
Fig. 3.11 TEM images of $MnWO_4$ sample M_1

3.6   Optical properties

The absorptive and emissive properties of bare and electron irradiated $MnWO_4$ samples are investigated in the optical study.

3.6.1 UV-Visible absorption studies in $MnWO_4$ samples

Fig. 3.12 shows the UV-Visible absorbance spectra of $MnWO_4$ samples M_1, M_2 and M_3. From the results, it can be observed that all the

samples have broad absorption peak. The absorption peaks of samples **M₂** and **M₃** are slightly shifted towards the longer wavelength region.
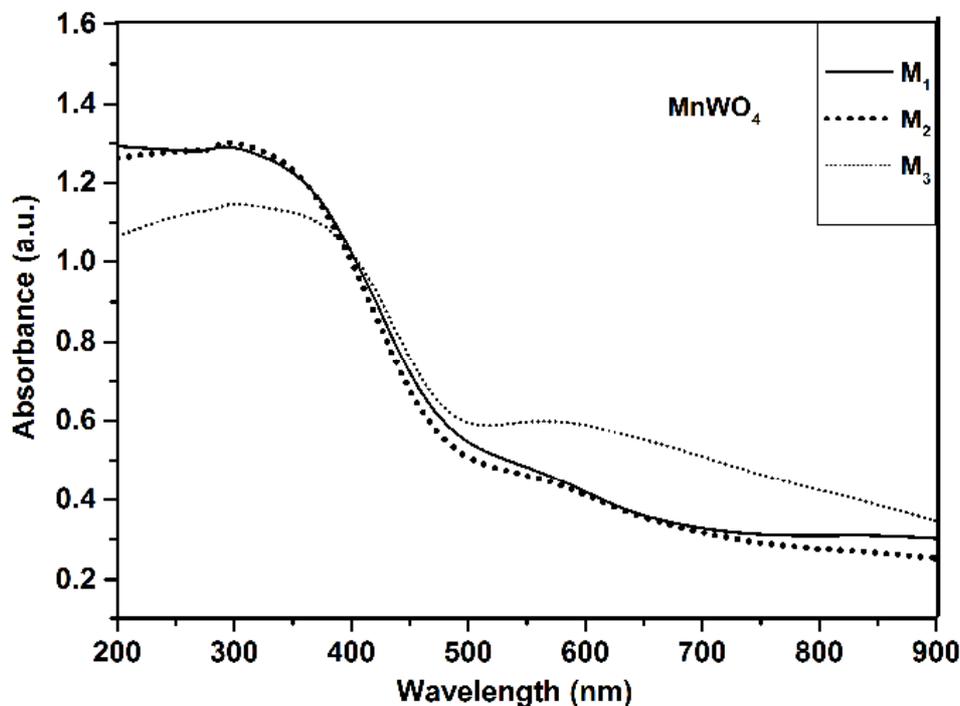
Fig. 3.12 UV-Visible spectra of MnWO₄ samples **M₁, M₂** and **M₃**

Optical bandgap is determined from the Tauc plot, as discussed in the section 2.3.8. The direct bandgap values obtained for samples **M₁, M₂** and **M₃** are 2.63, 2.58 and 2.54 eV, respectively (Fig. 3.13). This increase in bandgap with decrease in particle size confirms size effect [12].

The UV-Visible absorbance spectra of MnWO₄ are due to a metal-to-metal charge transfer. In MnWO₄, the partially filled 3d orbital of the Mn^{2+} ion acts as the highest occupied molecular orbital (HOMO) and an electron from this level is transferred to the unoccupied anti-bonding W 5d states [27].
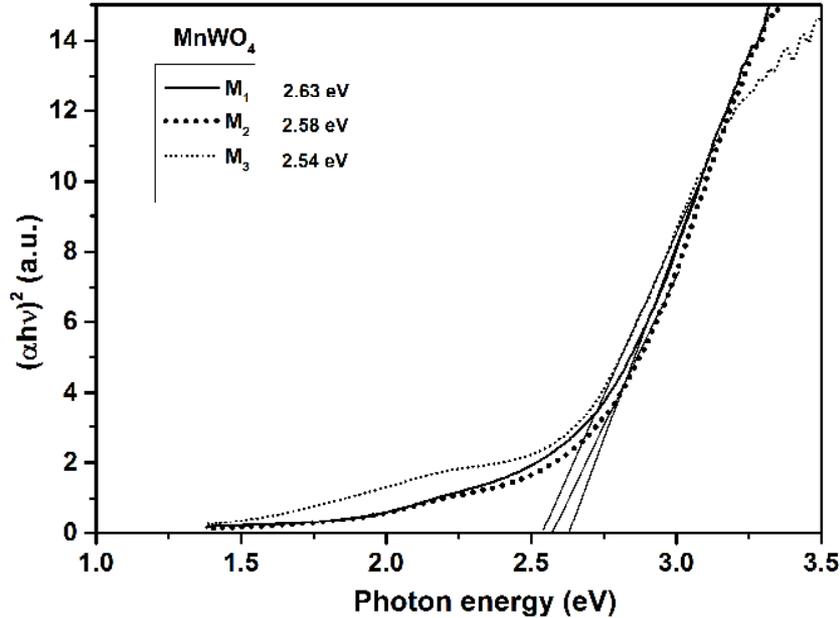
Fig. 3.13 Tauc plots of MnWO$_4$ samples **M$_1$**, **M$_2$** and **M$_3$**

MnWO$_4$ nanoparticles are useful for photocatalytic activities as their bandgap energy values are comparable to the energy of visible or UV light photons [25].

3.6.2 UV-Visible absorption studies of electron beam irradiated samples

The absorption spectra of samples **M$_1$, M$_1$(05)** and **M$_1$(10)** are shown in Fig. 3. 14. An increase in absorbance is observed in irradiated samples **M$_1$(05)** and **M$_1$(10)**. The optical bandgap values obtained from the Tauc plots (Fig. 3.15) for samples **M$_1$, M$_1$(05)** and **M$_1$(10)** are 2.63, 2.79 and 2.73 eV, respectively. It is seen that the bandgap of MnWO$_4$ nanoparticles shifts from 2.63 to 2.79 eV as particle size reduces from 26.03 to 23.41 nm and from 2.63 to 2.73 eV as size reduces from 26.03 to 24.46 nm. This increase in the bandgap is due to surface band bending and lattice expansion caused by electron irradiation [11].
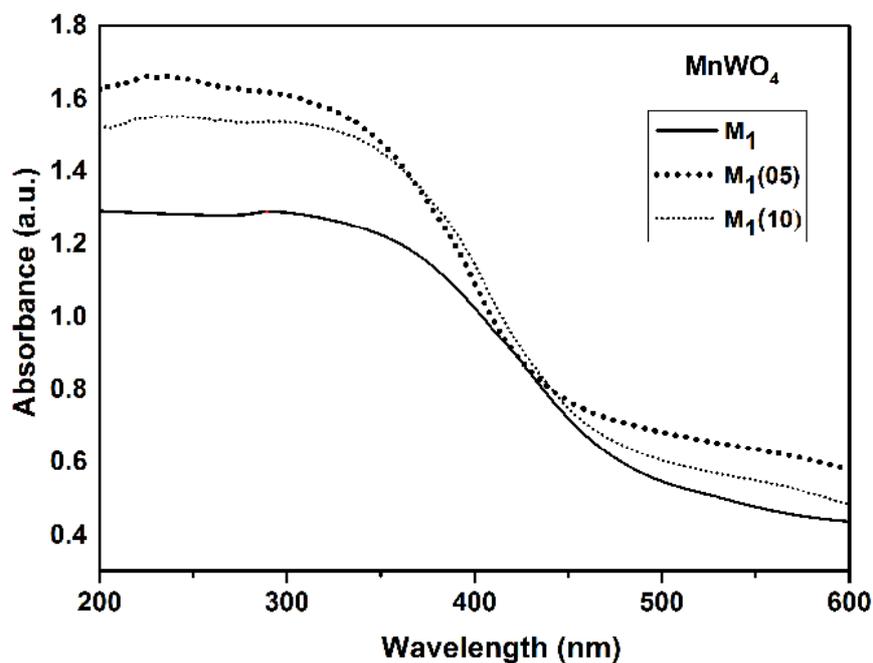
Fig. 3.14 UV-Visible absorbance spectra of bare and

electron beam irradiated MnWO₄ samples
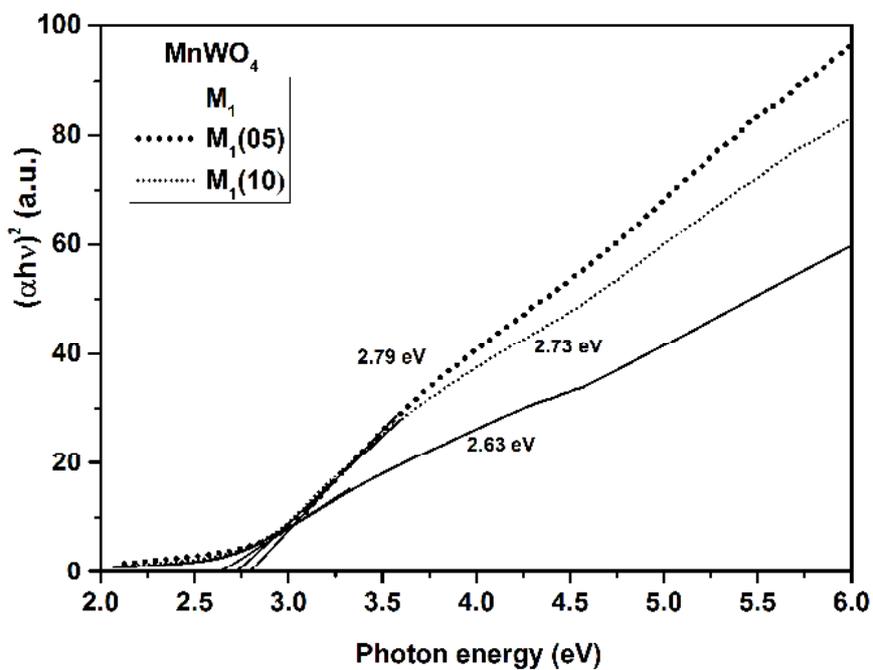
Fig. 3.15 Tauc plots of MnWO₄ samples **M₁**, **M₁(05)** and **M₁(10)**

3.6.3   Photoluminescence studies

3.6.3.1   *PL studies of MnWO₄ samples*

Room temperature photoluminescence spectra of samples **M₁**, **M₂** and **M₃** excited with 293 nm are shown in Fig. 3.16.
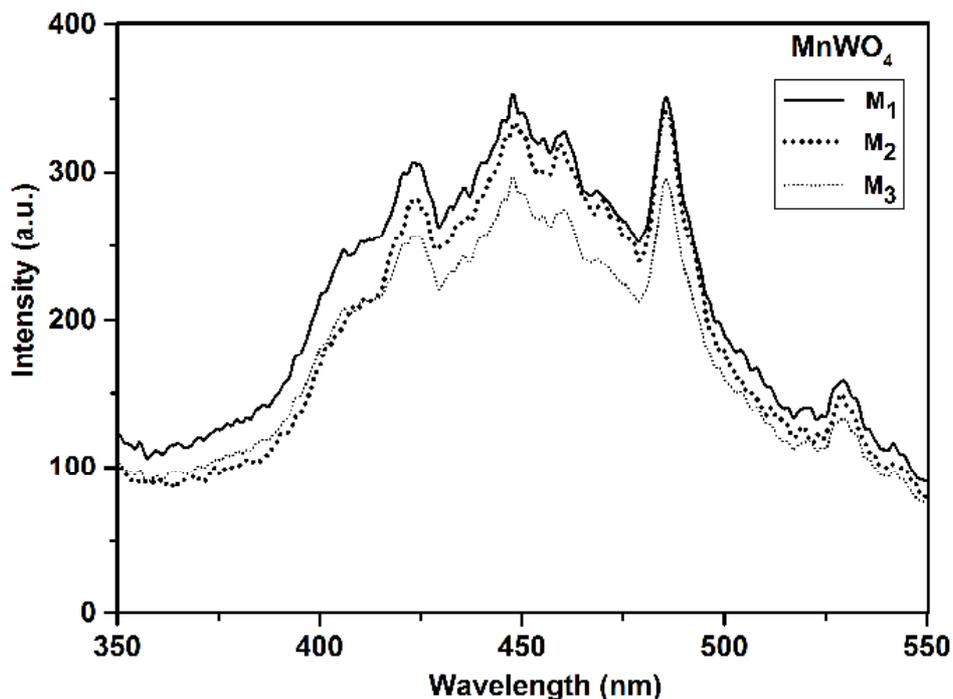
Fig. 3.16 PL spectra of MnWO₄ samples **M₁**, **M₂** and **M₃**

The PL spectra of the samples show emission bands at 423.62, 447.55, 460.45, 485.81 and 529.36 nm. These bands are attributed to the transition from the $^1A_1$ ground-state to the high vibration level of $^1T_2$ and from the low vibration level of $^1T_2$ to the $^1A_1$ ground state within the tetragonal WO_4^{2-} groups [12, 15, 28]. The large intensity for sample **M₁** is attributed to the increase in the trap states that give rise to luminescence, which is a combined effect of defect centres generated by oxygen vacancies, small particle size, and increased absorption over the UV and visible range [29].

3.6.3.2 *PL studies of electron beam irradiated MnWO₄ samples*

The pure and electron irradiated samples of $MnWO_4$ exhibit similar shape of PL curve (Fig. 3.17). The PL spectra of irradiated samples have larger intensities relative to unirradiated sample, which arise from defects and particle size variation caused by electron irradiation [12, 30]. Besides, intermediate energy levels are formed with favourable characteristics due to electron beam irradiation, which are necessary for recombination process. As a result, intensity of the PL emission is large for the electron irradiated samples. When the EB irradiation dose is increased above a certain dose level, the particles agglomerate and thereby reduce the number of fluorophores [12]. This possibly leads to a reduction in the fluorescence intensity of the sample **M₁(10)**.
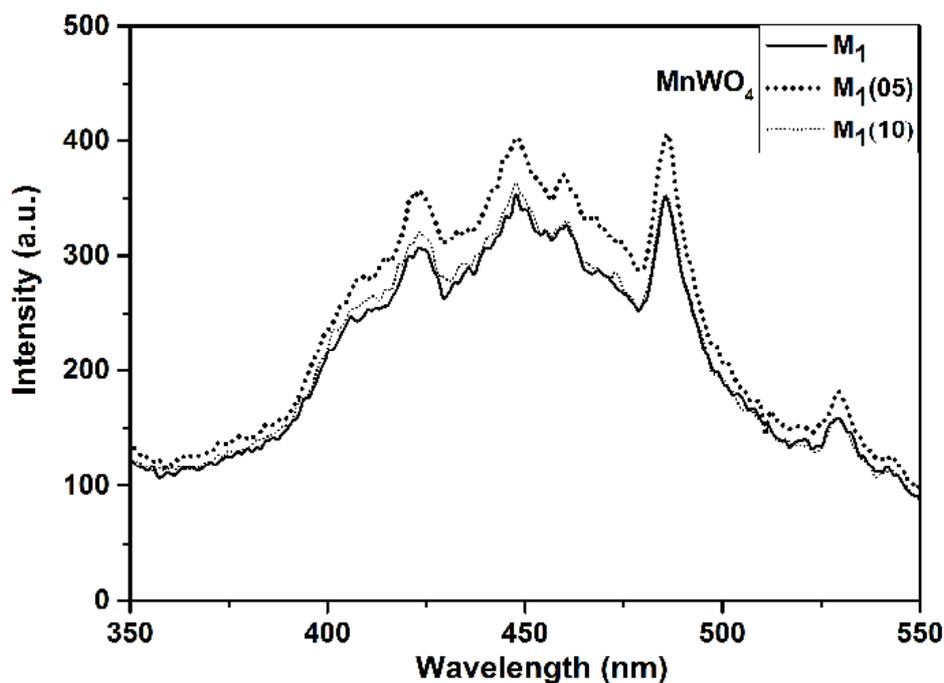
Fig. 3.17 PL spectra of MnWO₄ samples **M₁**, **M₁(05)** and **M₁(10)**

3.7 Electrical properties of MnWO$_4$ nanoparticles

In this section, DC and AC conductivity studies of bare and electron irradiated samples of nanocrystalline MnWO$_4$ are presented. In conjunction with ac studies, the frequency and temperature dependence of dielectric properties are investigated. The modifications in electrical properties induced by 8 MeV electron beam irradiation are also investigated.

3.7.1 DC electrical studies

3.7.1.1 *DC electrical studies of MnWO$_4$ samples*

The pellets used for DC studies are prepared using the method described in section 2.5. Conductivity measurements are done in **M$_1$**, **M$_2$** and **M$_3$** samples using two points probe method (section 2.5). The variation of DC conductivity with temperature of calcined samples **M$_1$**, **M$_2$** and **M$_3$** are plotted in Fig. 3.18. At 303 K, the values of σ_{DC} obtained are 1.30×10^{-8}, 1.23×10^{-8} and 1.12×10^{-8} mho-m^{-1} for **M$_1$**, **M$_2$** and **M$_3$**, respectively. At 463 K, the values of σ_{DC} are 6.41×10^{-5}, 4.81×10^{-5} and 2.81×10^{-5} mho-m^{-1}, respectively. From the Fig. 3.18, it can be seen that as the temperature increases σ_{DC} increases exponentially. At a given temperature, σ_{DC} is lower for the sample calcined at higher temperature.

The nature of the plots reveals that the conduction is thermally activated. The activation energy of each sample is found out by plotting the Arrhenius relation [31],

$$\sigma_{DC} = \sigma_0 e^{\frac{-E_a}{k_\beta T}},\tag{3.5}$$

where σ_0 is a pre-exponential term relating to conductivity, E_a the activation energy, T the absolute temperature of the sample and $k_\beta=1.38065 \times 10^{-23}$ m^{2}kg s^{-2} K^{-1}.
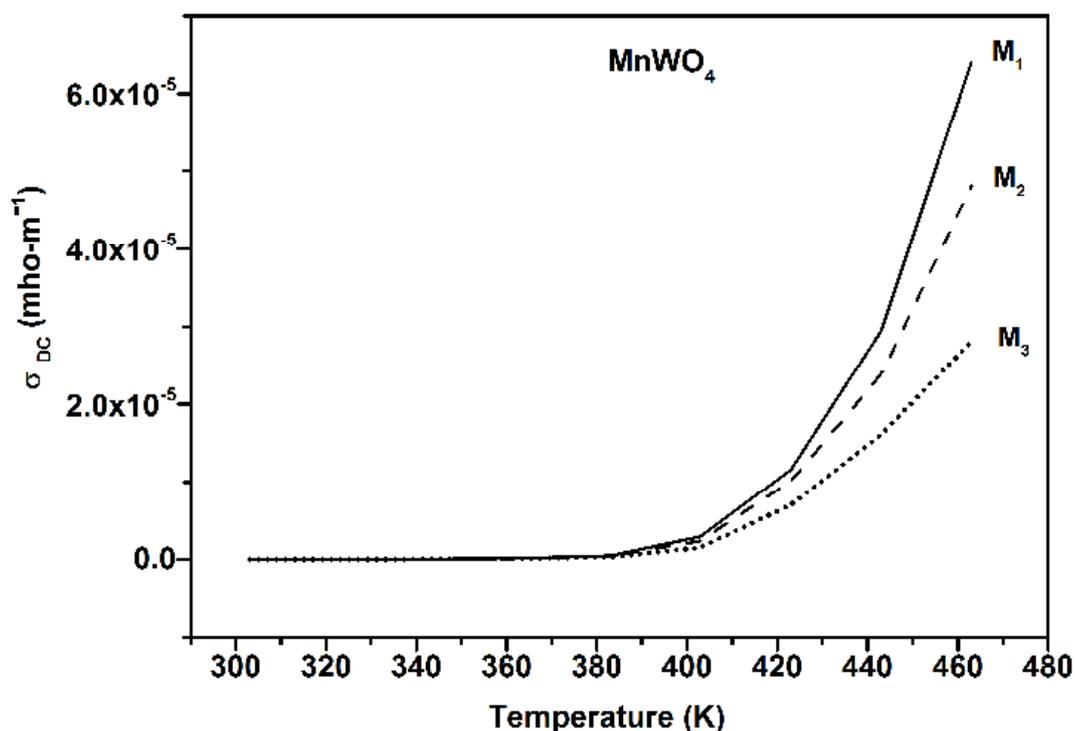
Fig. 3.18 DC conductivity of MnWO$_4$ samples

M$_1$, **M$_2$** and **M$_3$** as a function of temperature

The Arrhenius plot for samples **M$_1$**, **M$_2$** and **M$_3$** are shown in Fig. 3.19. The activation energy is calculated from the slope of the corresponding linear fits (Fig. 3.20). The values of activation energy obtained for **M$_1$**, **M$_2$** and **M$_3$** are 0.6929, 0.6766 and 0.6425 eV, respectively. Such low values of activation energy do not contribute to any intrinsic conduction as the bandgap values obtained for nanocrystalline MnWO$_4$ is about 2.6 eV. But, there is a rise in the conductivity with

temperature. This must be due to small polaron hopping as supported by reports in the literature [14, 17, 32, 33].
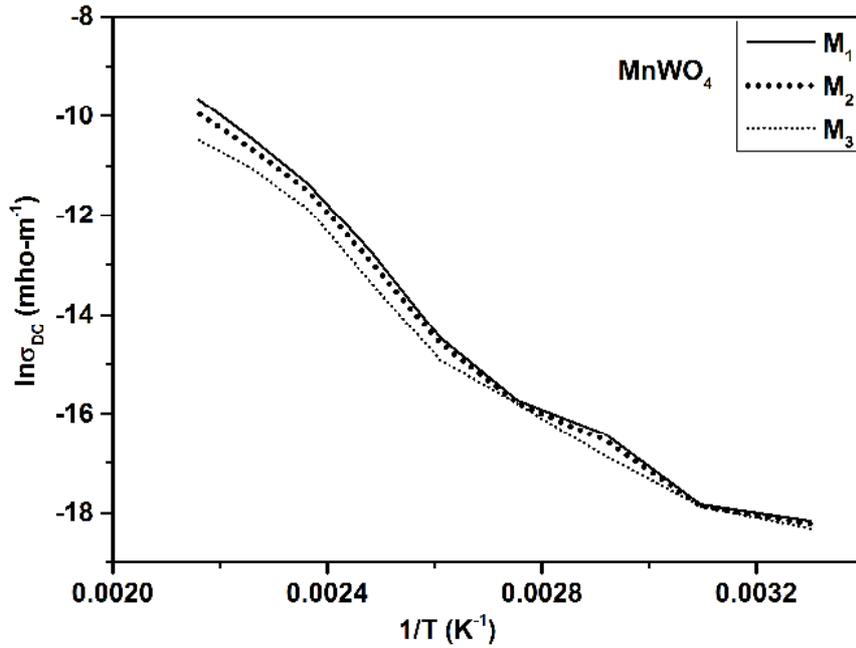
Fig. 3.19 Arrhenius plots of DC conductivity of MnWO$_4$ samples
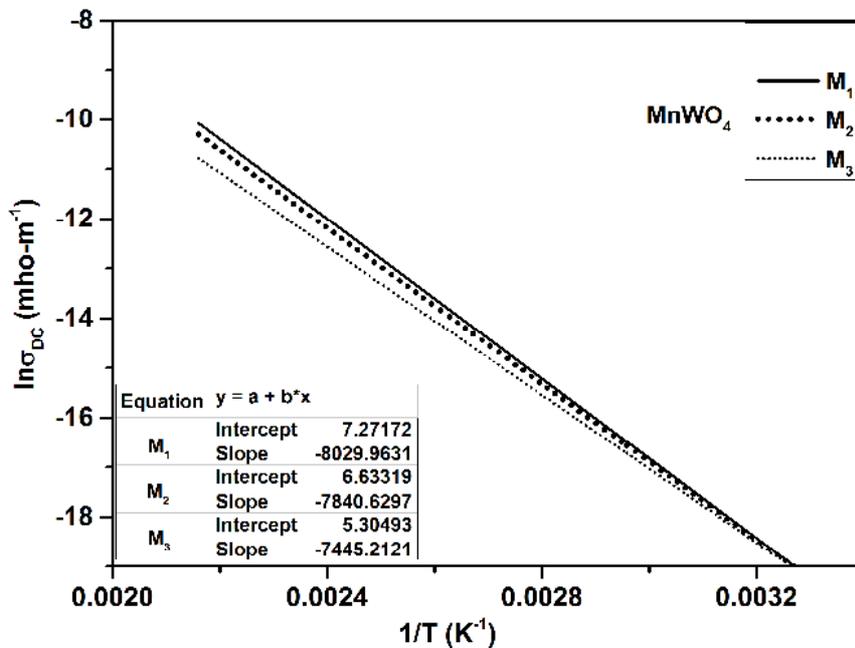
Fig. 3.20 The linear fits of Arrhenius plots of MnWO$_4$ samples **M$_1$**, **M$_2$** and **M$_3$**

In this type of conduction, the charge carriers hop from one site to the next. They get trapped in local traps with some lattice deformation leading to local polarization [31]. When they get sufficient thermal energy, they hop to the next site and so on. In $MnWO_4$, hopping is from Mn^{2+} to Mn^{3+} sites.

3.7.1.2 *DC electrical studies of electron irradiated MnWO₄*

The variation of DC conductivity (σ_{DC}) with temperature for the samples $\mathbf{M_1}$ and $\mathbf{M_1(05)}$ in the range from 300-460 K is shown in Fig. 3.21. The DC conductivity increases exponentially with temperature for the bare and electron irradiated samples. At 303 K, the values of σ_{DC} obtained are 1.30×10^{-8} and 3.25×10^{-6} mho-m^{-1} for $\mathbf{M_1}$ and $\mathbf{M_1(05)}$, respectively. These values at 463 K are 6.41×10^{-5} and 2.91×10^{-4} mho-m^{-1}, respectively. This confirms the semiconducting nature of the synthesized $MnWO_4$ nanoparticles. In the case of electron irradiated sample, a tenfold increase in DC conductivity is observed (Fig. 3.21).

The values of activation energy (E_a) of samples $\mathbf{M_1}$ and $\mathbf{M_1(05)}$ determined from Arrhenius plots are 0.6975 and 0.4350 eV, respectively. The activation energy needed for hopping is less for the irradiated sample because of the decrease in particle size due to electron irradiation. The lattice deformation occurring to the unit cells might have brought Mn^{2+} to Mn^{3+} closer. This reduces the hopping distances and the activation energy. So, it can be inferred that suitable dose of irradiation can improve the DC conductivity of $MnWO_4$. An important application of $MnWO_4$ nanocrystals

mentioned in the literature is humidity sensing [34, 35]. In brief, electron irradiation of suitable doses can help to design $MnWO_4$ based humidity sensor with better sensing capabilities.
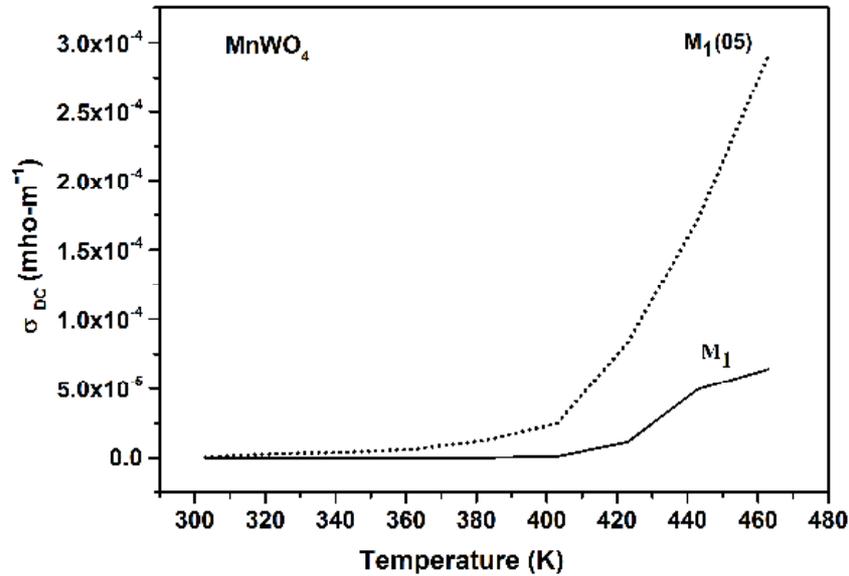
Fig. 3.21 DC conductivity of $MnWO_4$ samples M_1 and $M_1(05)$ as a function of temperature

3.7.2 AC electrical studies

In this section a detailed study of the temperature, frequency and grain size dependence on the dielectric properties and the AC conductivity of nanocrystalline $MnWO_4$ are presented. Effect of electron beam irradiation on the AC electrical properties are also investigated. Pellet samples are used for the AC electrical studies.

3.7.2.1 *Dielectric studies*

Dielectric constant

Fig. 3.22 represents the variation of dielectric constant with AC frequency of samples M_1, M_2 and M_3 at room temperature (303 K). The

real part of the dielectric constant (ε') for samples M_1, M_2 and M_3 are 2534.49, 164.03 and 4.07, respectively at 100 Hz. It shows that dielectric constant decreases with increase in calcination temperature. The dielectric constants of samples M_1, M_2 and M_3 are decreased to 13.55, 7.19 and 0.03, respectively as the frequency increased to 10 MHz. It shows that dielectric constant decreases with increase in frequency.
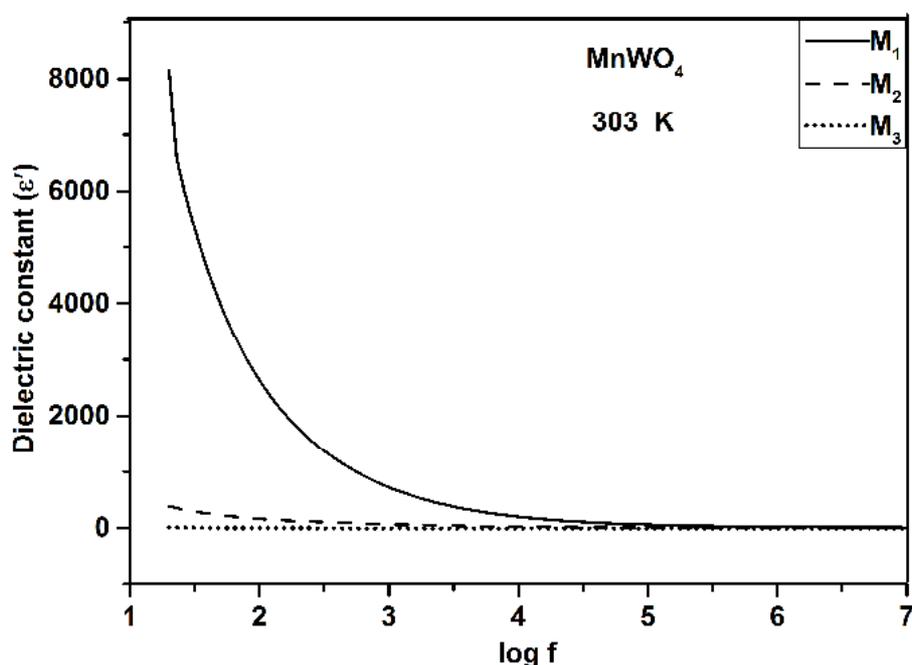
Fig. 3.22 Variation of dielectric constant with AC frequency of MnWO$_4$ samples at room temperature

The observations in the dielectric studies can be explained as follows. The dielectric properties of nanomaterials have great dependence on the heterogeneities, such as dangling bonds, vacancies, vacancy clusters, and microporosities present at the interfaces [36, 37]. These defects can cause a change of positive and negative space charge distribution in interfaces. When subjected to an electric field, these space charges move.

When they are trapped by defects, a lot of dipole moments are formed. In the low frequency region, it is easy for the dipole moments to follow the variation of electric field [36]. The major contribution to the dielectric constant in nanocrystalline samples at low frequencies is due to interfacial polarization [38]. The reason for the decrease in dielectric constant with increase in calcination temperature (or grain size) can be attributed to the decrease in grain boundary volume which diminishes the interfacial polarization.
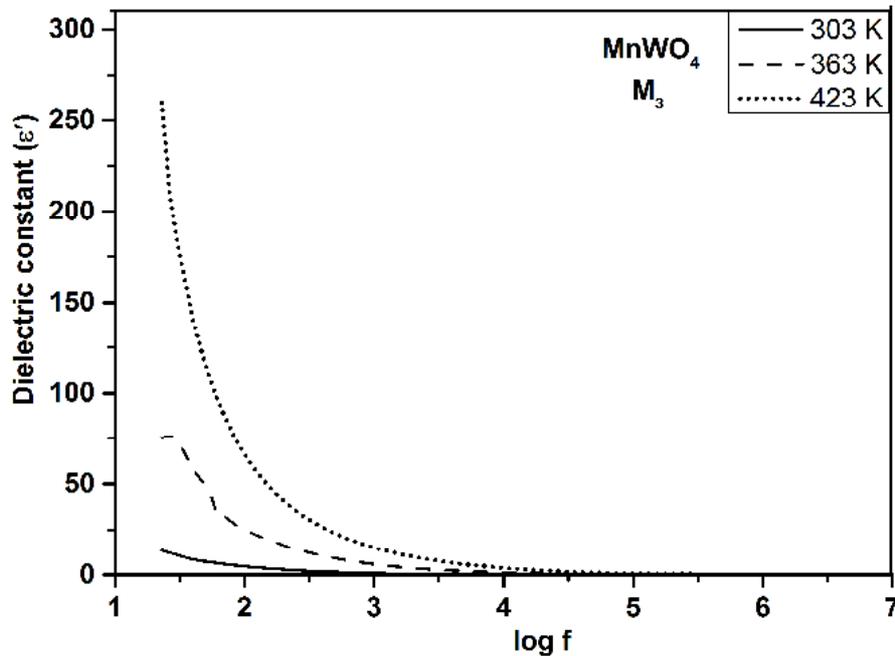
Fig. 3.23 Variation of dielectric constant with
AC frequency of MnWO$_4$ sample **M$_3$** at different temperatures

Fig. 3.23 represents the variation of dielectric constant with frequency of the sample **M$_3$** at different temperatures. At 100 Hz, the dielectric constant of **M$_3$** has values of 4.07, 22.18 and 57.12 at temperatures 303, 363 and 423 K, respectively. At 10 MHz, respective

values are 0.04, 0.07 and 0.16. It is observed that at any particular frequency the dielectric constant increases with increase in temperature and this temperature dependence is high in the low frequency region.

Interfacial and dipolar polarizations have linear dependence on temperature at lower frequencies [25, 37]. This is the reason for the large increase in the dielectric constant with temperature at lower frequencies. But, at higher frequencies the temperature dependence is not observed due to very low response of polarization to the changing electric field. In the high frequency regime dielectric contributions are mainly due to electronic polarizations, but their temperature dependence is negligible.

Loss tangent

The variation in loss tangent (Tan δ) as a function of frequency for samples **M$_1$**, **M$_2$** and **M$_3$** at room temperature are plotted in the Fig. 3.24. At 100 Hz, loss tangent values are 23.90, 4.81 and 3.80 for **M$_1$**, **M$_2$** and **M$_3$** respectively. The corresponding values of loss tangent at 10 MHz are 1.03, 0.79 and 0.65, respectively.

In nanophase materials, the heterogeneities present in the interface layers produce an absorption current, resulting in dielectric loss. Large absorption current due to the space charge polarization leads to dissipative losses. When the frequency is increased the response of dipoles to the changing field decreases and the loss tangent approaches very low constant values (Fig. 3.24). It can also be seen from Fig. 3.24 that loss tangent decreases with increase in calcination temperature. The loss tangent is

found to be a maximum for the sample (M_1) with smallest grain size. Absorption current decreases with decrease of grain boundary volume caused by an increase in grain size due to rise in calcination temperature. Hence, the dielectric loss decreases at any given frequency with increase in calcination temperature (or grain size).
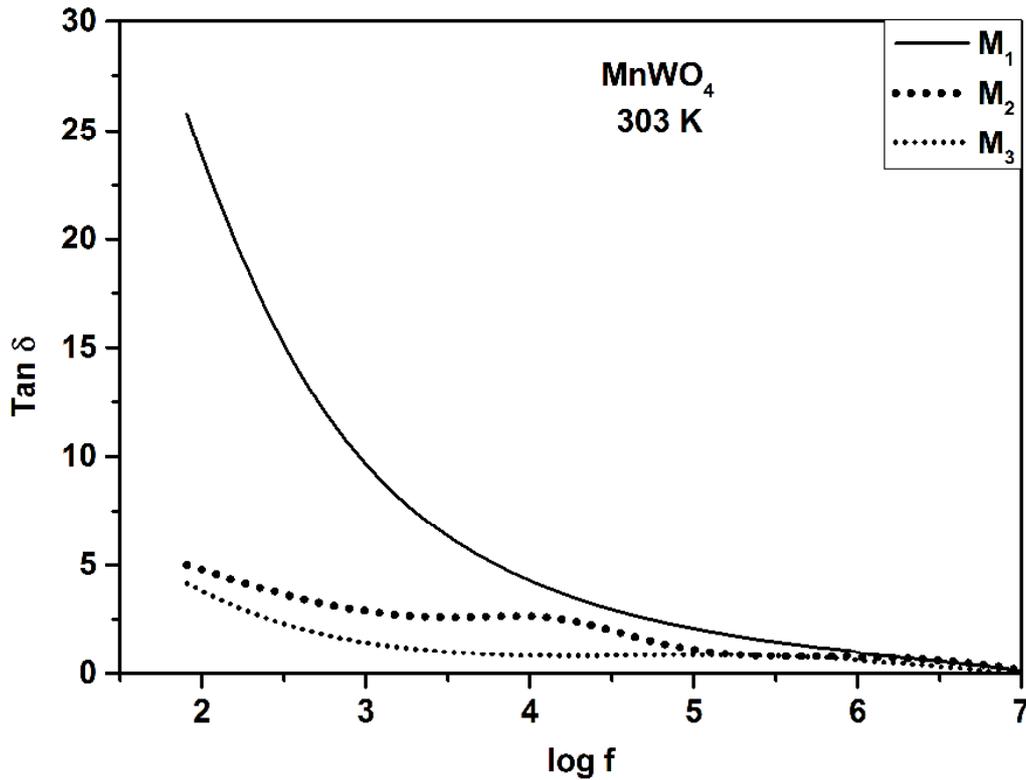
Fig. 3.24 Variation in loss tangent as a function of AC

frequency of MnWO$_4$ samples M_1, M_2 and M_3 at room temperature

Fig. 3.25 is a plot of Tan δ against log f in the case of sample M_3 at three different temperatures. The values of Tan δ at 100 Hz are 3.70, 5.39 and 8.00 at 303, 363 and 423 K, respectively. At low frequencies, the loss is high and gets elevated with increase in temperature.
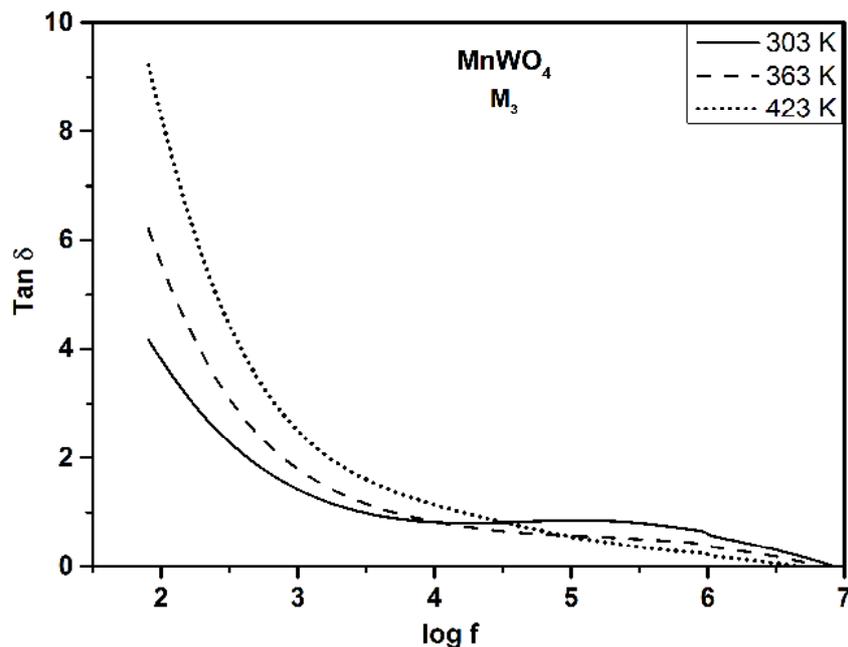
Fig. 3.25 Variation of loss tangent with AC frequency of $MnWO_4$

sample **M₃** at different temperatures

The loss in $MnWO_4$ can be explained by the electronic hopping model, which considers the frequency dependence of the localized charge carriers hopping in a random array of centres. This model is applicable for materials in which the polarization responds fast to the appearance of an electron on any one site so that the process may occur effectively into the final state [37]. At high frequencies, Tan δ becomes very less because the electron exchange interaction (hopping) between Mn^{+2} and Mn^{+3} cannot follow the alternatives of the applied AC electric field. This absorption current decreases with increase in the frequency of the applied field. At lower frequencies the hopping rate of charge carriers increases with increase in temperature. Thus, the loss tangent also increases with increase of temperature in the low frequency region [37].

3.7.2.2 *AC conductivity studies*

Fig. 3.26 represents the variation of AC conductivity (σ_E) of MnWO$_4$ samples **M$_1$, M$_2$** and **M$_3$** at room temperature with frequency of the applied AC. It is found that at low frequencies all the samples show almost frequency independent behavior. It is interesting that the frequency independent part of the curve shifts downward with increase in the grain size. Above 40 kHz, the curves show frequency dependence behavior.
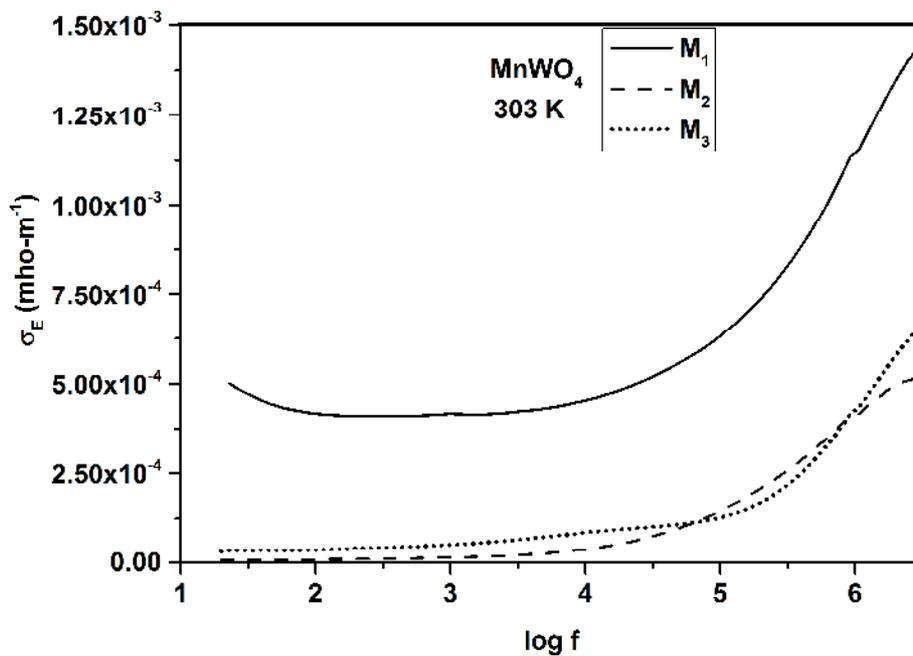
Fig. 3.26 Variation of AC conductivity (σ_E) of MnWO$_4$ samples **M$_1$, M$_2$** and **M$_3$** with AC frequency at room temperature

Fig. 3.27 represents the variation of σ_E of sample **M$_3$** with frequency at three different temperatures. Measured AC conductivity σ_E has a frequency independent but temperature dependent part σ_{dc}(T) due to band conduction. As expected, σ_{dc} is shifted upward as the temperature is raised. The frequency dependent part (σ_{ac}) arising from hopping is slightly greater

at higher temperature. The results of the AC measurements can be analyzed as follows.
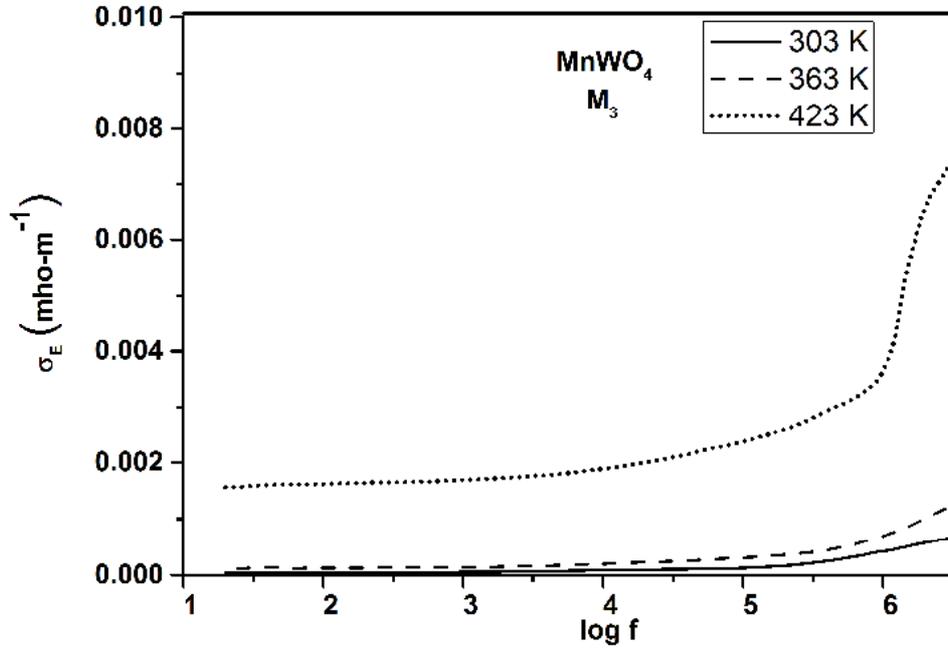
Fig. 3.27 Variation of AC conductivity (σ_E) with AC frequency of MnWO$_4$ sample **M$_3$** at different temperatures

Generally observations on the type of experimentally measured conductivity variations as in Fig. 3.26 and 3.27 can be represented by the relation [39,40],

$$\sigma_E(\omega) = \sigma_{dc}(T) + \sigma_{ac}(\omega) \qquad (3.6)$$

The frequency dependent part is given by the Jonscher's universal power law [41, 42] as,

$$\sigma_{ac}(\omega) = A\omega^n. \qquad (3.7)$$

Here, A is a constant, ω is the angular frequency and n is the power. The nature of variation in the frequency dependent part is determined by the value n, which is a temperature dependent exponent. Its value is usually

between 0 and 1. The values of *n* determined for the sample M_3 from the slope of log ω versus log [σ_{ac}] plots in Fig. 3.28 are 0.89, 0.80 and 0.84 at temperatures 303, 363 and 423 K, respectively. The values of *n* confirm that mechanism of conduction in the $MnWO_4$ sample is hole hopping [43].
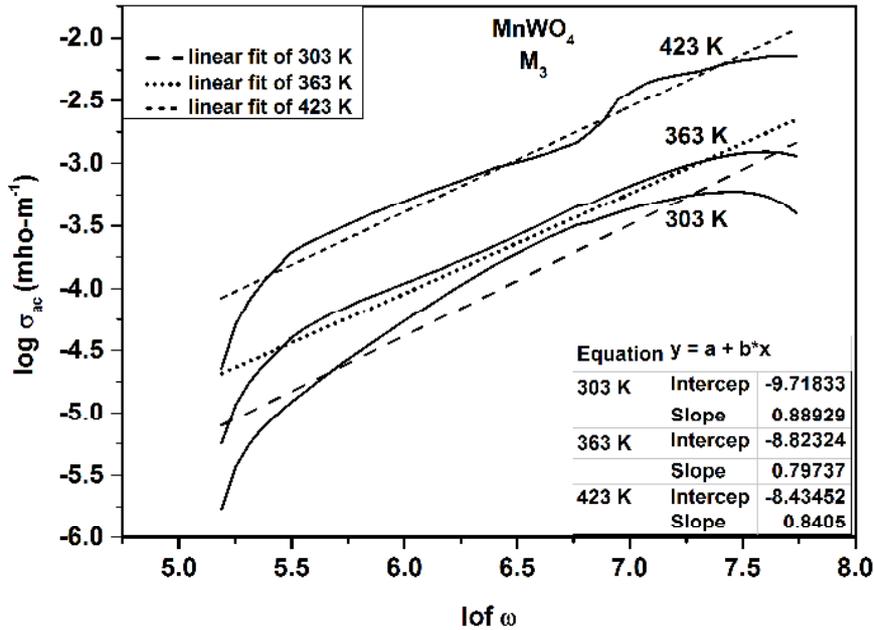
Fig. 3.28 log ω versus log [σ_{ac}] plots of $MnWO_4$ sample M_3

The *dc* part $\sigma_{dc}(T)$ of the AC conductivity is represented by the flat plateau in the curves of Fig. 3. 27. At 20 kHz, the values of $\sigma_{dc}(T)$ conductivity of sample M_3 are 9.67×10^{-5}, 2.30×10^{-4}, and 2.02×10^{-3} mho-m^{-1} at 303, 393 and 423 K, respectively. In the frequency range 40 kHz to 10 MHz (Fig. 3.27), AC conductivity obeys the power law. From equation 3.6, $\sigma_{ac}(\omega) = \sigma_E(T) - \sigma_{dc}(T)$. Values of $\sigma_{ac}(\omega)$ obtained at 40 kHz for the sample M_3 are 9.62×10^{-6}, 3.04×10^{-5}, 1.45×10^{-4} mho-m^{-1} at temperatures 303, 363 and 423 K, respectively. The corresponding values at 10 MHz are 3.90×10^{-4}, 0.00115 and 0.00721 mho-m^{-1}, respectively.

3.7.3   AC electrical studies of electron beam irradiated sample

To study the influence of electron beam irradiation on the AC electrical properties, samples **M₁** and **M₁(05)** are sintered at 400°C for 2 h.

3.7.3.1 *Dielectric studies*

Variation of dielectric constants of samples **M₁** and **M₁(05)** with frequency is shown in Fig. 3.29. At lower frequencies the dispersion is more. As the frequency increases the dispersion decreases gradually. Beyond 10 kHz the two graphs almost merge with each other. At 100 Hz, the values of ε' observed are 107.87 and 183.82 for the bare and irradiated samples, respectively. The corresponding values at 10 MHz are 6.53 and 7.27.
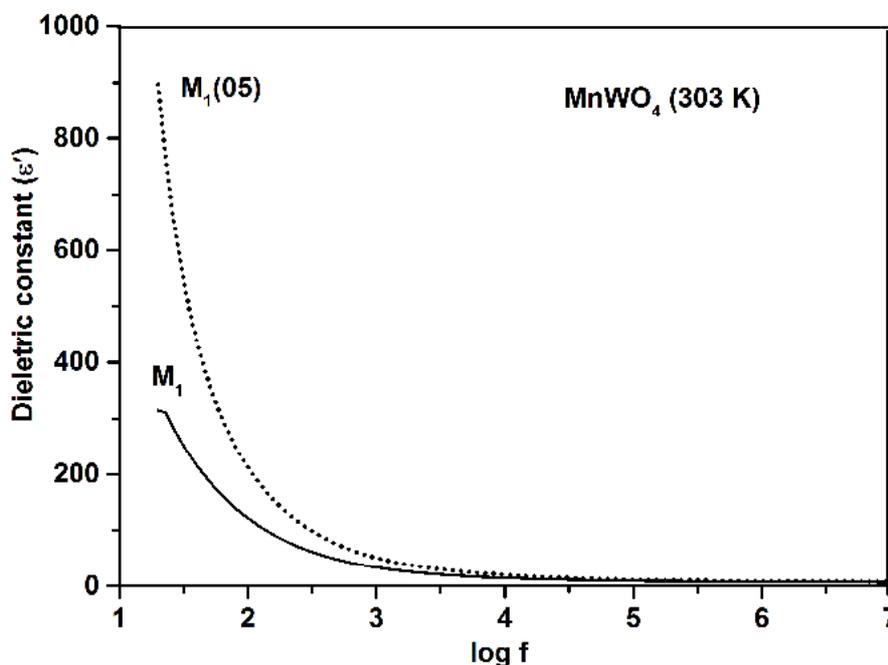
Fig. 3.29 Variation of dielectric constant with

AC frequency of MnWO$_4$ samples **M₁** and **M₁(05)**

It can be seen from Fig. 3.29 that at lower frequencies, the values of dielectric constants are elevated to higher values due to the increase of defects caused by electron beam irradiation [37, 44].

The dependence of Tan δ with frequency of samples M_1 and $M_1(05)$ is shown in Fig. 3.30. The values of Tan δ, at 100 Hz, are 127.71 and 224.14 for M_1 and $M_1(05)$, respectively.
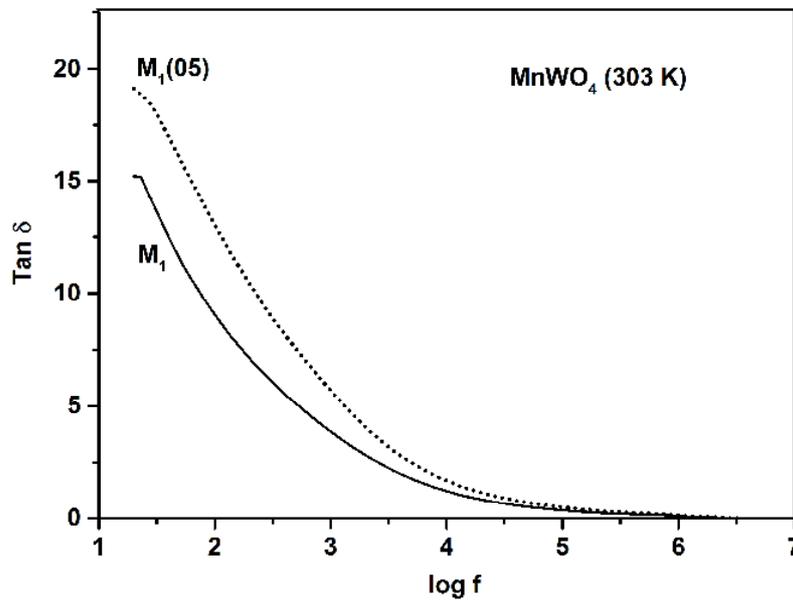
Fig. 3.30 Variation of loss tangent with AC frequency of MnWO₄ samples M_1 and $M_1(05)$

At lower frequencies loss tangent is greater in the irradiated sample (Fig. 3.30). This can be due to the increase in particle boundary volume when more defects are created as a result of electron beam irradiation.

3.7.3.2 *AC conductivity studies*

Fig. 3.31 depicts the changes in AC conductivity with frequency of bare and electron irradiated (5 kGy electron dose) MnWO₄ nanoparticles. At 100 Hz, the values of AC conductivity measured are 6.12×10^{-6} and

1.54×10^{-5} mho-m^{-1} for samples **M₁** and **M₁(05),** respectively. At 0.1 MHz, the values obtained are 1.89×10^{-5} and 3.21×10^{-5} mho-m^{-1}, respectively.
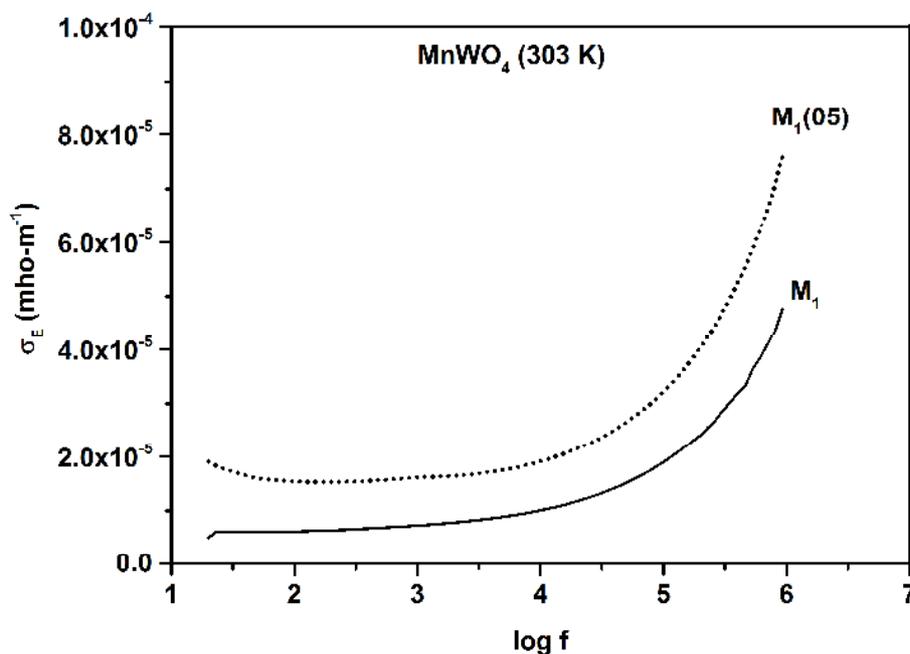
Fig. 3.31 Variation of AC conductivity with AC frequency of MnWO₄ samples **M₁** and **M₁(05)**

It is found that the DC part of the measured values is increased upon electron irradiation. The nature of AC conductivity variation obeys the universal power law $\sigma_{ac}(\omega) = A\omega^{n}$. The frequency exponent n is determined from the slope of the linear fits of log ω versus log $[\sigma_{ac}]$ curves in Fig. 3.32. Linear fits of log ω versus log $[\sigma_{ac}]$ plots of samples are shown in Fig. 3.33. For the sample (**M₁**) its value is 0.95 and for the irradiated sample it is 0. 57. Since n lies between 0 and 1, the AC conduction is due to ionic hopping [41]. Small value of activation energy and size reduction of crystallites caused by electron irradiation increase the hopping probability in sample **M₁(05)** [44].
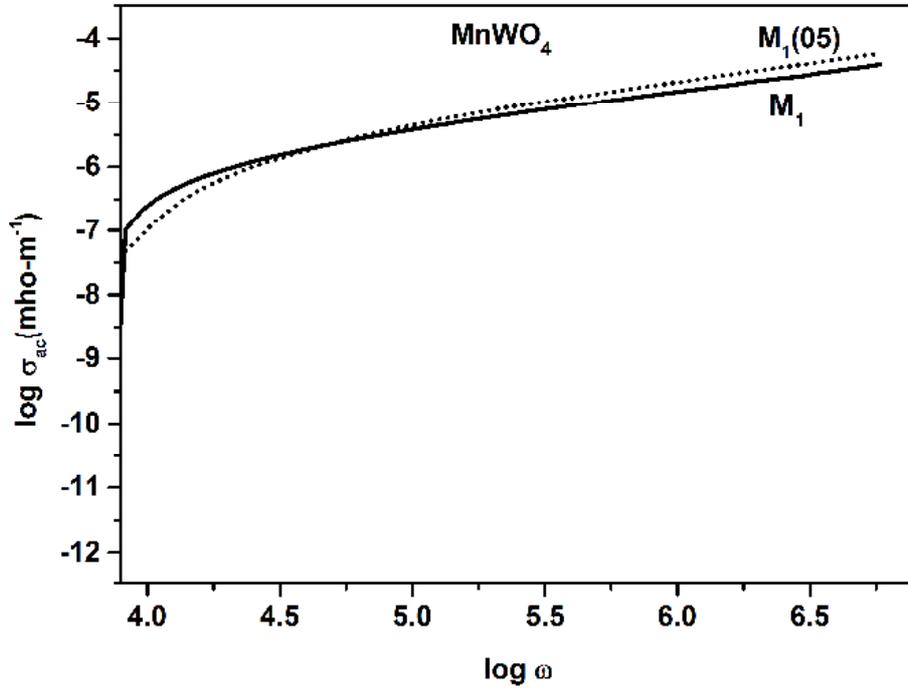
Fig. 3.32 The plot of log ω versus log [σ_{ac}] of MnWO$_4$ samples **M$_1$** and **M$_1$ (05)**
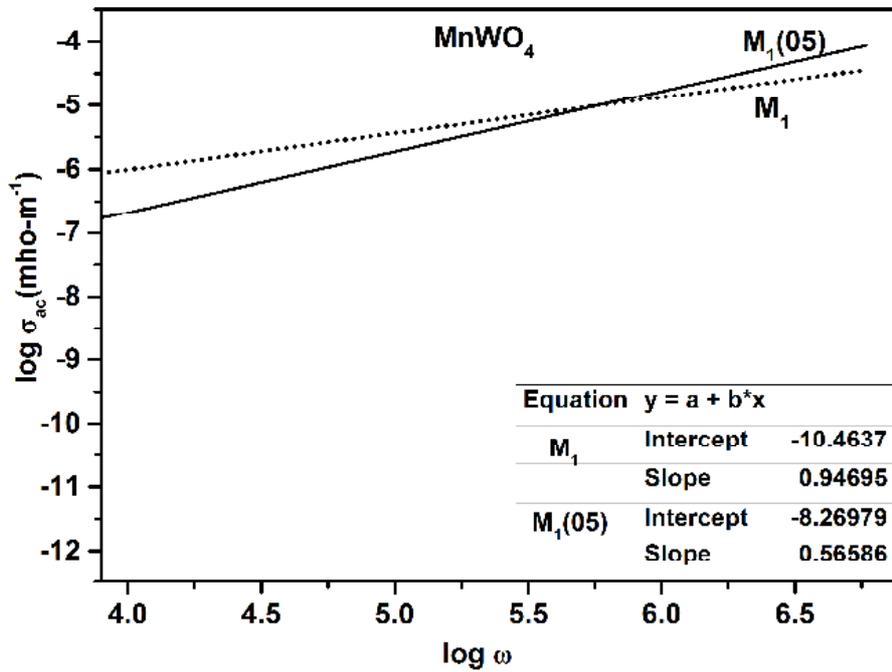
Fig. 3.33 Linear fit of log ω versus log [σ_{ac}] plot of MnWO$_4$

samples **M$_1$** and **M$_1$(05)**

3.8   Conclusion

➢   Nanophase $MnWO_4$ in powder form is successfully prepared by chemical precipitation method without using any surfactants. Thermal analysis found that $MnWO_4$ is thermally stable in the temperature range 390-850°C.

➢   The XRD analysis confirms the monoclinic wolframite structure for the synthesized $MnWO_4$. The crystallite size of the sample is found to increase with increase in the calcination temperature, which results in slight lattice contraction. Vibrational spectroscopic studies like FTIR and Raman studies confirm the formation of $MnWO_4$.

➢   The electron beam irradiated $MnWO_4$ samples exhibit a decrease in crystallite size with lattice expansion. But, aggregation of particles is more in electron irradiated samples. The electron beam irradiation results in the broadening and slight shift of Raman peaks.

➢   SEM analysis shows that the particles are aggregated to form micro-clusters and could not observe any regular shape for the particles or clusters. The EDS analysis confirms the presence of all the constituent elements in $MnWO_4$. TEM studies found bar-shaped morphology for the $MnWO_4$ particles with a width of 78 nm.

➢   The UV-Visible absorption maximum for $MnWO_4$ is found in the ultraviolet region and a bandgap of 2.63 eV is obtained for the sample calcined at 450 °C. A slight decrease in optical bandgap with increase in calcination temperature is also observed. This decrease in bandgap

is due to the slight elevation of particle size caused by the calcination. The PL spectra of $MnWO_4$ samples exhibit a wide photoluminescence spectrum having a number of shoulder peaks. The intensity of PL emission slightly decreases with increase in calcination temperature. The electron beam irradiation results in enhanced absorbance and modified optical bandgap. Besides, slightly enhanced PL emission is observed for the electron irradiated samples due to defects and particle size variation.

➢ Thermally activated polaronic DC conductivity is observed in $MnWO_4$ samples. The DC conductivity of $MnWO_4$ ranges from 10^{-6}-10^{-3} mho-m^{-1}. The AC electrical studies of $MnWO_4$ show that the values of dielectric constant and tangent loss increases with increase in temperature. But, they decrease with increase in grain size at low frequencies. The AC conductivity studies establish the universal power law dependence. The frequency independent part of the observed AC conductivity is lower in samples calcined at higher temperatures. But it becomes higher for a sample as the measurement temperature increases.

➢ Thermally activated polaronic DC conductivity is also observed in the irradiated sample of $MnWO_4$. DC electrical study confirms a ten-fold increase in conductivity for the electron irradiated sample. AC conductivity of electron irradiated samples increases with increase in frequency and shows the power law dependence. Compared to unirradiated sample the values of dielectric constant, tangent loss and

AC conductivity are elevated in the electron beam irradiated sample. Thus, the overall effect of electron beam irradiation in nanocrystalline $MnWO_4$ is that it modifies the structural, optical and electrical properties to certain extent.

References

1   X. A. López, A. F. Fuentes, M. M. Zaragoza, J. A. Díaz Guillén, J. S. Gutiérrez, A. L. Ortiz, and V. Collins-Martínez, International Journal of Hydrogen Energy **41** (48), 23312 (2016).

2   X. Li, T. Lunkenbein, J. Krohnert, V. Pfeifer, F. Girgsdies, F. Rosowski, R. Schlogl, and A. Trunschke, Faraday discussions **188** (0), 99 (2016).

3   U. M. García-Pérez, A. Martínez-de la Cruz, and J. Peral, Electrochimica Acta **81**, 227 (2012).

4   S.-J. Chen, X.-T. Chen, Z. Xue, J.-H. Zhou, J. Li, J.-M. Hong, and X.-Z. You, Journal of Materials Chemistry **13** (5), 1132 (2003).

5   H. Zhou, Y. Yiu, M. C. Aronson, and S. S. Wong, Journal of Solid State Chemistry **181** (7), 1539 (2008).

6   L. Zhang, C. Lu, Y. Wang, and Y. Cheng, Materials Chemistry and Physics **103** (2-3), 433 (2007).

7   Y.-X. Zhou, Q. Zhang, J.-Y. Gong, and S.-H. Yu, The Journal of Physical Chemistry C **112** (35), 13383 (2008).

8   Q. Zhang, W.-T. Yao, X. Chen, L. Zhu, Y. Fu, G. Zhang, L. Sheng, and S.-H. Yu, Crystal Growth & Design **7** (8), 1423 (2007).

9   P. Parhi, T. N. Karthik, and V. Manivannan, Journal of Alloys and Compounds **465** (1–2), 380 (2008).

10   W. Wu, W. Qin, Y. He, Y. Wu, and T. Wu, Journal of Experimental Nanoscience **7** (4), 390 (2012).

11   W. Tong, L. Li, W. Hu, T. Yan, X. Guan, and G. Li, The Journal of Physical Chemistry C **114** (36), 15298 (2010).

12   K. P. Priyanka, N. Aloysius Sabu, A. T. Sunny, P. A. Sheena, and T. Varghese, Journal of Nanotechnology **2013**, 1 (2013).

13   M. Ptak, M. Maczka, K. Hermanowicz, A. Pikul, and J. Hanuza, Spectrochimica acta. Part A, Molecular and biomolecular spectroscopy **86**, 85 (2012).

14   S. Saranya, S. T. Senthilkumar, K. V. Sankar, and R. K. Selvan, Journal of Electroceramics **28** (4), 220 (2012).

15   M. A. P. Almeida, L. S. Cavalcante, M. Siu Li, J. A. Varela, and E. Longo, Journal of Inorganic and Organometallic Polymers and Materials **22** (1), 264 (2011).

16   A. R. West, *Solid State Chemistry and Its Applications*. (Wiley, 1987).

17   C. J. Benedict, A. Rao, G. Sanjeev, G. S. Okram, and P. D. Babu, Journal of Magnetism and Magnetic Materials **397**, 145 (2016).

18   J. Ruiz-Fuertes, D. Errandonea, S. López-Moreno, J. González, O. Gomis, R. Vilaplana, F. J. Manjón, A. Muñoz, P. Rodríguez-Hernández, A. Friedrich, I. A. Tupitsyna, and L. L. Nagornaya, Physical Review B **83** (21) (2011).

19   W. S. Choi, K. Taniguchi, S. J. Moon, S. S. A. Seo, T. Arima, H. Hoang, I. S. Yang, T. W. Noh, and Y. S. Lee, Physical Review B **81** (20), 205111 (2010).

20   S. Muthamizh, R. Suresh, K. Giribabu, R. Manigandan, S. Praveen Kumar, S. Munusamy, and V. Narayanan, Journal of Alloys and Compounds **619**, 601 (2015).

21   M. N. Mancheva, R. S. Iordanova, D. G. Klissurski, G. T. Tyuliev, and B. N. Kunev, The Journal of Physical Chemistry C **111** (3), 1101 (2007).

22   L. H. Hoang, P. V. Hanh, N. D. Phu, X.-B. Chen, and W. C. Chou, Journal of Physics and Chemistry of Solids **77**, 122 (2015).

23   X. Lai, Y. Wei, D. Qin, Y. Zhao, Y. Wu, D. Gao, J. Bi, D. Lin, and G. Xu, Integrated Ferroelectrics **142** (1), 7 (2013).

24   L. H. Hoang, N. T. M. Hien, W. S. Choi, Y. S. Lee, K. Taniguchi, T. Arima, S. Yoon, X. B. Chen, and I.-S. Yang, Journal of Raman Spectroscopy **41** (9), 1005 (2010).

25   P. Van Hanh, L. Huy Hoang, P. Van Hai, N. Van Minh, X.-B. Chen, and I.-S. Yang, Journal of Physics and Chemistry of Solids **74** (3), 426 (2013).

26   F. Amano, K. Nogami, and B. Ohtani, The Journal of Physical Chemistry C **113** (4), 1536 (2009).

27   S. Dey, R. A. Ricciardo, H. L. Cuthbert, and P. M. Woodward, Inorganic chemistry **53** (9), 4394 (2014).

28   F. Zhang, Y. Yiu, M. C. Aronson, and S. S. Wong, The Journal of Physical Chemistry C **112** (38), 14816 (2008).

29   W. F. Zhang, M. S. Zhang, Z. Yin, and Q. Chen, Applied Physics B **70** (2), 261 (2000).

30   S. K. Gupta, R. Desai, P. K. Jha, S. Sahoo, and D. Kirin, Journal of Raman Spectroscopy **41** (3), 350 (2010).

31   F. Yakuphanoglu, Y. Aydogdu, U. Schatzschneider, and E. Rentschler, Solid State Communications **128** (2–3), 63 (2003).

32   R. Bharati, R. A. Singh, and B. M. Wanklyn, Journal of Physics and Chemistry of Solids **43** (7), 641 (1982).

33   R. Bharati, R. A. Singh, and B. M. Wanklyn, Journal of Materials Science **18** (5), 1540 (1983).

34   A. M. E. Suresh Raj, C. Mallika, O. M. Sreedharan, and K. S. Nagaraja, Materials Letters **53** (4–5), 316 (2002).

35   W. Qu, W. Wlodarski, and J.-U. Meyer, Sensors and Actuators B: Chemical **64** (1–3), 76 (2000).

36   C.-m. Mo, L. Zhang, and G. Wang, Nanostructured Materials **6** (5–8), 823 (1995).

37   N. Aloysius Sabu, K. Priyanka, S. Thankachan, A. T. Sunny, E. Mohammed, O. Jaseentha, and T. Varghese, Nanosystems: Physics, Chemistry, Mathematics **4** (3), 357 (2013).

38   S. Demirezen, A. Kaya, S. A. Yerişkin, M. Balbaşı, and İ. Uslu, Results in Physics **6**, 180 (2016).

39   R. M. Hill and A. K. Jonscher, Journal of Non-Crystalline Solids **32** (1–3), 53 (1979).

40   A. Kumar, B. P. Singh, R. N. P. Choudhary, and A. K. Thakur, Journal of Alloys and Compounds **394** (1–2), 292 (2005).

41   A. K. Jonscher, *Dielectric Relaxation in Solids*. (Chelsea Dielectric Press, London, 1983).

42   B. M. Greenhoe, M. K. Hassan, J. S. Wiggins, and K. A. Mauritz, Journal of Polymer Science Part B: Polymer Physics **54** (19), 1918 (2016).

43   M. G. Hutchins, O. Abu-Alkhair, M. M. El-Nahass, and K. Abdel-Hady, Journal of Non-Crystalline Solids **353** (44–46), 4137 (2007).

44   N. Aloysius Sabu, K. P. Priyanka, X. Sheena, E. M. Mohammed, and T. Varghese, IOP Conference Series: Materials Science and Engineering **73** (1), 012051 (2015).

****ജ✪ൽ****

Chapter - 4
STUDIES ON STRUCTURAL, OPTICAL AND ELECTRICAL PROPERTIES OF NANOCRYSTALLINE CALCIUM TUNGSTATE

Scheelite calcium tungstate ($CaWO_4$) is well known for its interesting structural and luminous peculiarities, and applications [1-6]. $CaWO_4$ powders are usually prepared by non-aqueous solvents methods as well as by solid-state reactions which require high temperature, longer reaction time and difficult reaction conditions. Different methods reported for the synthesis of nanocrystalline $CaWO_4$ includes hydrothermal [7-10], solvothermal [11], solution method [12, 13, 14], polymeric precursor method , sol-gel method [15, 16], surfactant assisted solution synthesis [17, 18], solution precipitation [19], microemulsion-based synthesis [20], and microwave assisted synthesis [21].

In the present work, $CaWO_4$ nanoparticles are synthesized by aqueous precipitation route. The samples calcined at different temperatures are used for characterization. The synthesis and characterization of nanocrystalline $CaWO_4$ are presented in this chapter. The study of the

influence of high energy electron beam irradiation on the material properties of the $CaWO_4$ calcined sample (350 °C) is also presented.

4.1   Synthesis of $CaWO_4$ nanoparticles

The reagents used for the synthesis of $CaWO_4$ are calcium nitrate $(Ca(NO_3)_2. 4H_2O$, 99.8 %, Sigma Aldrich) and sodium tungstate $(Na_2WO_4.2H_2O$, 99.9 %, Alfa Aesar) 0.1M aqueous solutions (100ml each) of sodium tungstate and calcium nitrate are allowed to react and the $CaWO_4$ precipitated is subjected to different preparation steps as described in section 3.1. The scheme of preparation of $CaWO_4$ is presented in Fig. 4.1. The chemical reaction can be expressed as follows

$$Ca(NO_3)_2 .4H_2O + Na_2WO_4 .2H_2O \rightarrow CaWO_4 + 2Na NO_3 + 6H_2O.$$

The calcination temperatures are fixed after performing the thermal analysis described in section 4.2. The $CaWO_4$ samples calcined at 350, 500 and 650 °C are designated as C_1, C_2 and C_3, respectively.

$CaWO_4$ powder sample calcined at 350 °C (C_1) is used for electron beam irradiation studies. Four different samples $C_1(2)$, $C_1(4)$, $C_1(6)$ and $C_1(8)$ are subjected to irradiation of 8 MeV electron doses of 2, 4, 6 and 8 kGy, respectively.
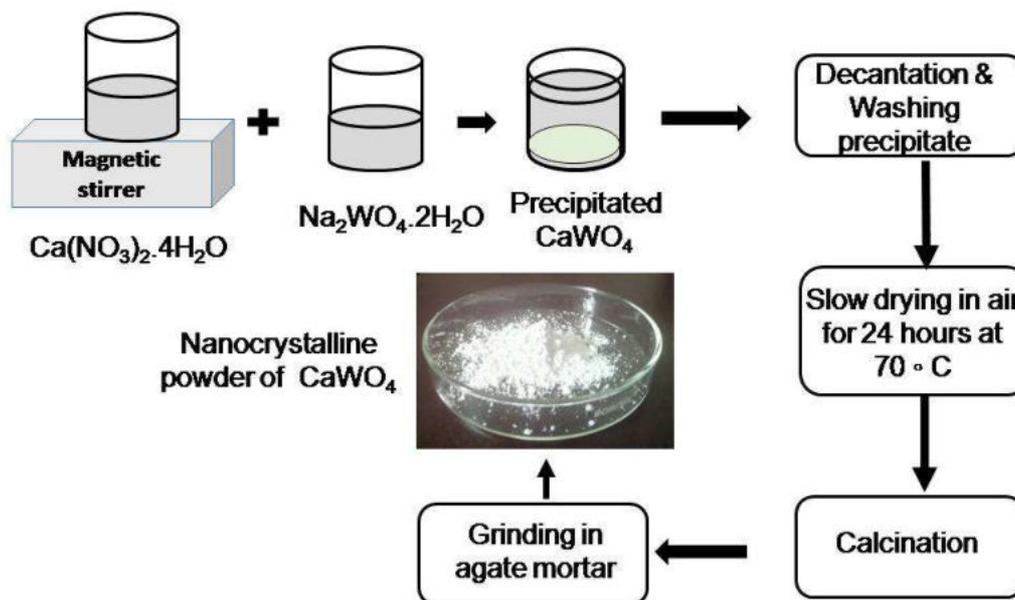
Fig. 4.1 Scheme of preparation of $CaWO_4$

4.2   Thermal analysis

TG and DTG curves of the calcium tungstate precursor are shown in Fig. 4.2. The TG and DTG patterns reveal three prominent weight losses centred on 65.69, 286.6 and 582.60 °C with an overall weight loss of ~2.71 % in the temperature range from 40-900 °C. The DTG pattern shows three endothermic peaks centred on 65.69, 286.6 and 582.60 °C. The first weight loss step of ~ 0.70 % represents the physisorbed and interlayer water [22]. The second weight loss ~0.76 % attributes to the loss of structural water (~one unit of H_2O). A third weight loss of ~ 1.25 % is due to the removal of chemisorptions found at certain sites (Ca-O_{water}) in the scheelite structure [22].
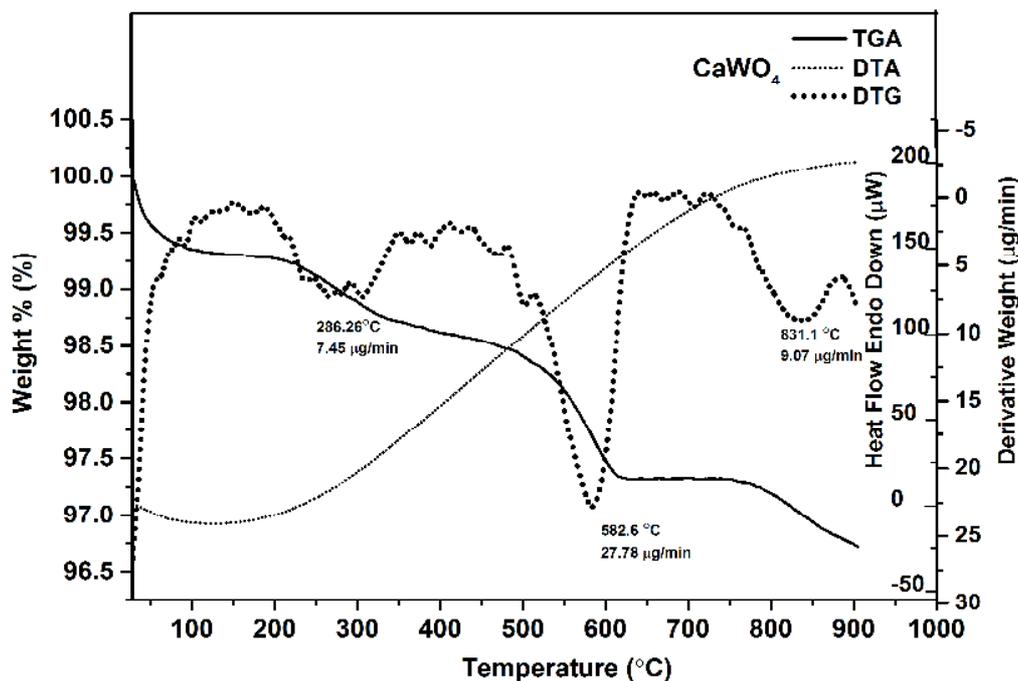
Fig. 4.2 TGA, DTG and DTA curves of $CaWO_4$ precursor

Above 582.60 up to 900 °C, no significant weight loss is observed. DTA curve from 200 to 850 °C is exothermic indicating the thermal crystallization of the sample. Thus, thermal studies show that the overall weight loss upon heating is very less and $CaWO_4$ is thermally stable.

4.3   Structural characterization

4.3.1   XRD analysis of $CaWO_4$ samples

The crystal structure of calcium tungstate nanoparticles are studied using Bruker D8 Advance X-ray diffractometer (λ=1.5406 Å) with Cu (K_α) radiation in the 2θ range from 10 to 70°. Fig. 4.3 shows the XRD patterns of $CaWO_4$ samples **C₁, C₂** and **C₃**.
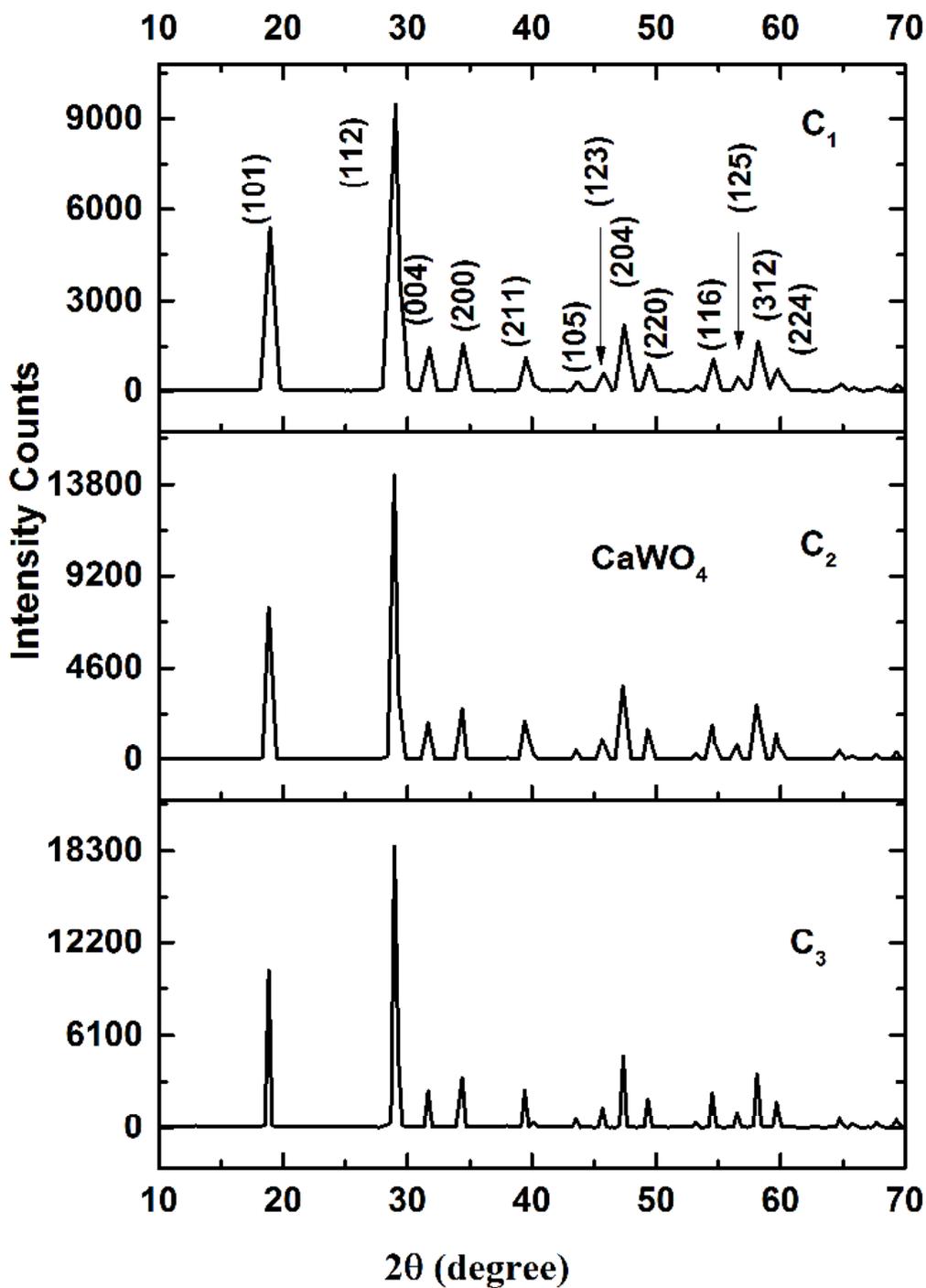
Fig. 4.3 XRD patterns of CaWO$_4$ samples **C$_1$**, **C$_2$** and **C$_3$**

The XRD confirms that the peaks obtained for $CaWO_4$ match well with the data given in JCPDS Card No**.** 77-2235. All XRD patterns obtained indicate highly crystalline $CaWO_4$ with a scheelite-type tetragonal structure and a space group $I4_1/a$ in a C_{4h}^6 symmetry [23]. The crystallite size is estimated from the Scherrer's equation (2.2). The average crystallite sizes calculated are 18.45, 25.32, and 39.67 nm for samples **C_1, C_2** and **C_3,** respectively. At higher calcination temperatures, XRD patterns show much sharper peaks as a result of increase in size of the particles. The lattice parameters are calculated from the d-spacing for peaks having Miller indices (hkl) using the equation [24],

$$\frac{1}{d^2} = \frac{h^2 + k^2}{a^2} + \frac{l^2}{c^2}, \qquad\qquad (4.1)$$

for the tetragonal unit cell $(a = b \neq c, \alpha = \beta = \gamma = 90°)$. The unit cell volume is obtained using the equation,

$$V = a^2 c, \qquad\qquad (4.2)$$

Table 4.1 presents a comparison of the values of lattice constants and unit cell volume calculated with those in the JCPDS file No. 77-2235 for $CaWO_4$. It shows slight increase in lattice constants with increase in calcination temperature. This results in an increase in the unit cell volume or lattice expansion.

Table 4.1 Lattice constants and unit cell volume of $CaWO_4$ samples

Sample	Unit cell parameters (Å)		Unit cell volume (Å^3)	Average crystallite size (nm)
	a	*c*		
JCPDS Card No. 77-2235	5.1936	11.2552	303.59	--
C_1	5.2114	11.2652	305.95	18.45
C_2	5.2222	11.2976	308.10	25.32
C_3	5.2219	11.2864	307.75	39.67

4.3.2   XRD analysis of electron beam irradiated $CaWO_4$ samples

The XRD patterns of bare and the electron irradiated samples are shown in Fig. 4.4. Table 4.2 shows that the position of the major peaks in $C_1(2)$ and $C_1(4)$ are shifted to lower (2θ) values when irradiated with 2 and 4 kGy doses. Besides, the full width at half maximum (FWHM) of the major peaks in $C_1(2)$ and $C_1(4)$ are reduced due to electron irradiation. However, the position of the major peaks in $C_1(6)$ and $C_1(8)$ are shifted back to higher (2θ) values when electron irradiation doses increases to 6 and 8 kGy. Also, it can be seen that the FWHM of samples $C_1(6)$ and $C_1(8)$ are increased due to higher electron doses (6 and 8 kGy). Corresponding to the changes discussed above, the crystallite size calculated for samples C_1, $C_1(2)$, $C_1(4)$, $C_1(6)$ and $C_1(8)$ are 20.52, 23.62, 24.75, 23.66 and 19.96 nm, respectively.
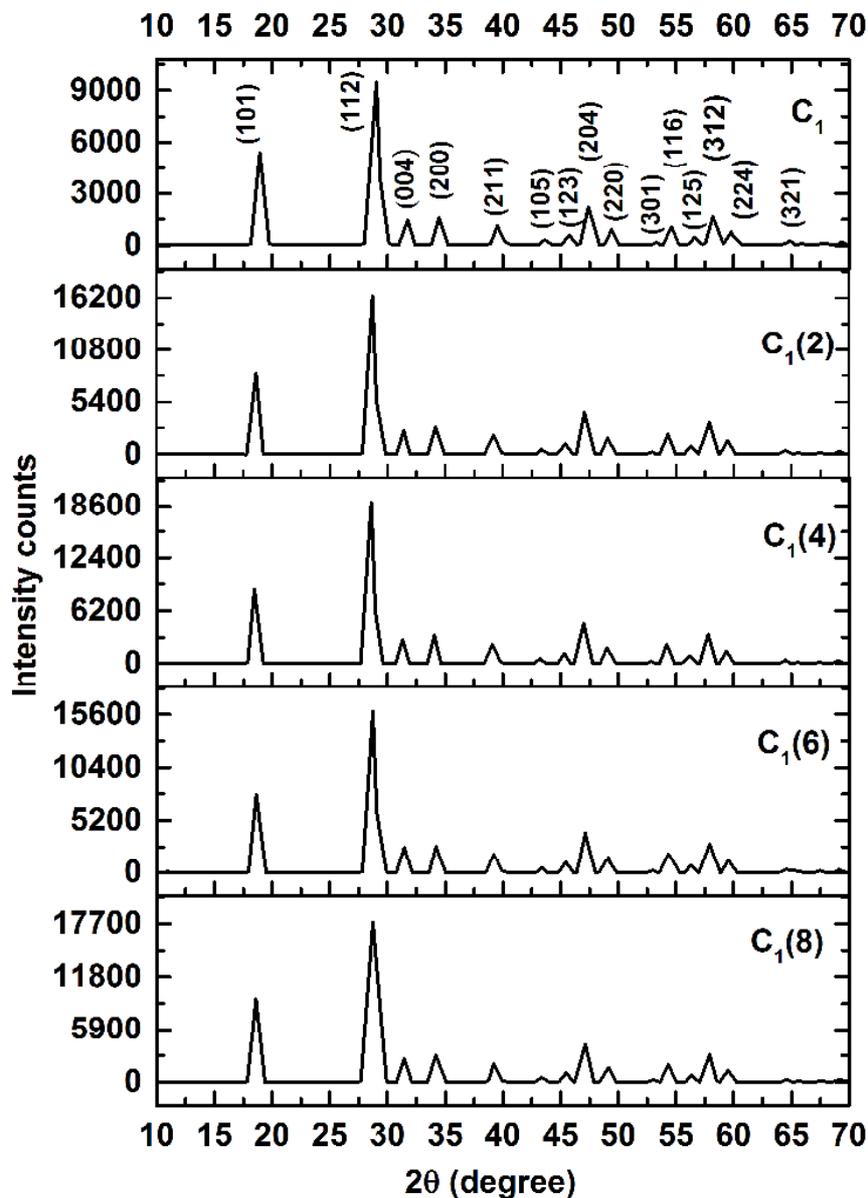
Fig. 4.4 XRD patterns of CaWO₄ samples **C₁, C₁ (2), C₁(4), C₁(6)** and **C₁(8)**

The change in crystallite size with electron dose can be explained as follows. Lower electron doses cause slight atomic displacements leading to the growth of crystallites. But at higher doses, electron irradiation cannot promote crystallite growth due to disorder. It is reported that due to residual

stress, strain is generated in the sample by stretching or compressing the bonds between atoms [23, 25]. The increase in lattice spacing can be attributed to the residual stretching strain induced by irradiation.

Table 4.2 XRD data of bare and irradiated $CaWO_4$ samples

Sample	Major peak (2θ degree)	FWHM of major peak (rad)	Unit Cell Parameters (Å)		Unit cell volume ($Å^3$)	d value (Å)	Crystallite size from major peak (nm)	Average crystallite size (nm)
			a	c				
C_1	29.045	0.0077	5.2114	11.2652	305.95	3.07	18.50	20.52
$C_1(2)$	28.703	0.0069	5.2114	11.2652	313.04	3.11	20.66	23.62
$C_1(4)$	28.604	0.0061	5.2521	11.4149	314.88	3.11	21.92	24.75
$C_1(6)$	28.746	0.0070	5.2402	11.3674	312.14	3.10	20.29	23.66
$C_1(8)$	28.741	0.0077	5.2401	11.3673	312.13	3.10	18.48	19.96

The crystallite size is found to increase with increase in electron dose up to 4 kGy and there after it decreases as the electron dose increases (Table 4.2). It is reported that there is a critical irradiation dose for each material and is dependent upon particle size [23, 26]. In short, the changes in unit cell volume and the strain induced are the indication of defects produced during electron irradiation.

4.4   Vibrational spectroscopy of $CaWO_4$ nanoparticles

FTIR spectroscopy is used for investigating the formation of $CaWO_4$. While the Raman spectroscopy is used for identifying the different modes of molecular vibrations in $CaWO_4$ molecule.

Vibrational spectroscopy can be employed as a probe to investigate the degree of structural order-disorder at short range in the materials. Group theory calculation shows 26 different vibration modes (Raman and infrared) for $CaWO_4$ crystal as indicated by the equation,

$$\Gamma_{(Raman+Infrared)} = 3A_g + 5A_u + 5B_g + 3B_u + 5E_g + 5E_u, \qquad (4.3)$$

where A_g, B_g and E_g are the Raman-active modes. They are given by the equation,

$$\Gamma_{(Raman)} = 3A_g + 5B_g + 5E_g. \qquad (4.4)$$

In equation 4.3, $4A_u$ and $4E_u$ of $5A_u$ and $5E_u$ modes are IR active. One A_u and one E_u modes are acoustic vibrations, and $3B_u$ vibrations are silent modes [27, 28].

4.4.1   FTIR spectroscopy of $CaWO_4$

The FTIR spectra of $CaWO_4$ nanoparticles $\mathbf{C_1}$, $\mathbf{C_2}$ and $\mathbf{C_3}$ are shown in Fig. 4.5. The spectra indicate absorption peaks centred on 448 and 812 cm^{-1} in the range from 400 to 1000 cm^{-1}. The sharp absorption peak at 448 cm^{-1} corresponds to the bending vibration of W-O bond. The absorption peak centred on 812 cm^{-1} is assigned to the anti-symmetric stretching vibration in the [WO_4] group. The bands at 3431 and 1634 cm^{-1} correspond

to the O-H stretching and H-O-H bending vibrations, respectively due the presence of surface adsorbed water [18, 29-31]. The peak positions are not affected by increase in calcination temperature indicating the presence of the same molecular species in samples C_1, C_2 and C_3.
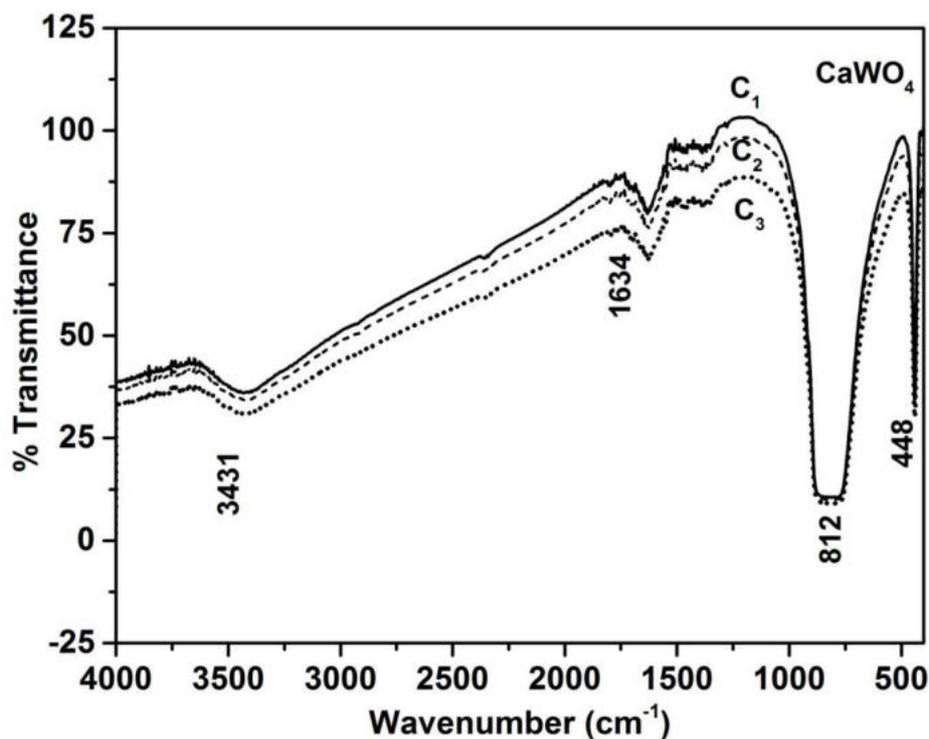
Fig. 4.5 FTIR spectra of $CaWO_4$ samples C_1, C_2 and $C3$

4.4.2   Raman spectroscopy of $CaWO_4$

Raman vibration modes can be divided into two groups, internal and external modes. The internal vibrations are caused by vibrations within the $[WO_4]^{2-}$ cluster. The external vibrations are related to the lattice phonon or motion of $[CaO_8]$ clusters [23]. The room temperature Raman spectra of $CaWO_4$ samples C_1, C_2 and C_3 are shown in Fig. 4.6.
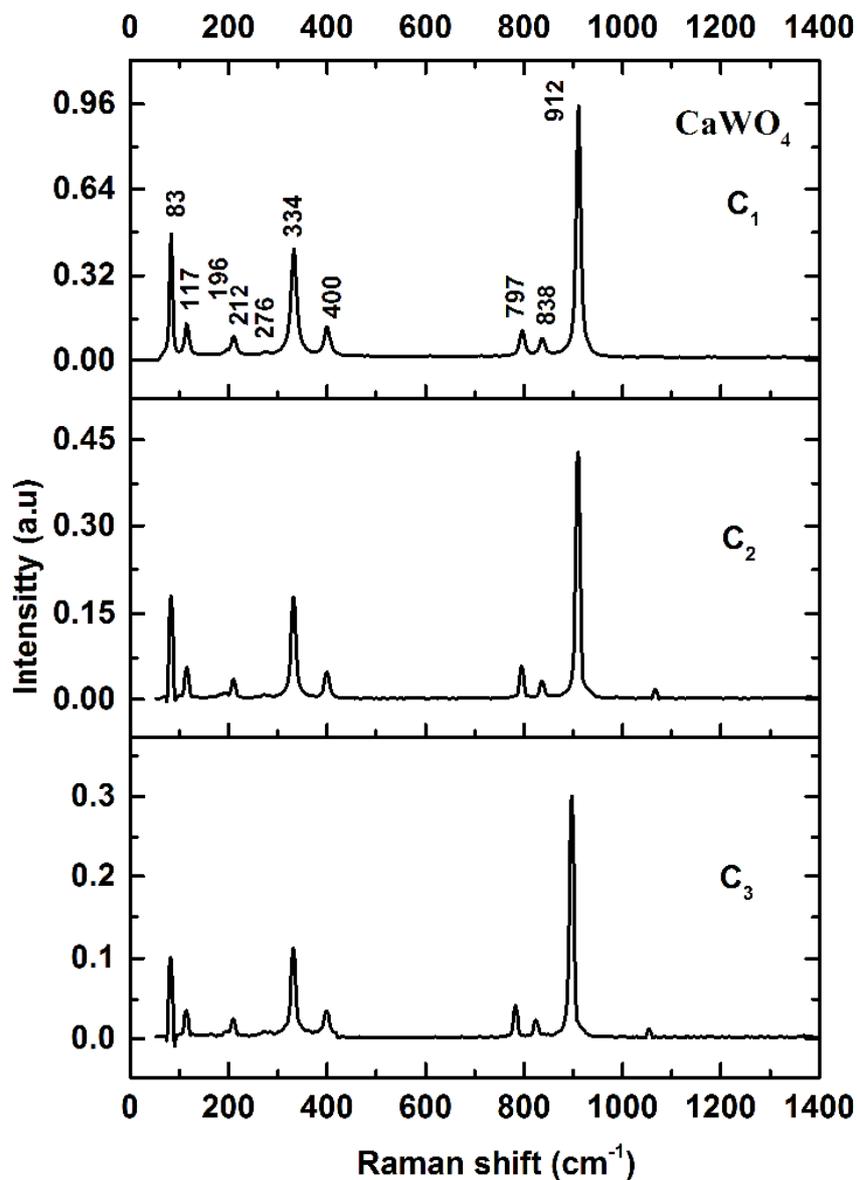
Fig. 4.6 Raman spectra of CaWO$_4$ samples **C$_1$**, **C$_2$** and **C$_3$**

In CaWO$_4$ (**C$_1$**) sample, 10 Raman modes are detected and labelled. The Raman band at 911 cm^{-1} occurs due to the symmetric stretching and those at 838 and 797 cm^{-1} occur due to the anti-symmetric bending in the [WO$_4$]$^{2-}$ cluster. The peak at 400 cm^{-1} is assigned to the anti-symmetric bending and the one at 334 cm^{-1} to the symmetric bending in the O-W-O

bond. The Raman shift due to the free rotation is observed at 212 cm^{-1}. The shift observed at 117 cm^{-1} is assigned to the symmetric stretching and the one at 83 cm^{-1} to the symmetric bending in the [CaO$_8$] cluster [5, 23, 30]. Raman modes of CaWO$_4$ samples along with literature values are presented in Table 4.3. It can be seen from the table that Raman peaks, except the peak formed at 400 cm^{-1}, shift slightly to the lower wavenumber side as the calcination temperature increases. These changes are caused by small changes in vibrational amplitudes as a result of improvement in crystallinity upon calcination.

Table 4.3 Comparison of Raman modes of CaWO$_4$ with literature values

Vibration modes	Raman shift (cm^{-1}) for calcined CaWO$_4$ samples			
	C_1	C_2	C_3	Literature [30]
E_g	83	81	80	84
B_g	117	115	114	117
E_g	196	193	192	195
B_g	212	211	208	210
E_g	--	--	--	218
A_g	276	272	271	275
E_g	--	--	--	--
A_g/B_g	334	331	331	336
E_g	400	400	400	401
B_g	-	-	-	409
E_g	797	795	794	797
B_g	838	837	832	838
A_g	912	910	909	912

4.4.3 Raman spectroscopy of electron irradiated CaWO$_4$

Raman spectroscopic technique is capable of detecting small changes in crystal structure caused by calcination or electron irradiation [32, 33]. The room temperature Raman spectra of the irradiated samples of nanocrystalline CaWO$_4$ are shown in Fig. 4.7. Table 4.4 shows that electron beam irradiation of CaWO$_4$ samples cause slight variations in certain peaks. A new peak at 1053 cm^{-1} is observed for the irradiated samples **C$_1$(2)** and **C$_1$(4)** . This might be due to the formation of dangling bonds as a result of electron beam irradiation [23, 33]. But, this peak disappears when irradiated with higher doses (6 and 8 kGy). XRD results of irradiated samples (Table 4.2) show an increase in volume of unit cell. But, the percentage increase in volume upon irradiation is very small. Hence, only slight changes are seen in the lattice parameters of irradiated CaWO$_4$ samples. Correspondingly, the changes in the positions of Raman modes are small. However, these small changes in the peak positions can influence the properties of samples. Table 4.4 shows the presence of highest frequency A_g vibration at 334 cm^{-1}. This is an indication of distortion in the surroundings of the tetrahedral anion [30]. Also, Table 4.4 shows that A_g vibration shifts to 332 cm^{-1} in the irradiated samples **C$_1$(2)**, **C$_1$(4)** and **C$_1$(6)**. In sample **C$_1$(8)**, Raman peak shifts back to 334 cm^{-1}. These changes in the A_g vibration can induce changes in the optical properties of the material.
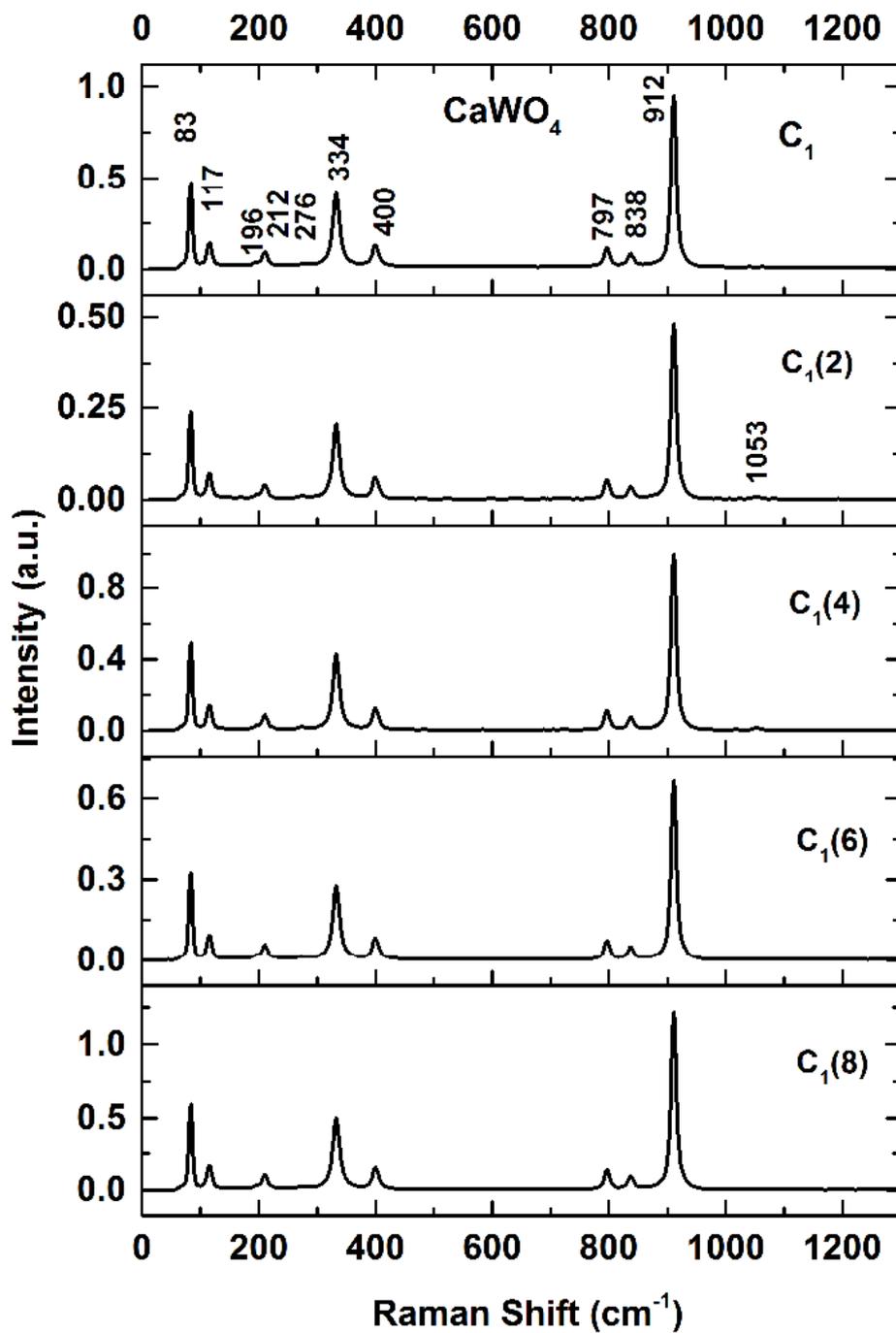
Fig. 4.7 Raman spectra of CaWO$_4$ samples **C$_1$**, **C$_1$(2)**, **C$_1$(4)**, **C$_1$(6)** and **C$_1$(8)**

Table 4.4 Raman modes of $CaWO_4$ samples C_1, $C_1(2)$, $C_1(4)$, $C_1(6)$ and $C_1(8)$

Vibration modes	Raman shift (cm^{-1})				
	C_1	$C_1(02)$	$C_1(04)$	$C_1(06)$	$C_1(08)$
E_g	83	83	83	83	83
B_g	117	117	114	114	114
E_g	196	193	192	195	196
B_g	212	211	211	211	211
E_g	--	--	--		--
A_g	276	276	276	274	272
E_g	--	--	--	--	--
B_g	334	332	332	332	332
A_g	334	332	332	332	334
E_g	400	400	400	400	400
B_g	-	-	-	-	-
E_g	797	797	797	797	797
B_g	838	838	838	838	838
A_g	911	910	909	910	910

4.5 Electron microscopy

The morphology, shape, distribution and composition of nanocrystalline $CaWO_4$ are investigated using electron microscopy techniques and the energy dispersive X-ray spectroscopy.

4.5.1 SEM analysis of $CaWO_4$ samples

SEM micrographs of the samples C_1, C_2 and C_3 are shown in Fig. 4.8. The images show that the products are composed of a number of nanosized particles in clusters. Dumb-bell shaped clusters are visible in the

image for **C₁.** But, the morphology of **C₂** and **C₃** changes as the calcination temperature increases.
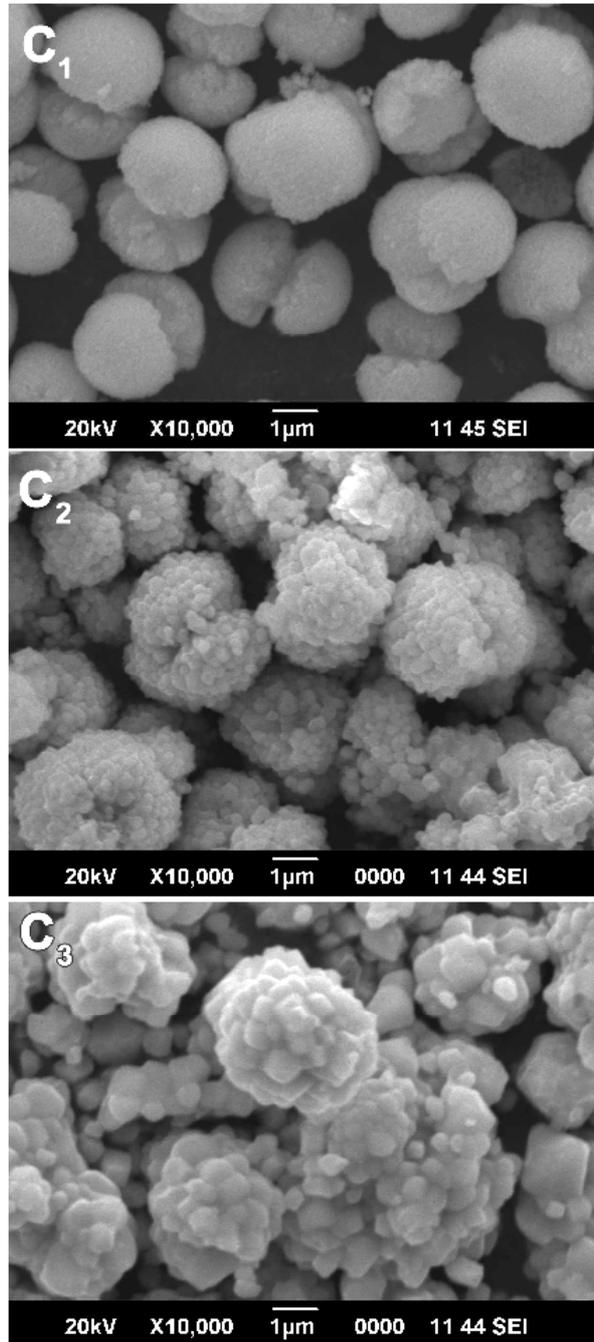
Fig. 4.8 SEM images of CaWO₄ samples **C₁, C₂** and **C₃**

The change in morphology occurs due to the fact that the scheelite-type structures tend to be faceted and aligned by docking processes as calcination temperature increases, involving crystallographic fusion between some faces with lower surface energy [23, 31, 34]. The self assembly of nanoparticles into certain shapes is to reduce the surface energy.

SEM micrographs of the bare (**C₁**) and electron irradiated (**C₁(6)**) samples are shown in Fig. 4.9. It is observed that some fragmentation of the clusters occurred in the irradiated sample.
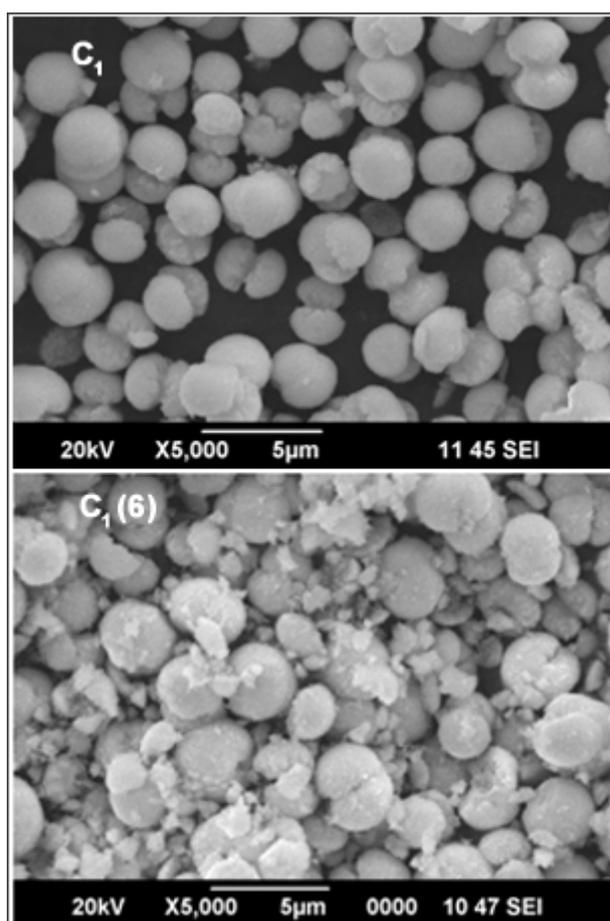
Fig. 4.9 SEM images of bare and irradiated $CaWO_4$ nanoparticles

4.5.2 EDS of CaWO$_4$

The compositional analysis of the sample **C$_1$** is done by energy dispersive X-ray spectroscopy, which is carried out in conjunction with the SEM analysis. The EDS pattern of CaWO$_4$ nanoparticles is shown in Fig. 4.10.
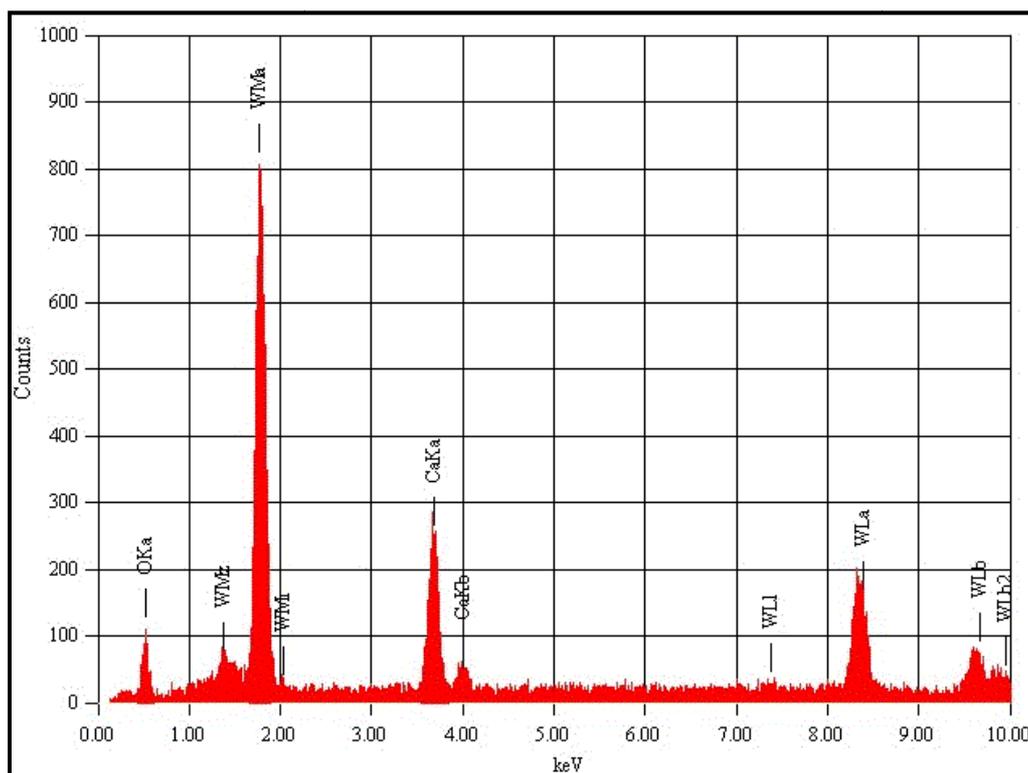
Fig. 4.10 EDS of synthesized CaWO$_4$ nanoparticles

Table 4.5 EDS data of CaWO$_4$ sample **C$_1$**

Element	Series	(keV)	Mass%	Atom%
O	K	0.525	4.02	22.99
Ca	K	3.69	16.4	37.42
W	M	1.774	79.58	39.59
Total		--	100	100

The peaks in the spectrum confirm that the product contains Ca, W and O only. The intense signal near at 1.774 keV indicates that W is the major element. The elements present in the sample and their percentage occurrence are given in the Table 4.5.

4.5.3 TEM analysis of $CaWO_4$

TEM images of $CaWO_4$ nanoparticles calcined at 350 ^{0}C (C_1) are shown in Fig. 4.11.
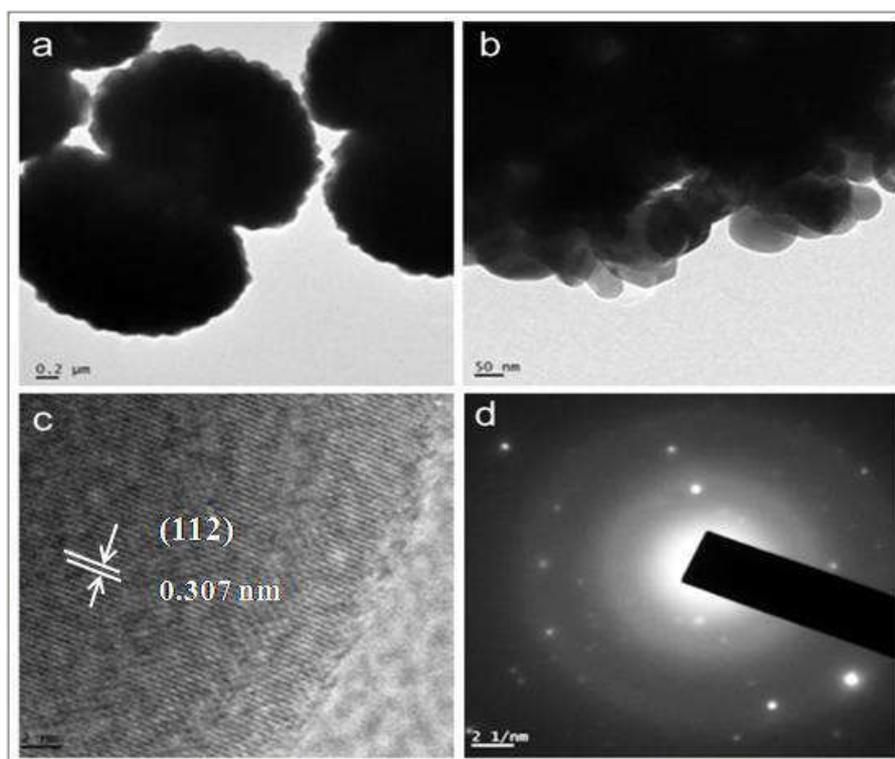
Fig. 4.11 TEM images of $CaWO_4$ sample C_1

It can be seen from the TEM bright field images (Fig. 4.11a and b) that the particles exhibit almost spherical shape. Most of the particles are agglomerated and their average diameter is found to be ~82 nm. HRTEM image of the sample C_1 is shown in Fig. 4.11 (c). Average *d* value obtained

from HRTEM image is 0.307 nm and matches with the plane (112). Fig. 4.11 (d) shows selected area electron diffraction (SAED) pattern of sample C_1, which confirms that $CaWO_4$ nanoparticles are polycrystalline.

4.6   Optical properties

4.6.1   UV-Visible spectra of $CaWO_4$

The absorbance of the calcined samples is determined from their diffuse reflectance measurements using UV-Visible spectrophotometer as mentioned in section 2.3.8. Fig. 4.12 shows the UV-Visible absorption spectra of samples C_1, C_2 and C_3. Sample C_1 shows absorption peak at 258.60 nm. This peak is due to the inter band transitions between the valence and the conduction bands. From the figure, it can be observed that the peaks of samples C_2 and C_3 are shifted towards the longer wavelength region. This red shift occurs due to particle size elevation caused by the calcination.
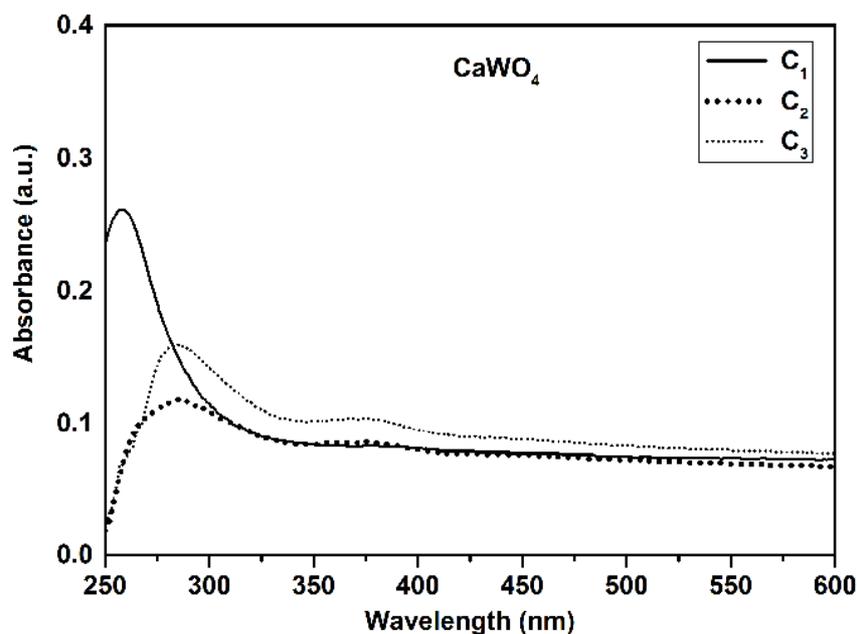
Fig. 4.12 UV-Visible spectra of $CaWO_4$ samples C_1, C_2 and C_3

The optical bandgap energy is calculated using the Tauc relation (Eqn. 2.5). Tungstates having general formula AWO_4 (A= Ca, Sr, Ba) exhibit an absorption spectrum governed by direct electronic transitions [35]. The optical bandgap is determined from the extrapolation of the straight line portion of $(\alpha h v)^2$ versus hv plot to $(\alpha h v)^2 = 0$. The optical bandgap values obtained from the Tauc plots (Fig. 4.13) for samples C_1, C_2 and C_3 are 4.12, 3.58 and 3.50 eV, respectively. It shows that the bandgap energy increases with decrease in particle size, which confirms quantum size effect [8]. Not that the dependence of bandgap on particle size is not linear.
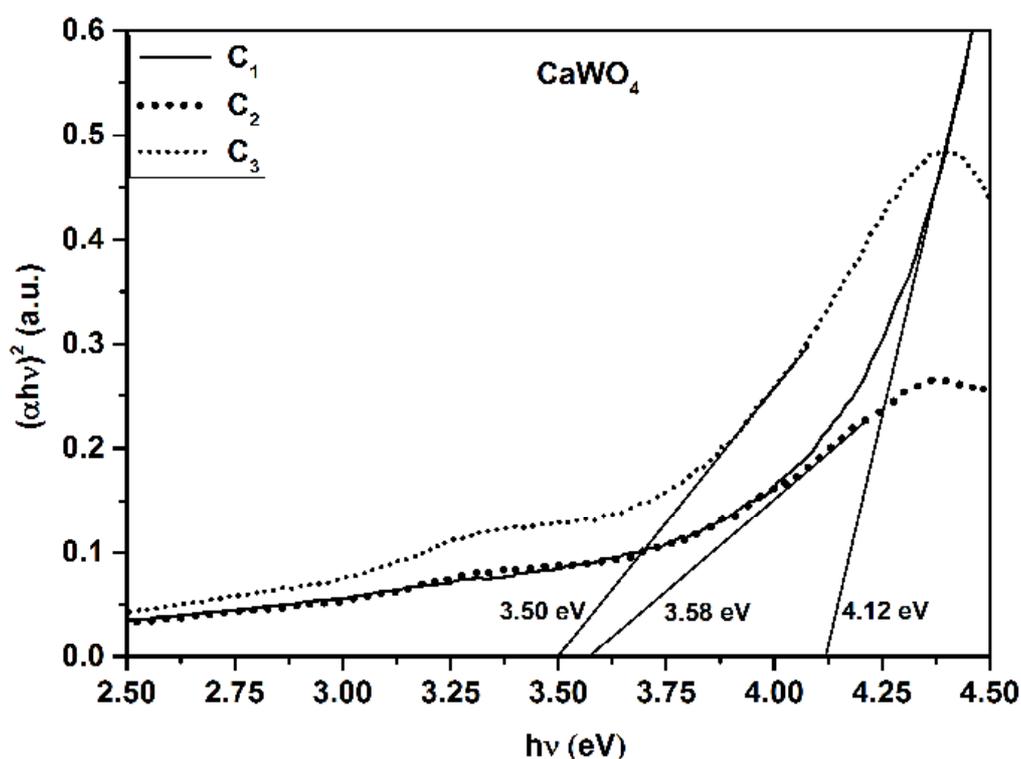
Fig. 4.13 Tauc plots of $CaWO_4$ samples C_1, C_2 and C_3

4.6.2 UV-Visible absorption study of irradiated CaWO$_4$ samples
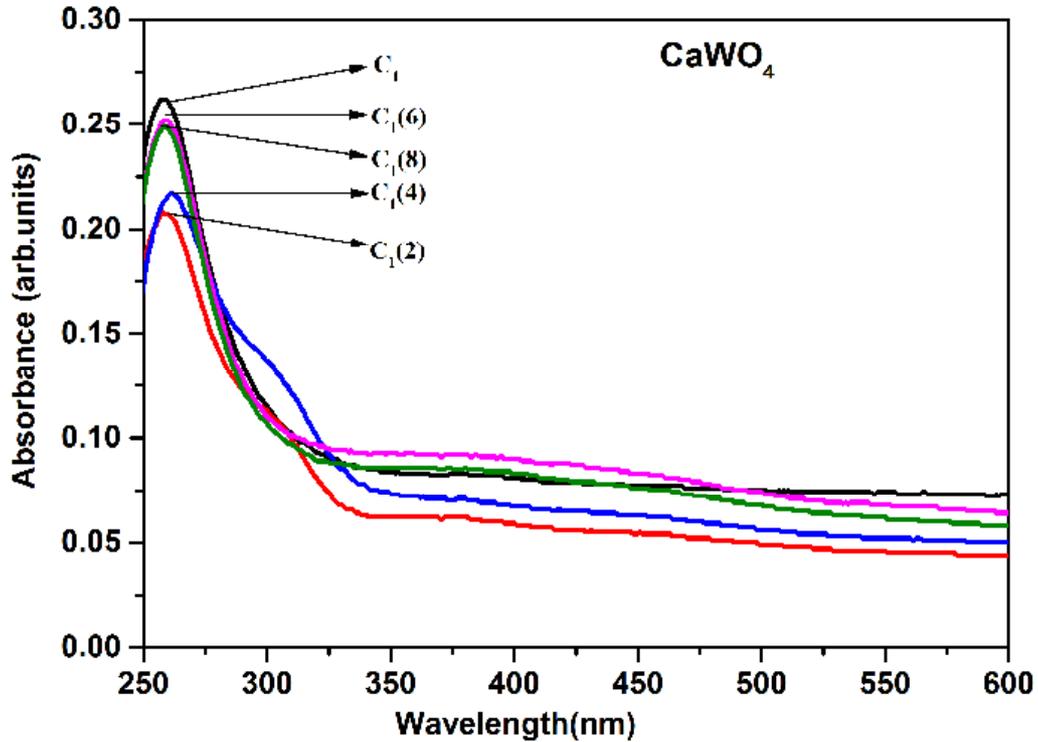
Fig. 4.14 UV-Visible absorption spectra of CaWO$_4$
samples **C$_1$, C$_1$(2), C$_1$(4), C$_1$(6) and C$_1$(8)**

The UV-Visible absorption spectra of samples **C$_1$, C$_1$(2), C$_1$(4), C$_1$(6),** and **C$_1$(8)** are shown in Fig. 4.14. The figure demonstrates slight variations in the absorption peak positions of the irradiated samples. The shift in peak position is due to particle size variation caused by electron beam irradiation. The intensity of absorption is found to be less in electron beam irradiated samples. The Fig. 4.14 also confirms shift in absorption edges due to electron beam irradiation. The observed shifts in the absorption edge could be attributed to the variation in particle size [36].

The optical bandgap values of the samples are measured from the Tauc plots. The bandgap values observed are 4.12, 4.20, 4.08, 4.22 and 4.25 eV, respectively for samples C_1, $C_1(2)$, $C_1(4)$, $C_1(6)$ and $C_1(8)$. The changes in bandgap values are due to the small changes in particle size upon electron beam irradiation [23]. The variation of crystallite size and bandgap with increasing electron dose is given in the Table. 4.6.

Table 4.6 The crystallite size and optical bandgap of
bare and electron irradiated $CaWO_4$ samples

Samples	Crystallite size (nm)	Bandgap (eV)
C_1	20.52	4.12
$C_1(2)$	23.62	4.20
$C_1(4)$	24.75	4.08
$C_1(6)$	23.66	4.22
$C_1(8)$	19.96	4.25

4.6.3   Photoluminescence studies

4.6.3.1 *PL studies of CaWO₄ samples*

The PL spectra of samples calcined at three different temperatures are shown in Fig. 4.15, when excited with 270 nm. A broad emission peak centred on 357.15 nm is observed in the case of sample C_1. This peak position is much different from the characteristic PL emission peak in the blue region (420 to 440 nm) reported in the literature [7, 21, 37, 38]. This varied behaviour can be attributed to the incomplete crystallization in the sample calcined at 350°C. But for samples C_2 and C_3, broad emission peaks

are centred on 422 and 424 nm, respectively. This red shift in emission peak is due to the increase in particle size caused by calcination [23]. The intensity of emission peaks decreases with increase in calcination temperature, which can be attributed to the decrease in the intrinsic disorders due to the improved crystallinity of the calcined $CaWO_4$ samples.
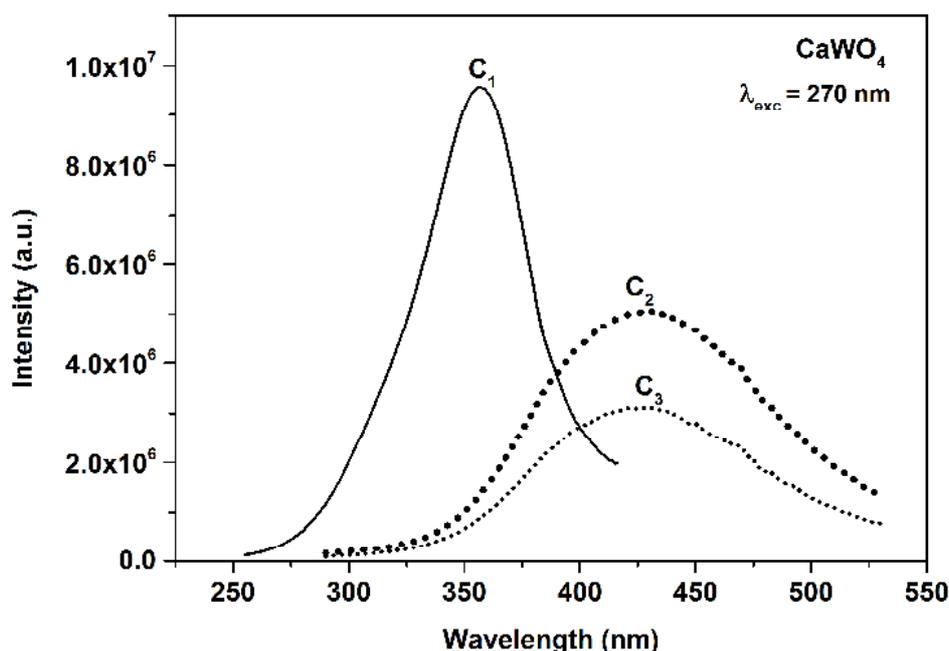
Fig. 4.15 PL spectra of $CaWO_4$ samples C_1, C_2 and C_3

In short, the light-emitting properties of the calcium tungstate crystal are greatly influenced by calcination temperature. PL emission can be tuned in the UV- Visible (350-430) region by calcination.

4.6.3.2 *PL studies of electron irradiated samples*

The PL spectra of bare sample C_1 and the irradiated samples $C_1(2)$, $C_1(4)$, $C_1(6)$ and $C_1(8)$ are shown in Fig. 4.16. In the bare sample **C1**, PL peak appears at 357.15 nm, which is in the ultraviolet region. But when the

sample is irradiated with an electron dose of 2 kGy, the peak position is found to be red shifted to the usual blue emission region (around 422 nm). This is because of irradiation induced non-thermal re-crystallization in $CaWO_4$ powder [39]. It is interesting to note that the PL peaks get blue shifted with further increase in the electron dose [Fig. 4.16]. The characteristic blue emission is quenched and PL emission peak gradually shifts back to the ultraviolet region. This new behaviour is due to the variation in intrinsic defects caused by electron beam irradiation [23, 40]. In brief, electron beam irradiation of suitable dose is useful in tuning the PL emission of $CaWO_4$ in the UV-Visible range with increased intensity.
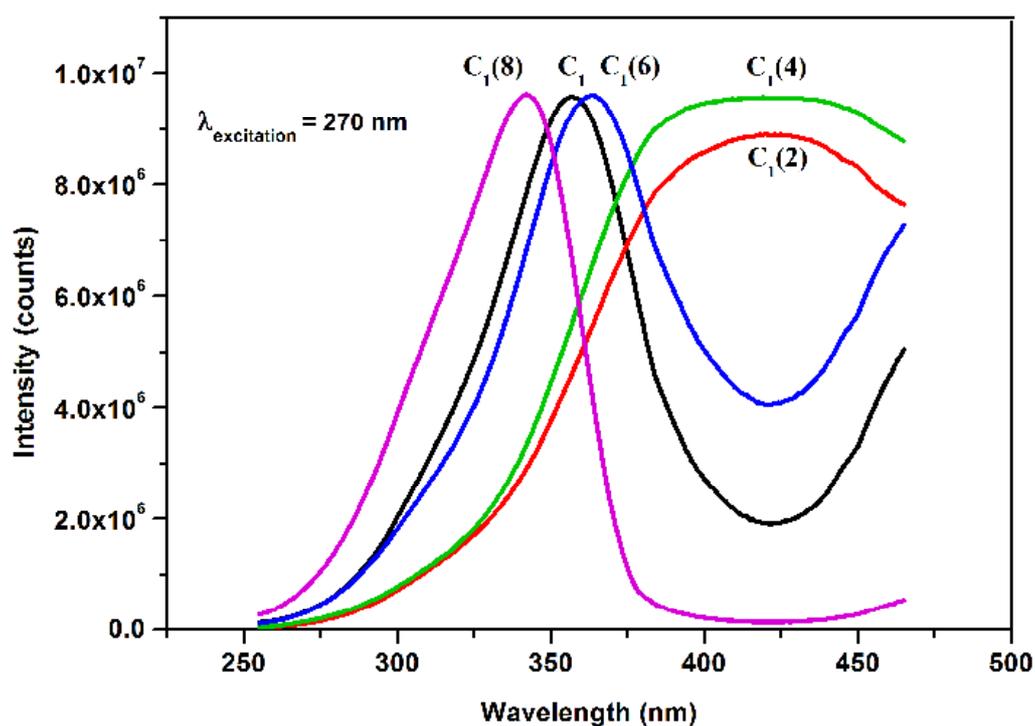
Fig. 4.16 PL spectra of $CaWO_4$ samples C_1, $C_1(2)$, $C_1(4)$, $C_1(6)$ and $C_1(8)$

4.7   Electrical properties

Electrical studies of nanocrystalline $CaWO_4$ are carried out, as described in section 2.5. The results and discussions on the experimental data are presented in this section.

4.7.1 DC electrical studies

4.7.1.1 *DC electrical studies of CaWO$_4$ samples*

Plot of DC conductivity versus temperature for samples C_1, C_2 and C_3 are shown in Fig. 4.17. At 303 K, the values of σ_{DC} are 5.30×10^{-9}, 4.30×10^{-9} and 3.87×10^{-9} mho-m^{-1}for C_1, C_2 and C_3, respectively. At 463 K, the values of σ_{DC} are 8.07×10^{-6}, 6.59×10^{-6} and 5.36×10^{-6} mho-m^{-1}, respectively. An exponential increase in σ_{DC} with increase in temperature is observed. Thus, the DC conductivity is thermally activated. At a given temperature, σ_{DC} is lower for the sample calcined at higher temperature.
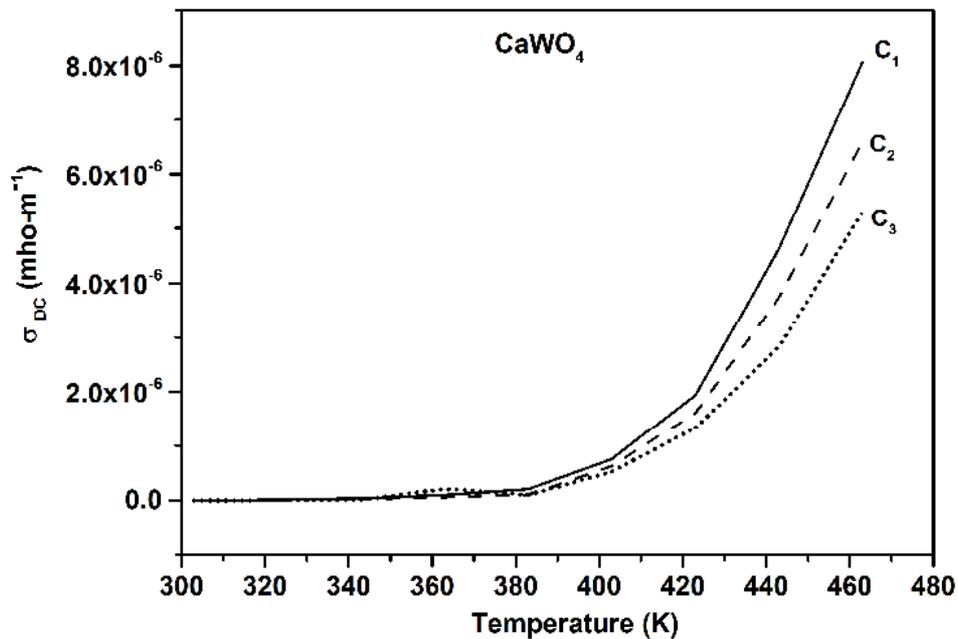
Fig. 4.17 DC conductivity of $CaWO_4$ samples C_1, C_2 and C_3

The reletionship between σ_{DC} and temperture is given by the Arrhenius relationship (eqn. 3.5). The Arrhenius plots for the calcined samples are shown in Fig. 4.18. The activation energies for **C₁**, **C₂** and **C₃** are determined from the slopes of the linear fit to the Arrhenius plots (Fig. 4.19). The activation energy values obtained are 0.5667 and 0.5680 and 0.5717eV for **C₁**, **C₂** and **C₃**, respectively. The low values of activation energy show that DC conduction in $CaWO_4$ is by hopping of charges.
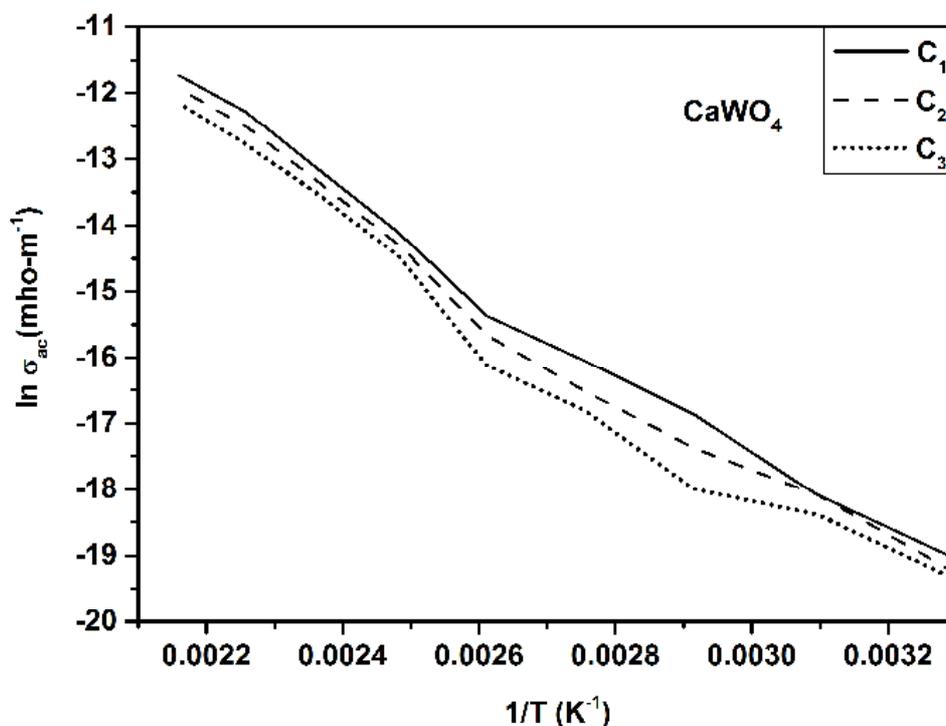
Fig. 4.18 Arrhenius plots of DC conductivity of $CaWO_4$ samples **C₁**, **C₂** and **C₃** as a function of temperature
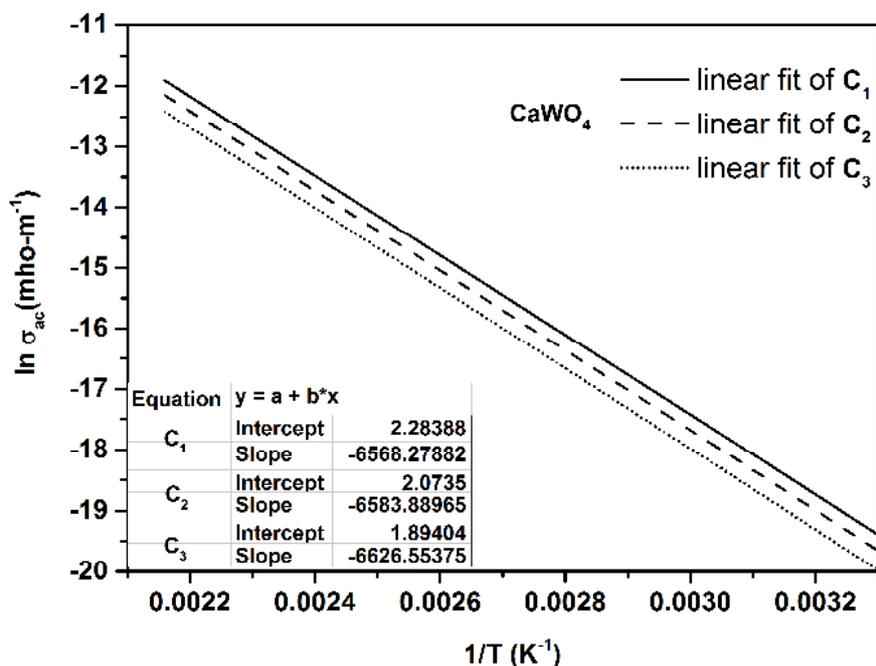
Fig. 4.19 The linear fits of Arrhenius plots of CaWO$_4$

samples **C$_1$, C$_2$** and **C$_3$**

4.7.1.2 *DC electrical studies of irradiated CaWO$_4$ sample*

The variation in DC conductivity with temperature of bare (**C$_1$**) and irradiated (**C$_1$(04)**) samples is plotted in Fig. 4.20. The values of DC conductivity at 303 K are 5.30×10^{-9} and 1.54×10^{-8} mho-m^{-1} for samples **C$_1$** and **C$_1$(04)**, respectively. At 463 K the corresponding values are 8.07×10^{-6} and 8.22×10^{-5} mho-m^{-1}, respectively.

It is found that the conductivity increases with increase in temperature. As descrbed in section 4.7.1.1 the activation energy values are determined from the Arrhenius relationshp between σ_{DC} and temperature. The values obtained are 0.5644 and 0.7281eV for **C$_1$** and **C$_1$(04)**, respectively. These values confirm that DC conduction in CaWO$_4$ is by hopping of charges. The conductivity of **C$_1$(4)** is large compared to **C$_1$** and

the dispersion is more at higher temperature. From XRD analysis, it is found that the crystallite size is highest for sample $C_1(4)$ which tend to decrease the contribution to DC conduction by hopping process. But, the conductivity shifts upwards for the irradiated sample $C_1(4)$. The reason for this observation is that new charge centres will be created during electron beam irradiation that results in an increase in the number of hopping as temperature increases [41].
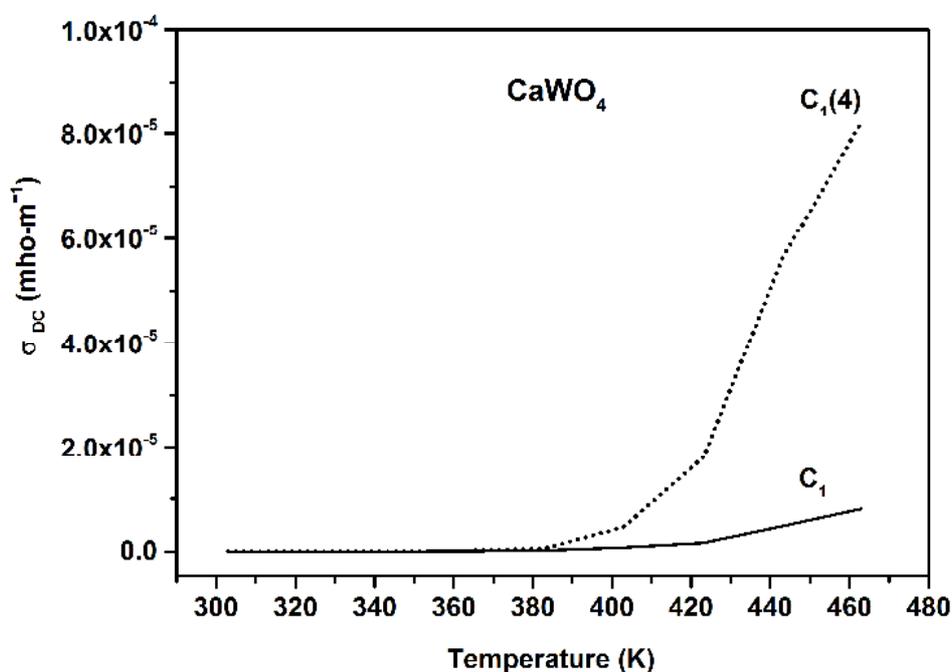
Fig. 4.20 DC conductivity of CaWO$_4$ samples C_1 and $C_1(4)$

4.7.2 AC electrical studies of CaWO$_4$ samples

The AC studies are carried out using circular pellets by measuring their capacitance and loss tangents. The measurements are taken using an impedance analyzer (Wayne Kerr 6500 B), described in chapter 2. Data are collected by varying frequency and temperature.

4.7.2.1 *Dielectric studies*

Dielectric constant

Fig. 4.21 shows the variation of dielectric constant (ε') with frequency at 303 K for samples C_1, C_2 and C_3. At 303 K, the values of ε' are 118.06, 30.08 and 10.66 at 100 Hz for the samples C_1, C_2 and C_3 respectively, which decreases to 5.35, 6.06 and 6.29 at 10 MHz.
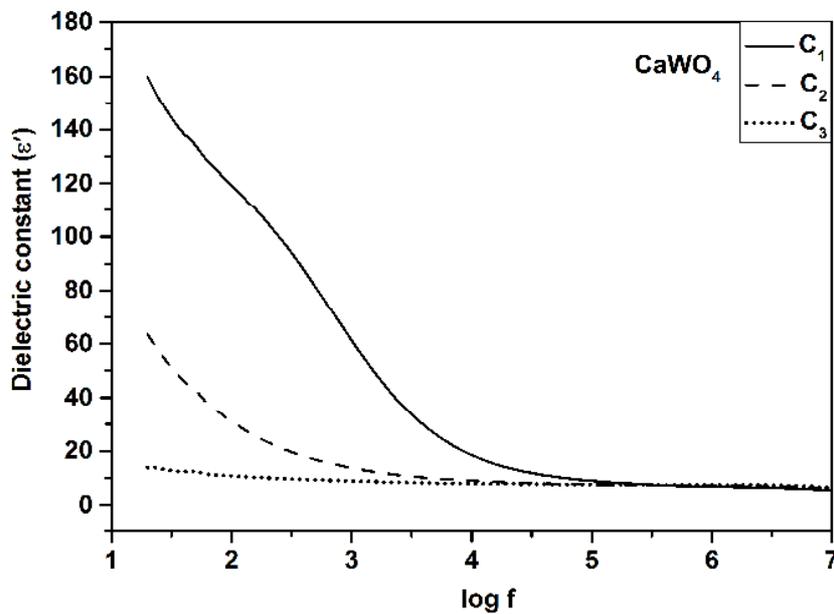
Fig. 4.21 Variation of dielectric constant with frequency of CaWO$_4$
samples C_1, C_2 and C_3 at temperature 303 K

It is seen that the dielectric constant for all the samples are high at low frequencies which decreases rapidly as frequency increases, attaining a constant value at higher frequencies. When the frequency is low, different polarizations get enough time to orient in accordance with the changing field. But, at higher frequencies their response is very low. The Fig.4.21 shows that dielectric constant decreases with increase in calcination temperature. The reason is that grain size increases with calcination

temperature. As the grain size increases, the increase in volume of the particle causes a decrease in the volume of the interfaces. This leads to decrease in space charge polarization. But, the contribution to ε' by electronic polarization from within the particles increases [41, 42]. The overall effect is a decrease in ε' with increase in grain size.

Fig. 4.22 shows variation of ε' for sample **C$_3$** at temperatures 303, 363, and 423 K. At 1 kHz the values of ε' are 8.68, 8.89 and 9.41 corresponding to 303, 363, and 423 K, respectively. When the temperature is increased, more and more dipoles are oriented, resulting in an increase in dielectric constant at any frequency [43]. At very high frequencies (MHz), the charge carriers would have started to move before the field reversal occurs and ε' falls to a small value.
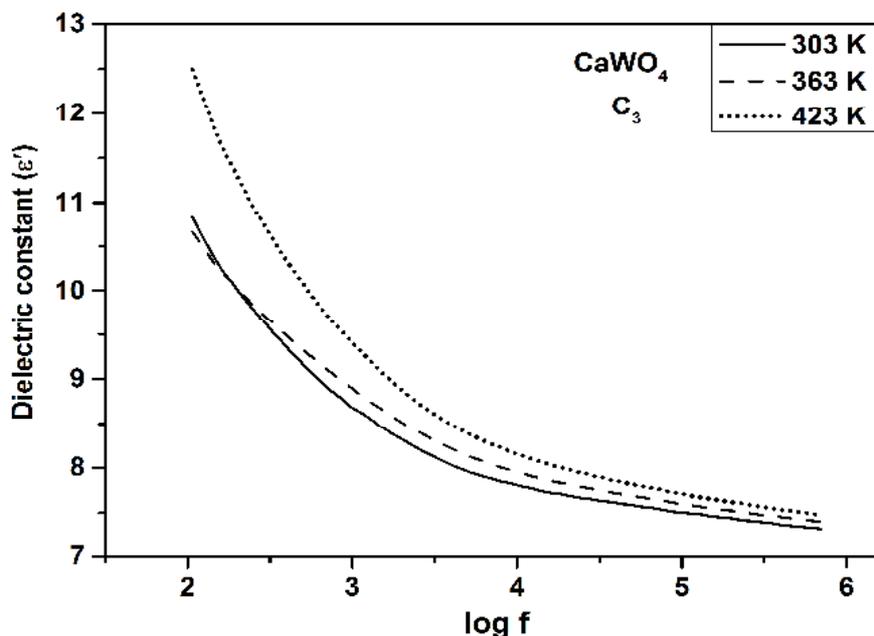
Fig. 4.22 Variation of dielectric constant with frequency of CaWO$_4$ sample **C$_3$** at different temperatures

Loss Tangent

The frequency dependence of loss tangent (Tan δ) of samples C_1, C_2 and C_3 at 303 K is shown in Fig. 4.23. At 100 Hz, the dissipation factor Tan δ has a value of 2.54, 3.41 and 0.92. But at 0.5 MHz, Tan δ decreases to 0.18, 0.04 and 0.03 for C_1, C_2 and C_3, respectively.
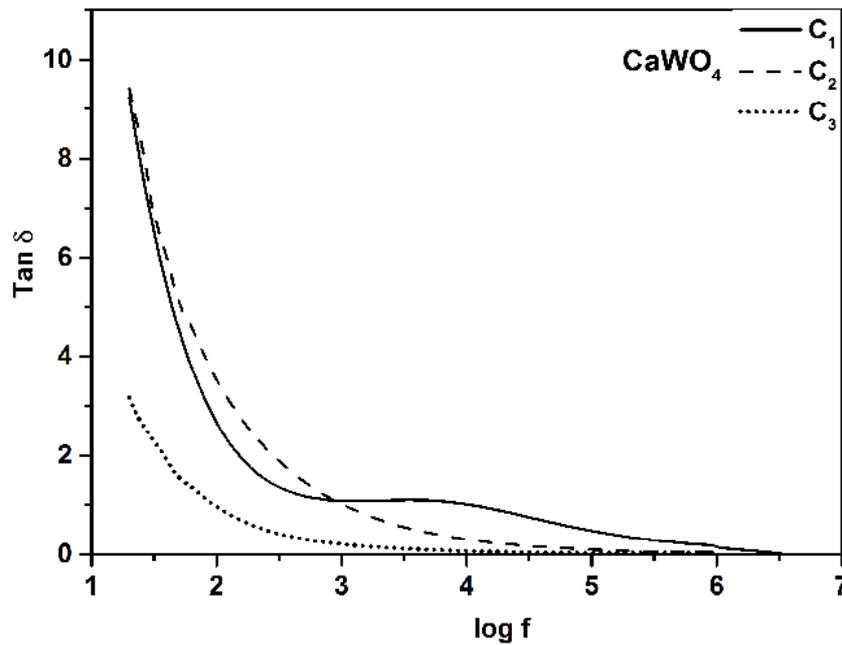
Fig. 4.23 Frequency dependence of dielectric loss of $CaWO_4$ samples C_1, C_2 and C_3

The decrease in Tan δ takes place when the dielectric response of polarizations to the frequency decreases. The inhomogeneities present in the interface layers of $CaWO_4$ nanocrystals produce an absorption current resulting in dielectric loss [41]. This absorption current decreases with increase in frequency of the applied field.

Fig. 4.24 represents the variation of Tan δ with frequency of sample C_3 at 303, 393 and 423 K. For the sample C_3 at 1 kHz, the values of Tan δ

are 0.15, 0.25 and 0.24 for temperature 303, 363 and 423 K, respectively. The corresponding values at 0.5 MHz are 0.030, 0.025 and 0.027 respectively.
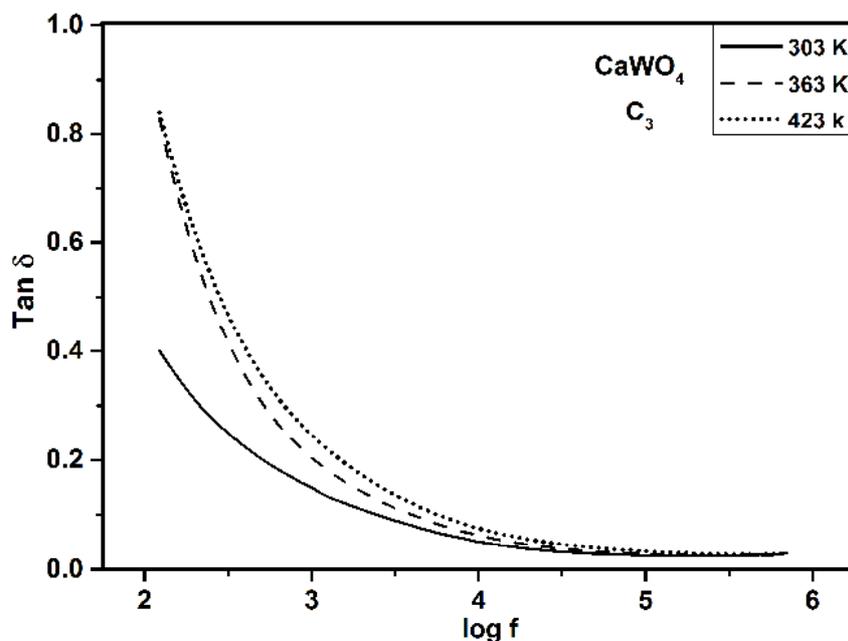
Fig. 24 Frequency dependence of dielectric loss of $CaWO_4$

sample **C_3** at three different temperatures

The hopping probability per unit time increases with increase in temperature. Correspondingly, the loss tangent elevated with temperature at a specific frequency. The loss in $CaWO_4$ can be explained using the electronic hopping model, which considers the frequency dependence of the localised charge carriers hopping in a random array [42]. This model is applicable for materials in which the polarisation responds rapidly to the appearance of an electron on any one site so that the transition may be said to occur effectively into the final state [44]. In the high frequency region, tan δ becomes almost zero because the electron exchange interaction

(hopping) cannot follow the alternatives of the applied AC electric field beyond a critical frequency.

4.7.2.2   *AC conductivity studies*

Fig. 4.25 shows the variation of AC conductivity (σ_E) of samples C_1, C_2 and C_3 with frequency. At 3 kHz for C_1, C_2 and C_3, the measured AC conductivity values are 1.94 X 10^{-6}, 7.2 x 10^{-7} and 1.05 X 10^{-7}mho-m^{-1} respectively at 303 K. At 1 MHz, the corresponding values are 2.93 X 10-5, 1.46 X 10^{-5} and 1.10 X 10^{-5} mho-m^{-1}.
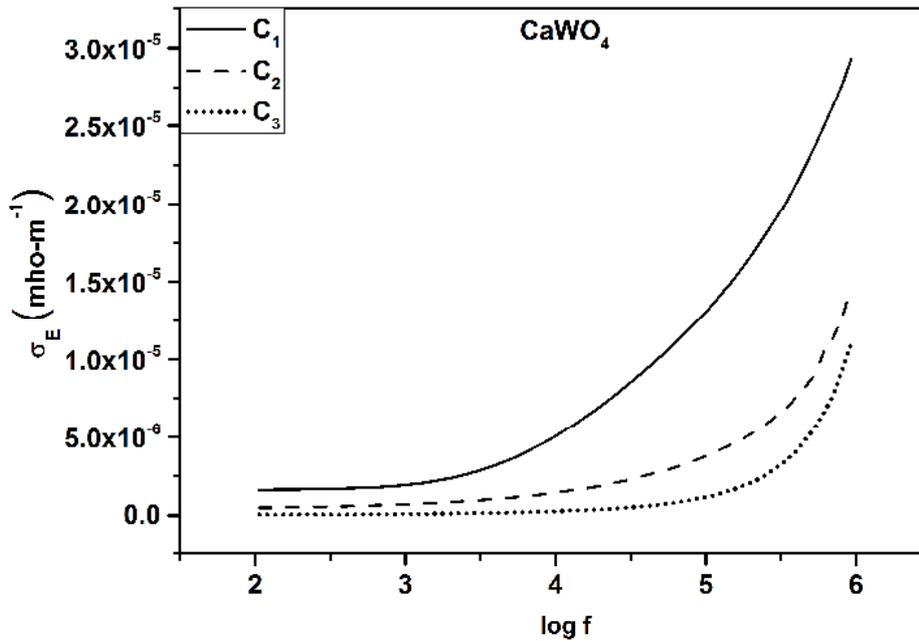
Fig. 4.25 Variation of AC conductivity (σ_E) of CaWO$_4$
samples C_1, C_2 and C_3 with frequency

The nature of variation is almost similar for all the samples, but the conductivity values shift downwards as the grain size increases. Initially, the AC conductivity has a small steady value which increases at higher

frequencies. At lower frequencies up to about 1 kHz, the variation in the AC conductivity has no frequency dependence. Beyond this frequency, AC shows frequency dependence in accordance with the universal power law (eqn. 3.7).

Fig. 4.26 shows the nature of variation of conductivity of sample C_3 at 303, 393 and 423 K. At 3 kHz, the AC conductivity measured for sample C_3 is 7.20×10^{-8}, 1.01×10^{-7} and 1.28×10^{-7} mho-m^{-1} at 303, 363 and 423 K, respectively. At 0.5 MHz, the respective values of AC conductivity are 3.58×10^{-6}, 3.56×10^{-6} and 4.03×10^{-6} mho-m^{-1}. Here also, the universal power law (equation 3.7) can be applied to explain the observed variations in conductivity with frequency and temperature.
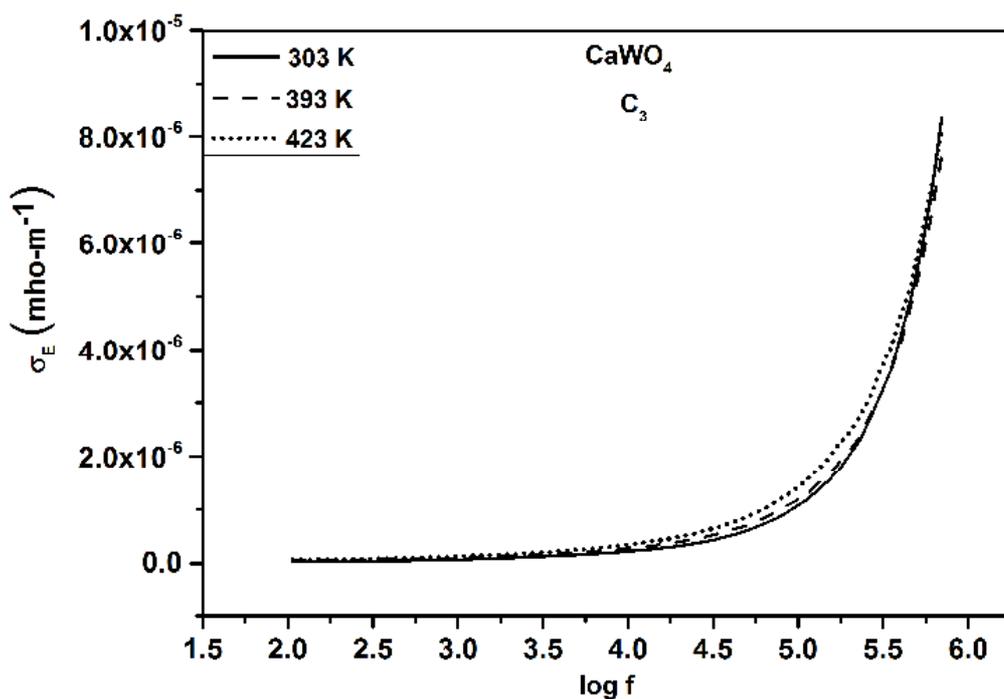
Fig. 4.26 Variation of the AC conductivity of CaWO$_4$ sample C_3
with frequency at different temperatures

Plots of log ω versus log [σ_{ac}] for sample **C$_3$** are given in Fig. 4.27. The frequency exponents are determined from the slopes of linear fit of log ω versus log [σ_{ac}], given in Fig. 4.28. The values obtained for the exponent (*n*) in the power law are 0.95, 0.97 and 0.97 at temperatures 303, 393 and 423 K, respectively.
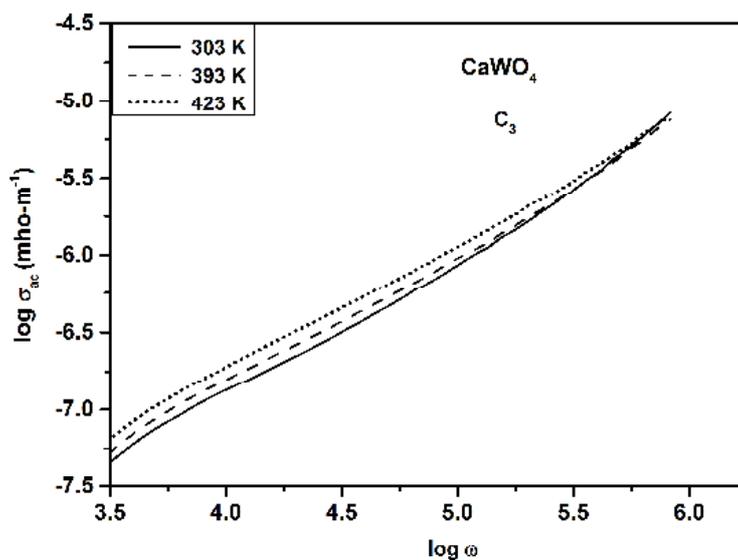
Fig. 4.27 log ω versus log [σ_{ac}] plots of CaWO$_4$ sample **C$_3$**
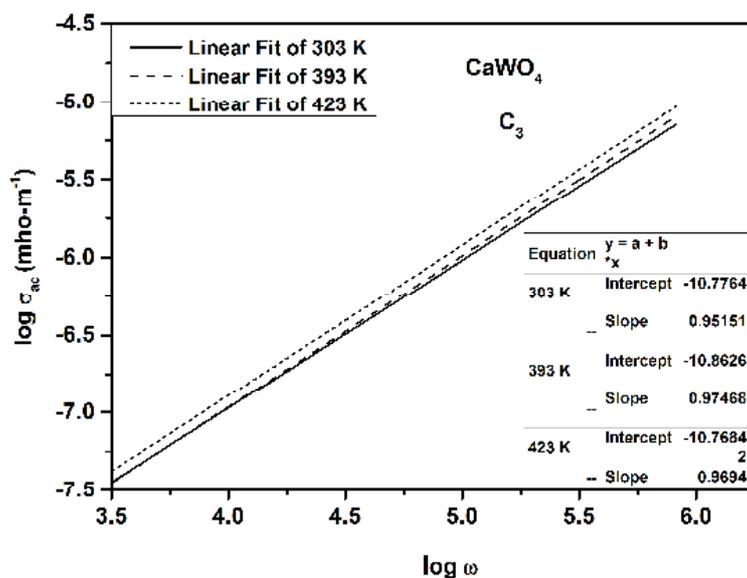
Fig. 4.28 Linear fits of log ω versus log [σ_{ac}] plots of CaWO$_4$ sample **C$_3$**

(Inset table presents the results of linear fit)

It is clear from the figure that the conductivity increases as frequency increases, which confirms to small polaron hopping [41].

4.7.3   AC electrical studies of electron beam irradiated $CaWO_4$ sample

Effect of electron beam irradiation on the AC electrical properties of $CaWO_4$ sample is presented in this section.

4.7.3.1 Dielectric *studies*

Dielectric constant

The dielectric constant of electron beam irradiated sample $C_1(4)$ is much higher at lower frequencies compared to the bare sample C_1 as is evident from the Fig. 4.29. At 100 Hz the value of dielectric constant are 120.85 and 863.61 for the bare and electron irradiated samples, respectively. The corresponding values at 6 MHz are 6.76 and 11.21.
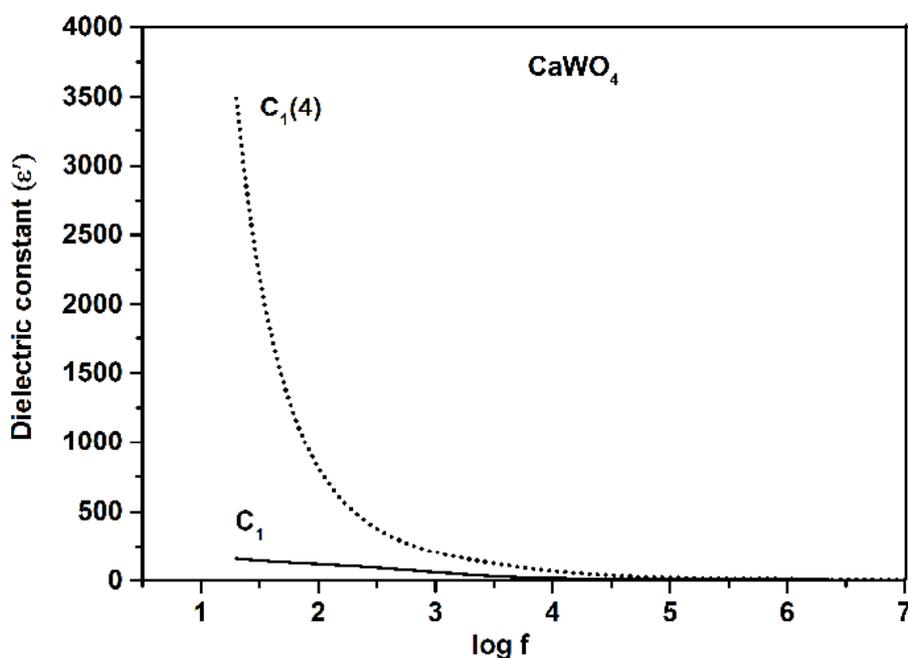
Fig. 4.29 Variation of dielectric constant of $CaWO_4$ samples C_1 and $C_1(4)$ as a function of frequency

Loss tangent

The variation in the loss tangent of samples C_1 and $C_1(4)$ with frequency at 303 K is depicted in Fig. 4.30. The value of **tan δ** for samples C_1 and $C_1(4)$ at 100 Hz are 2.54 and 29.80, respectively. These values are changed to 0.18 and 0.74 at 1 MHz. Thus, the loss tangent is also higher for the electron irradiated sample.
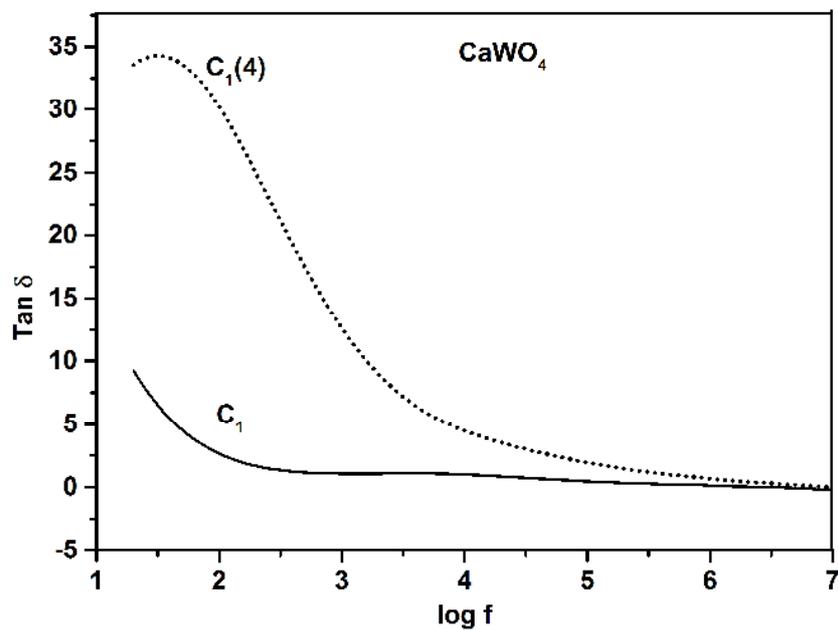
Fig. 4.30 Variation of loss tangent with AC frequency of CaWO₄ samples C_1 and $C_1(4)$

The increased dielectric constant and loss tangent in the irradiated sample can be attributed to the increase in defects leading to greater polarization.

4.7.3.2 AC *electrical studies*

Fig. 4.31 presents the variation of AC conductivity (σ_E) of samples C_1 and $C_1(4)$ as a function of frequency at 303 K. The values of σ_E at 3 kHz

for samples C_1 and $C_1(4)$ are 3.69×10^{-6} and 1.45×10^{-4} mho-m^{-1}, respectively. The corresponding values of σ_E at 1 MHz are 5.03×10^{-5} and 4.30×10^{-4} mho-m^{-1}, respectively. Thus, AC conductivity is large for electron beam irradiated sample.
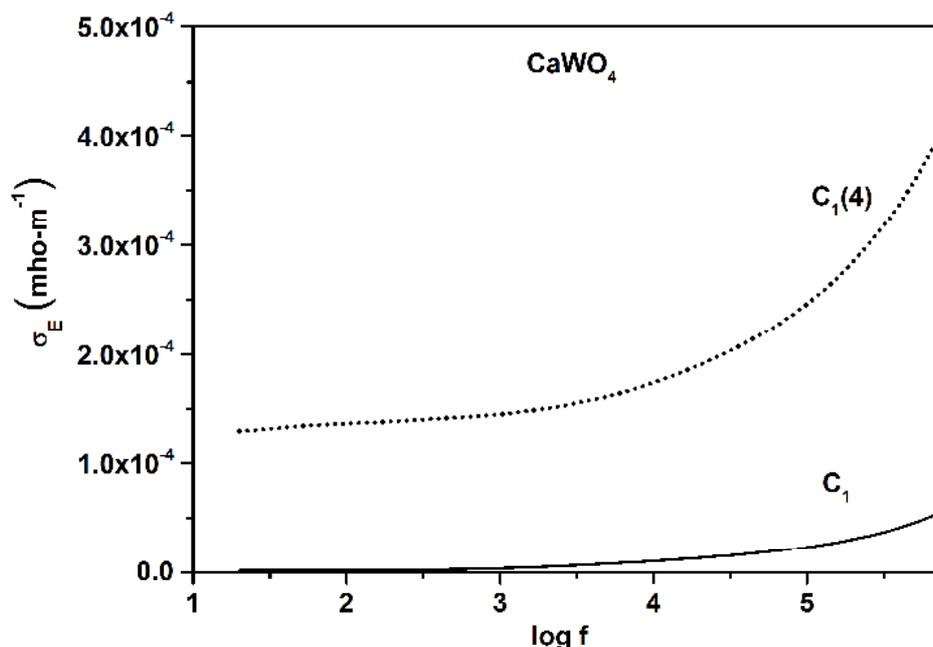
Fig. 4.31 Variation in AC conductivity of CaWO$_4$ samples
C_1 and $C_1(4)$ as a function of frequency

As discussed in chapter 3, the variation of AC conductivity with frequency can be explained using the universal power law [59]. The frequency independent part of the curve is found to be shifted upwards. The values given by $\sigma_{ac}(\omega) = \sigma_E(T) - \sigma_{dc}(T)$ for samples C_1 and $C_1(4)$ at 1 kHz are respectively 1.89×10^{-6} and 1.38×10^{-4} mho-m^{-1}. The respective values at 1 MHz are 6.25×10^{-5} and 4.31×10^{-4} mho-m^{-1}. This variation in AC conductivity with frequency is given by $\sigma_{ac} = A\omega^n$, where A is a temperature dependent constant and n is the frequency exponent. The

values of frequency exponent determined from the slope of log ω versus log [σ_{ac}] plot shown in Fig. 4.32 are 0.56 and 0.52, respectively for **C$_1$** and **C$_1$(4)** samples. According to theory, the value of *n* is between 0 and 1. The values obtained in this study indicate hopping conduction in CaWO$_4$ [41].
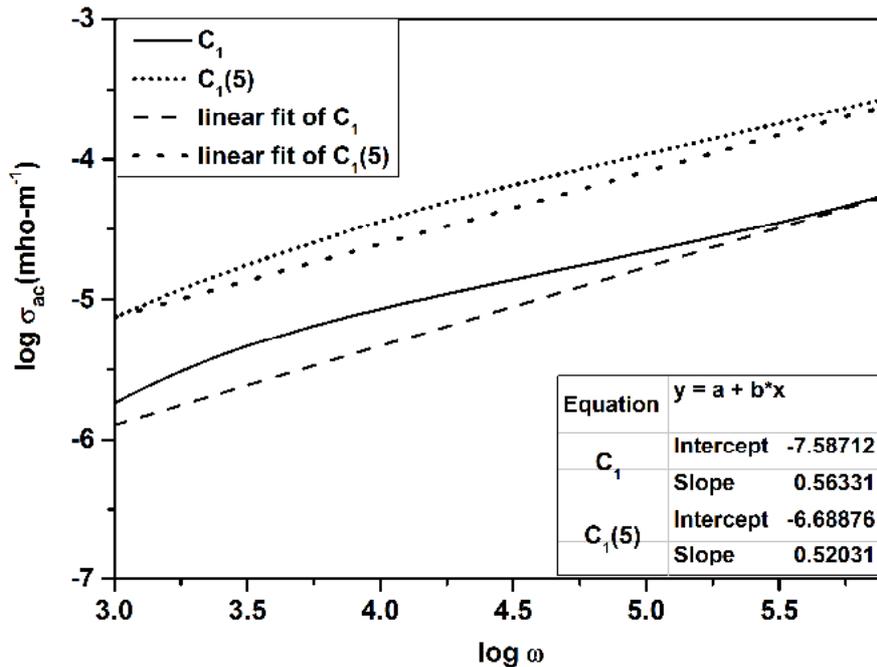
Fig. 4.32 log ω versus log [σ_{ac}] plots of CaWO$_4$

It is reported in the literature that the contribution to AC conductivity by the grain boundaries is higher than that due to the grains and is attributed to the trapping of electrons in the grain boundaries [45, 46]. Due to electron beam irradiation a number of trap states are created which enhance the hopping conduction.

4.8   Conclusion

The following conclusions are drawn from the systematic studies of structural, optical and electric characterization of nanocrystalline CaWO$_4$.

➢ Thermal analysis confirms that $CaWO_4$ synthesized by simple chemical precipitation method is thermally stable.

➢ XRD studies of $CaWO_4$ samples confirm tetragonal scheelite structure with a space group $I4_1/a$ in a C_{4h}^6 symmetry for $CaWO_4$. The average crystallite size is found to increase from 18.50 to 39.67 nm with increase in calcination temperature from 350 to 650 °C. XRD calculations show a lattice expansion in this structure on increasing the calcination temperature. The crystallite size of $CaWO_4$ is found to vary with electron irradiation dose due to the variations in defects and crystallization.

➢ The FTIR and Raman spectroscopic studies confirm the formation of $CaWO_4$. The Raman bands are modified slightly during electron irradiation process. In the samples irradiated with 2 and 4 kGy, a new Raman band is observed at 1053 cm^{-1}.

➢ SEM images show dumb-bell shaped $CaWO_4$ nanoclusters formed by growth in certain directions. The morphology gets changed as the calcination temperature increases due to aggregation of more and more particles to the cluster. The EDS analysis confirms the presence of all the elements in $CaWO_4$. The aggregation of nanoparticles produced thick contrast in the TEM image. Average size of the particles is ∼82 nm.

➢ UV-Visible absorption spectroscopic studies of $CaWO_4$ samples show red shift in the absorption edge as well as reduction in the bandgap due to calcination. A bandgap of 4.12 eV is obtained for $CaWO_4$

nanoparticles calcined at 350 °C. The electron beam irradiation creates modifications in optical absorption and bandgap with electron dose.

➢ The PL emission peak shifts from UV to visible range (350-430 nm) as the calcination temperature rises from 350 to 650°C. The PL intensity is found to decrease as the particle size increases due to calcination. It is found that electron beam irradiation creates drastic changes in the PL property of the material. Besides, the electron beam irradiation of suitable dose can be useful in tuning the PL emission of $CaWO_4$ in the UV-visible range with enhanced intensity. An advantage of electron irradiation over calcination treatment is that it can be used for tuning the PL emission without much variation in the particle size.

➢ DC electrical studies show an exponential increase in conductivity with temperature. The low values of activation energy (~0.57 eV) confirm the DC conduction by hopping process. The DC conductivity decreases with increase in calcination temperature.

➢ Dielectric studies revealed the usual relaxation processes relating to the different types of polarizations. The dielectric constant for all the samples are high at low frequencies, which decreases rapidly as frequency, increases, attaining a constant low value at higher frequencies. The samples calcined at higher temperatures show lower values of dielectric constant and loss tangent. The AC conductivity shows power law dependence.

> ➢ The DC conductivity of the electron irradiated sample is higher due to the creation of new charge centres. In the irradiated $CaWO_4$ sample, the dielectric constant and loss tangent are higher at lower frequencies. But at higher frequencies, the loss tangent is very small. It is found that electron beam irradiation enhances the AC conductivity of nanocrystalline $CaWO_4$.

References

1   Kröger, *Some Aspects of the Luminescence of Solids*. (Elsevier, Amsterdam, 1948).

2   V. Nagirnyi, E. Feldbach, L. Jönsson, M. Kirm, A. Lushchik, C. Lushchik, L. L. Nagornaya, V. D. Ryzhikov, F. Savikhin, G. Svensson, and I. A. Tupitsina, Radiation Measurements **29** (3–4), 247 (1998).

3   S. Oishi and M. Hirao, Journal of Materials Science Letters **8** (12), 1397 (1989).

4   M. J. Treadaway, The Journal of Chemical Physics **61** (10), 4003 (1974).

5   L. S. Cavalcante, V. M. Longo, J. C. Sczancoski, M. A. P. Almeida, A. A. Batista, J. A. Varela, M. O. Orlandi, E. Longo, and M. S. Li, CrystEngComm **14** (3), 853 (2012).

6   D. Errandonea, M. Somayazulu, and D. Häusermann, physica status solidi (b) **231** (1), R1 (2002).

7   S. Liu, S. Tian, and R. Xing, CrystEngComm **13** (24), 7258 (2011).

8   Y. Su, G. Li, Y. Xue, and L. Li, The Journal of Physical Chemistry C **111** (18), 6684 (2007).

9   W.-S. Wang, L. Zhen, C.-Y. Xu, L. Yang, and W.-Z. Shao, The Journal of Physical Chemistry C **112** (49), 19390 (2008).

10   J. Yu, K. Huang, L. Yuan, and S. Feng, New Journal of Chemistry **38** (4), 1441 (2014).

11   S.-J. Chen, J. Li, X.-T. Chen, J.-M. Hong, Z. Xue, and X.-Z. You, Journal of Crystal Growth **253** (1-4), 361 (2003).

12   M. A. M. A. Maurera, A. G. Souza, L. E. B. Soledade, F. M. Pontes, E. Longo, E. R. Leite, and J. A. Varela, Materials Letters **58** (5), 727 (2004).

13   W. Hu, W. Tong, L. Li, J. Zheng, and G. Li, Physical chemistry chemical physics : PCCP **13** (24), 11634 (2011).

14   J. Liu, Q. Wu, and Y. Ding, Journal of Crystal Growth **279** (3-4), 410 (2005).

15   G. L. Katelnikovas A, Millers D, Pankratov V, and Kareiva A, Lithuanian Journal of Physics **47** (1), 63 (2007).

16   P. Y. Jia, X. M. Liu, G. Z. Li, M. Yu, J. Fang, and J. Lin, Nanotechnology **17** (3), 734 (2006).

17   Q. Zhang, W.-T. Yao, X. Chen, L. Zhu, Y. Fu, G. Zhang, L. Sheng, and S.-H. Yu, Crystal Growth & Design **7** (8), 1423 (2007).

18   X. Lai, Y. Wei, D. Qin, Y. Zhao, Y. Wu, D. Gao, J. Bi, D. Lin, and G. Xu, Integrated Ferroelectrics **142** (1), 7 (2013).

19   B. A. Hernandez-Sanchez, T. J. Boyle, H. D. Pratt, M. A. Rodriguez, L. N. Brewer, and D. R. Dunphy, Chemistry of materials : a publication of the American Chemical Society **20** (21), 6643 (2008).

20   M. Mai and C. Feldmann, Journal of Materials Science **47** (3), 1427 (2011).

21   Q. Li, Y. Shen, and T. Li, Journal of Chemistry **2013**, 5 (2013).

22   T. G. Cooper and N. H. de Leeuw, Surface Science **531** (2), 159 (2003).

23   N. Aloysius Sabu, K. P. Priyanka, S. Ganesh, and T. Varghese, Radiation Physics and Chemistry **123**, 1 (2016).

24   A. R. West, *Solid State Chemistry and Its Applications*. (Wiley, 1987).

25   S. Kumar, K. Asokan, R. K. Singh, S. Chatterjee, D. Kanjilal, and A. K. Ghosh, Journal of Applied Physics **114** (16), 164321 (2013).

26   H. Wang and S. Lu, Physicochemical Problems of Mineral Processing **50** (**1**), 79 (2014).

27   T. T. Basiev, A. A. Sobol, Y. K. Voronko, and P. G. Zverev, Optical Materials **15** (3), 205 (2000).

28   T. Thongtem, S. Kaowphong, and S. Thongtem, Applied Surface Science **254** (23), 7765 (2008).

29   P. Tarte and M. Liegeois-Duyckaerts, Spectrochimica Acta Part A: Molecular Spectroscopy **28** (11), 2029 (1972).

30   L. Gracia, V. r. M. Longo, L. c. S. Cavalcante, A. Beltrán, W. Avansi, M. x. S. Li, V. R. Mastelaro, J. A. Varela, E. Longo, and J. Andrés, Journal of Applied Physics **110** (4), 043501 (2011).

31   N. Aloysius Sabu, X. Francis, J. Anjaly, S. Sankararaman, and T. Varghese, The European Physical Journal Plus **132** (6), 290 (2017).

32   R. Brunetto, G. A. Baratta, and G. Strazzulla, Journal of Applied Physics **96** (1), 380 (2004).

33   Y. Xu, L. Shi, X. Zhang, K. Wong, and Q. Li, Micron **42** (3), 290 (2011).

34   V. M. Longo, L. Gracia, D. G. Stroppa, L. S. Cavalcante, M. Orlandi, A. J. Ramirez, E. R. Leite, J. Andrés, A. Beltrán, J. A. Varela, and E. Longo, The Journal of Physical Chemistry C **115** (41), 20113 (2011).

35   R. Lacomba-Perales, J. Ruiz-Fuertes, D. Errandonea, D. Martínez-García, and A. Segura, EPL (Europhysics Letters) **83** (3), 37002 (2008).

36   K. A. Bogle, S. D. Dhole, and V. N. Bhoraskar, Radiation Effects and Defects in Solids **159** (3), 157 (2004).

37   L. Sun, M. Cao, Y. Wang, G. Sun, and C. Hu, Journal of Crystal Growth **289** (1), 231 (2006).

38   L. Li, Y. Su, and G. Li, Applied Physics Letters **90** (5), 054105 (2007).

39   A. Meldrum, L. A. Boatner, and R. C. Ewing, Journal of Materials Research **12** (7), 1816 (1997).

40   I. A. Buyanova, M. Wagner, W. M. Chen, B. Monemar, J. L. Lindström, H. Amano, and I. Akasaki, Applied Physics Letters **73** (20), 2968 (1998).

41   N. Aloysius Sabu, M. S. Rintu, E. M. Muhammed, and T. Varghese, Nanosystems: Physics, Chemistry, Mathematics, 599 (2016).

42   N. Aloysius Sabu, K. Priyanka, S. Thankachan, A. T. Sunny, E. Mohammed, O. Jaseentha, and T. Varghese, Nanosystems: Physics, Chemistry, Mathematics **4** (3), 357 (2013).

43   K. Priyanka, S. Joseph, M. E. Smitha Thankachan, and T. Varghese, Journal of Basic and Applied Physics Feb **2** (1), 105 (2013).

44   V. R. K. Murthy and J. Sobhanadri, physica status solidi (a) **36** (2), K133 (1976).

45   J. Jose and M. Abdul Khadar, Materials Science and Engineering: A **304–306**, 810 (2001).

46   C. Durand, X. Zhang, J. Fowlkes, S. Najmaei, J. Lou, and A.-P. Li, Journal of Vacuum Science & Technology B, Nanotechnology and Microelectronics: Materials, Processing, Measurement, and Phenomena **33** (2), 02B110 (2015).

****ೞ✪ೞ****

Chapter - 5

STUDIES ON STRUCTURAL, OPTICAL AND ELECTRICAL PROPERTIES OF POLYANILINE COMPOSITES

The synthesis and characterization of polyaniline composites of nanocrystalline $MnWO_4$ and $CaWO_4$ are presented in this chapter. The structural, optical and electrical property changes due to the formation of the PANI- metal tungstate composites are also discussed. The effect of high energy electron beam irradiation on the properties of PANI-$MnWO_4$/$CaWO_4$ nanocomposites is also studied.

5.1 Synthesis of polyaniline nanocomposite

5.1.1 Synthesis of PANI

Emeraldine salt (PANI-ES) is prepared by *in situ* oxidative polymerization of aniline monomer in an acidic medium in the presence of a suitable oxidant [1-4]. Aniline monomers after double distillation (9.3 ml) is added to 1 M HCl (200 ml) and stirred well. APS (11.4 gm) is dissolved in distilled water to make 50 ml of solution. It is then added drop by drop to the above mixture with constant stirring. The solution gradually turns into

dark green colour, indicating the formation of PANI. The mixture is stirred over a period of 4 h and left at room temperature overnight to complete the polymerization. The dark green precipitate is collected by filtration and washed several times with distilled water until the filtrate turned colourless. The product is dried in an oven at 50 °C for 48 h to get flakes of protonated PANI. The PANI is then ground into fine powder using an agate mortar.

5.1.2 Synthesis of PANI-MnWO$_4$ nanocomposite

Synthesis method described in section 5.1.1 is employed to synthesize PANI-MnWO$_4$ composite. For this 1.51 gm (0.50% mol) of MnWO$_4$ powder calcined at 450 ℃ is dispersed in 10 ml of ethanol by ultrasonication for 30 minutes. It is then added in portions during the oxidative polymerization of aniline discussed in section 5.1.1. The solution gradually turns into dark green colour, indicating the formation of PANI composite. The mixture is stirred over a period of 10 h and left at room temperature overnight to complete the polymerization. The dark green precipitate is collected by filtration and washed several times. The product is then dried to get flakes of PANI-MnWO$_4$ composite.

5.1.3 Synthesis of PANI-CaWO$_4$ nanocomposite

The PANI-CaWO$_4$ nanocomposite is also synthesized using the same method discussed in section 5.1.2. In this case, 1.44 gm (0.50 % mol) of CaWO$_4$ calcined at 650 ℃ dispersed in 10 ml of ethanol is used to form the nanocomposite.

5.2 Characterization of PANI-MnWO$_4$ nanocomposite

5.2.1 Thermal analysis

The TGA/DTA curves of PANI-MnWO$_4$ composite are shown in Fig. 5.1. The sample is heated from room temperature to 720 ℃ at 10 ℃/min. TGA/DTG curve exhibits three prominent weight losses centred on temperatures 82.16, 286.16 and 541.35 ℃.
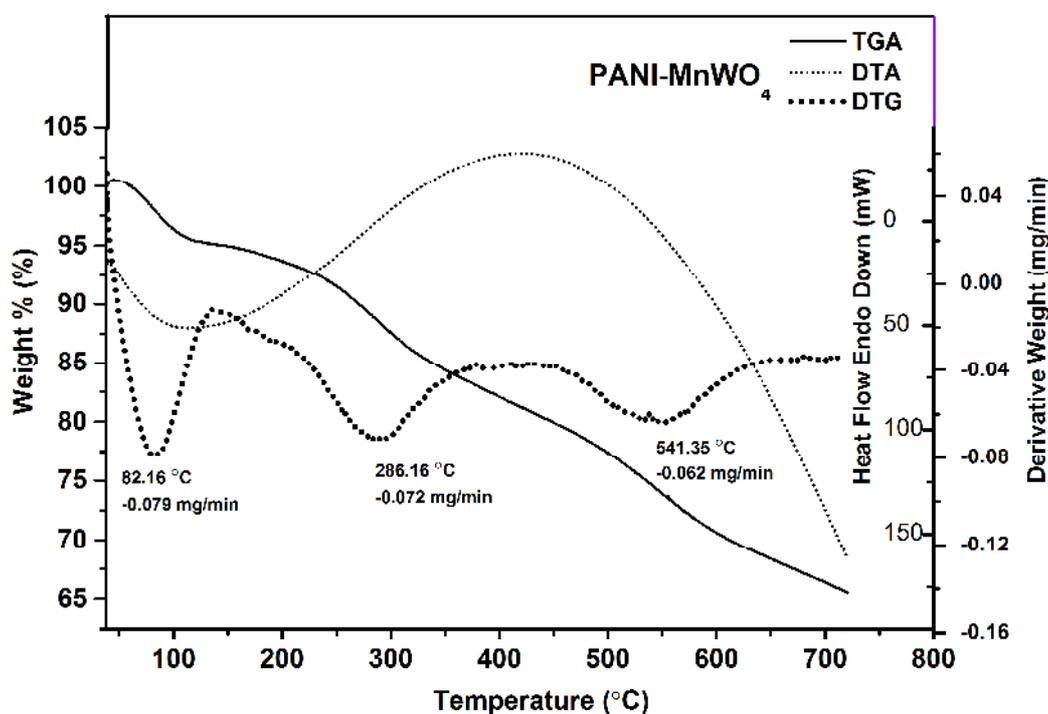
Fig. 5.1 TGA/DTA curves of PANI-MnWO$_4$ nanocomposite

The first weight loss corresponds to the loss of water and impurities in the sample. The second weight loss observed centred on 286.16 ℃ is due to the liberation of HCl molecules from PANI [5-8]. Third weight loss at 541.35 ℃ is attributed to the decomposition of the PANI backbone. The exothermic nature of the DTA curve centred on 425 ℃ suggests that some cross linking of PANI-chain takes place at this temperature [4, 9, 10]. As

dedoping of PANI in the composite occurs beyond 250 ºC, the electrical conductivity of the composite may decrease beyond this temperature. The overall weight loss observed is 35% when heated from 40 to 700 ºC. This confirms that the thermal stability of PANI in the composite is slightly higher.

5.2.2 Structural characterization

5.2.2.1 *XRD study*

Fig. 5.2 represents the XRD pattern for PANI-ES, nanocrystalline $MnWO_4$ and PANI-$MnWO_4$ composite. For pure PANI, three broad peaks are observed at 2θ values 14.65º, 20.15º and 25.27º, which correspond to (011), (020) and (200) planes of PANI, respectively. In Fig. 5.2, the peak centred at $2\theta = 20.15º$ for PANI may be attributed to periodicity parallel to the polymer chain. The major peak at $2\theta = 25.27º$ may be due to the periodicity perpendicular to the polymer chain [11-14]. This peak is related to the conjugation length of π-electrons in PANI-ES. The XRD analysis shows the presence of local crystalline centres in PANI, as reported in the literature [7, 15, 16]. XRD results of $MnWO_4$ and PANI- $MnWO_4$ are compared in Table 5.1.

The results of XRD pattern of pure $MnWO_4$ calcined at 450 ºC are discussed in section 3.3.1. In the present case, all the major peaks for $MnWO_4$ are found in the XRD spectrum of the composite also. But, peaks are broadened, indicating reduction in crystallite size. The full width at half maximum is almost double for the composite (Table 5.1).
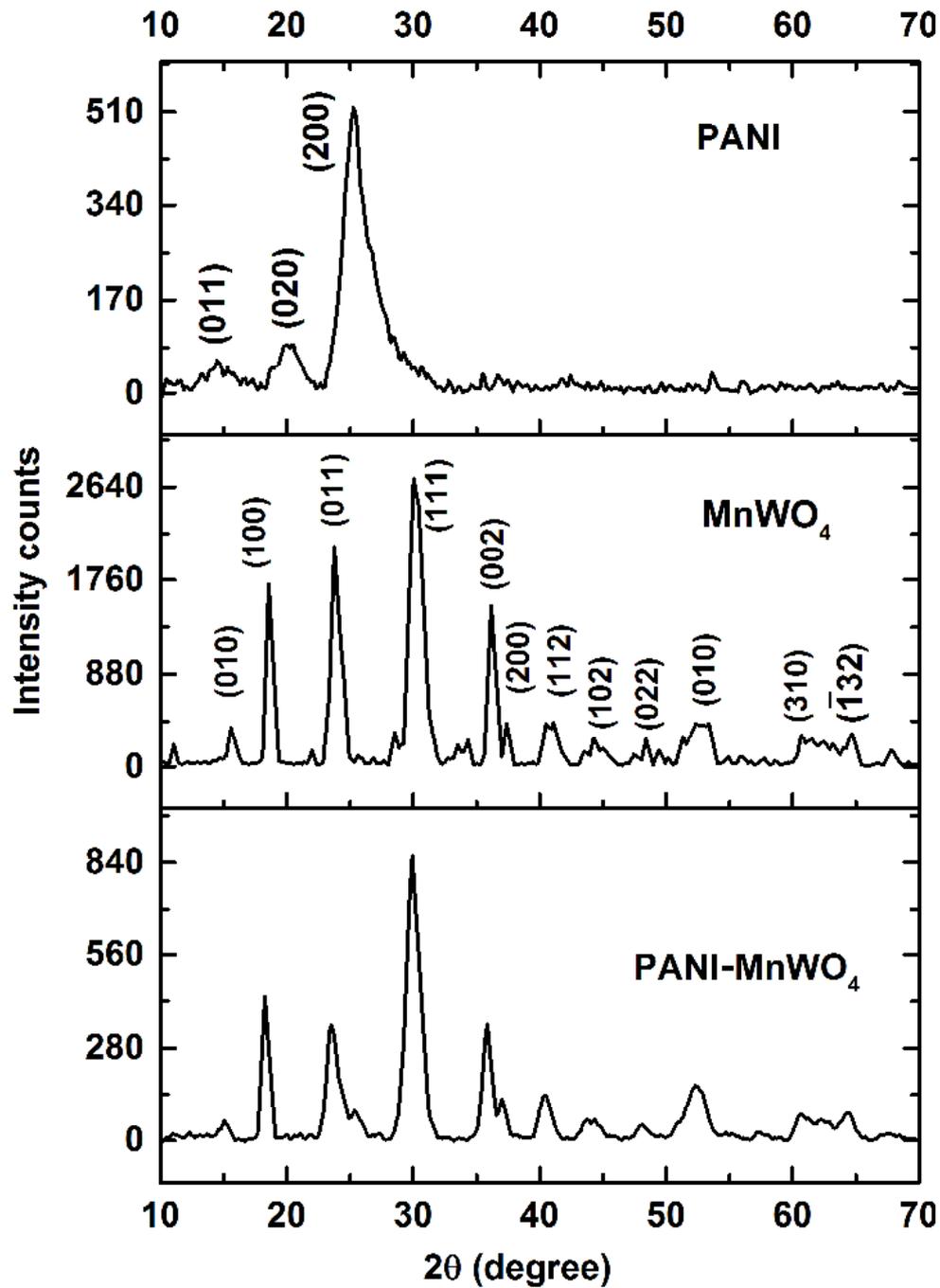
Fig. 5.2 XRD patterns of PANI, MnWO$_4$ and PANI-MnWO$_4$
nanocomposite

The average crystallite size of the composite calculated using the

Scherrer equation (Eqn. 2.2) is found to be 11.50 nm, which is only half of

the original crystallite size (26.03 nm) of $MnWO_4$. This indicates that $MnWO_4$ nanoparticles got dispersed during the polymer composite formation. The Fig. 5.2 and Table 5.1 show that the XRD peaks of PANI-$MnWO_4$ composite are slightly shifted towards the lower 2θ values indicating an increase in the *d*-spacing. This is due to the interaction between the tungstate and the polymer chain.

Table 5.1 XRD results of $MnWO_4$ sample M_1 and PANI-$MnWO_4$ composite

Sample	Major peaks (hkl)	2θ (degree)	FWHM (degree)	d (Å)	Average crystallite Size (nm)
$MnWO_4$ (**M_1**)	(100)	18.57	0.289	4.76	26.03
	(011)	23.77	--	3.74	
	(111)	30.03	--	2.97	
	(002)	36.15	0.365	2.48	
PANI-$MnWO_4$ composite	(100)	18.25	0.477	4.86	11.50
	(011)	23.53	0.912	3.78	
	(111)	29.93	1.030	2.98	
	(002)	35.66	--	2.52	

5.2.2.2 *XRD study of electron beam irradiated samples*

XRD spectra of bare and electron beam irradiated PANI-$MnWO_4$ nanocomposite samples are shown in Fig. 5.3. Average crystallite sizes calculated are 11.50, 10.85, 8.51 nm respectively for 0, 4 and 8 kGy irradiated samples.
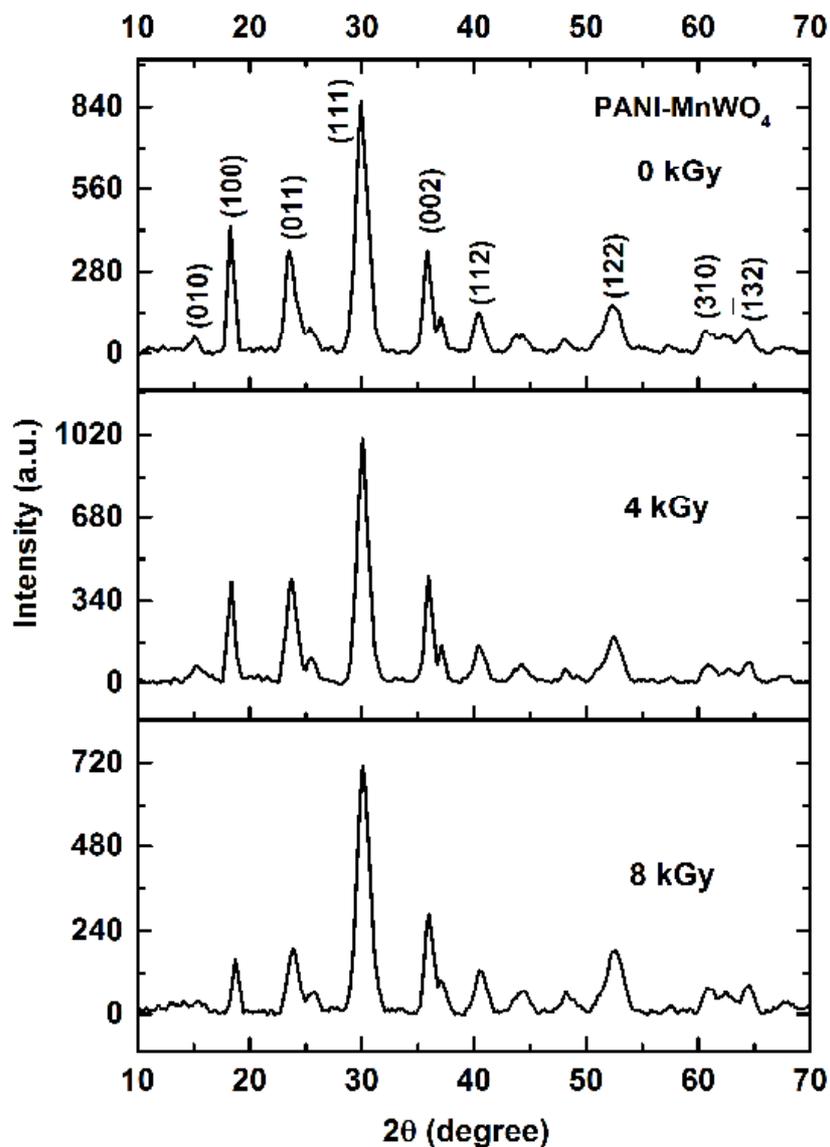
Fig. 5.3 XRD patterns of unirradiated and electron beam irradiated

PANI-MnWO$_4$ nanocomposite

As the crystallized regions in PANI are much less compared to the amorphous regions, their contribution to the intensity in XRD pattern is small. Hence, it is difficult to observe the PANI peaks in the composite. A close observation of the data (Table 5.2) shows that there is a slight shift in the XRD peaks to higher 2θ values as the electron dose is increased from 0

to 8 kGy. Hence, small decrease in *d*-values is observed. This is due to the irradiation induced strains in the composite. In addition, average crystallite size of the composite decreases with increase in electron irradiation dose.

Table 5.2 XRD results of bare and irradiated PANI-MnWO$_4$ samples

Sample	Major peaks (hkl)	2θ (degree)	FWHM (degree)	*d* (Å)	Average crystallite size (nm)
PANI-MnWO$_4$ (0 kGy)	(100)	18.25	0.477	4.86	
	(011)	23.53	0.912	3.78	11.50
	(111)	29.93	1.030	2.98	
	(002)	35.66	--	2.52	
PANI-MnWO$_4$ (4 kGy)	(100)	18.36	0.519	4.83	
	(011)	23.69	0.88	3.75	10.85
	(111)	30.06	1.005	2.97	
	(002)	35.96	--	2.50	
PANI-MnWO$_4$ (8 kGy)	(100)	18.72	0.540	4.74	
	(011)	23.52	1.056	3.78	8.51
	(111)	30.07	1.231	2.97	
	(002)	36.003	--	2.49	

5.2.3 FTIR spectroscopy

5.2.3.1 *FTIR spectroscopy of bare PANI-MnWO$_4$ composite*

The FTIR spectra of PANI-ES, MnWO$_4$ and PANI-MnWO$_4$ are presented in Fig. 5.4. The absorption peaks detected in the three cases are labelled in the figure. The C=N vibration observed in PANI at 1643 cm^{-1} is shifted to 1651 cm^{-1} in the composite. The peaks observed for PANI at 1557 and 1508 cm^{-1} are assigned to the stretching vibration of quinoid (–N=

(C_6H_4) =N–) ring and benzenoid (–(C_6H_4)–) ring, respectively. These peaks are slightly shifted to 1556 and 1510 cm^{-1} in the PANI-MnWO$_4$ composite. The band observed at 1292 cm^{-1} is strengthened by the protonation of PANI and attributes to the C-N stretching of secondary amine [17]. This peak, shifts to 1290 cm^{-1} in the PANI-MnWO$_4$ composite. The protonation of polyaniline induces absorption peak at 1238 cm^{-1} in PANI and PANI-MnWO$_4$ composite. The presence of this peak in PANI and its composite is a measure of the π-electron delocalization that determines their conducting nature [18].
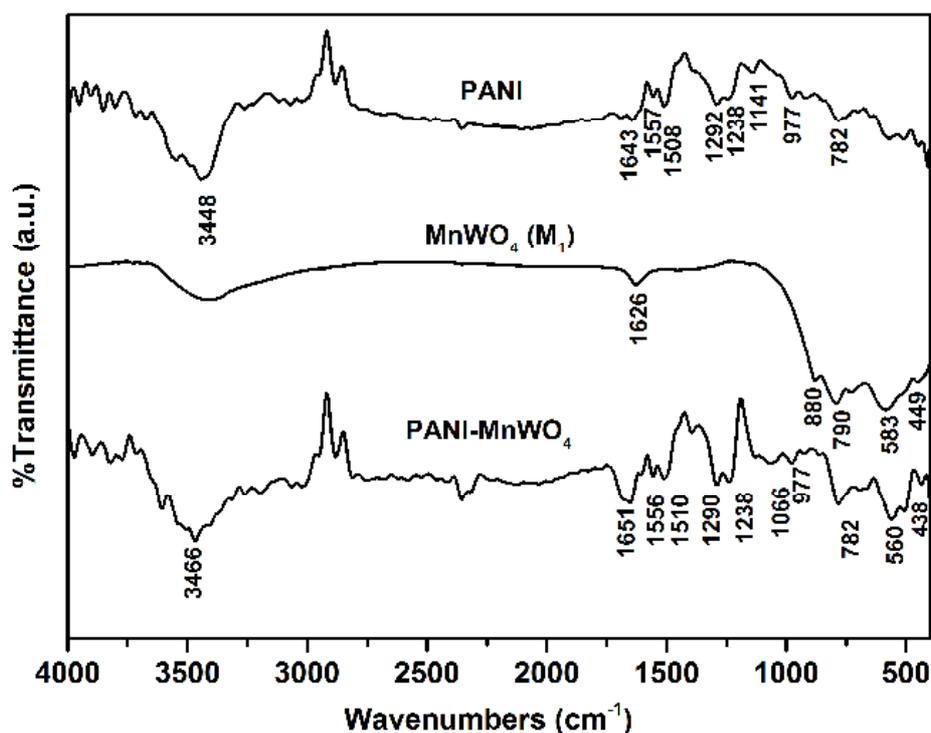
Fig. 5.4 FTIR spectra of PANI-ES, MnWO$_4$ (**M$_1$**) and PANI-MnWO$_4$

The band at 1141cm^{-1} in PANI-ES spectrum is due to the excess HCl doping. This is assigned to the vibration of mode of –NH$^+$= structure,

formed during protonation [19-21]. This band shifts to 1066 cm^{-1} in the composite material due to the interaction between MnWO$_4$ nanoparticles and PANI-ES. The absorption peak at 977 cm^{-1} in PANI and PANI-MnWO$_4$ composite is assigned to the stretching of the C-H out of plane bending. The peak at 782 cm^{-1} in PANI is assigned to the N-H wagging. The major absorption peaks of MnWO$_4$ at 880, 790, 583 and 449 cm^{-1} are described in section 3.4.1. In PANI-MnWO$_4$ composite, the peak at 880 cm^{-1} is not distinct. Other peaks related to MnWO$_4$ are shifted to 782, 560 and 438 cm^{-1}, respectively. This shift is due to the the Vander Waal's interaction between MnWO$_4$ and polyaniline chain [22]. These shifts in peak of MnWO$_4$ in the composite confirm the composite formation.

5.2.3.2 *FTIR spectroscopy of electron beam irradiated PANI-MnWO$_4$*

FTIR spectra of bare (0 kGy) and electron beam irradiated (4 and 8 kGy) PANI-MnWO$_4$ nanocomposite samples are shown in Fig. 5.5. The C=N vibration observed in PANI-MnWO$_4$ at 1651 cm^{-1} disappears in the electron beam irradiated samples. The peak at 1510 cm^{-1} in the unirradiated sample, arising from the stretching vibration of benzenoid ($-(C_6H_4)-$) ring, shifts to 1476 cm^{-1}in the irradiated samples. The absorption peak at 1066 cm^{-1}, due to the vibration of mode of $-NH^+=$ structure in the bare composite, shifts to 1107 cm^{-1} in the irradiated samples. Moreover the increased intensity of absorption of this peak indicates increased doping of the PANI chain. Electron beam irradiation of suitable dose causes some chain scission that leads to improvement in ordering of PANI. Accordingly

improved electrical conduction is expected in the composite. Thus, the IR absorption in PANI-MnWO$_4$ gets modified after electron beam irradiation.
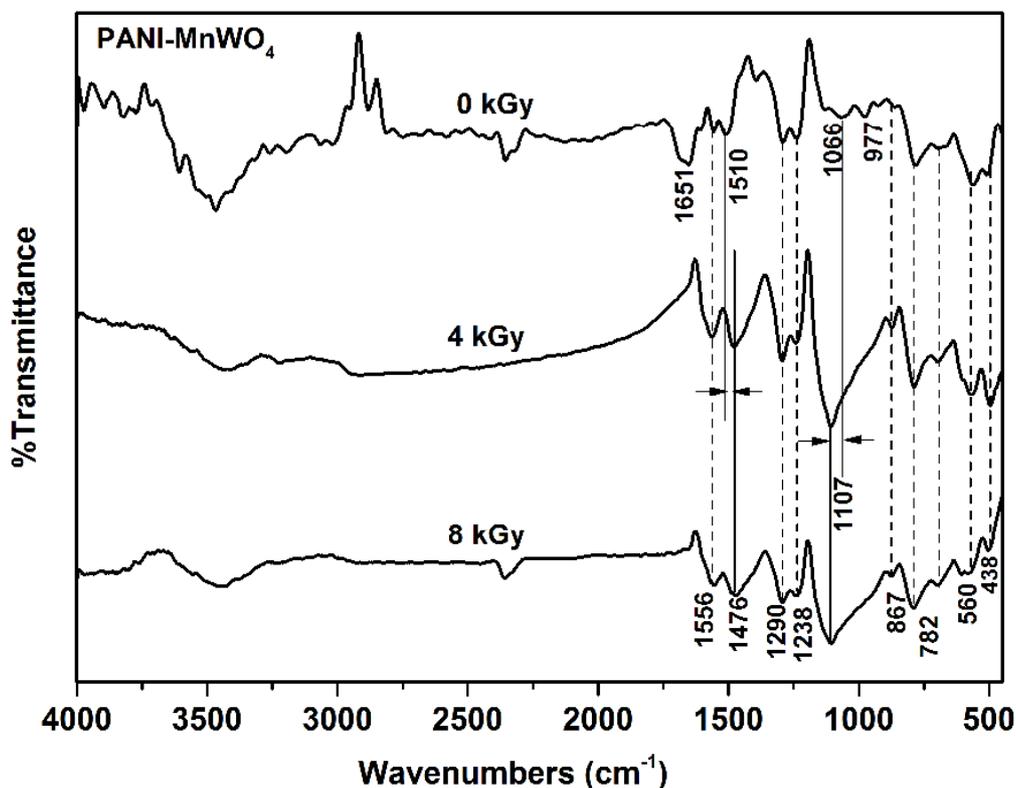
Fig. 5.5 FTIR spectra of unirradiated and electron beam irradiated PANI-MnWO$_4$

5.2.4 Electron microscopy

The morphology of the composite is studied using FE-SEM and TEM analysis. The elemental composition is confirmed using EDS.

5.2.4.1 *FE-SEM analysis of PANI and PANI-MnWO$_4$ nanocomposite*

The FE-SEM image of PANI-ES is shown in Fig. 5.6. The interconnected fibre (clew) like morphology is seen throughout. The diameter of the fibre is less than 80 nm.
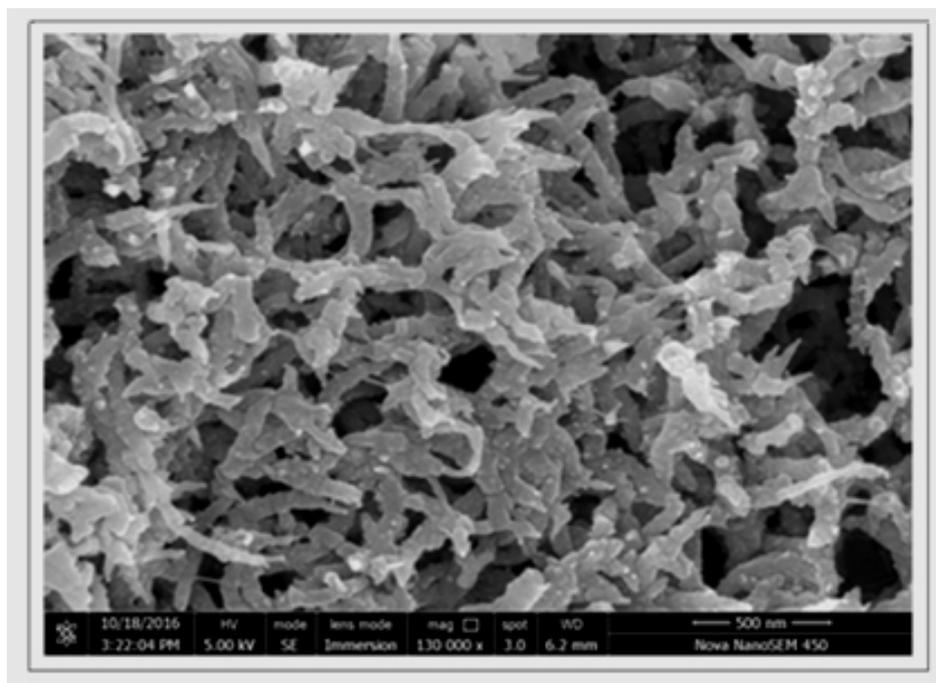
Fig. 5.6 FE-SEM images of PANI-ES
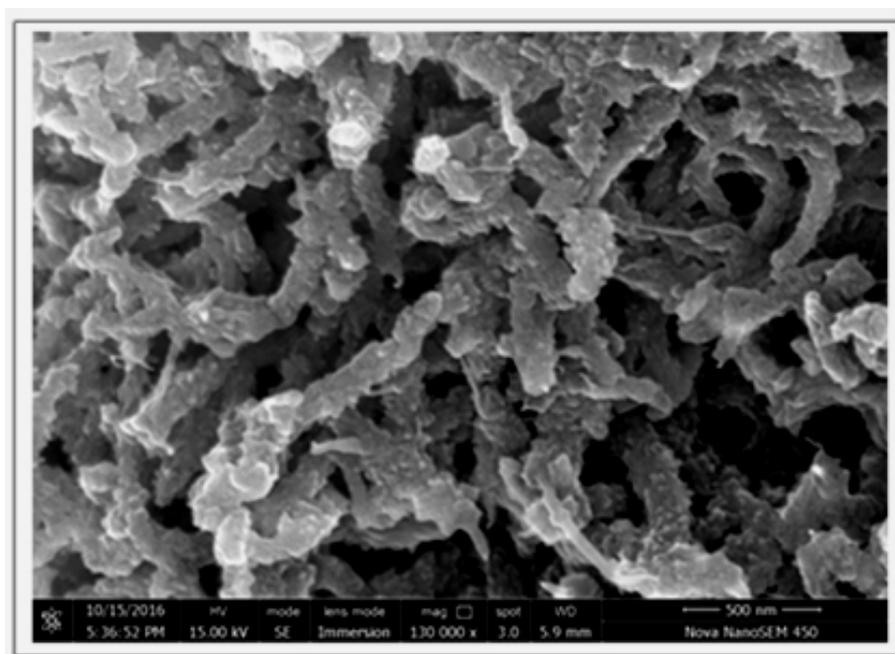
Fig. 5.7 FE-SEM image of PANI-MnWO$_4$

The FE-SEM image for the PANI-MnWO$_4$ composite is shown in Fig. 5.7. In the magnified image, clew like fibres connected to each other are visible. The diameter of the fibre is about 80 nm. Compared to FESEM images of PANI-ES, some morphological changes are observed in the composite, which may be due to the incorporation of MnWO$_4$ in the PANI fibres.

5.2.4.2 *Compositional analysis*

The elemental composition of the composite is carried out using EDS, which is obtained in conjunction with the SEM measurements. The spectrum obtained is shown in Fig. 5.8.
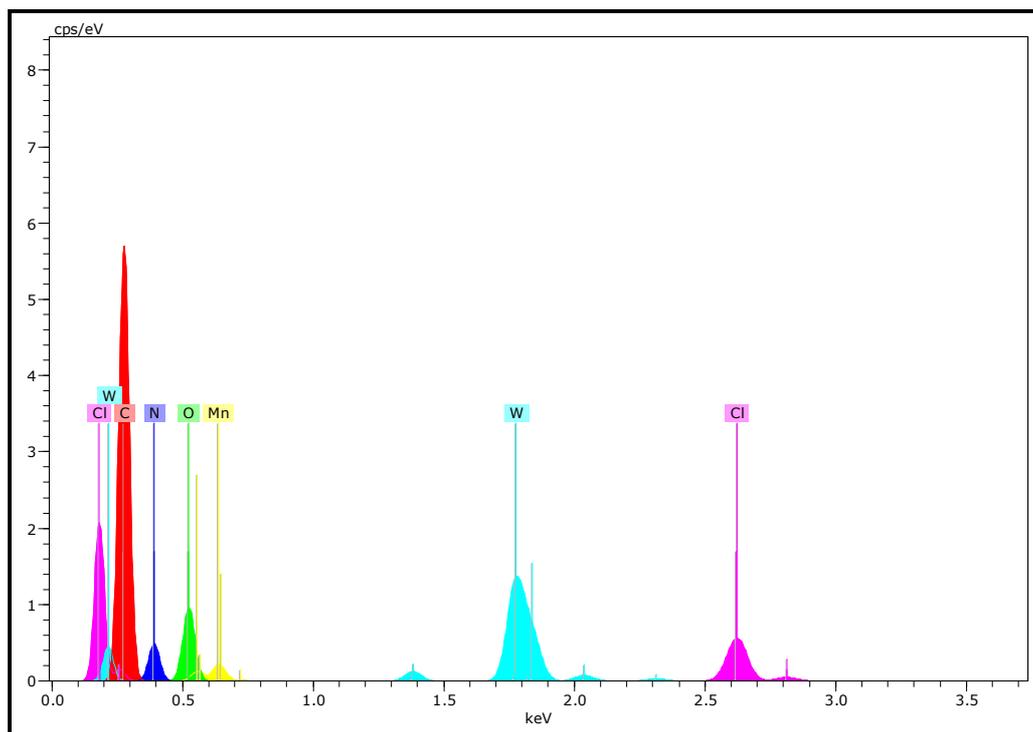
Fig. 5.8 EDS of PANI-MnWO$_4$ composite

The elements present in the composite are Mn, W, O, C, N and Cl. Hydrogen being light element cannot be detected in the EDS. But its presence is confirmed by the occurrence of the peaks of hydrogen containing functional groups in the FTIR spectra discussed in section 5.2.3. No impurity or loss of chemical elements is detected from the EDS spectrum. Moreover, the elements present in the constituents before the formation of the composite are also confirmed in the final product. The percentage occurrence of each element in the composite is given in Table. 5.3.

Table 5.3 EDS data of PANI-MnWO$_4$

Element	Series	Mass%	Atom%
C	K	53.48	61.40
O	K	21.54	18.56
N	K	19.54	19.40
Mn	K	0.63	0.16
W	L	3.93	0.29
Cl	K	0.87	0.34
Total		100	100

5.2.4.3 *TEM analysis of PANI-MnWO$_4$ nanocomposite*

The TEM images for PANI-ES are shown in Fig. 5.9. Bead shaped nanoparticles connected together are seen in Fig. 5.9(a). The average size of the particles is 8 nm. High resolution images in Fig. 5.9 (b) and (c) show

that some regions are crystalline and are compatible with the XRD studies. The separation between the crystal planes measured from figure (c) is 0.35 nm. Fig. 5.9(d) shows the SAED pattern. The three peaks found in the XRD pattern for PANI-ES namely (011), (020) and (200) are also seen in the SAED pattern [11-14]. This also confirms that the synthesized PANI-ES has some crystalline centres.
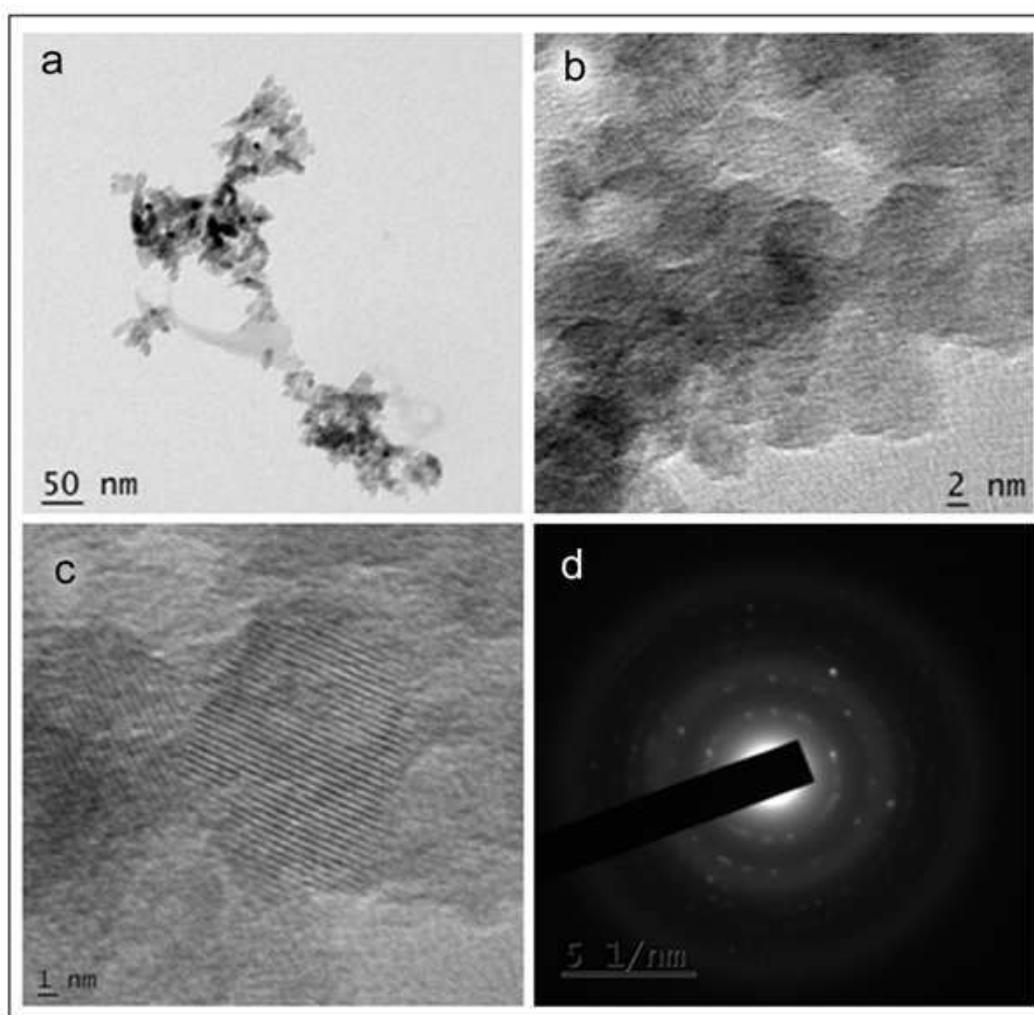
Fig. 5.9 TEM images of PANI-ES: (a) Bright field image, (b) and (c) HRTEM images, and (d) SAED pattern
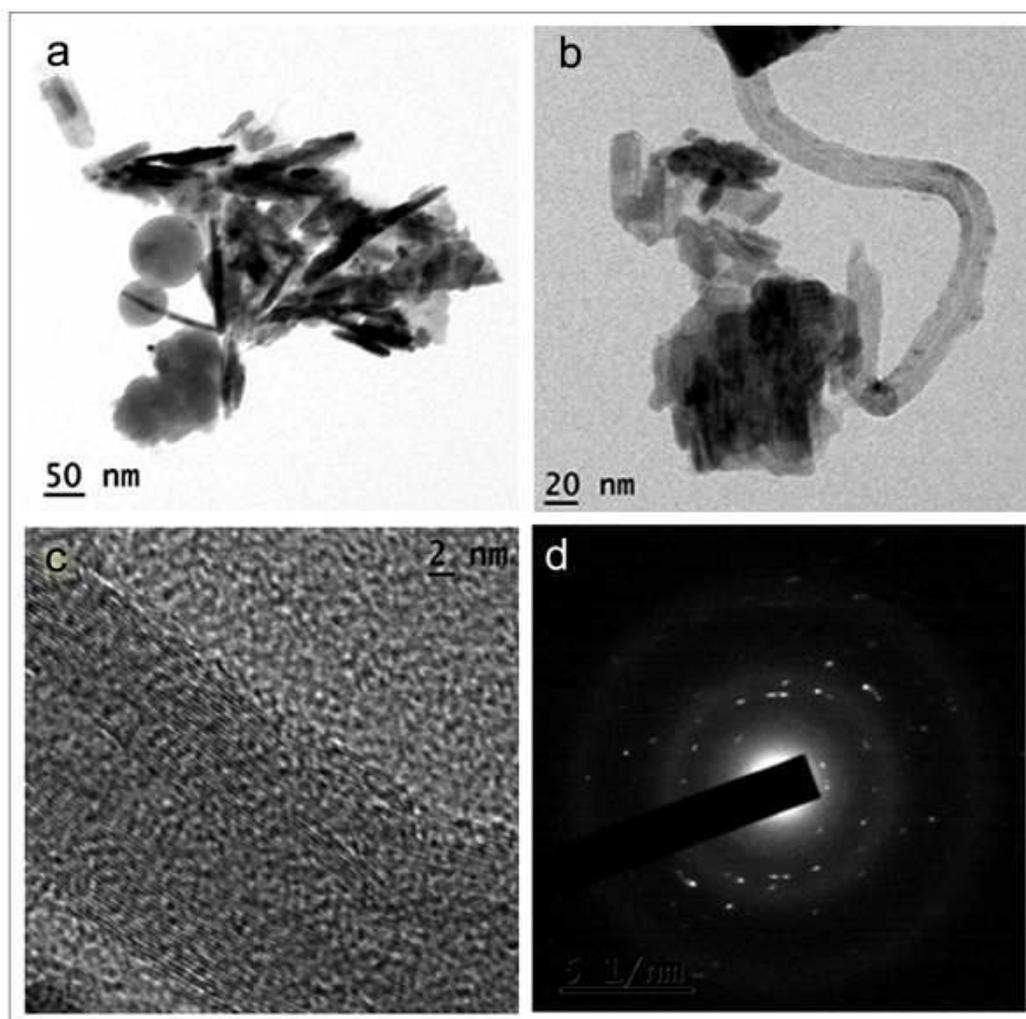
Fig. 5.10 TEM images of PANI-MnWO$_4$ composite: (a) and (b) bright field images, (c) HRTEM image and (d) SAED pattern

The TEM images of PANI-MnWO$_4$ nanocomposite are presented in Fig. 5.10. Nanosized structures are visible in the composite. The Fig. 5.10 (a) and (b) show the presence of spherical, fibre like and rod shaped structures in the composite. Nanofibre of diameter about 14 nm is shown in the Fig. 5.10(b). It can be seen from Fig. 5.10(c) that some crystalline channels are separated by amorphous regions. These inter facial regions are

important when the electrical properties are discussed. The Fig. 5.10(c) again depicts some crystalline regions embedded in amorphous regions. The SAED pattern shows the presence of crystalline peaks in PANI-MnWO$_4$ composite.

5.2.5 UV-Visible spectroscopy

The UV-Visible absorption studies are performed both in bare and electron beam irradiated samples.

5.2.5.1 *UV-Visible spectroscopy of PANI-MnWO$_4$ composite*

The UV-Visible absorption spectra after performing the Kubelka Munk transformation of the diffuse reflectance for PANI and PANI-MnWO$_4$ composite are shown in the Fig. 5.11. Two major absorptions peaks centred on 372 and 648 nm are obtained for protonated PANI. The first broad peak centred on 372 nm is blue shifted to 338 nm and the second one centred on 648 nm is red shifted to 665 nm in the composite material.

According to literature reports, the first transition is due to π-π^* electronic transition in the phenyl ring of the polymer backbone and the second transition is due to the inter band charge transfer associated with excitation of the benzenoid to the quinoid moieties [13, 23, 24]. Though the first absorption peak is centred on 338 nm, it extends without much variation up to 420 nm. The broad absorption ranges from 375 to 425 nm is due to polaron-π^* transition and is characteristic of the emaraldine salt form of PANI [18].
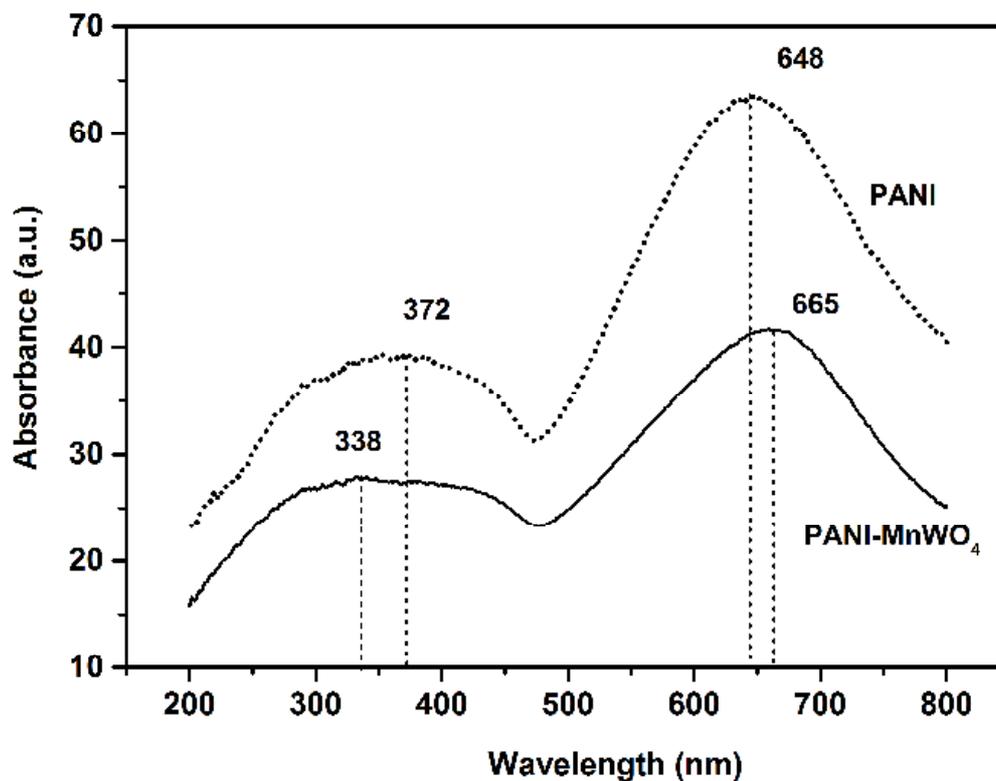
Fig. 5.11 UV-Visible absorption spectra of PANI and PANI-MnWO$_4$

Energy gap is determined for PANI and PANI-MnWO$_4$ composite from Tauc plot, shown in Fig. 5.12. The bandgap obtained for PANI-ES is 1.50 eV. For the composite the optical bandgap value obtained is 1.48 eV. This slight change in bandgap resulted from the interaction between its constituents. Reduced bandgap in polaronic states is reported by Deb et al. [25]. The bandgap reported for PANI-ES from absorption spectrum studies is 1.50 eV and is interpreted as excitation to polaron band [26, 27]. Observed bandgap can be explained by the polaron lattice structure proposed by Stafstrom et al. [24, 28].
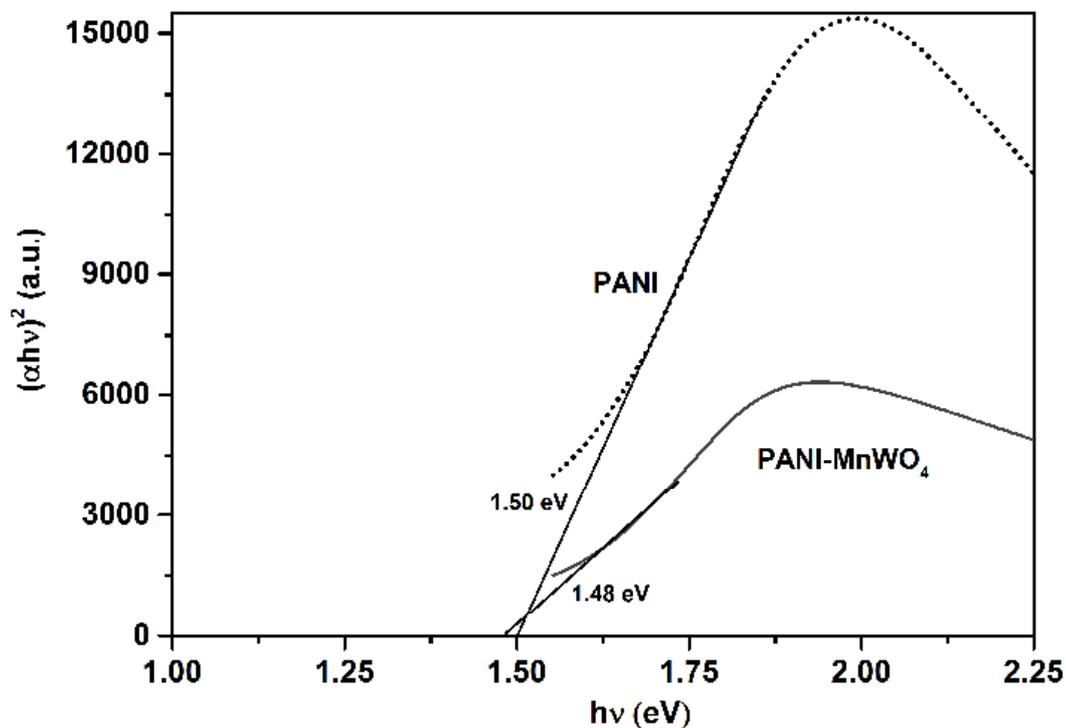
Fig. 5.12 Tauc plot of PANI and PANI-MnWO$_4$

5.2.5.2 *UV-Visible spectroscopy of electron beam irradiated PANI-MnWO$_4$ composite*

The UV-Visible absorption spectra of bare (0 kGy) and electron beam irradiated (4 and 8 kGy) PANI-MnWO$_4$ composite samples are shown in Fig. 5.13. It can be seen from Fig. 5.13 that the absorption peaks are blue shifted for the electron irradiated sample. It is interesting that the absorbance increases with increase in electron dose.
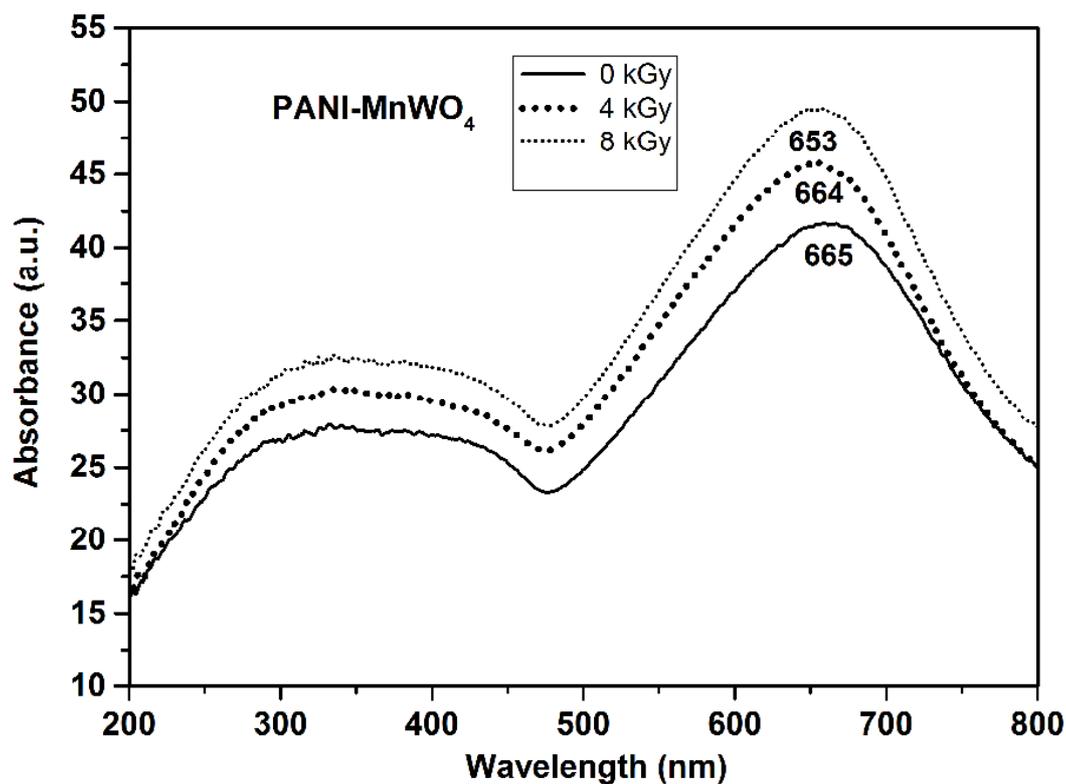
Fig. 5.13 UV-Visible absorption spectra of unirradiated and
electron beam irradiated PANI-MnWO$_4$

The bandgap values estimated from Tauc plots (Fig. 5.14) of the irradiated samples with doses 0, 4 and 8 kGy are 1.48, 1.51 and 1.52 eV, respectively. Since the percentage of MnWO$_4$ in the composite is small and the absorption due to PANI is very high, contribution from the former is not distinct in the composite form.
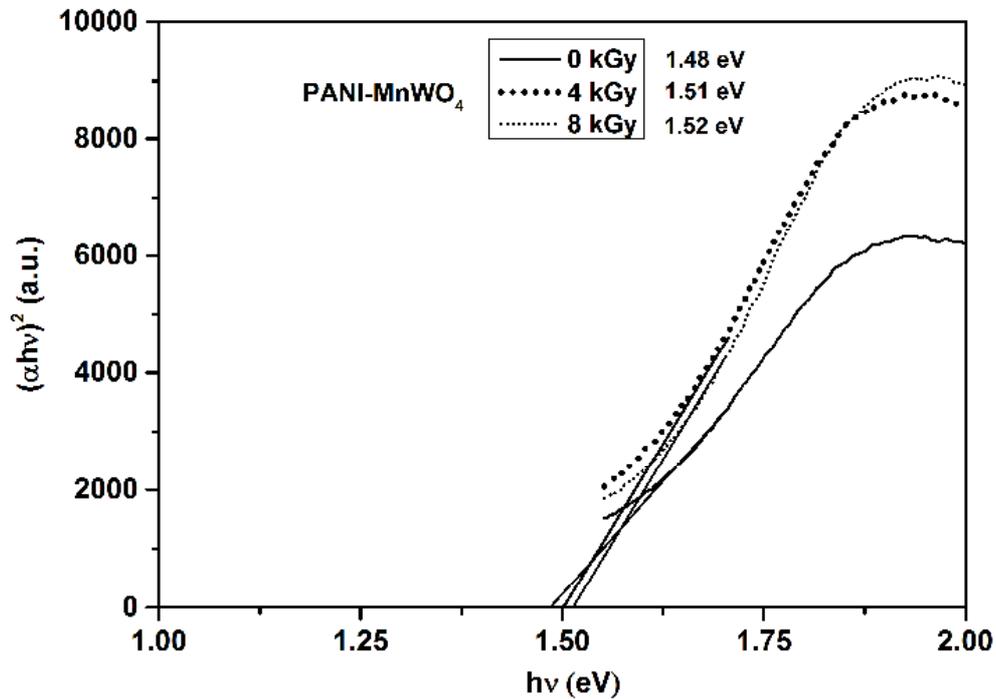
Fig. 5.14 Tauc plot of the bare and irradiated PANI-MnWO$_4$

5.3 Electrical properties

In this section, the DC and AC conductivities are discussed. Also the dielectric response of the bare and irradiated samples is compared.

5.3.1 DC electrical studies of PANI-MnWO$_4$ composite

The variation in the conductivity of PANI-ES, bare and electron beam irradiated PANI-MnWO$_4$ composite are shown in Fig. 5.15. At 303 K, DC conductivity values are 0.00042, 0.0023, 0.0036 and 0.0033 S-cm^{-1} for the PANI-ES, 0, 4 and 8 kGy irradiated PANI-MnWO$_4$ nanocomposite, respectively. At 463 K, the corresponding values become 0.00087, 0.0031, 0.010 and 0.009 S-cm^{-1}. Fig. 5.15 demonstrates that the DC conductivity is larger for the electron beam irradiated samples.

In all the cases, the conductivity is found to increase with increase in temperature. This type of thermally activated DC conductivity has been observed with many other polyaniline composites and other conducting polymers [29,30]. It is generally accepted that this type of conduction is due to the hopping of charge carriers [31]. Though a bad conductor is added to the PANI to form the composite, the conductivity gets doubled because of synergistic effect of $MnWO_4$ molecule with the PANI-chain [32]. The reason for the enhanced DC conductivity in the irradiated sample is the ordering and the effective increase in doping of the PANI chain in the composite induced by the electron beam irradiation. Also, the electron dose affected the material properties [33]. It has been reported that the electrical conductivity of polyaniline based composite enhanced upon irradiation by gamma, electron beam or UV radiations [34]. Moreover, the enhanced electrical conductivity of electron irradiated PANI-$MnWO_4$ composite can be suitable for potential application like antistatic coatings and EMI shielding. Further investigation is needed to decide the optimum ratio of the components in the composite and suitable electron dose.

The conductivity values obtained are similar to that for semiconductors. In the present case the values fall in the range of 10^{-3} to 10^{-2} Scm^{-1}. These values of conductivity are many orders greater than that of many conventional polymers (10^{-9} Scm^{-1}). According to previous reports on composites of polyaniline, this type of DC conductivity takes place by the hopping process due to wide range of localized states and the increase in conductivity in the composite must be due to the shifting of the Fermi level

[35, 36]. Though the added nanoparticles have poor conductivity, their presence in the composite has resulted in better DC conductivity than that of pure PANI (Fig. 5.15).
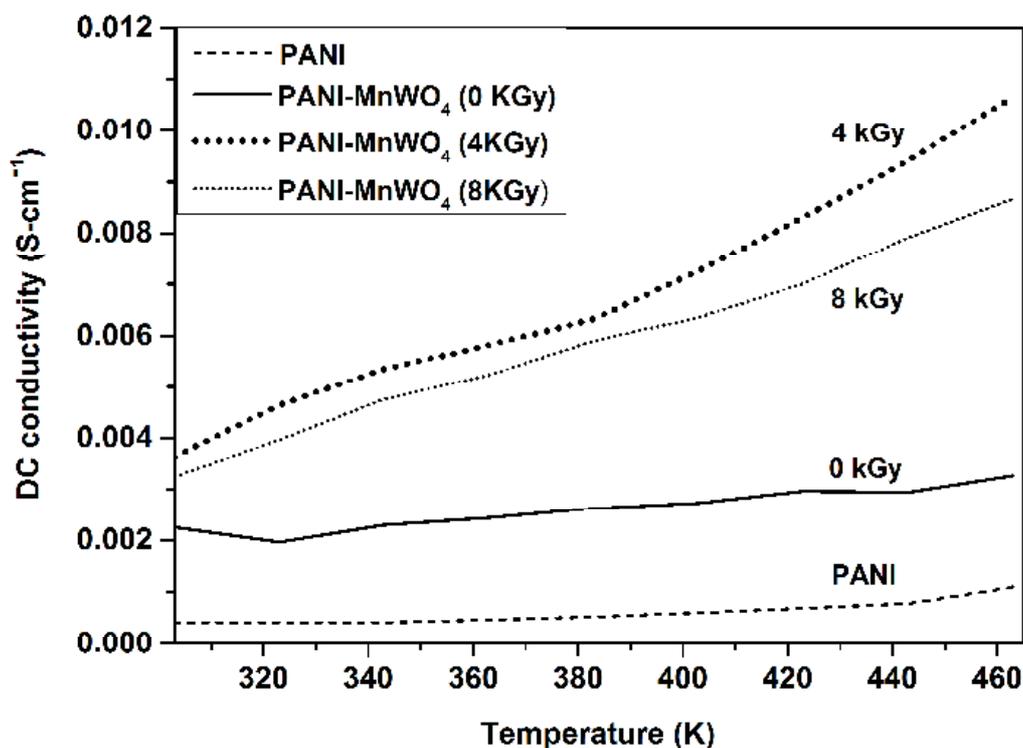
Fig. 5.15 Variation in the DC conductivity of PANI-ES, PANI-MnWO$_4$ and electron beam irradiated PANI-MnWO$_4$ with temperature

5.3.2 AC electrical

AC electrical studies include determination of the frequency dependence of the dielectric constant and tangent loss for the unirradiated and electron beam irradiated samples of PANI-MnWO$_4$ nanocomposite.

5.3.2.1 *Dielectric studies of PANI-MnWO₄ composite*

Dielectric constant

Dielectric constants at different frequencies are calculated from the measured values of capacitance at the corresponding frequencies. Fig. 5.16 shows the frequency dependence of the dielectric constant for the unirradiated (0 kGy) and irradiated (4 and 8 kGy) PANI-MnWO$_4$ nanocomposite in the range 20 Hz to 2 MHz at room temperature.
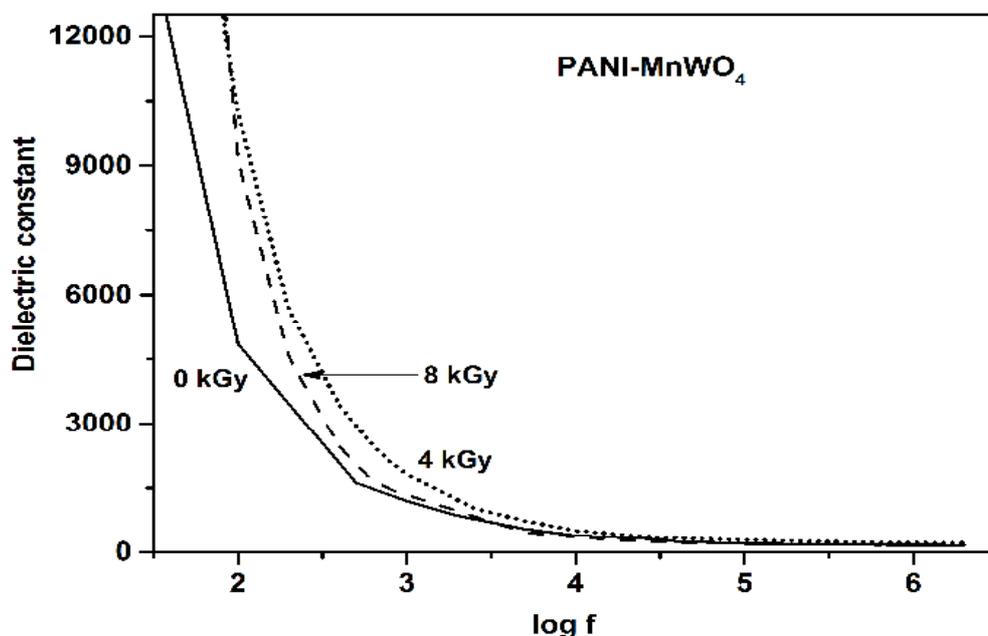
Fig. 5.16 Frequency dependence of the dielectric constant in the unirradiated and irradiated PANI-MnWO$_4$

The value of dielectric constant is very high initially and decreases exponentially with log f. Its value at 100 Hz is 4752, 10220 and 9220 for the 0 kGy, 4 and 8kGy irradiated samples, respectively. The dielectric constant got doubled in the irradiated case. At 1MHz the corresponding values are 166, 260 and 213 for the three samples. The decrease in

dielectric constant with frequency is due to dielectric relaxation [22, 37, 38]. At lower frequencies charges accumulate at the interfaces of conducting PANI and $MnWO_4$ particles which results in Maxwell-Wagner-Sillars interfacial polarization [39, 40]. This phenomenon also contributes to dielectric relaxation.

Dielectric loss

The variations in loss tangents with **log f** for the bare and electron irradiated samples are shown in Fig. 5.17. The loss tangents observed at 10 kHz for the bare (0 kGy), 4 and 8 kGy irradiated samples are 8.49, 6.48 and 5.37, respectively. Low values of loss tangents are seen in the case of the irradiated samples. The corresponding values at 2 MHz are 0.31, 0.42 and 0.27 respectively. The dielectric losses are due to conduction losses.
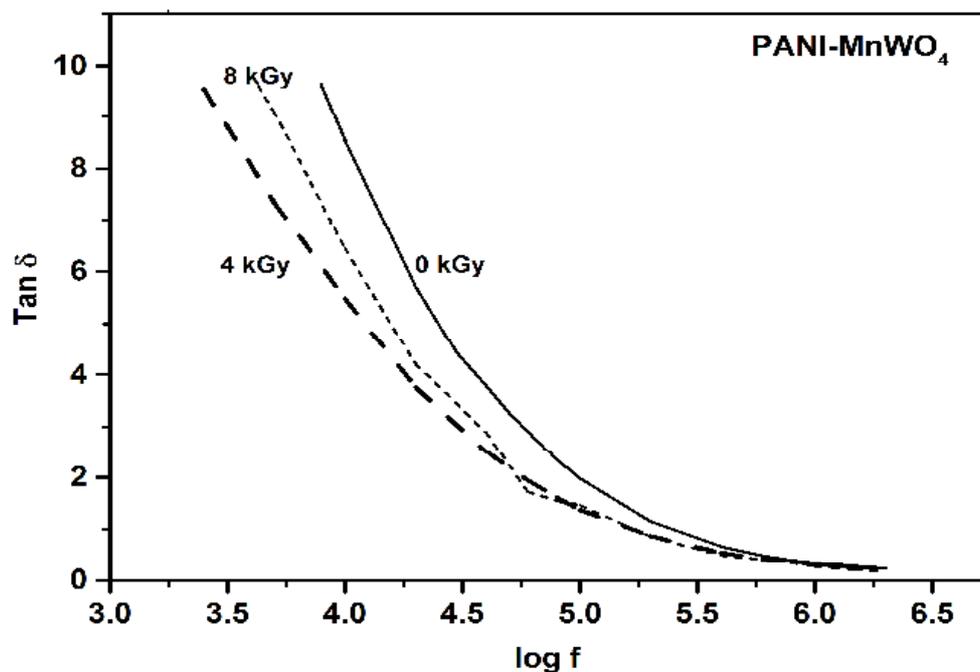
Fig. 5.17 Variation of loss tangent of the bare and
electron irradiated PANI-MnWO$_4$

5.3.2.2 *AC conductivity studies*

The variation in AC conductivity as a function of frequency is shown in Fig. 5.18. An exponential increase in AC conductivity is observed in the three cases. At 4 kHz, the values of AC conductivity are 0.0017, 0.00151 and 0.0012 Scm^{-1} for the unirradiated, 4 and 8 kGy irradiated samples, respectively. At 1 MHz, the corresponding values are 0.0031, 0.0036 and 0.0024 Scm^{-1}. In the case of 4 kGy the AC conductivity over rides that of the unirradiated sample at higher frequencies.
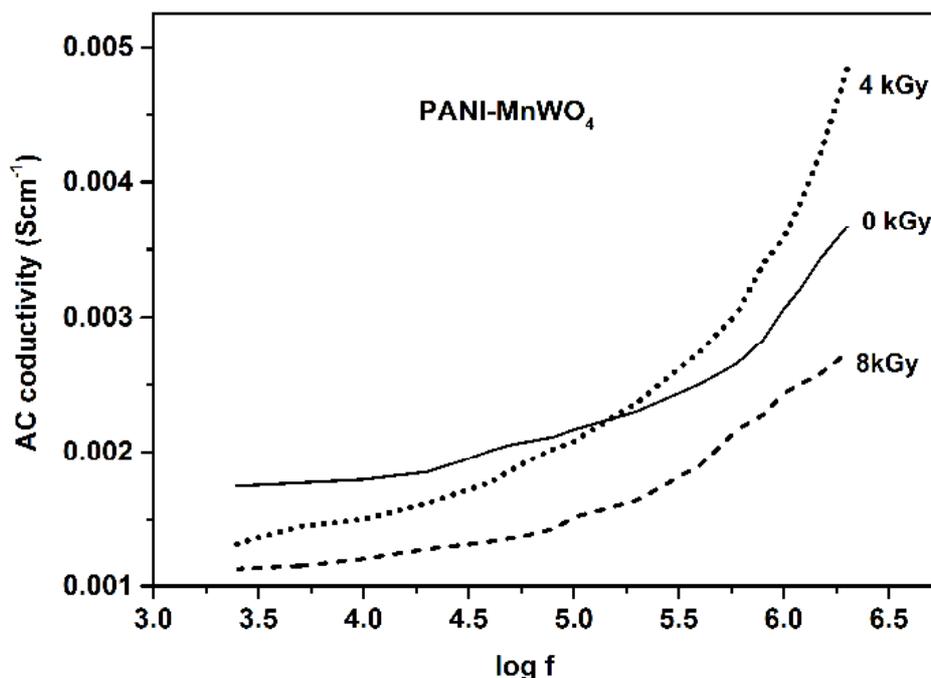
Fig. 5.18 Variation in AC conductivity as a function of frequency in unirradiated and irradiated samples of PANI-MnWO$_4$

It is very clear from the three curves (Fig. 5.18) that the AC conductivity is greatly affected with electron beam irradiation dose. The inter-chain separation is affected by irradiation [41]. The motion of delocalized electrons through the polymer back bone and hopping of

electrons between nearest redox sites on the polymer chain contributes to AC conduction in PANI-composites [42]. Depending on the dose, chain-scission, cross-linking and change in the ordering of the chains occurs leading to the observed variations in the AC conductivity of the irradiated sample [43].
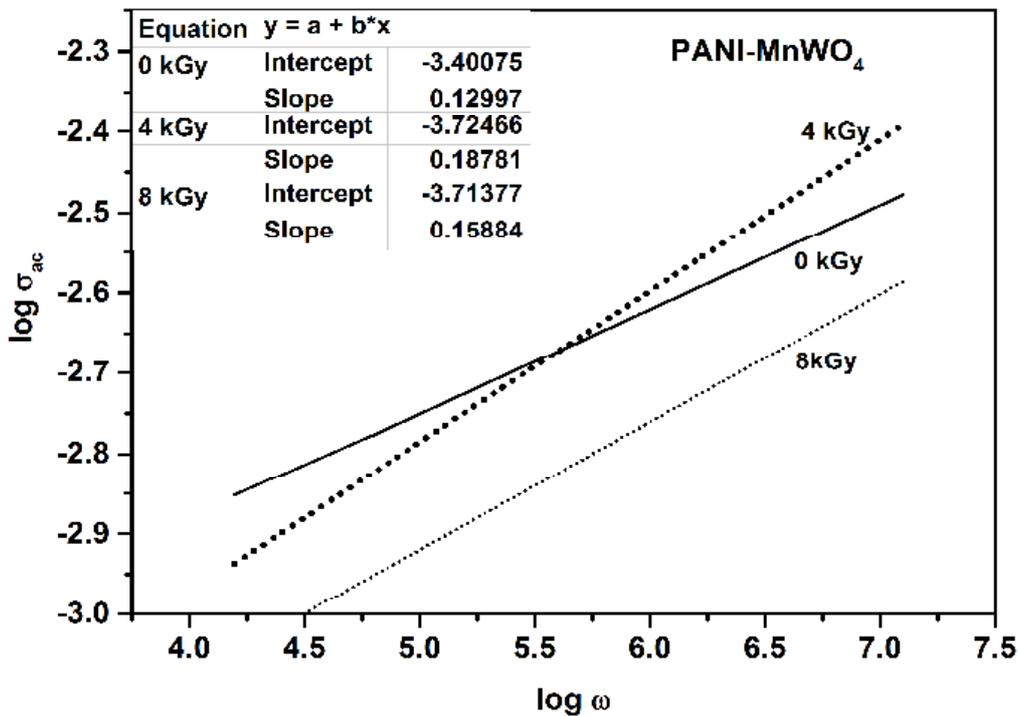
Fig. 5.19 Linear fits of log ω versus log [σ_{ac}] plots

A linear fits of **log ω** versus **log [σ_{ac}]** plots are given in Fig. 5.19. The AC studies in many polyaniline composites, reports the power law behaviour. In the case of PANI-MnWO$_4$ also the power law dependence given by $\sigma_{ac}(\omega) = A\omega^n$ is satisfied [30, 44-46]. Values of n determined from the slopes of the linear fit in Fig. 19 are 0.13, 0.19 and 0.16 for the unirradiated, 4 and 8 kGy irradiated composites, respectively. These values

are between 0 and 1. Hence, the contribution to the conduction by hopping process is confirmed.

5.4 Characterization of PANI-CaWO$_4$ nanocomposite

5.4.1 Thermal analysis

The TGA/DTA curves obtained for PANI- CaWO$_4$ composite when heated in oxygen atmosphere are shown in Fig. 5.20. The solid curve represents the weight loss occurring to the sample when it is heated from 40 to 850 ℃. It shows mainly two weight losses centred on 83.63 and 568.45℃.
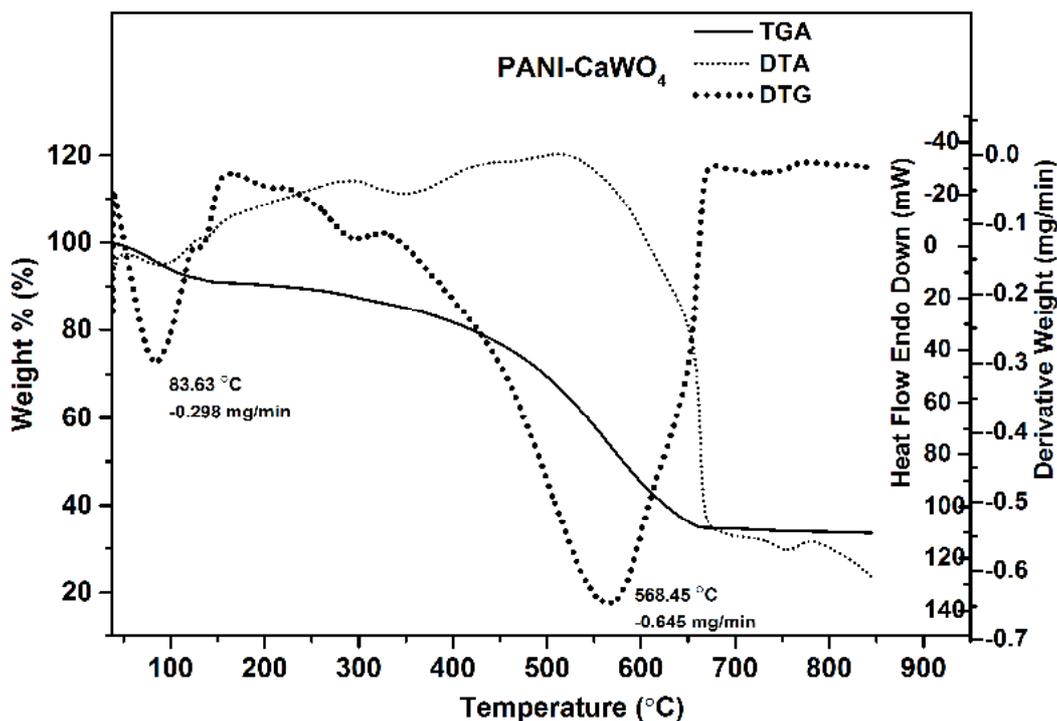
Fig. 5.20 TGA/DTA curves of PANI-CaWO$_4$ composite

The first weight loss is due to the removal of moisture from the composite [7]. The loss of HCl molecules in this case is not as sharp and

fast as in the case of PANI-MnWO$_4$ composite. The decomposition of PANI-chain begins around 450 ºC and is maximized at 568.45 ºC and is completed around 675 ºC. The residue must be CaWO$_4$ as it is very stable to heating up to 900 ºC. In the present case the overall weight loss, when heated up to 700 ºC, is about 65%. The wide exothermic nature of the DTA curve from 150 to 500 ºC suggest the cross linking occurring in the PANI. TGA results suggest that heating beyond 250 ºC set an upper application limit of temperature because the elimination of the dopant results in loss of conductivity [47].

5.4.2 Structural characterization

5.4.2.1 *XRD study*

XRD patterns of PANI-ES, CaWO$_4$ and PANI-CAWO$_4$ are shown in Fig. 5.21. As discussed in section 5.2.2.1, for PANI-ES, the peak centred at $2\theta = 20.15º$ is attributed to periodicity parallel to the polymer chain, while the peaks at $2\theta = 25.27º$ is due to the periodicity perpendicular to the polymer chain [11-13]. This indicates that there are local crystalline centres embedded in amorphous PANI [48]. The XRD pattern of nanocrystalline CaWO$_4$ is discussed in detail in section 4.3.1. It has a scheelite-type tetragonal structure and a space group $I4_1/a$ in a C_{4h}^6 symmetry (JCPDS number 77-2235). In the case of PANI-CaWO$_4$ nanocomposite the XRD profile shown cannot display clearly the peaks associated with PANI-ES as they are of very low intensities. All the peaks and d-spacing detected correspond to the records in JCPDS file no. 77-2235 for CaWO$_4$. Therefore,

it may be concluded that the crystal structure of $CaWO_4$ is retained in the composite. The average particle size calculated for $CaWO_4$ and PANI-$CaWO_4$ are 39.67 and 35.24 nm, respectively.
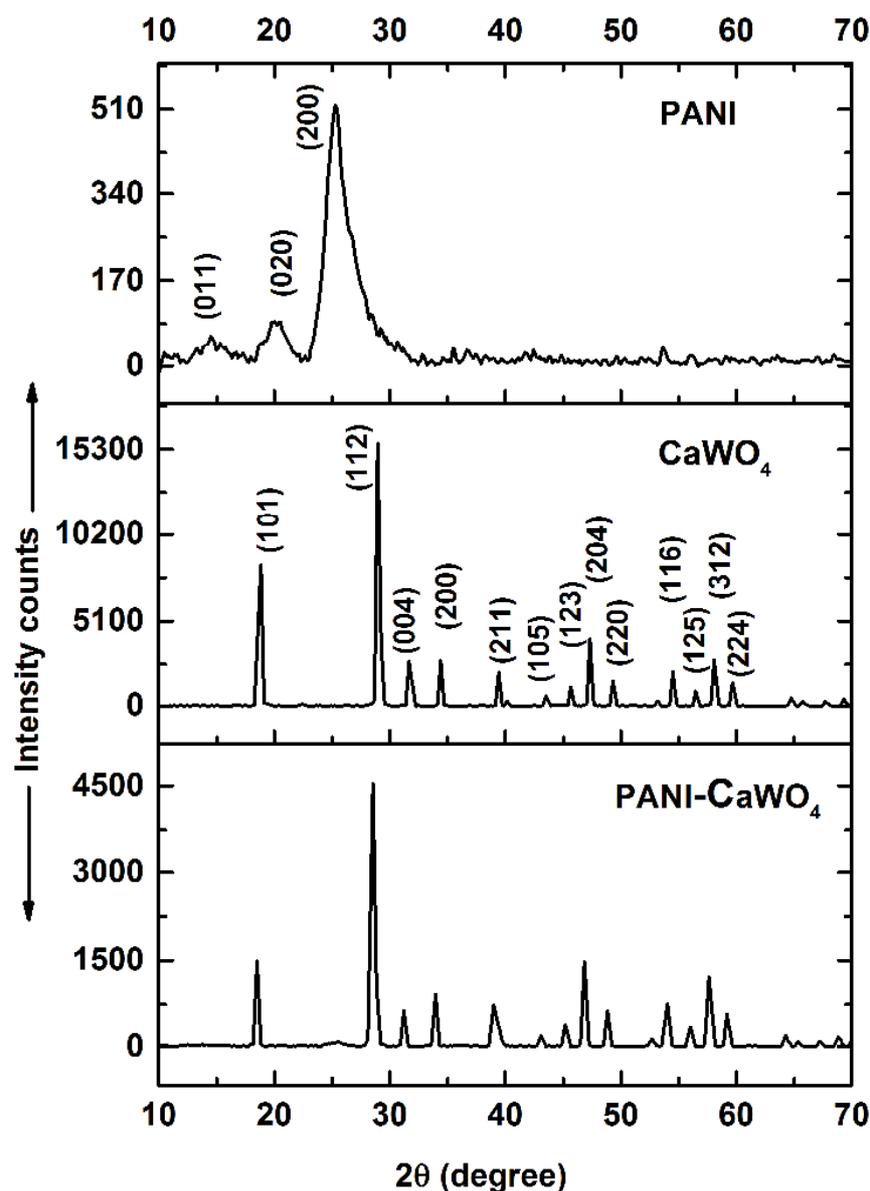
Fig. 5.21 XRD patterns of PANI, $CaWO_4$ and PANI-$CaWO_4$ nanocomposite

Table 5.4 represents the XRD data related to the major peaks of $CaWO_4$ (**C₃**) before and after the composite formation. It can be seen from

the table that the major peak positions of $CaWO_4$ are slightly shifted to lower 2θ values in the composite. Accordingly there is a slight increase in the d spacing.

Table 5.4 XRD results for $CaWO_4$ and PANI-$CaWO_4$ composite

Sample	Major peaks (hkl)	2θ (degree)	FWHM (degree)	d (Å)	Average crystallite size (nm)
CaWO₄ (**C₃**)	(101)	18.88	0.182	4.71	
	(112)	28.99	0.183	3.08	39.67
	(204)	47.32	0.223	1.92	
	(312)	58.09	0.278	1.59	
PANI-CaWO₄ composite	(101)	18.49	0.219	4.79	
	(112)	28.53	0.225	3.13	35.24
	(204)	46.85	0.253	1.94	
	(312)	57.63	0.311	1.60	

5.4.2.2 *XRD study of electron beam irradiated PANI-CaWO₄*

Fig. 5.22 shows the XRD patterns obtained for unirradiated (0 kGy) and electron beam irradiated (4 and 8 kGy) PANI-$CaWO_4$ nanocomposite. The major peaks obtained are labelled. It is interesting to find that the intensity of PANI peaks is more visible for the electron beam irradiated samples. This indicates improvement in the conjugation length for delocalizing the π- electrons. So an improvement in the electrical conductivity for the electron beam irradiated samples of polyaniline composites can be predicted.
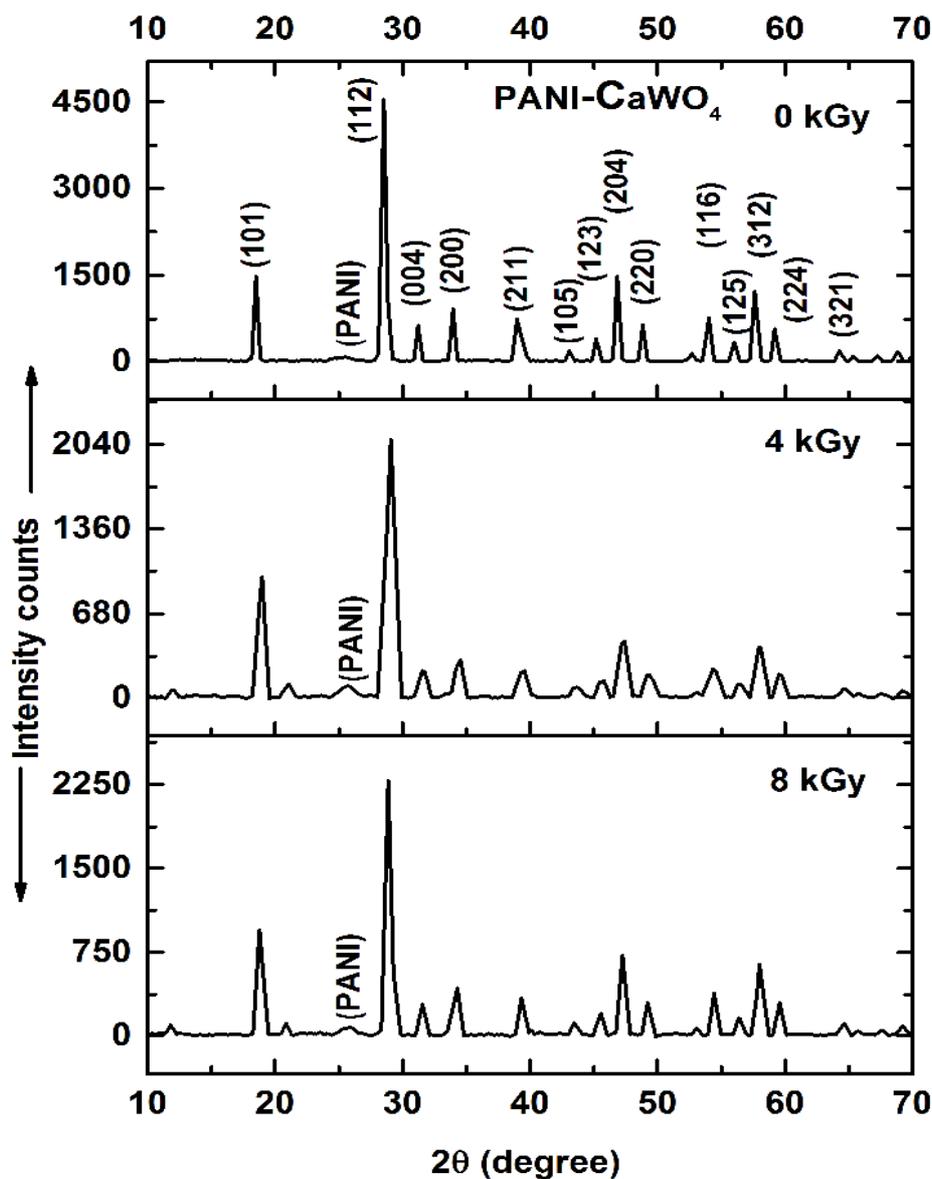
Fig. 5.22 XRD patterns of unirradiated and electron beam
irradiated PANI-CaWO$_4$ nanocomposite

The major peaks of CaWO$_4$ (**C$_3$**), their 2θ values, FWHM and d spacing, before and after the composite formation with polyaniline, are given in the Table 5.5. The average crystallite sizes estimated are 35.24, 13.19 and 20.77 nm for samples irradiated with electron doses of 0, 4 and 8 kGy, respectively.

Table 5.5 XRD results for bare and electron irradiated PANI-CaWO$_4$ samples

Sample	Major peaks (hkl)	2θ (degree)	FWHM (degree)	d (Å)	Average crystallite size (nm)
PANI-CaWO$_4$ (0 kGy)	(101)	18.49	0.219	4.79	
	(112)	28.53	0.225	3.13	35.24
	(204)	46.85	0.253	1.94	
	(312)	57.63	0.311	1.60	
PANI-CaWO$_4$ (4 kGy)	(101)	18.96	0.542	4.69	
	(112)	29.08	0.651	3.07	13.19
	(204)	47.38	0.670	1.92	
	(312)	57.96	0.726	1.59	
PANI-CaWO$_4$ (8 kGy)	(101)	18.78	0.379	4.72	
	(112)	28.88	0.429	3.13	20.77
	(204)	47.23	0.391	1.92	
	(312)	58.00	0.424	1.59	

Though electron beam irradiation produces defects, it brings about more order in the PANI matrix. But the intensities of the CaWO$_4$ peaks become greatly reduced. The reason attributes to the size reduction as well as the formation of thin PANI layers over CaWO$_4$ particles. This observation is supported by similar results reported in other polyaniline composites [32]. The large reduction in crystallite size of the composite after electron irradiation can result in changes in material properties.

5.4.3 FTIR spectroscopy

5.4.3.1 *FTIR analysis of PANI-CAWO₄ nanocomposite*

Fig. 5.23 shows the FTIR spectra of PANI, $CaWO_4$ and $PANI-CaWO_4$ nanocomposite. The FTIR absorption modes are discussed in section 5.2.3.1. The characteristic N-H stretching frequencies are found to centre on 3348 cm^{-1}. The chemical bonds responsible for the absorption peaks related to $CaWO_4$ have been discussed in the section 4.4.1. The broad peak at 812 cm^{-1} in the IR spectrum for $CaWO_4$ becomes sharp in the composite. The peak at 448 cm^{-1} got shifted to 492 cm^{-1} in the composite. Another change observed is the shift of peak at 1141 cm^{-1} in PANI-ES to 1101 cm^{-1}.
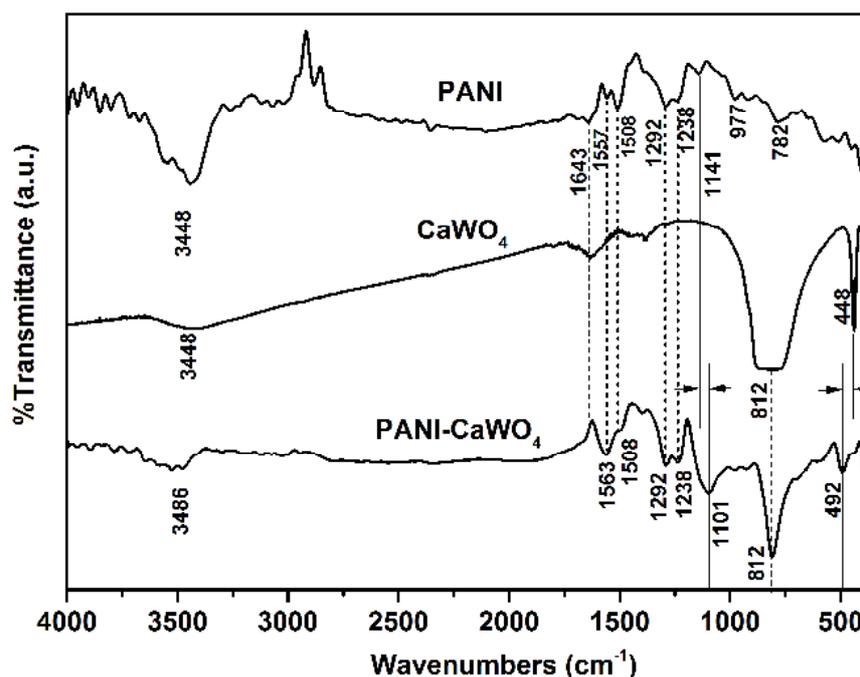
Fig. 5.23 FTIR spectra of PANI-ES, $CaWO_4$ and PANI- $CaWO_4$ nanocomposite

The anti-symmetric stretching vibration of the $[WO_4]$ and the bending vibration of W-O bond in $CaWO_4$ are modified due to interaction with PANI. The quinoid and benzenoid ring stretching vibrations at 1643,

1557 cm $^{-1}$ are also affected by the presence of $CaWO_4$ in the composite. All other major bands observed in PANI appear in the composite product also. These observations confirm the formation of the PANI-$CaWO_4$ nanocomposite.

5.4.3.2 *FTIR analysis of electron beam irradiated PANI-CAWO$_4$*

FTIR spectra of unirradiated, and electron beam irradiated (4 and 8 kGy) PANI-$CaWO_4$ nanocomposite are shown in the Fig. 5.24. The prominent absorption bands found in the PANI-$CaWO_4$ composite are retained in the irradiated samples. Two new feeble absorption bands are found at 676 and 602 cm $^{-1}$ in the electron irradiated samples. Thus the interaction between the metal ions with PANI-ES introduces new vibrations in the [WO$_4$] stretching vibrations.
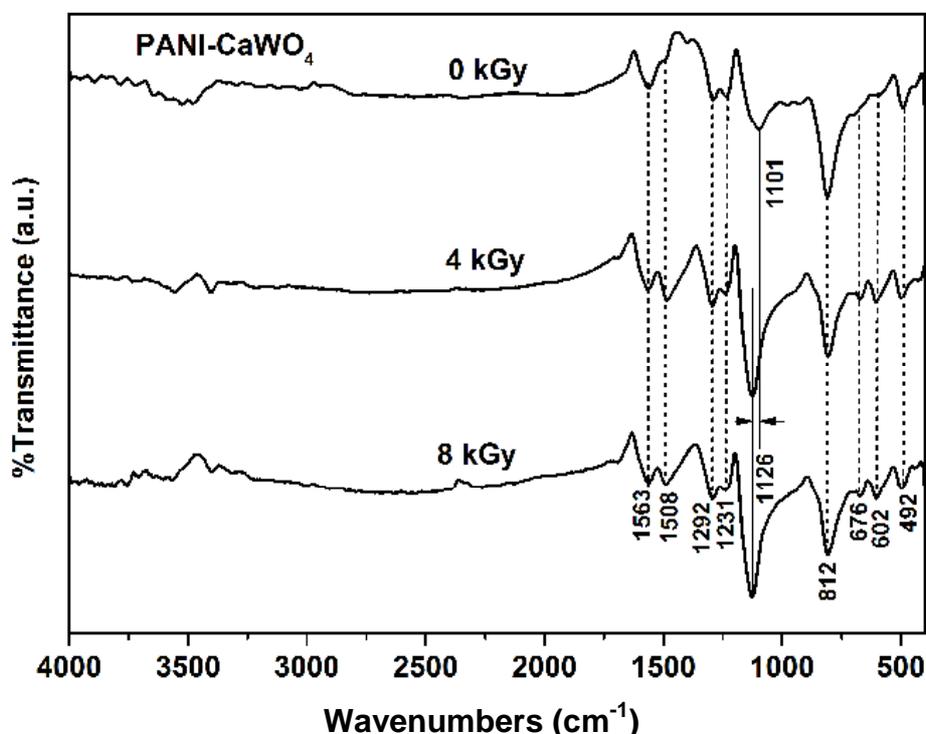
Fig. 5.24 FTIR spectra of unirradiated and electron beam irradiated PANI-$CaWO_4$

The band at 1101 cm^{-1} shifts to 1125 cm^{-1} in the irradiated samples. This shift is due to the Vander Waal's interaction between CaWO$_4$ and polyaniline chain similar to literature report on polyaniline/CdO nanocomposite [22]. In this case the absorption is stronger and hence, an increase in the charge delocalization is expected. The FTIR analysis of the composite shows no degradation due to electron beam irradiation.

5.4.4 Electron microscopy

The morphology, size and shapes of the composite are studied using FE-SEM and TEM analysis.

5.4.4.1 *FE-SEM analysis of PANI-CaWO$_4$ nanocomposite*

The FE-SEM image for PANI-CaWO$_4$ is shown in the Fig. 5.25. Irregular and regular shaped structures are seen in the FE-SEM images. Rod shaped structure of different diameters is seen in the image. CaWO$_4$ nanoparticles embedded in the polymer matrix are also visible in the figure.
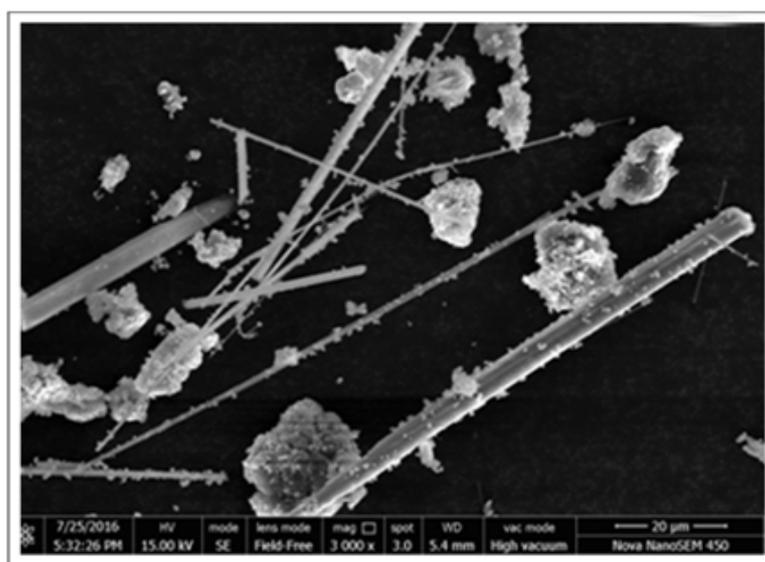
Fig. 5.25 FE-SEM image of PANI-CaWO$_4$ nanocomposite

5.4.4.2 *Compositional analysis of PANI-CaWO$_4$ nanocomposite*

The EDS spectrum obtained is shown in Fig. 5.26. The elements detected in the PANI-CaWO$_4$ nanocomposite are carbon, oxygen, nitrogen, calcium, tungsten and chlorine. Hydrogen being a light element is not detected in the EDS analysis. But, its presence can be confirmed from the presence of different hydrogen containing functional groups in the FTIR spectrum. The EDS data is presented in Table 5.6.
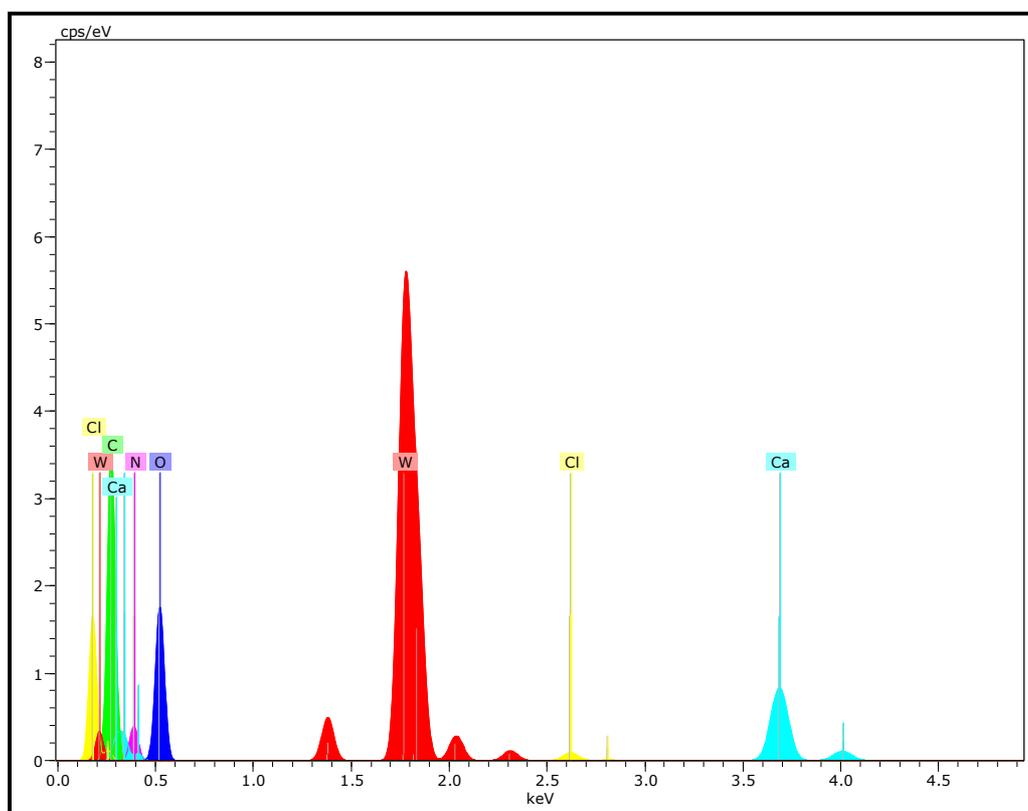
Fig. 5.26 EDS spectrum of PANI-CaWO$_4$ nanocomposite

Table 5.6 The EDS data of PANI-CaWO$_4$

Element	Series	Mass%	Atom%
C	K	22.28	58.54
O	K	9.80	19.34
N	K	4.02	9.05
Ca	K	3.16	2.49
W	L	60.53	10.39
Cl	K	0.21	0.19
Total		100	100

5.4.4.3 *TEM analysis of PANI-CaWO$_4$ nanocomposite*

The TEM images of PANI-CaWO$_4$ composite are shown in Fig. 5.27. Figures (a) and (b) are images showing two different magnifications. They show beads like PANI-ES entangled around CaWO$_4$ nanoparticles. The HRTEM image (Fig. 5.27 (c)) shows crystalline as well as amorphous regions. The boundary between these regions is called interfacial region which plays important role in interpreting the dielectric properties. The Fig. 5.27 (d) shows SAED pattern of the composite.
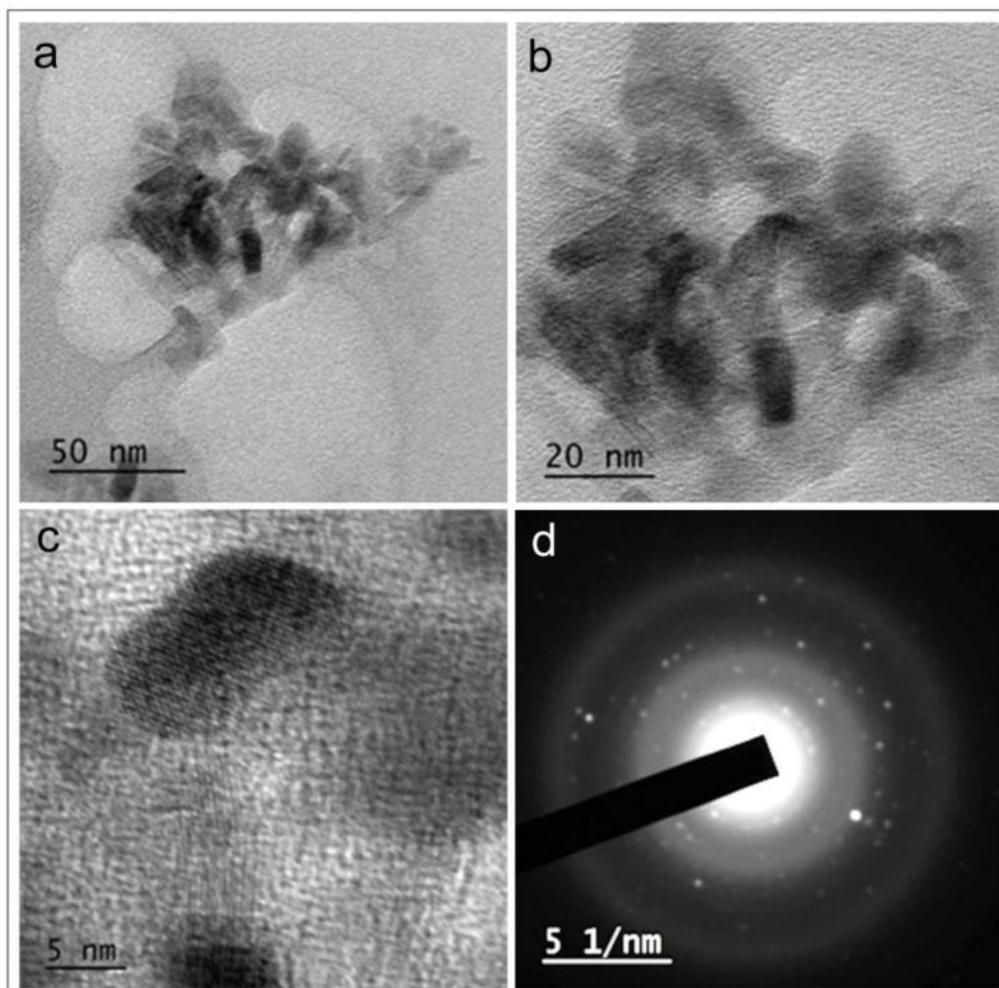
Fig. 5.27 TEM images of PANI-CaWO$_4$ nanocomposite

5.4.5 UV-Visible spectroscopy

5.4.5.1 *UV-Visible spectroscopy of PANI-CaWO$_4$composite*

UV-Visible absorption spectra of HCl doped PANI and PANI-CaWO$_4$ nanocomposite are shown in Fig. 5.28 (a). PANI has two absorption peaks. These absorption peaks are formed at 372 and 648 nm in the UV-Visible spectrum for PANI. In the composite the corresponding peaks are formed at 430 and 685 nm, respectively. Also the absorbance is found to be lower for

the composite. The absorbance spectra in Fig. 28 (a) show that both PANI and its composite are good absorbers of UV-Visible radiations [14].
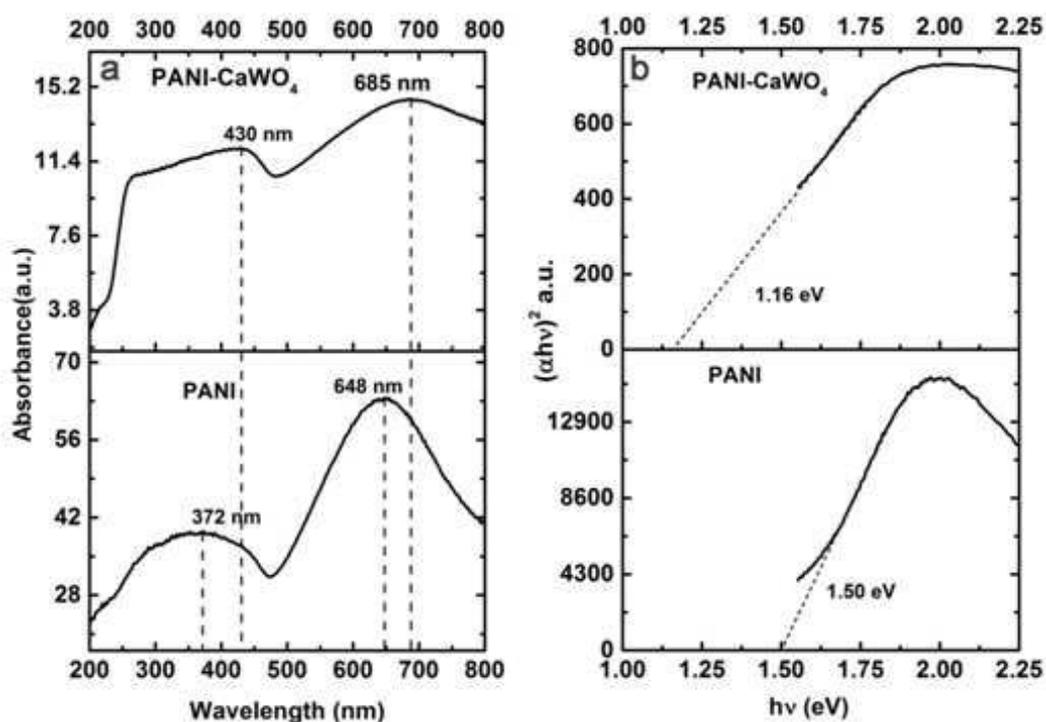
Fig. 5.28 (a) UV-Visible spectra and (b) Tauc plots of PANI and

PANI-CaWO₄

The Tauc plots for PANI and PANI-CaWO₄ are shown in Fig. 5.28 (b). The bandgaps obtained are 1.50 and 1.16 eV for PANI and PANI-CaWO₄, respectively.

5.4.5.2 *UV-Visible spectroscopy of irradiated PANI-CaWO₄*

UV-Visible absorption spectra of bare (0 kGy) and irradiated (4and 8 kGy) composites are shown in Fig. 5.29. In the samples irradiated with 4 kGy, the absorption peaks are centred on 412 and 677 nm. But for the sample irradiated with 8 kGy, the absorption peaks are shifted to 410 and

680 nm, respectively. These shifts in peaks occur due to the variation in the interaction of CaWO$_4$ with PANI in the composite due to the crystallite size variation of CaWO$_4$ upon electron irradiation. The intensity of absorption first increases with 4 kGy dose, but shows a slight decrease for 8 kGy dose. This might be due to ordering of PANI-chains at lower electron doses after chain scission.
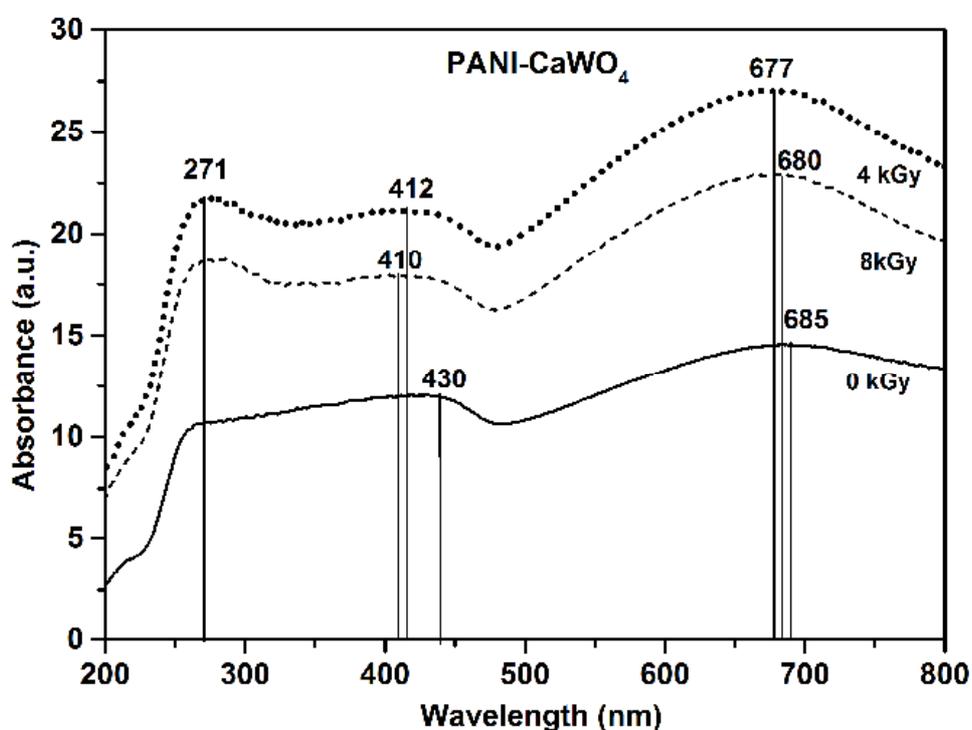
Fig. 5.29 UV-Visible spectra of the bare and irradiated PANI-CaWO$_4$

The bandgaps determined from the Tauc plot in Fig. 5.30 are 1.16, 1.29 and 1.28 eV respectively for the 0, 4 and 8 kGy irradiated samples. These values are less than the bandgap for the doped PANI. This indicates changes within the highest occupied molecular orbital (HOMO) and lowest unoccupied molecular orbital (LUMO) bands as a result of composite formation. These facts confirm the interaction between PANI and CaWO$_4$

nanoparticles. Also an additional peak appears in the electron irradiated samples centred on 271 nm, which corresponds to the absorption due to $CaWO_4$ nanoparticles as a result of irradiation damages.
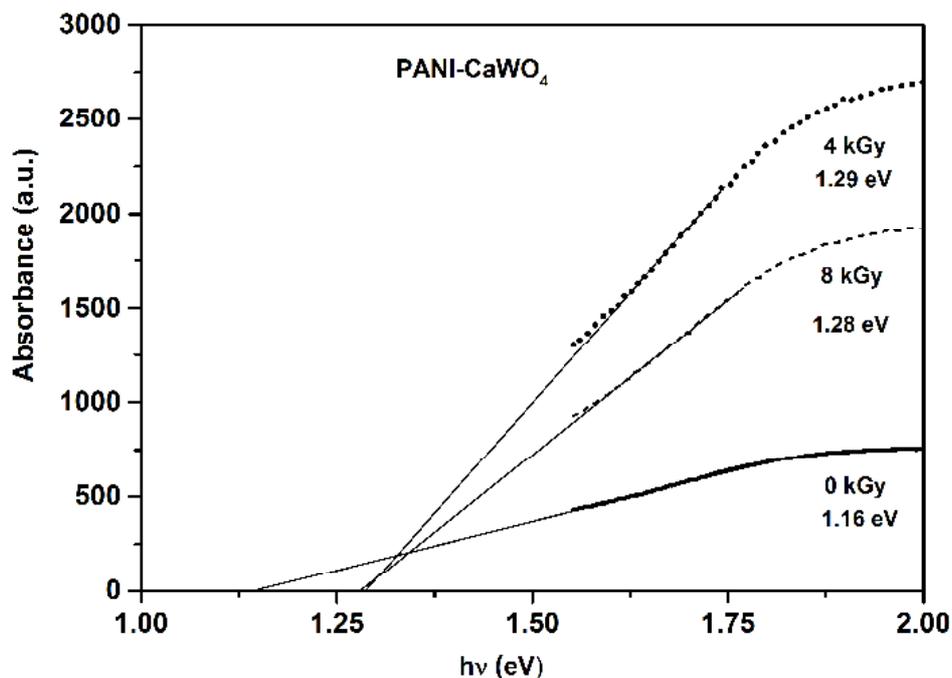
Fig. 5.30 Tauc plots of the unirradiated and irradiated

PANI-CaWO$_4$ samples

The appearance of a bump in the first absorption peak indicates that the UV absorbance increases upon irradiation. These observations strengthen the formation of new polaron bands. It is found that in PANI-CaWO$_4$ composite the bandgap decreased to 1.16 eV compare to the bandgap of 1.50 eV of PANI-ES. The decrease in the optical bandgap in the present system may be due to reduction in the disorder of the system and increase in the density of defect states [35]. Though $CaWO_4$ is a wide-bandgap semiconductor, the small bandgap obtained for PANI-CaWO$_4$ attributes to the formation of PANI films over $CaWO_4$ nanoparticles.

5.5 Electrical properties

5.5.1 DC conductivity of PANI-CaWO$_4$ composite

The variations in DC conductivity of PANI-ES, 0, 4 and 8 kGy irradiated PANI-CaWO$_4$ nanocomposite with temperature are plotted in the Fig. 5.31. At 303 K, the DC conductivity values are 0.00042, 0.0015, 0.0016 and 0.0015 S-cm^{-1} for the PANI-ES, 0, 4 and 8 kGy irradiated PANI-CaWO$_4$ nanocomposite, respectively. At 443 K, the corresponding values of DC conductivity become 0.0012, 0.0032, 0.0036 and 0.0035 S-cm^{-1}, respectively. The DC conductivity is higher in the composite samples than in pure PANI-ES. The mechanism of conduction in PANI-CaWO$_4$ nanocomposite is similar to that for PANI-MnWO$_4$, as discussed in section 5.3.1. In the 4 kGy electron beam irradiated sample, the values of DC conductivity are slightly elevated.
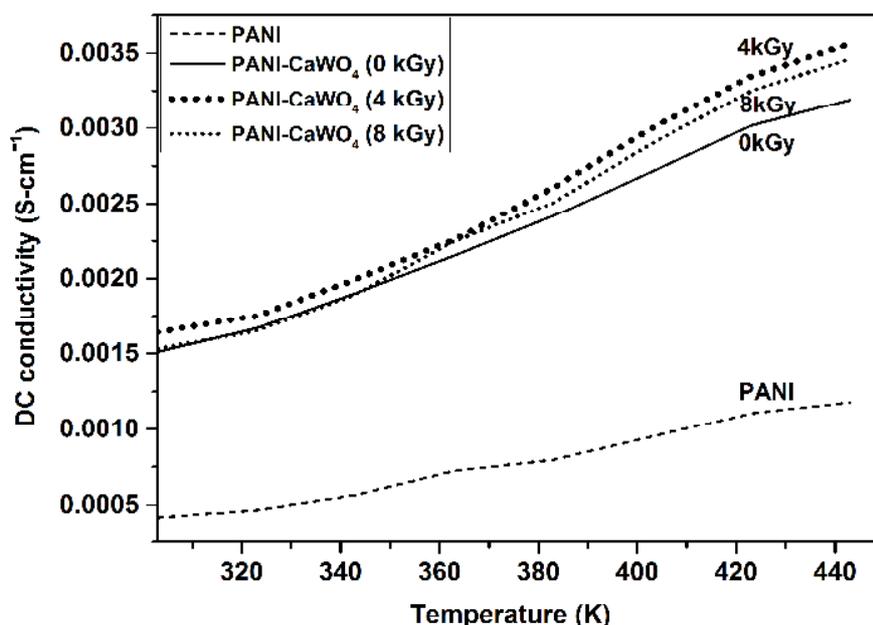
Fig. 5.31 Variation in DC conductivity with temperature of PANI-ES, PANI-CaWO$_4$ and 4 kGy irradiated PANI-CaWO$_4$

The presence of $CaWO_4$ causes increased delocalization length that is reflected in the improved DC conductivity in the composite. Similar observation in other PANI composite supports this observation [49]. The Fig. 5.31 shows that the DC conductivity increases with temperature, which confirms semiconducting nature of the composite sample.

5.5.2 AC electrical studies

5.5.2.1 *Dielectric studies of PANI-CaWO₄ nanocomposite*

Dielectric constant

The variation of dielectric constant of 0, 4 and 8 kGy electron beam irradiated PANI-$CaWO_4$ samples as a function of frequency is shown in the Fig. 5.32. The values of dielectric constant at 100 Hz are 27838, 28974 and 22168 for the 0, 4 and 8 kGy irradiated samples. At 1MHz, the respective values are 122, 153 and 121. All samples show similar type of variation in dielectric constant. Initially at lower frequencies the value of dielectric constant is very high. It decreases with increasing frequencies showing dielectric relaxation. Interfacial polarisation contributes to the unusually high values of dielectric constant. Besides interfacial polarization, the compound exhibits different types of polarizations (dipolar, atomic, ionic, electronic etc.) which contribute to decrease in dielectric constant with increase in AC frequency [50]. The overall behaviour is a dielectric relaxation.
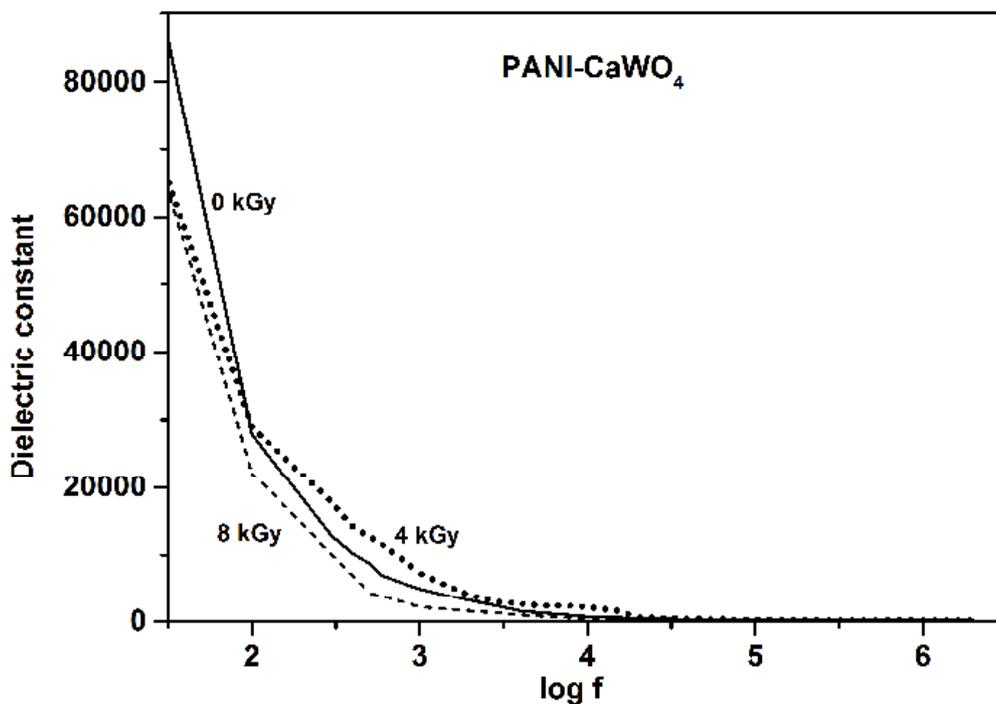
Fig. 5.32 Variation of dielectric constant with frequency of electron beam

irradiated PANI-CaWO$_4$ samples

Dielectric loss

Fig. 5.33 presents the variation of Tan δ with log f for PANI-CaWO$_4$ samples irradiated with 0, 4 and 8 kGy electron doses. The values of Tan δ at 100 Hz are 8.63, 8.4 and 6.73 for samples irradiated with 0, 4 and 8 kGy doses, respectively. The loss tangent is high at lower frequencies and decreases with increase in frequency. Besides, loss tangent shows a slight decrease with increase in electron dose.
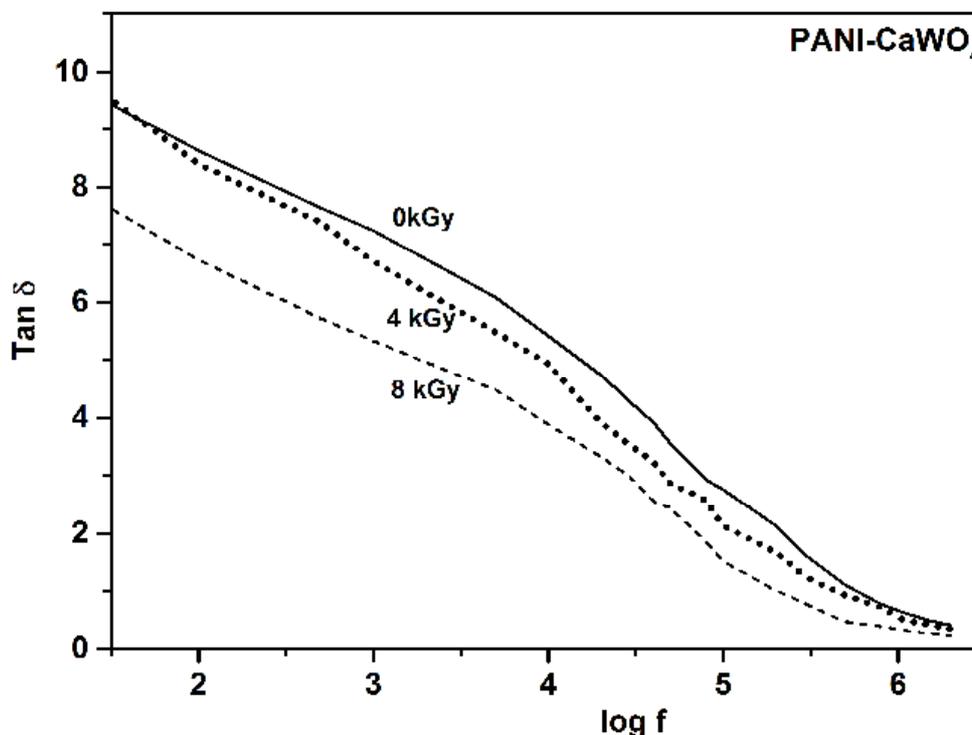
Fig. 5.33 Variation in the loss tangent with log f of the

electron irradiated PANI-CaWO$_4$ samples

The large dielectric constant and low dielectric loss composite material is useful for potential applications like micro-actuators and metal oxide semiconductor applications [51].

5.5.2.2 *AC conductivity studies*

The frequency dependence of AC conductivity of 0, 4 and 8 kGy irradiated samples is given in the Fig. 5.34. The values of AC conductivity at 100 Hz are 0.0014, 0.0016 and 0.00050 Scm^{-1} for 0, 4 and 8 kGy irradiated samples, respectively. At 1 MHz, the corresponding values are 0.0044, 0.0044 and 0.0023 Scm^{-1}. The AC conductivity in the irradiated samples is slightly reduced with increase in irradiation dose.
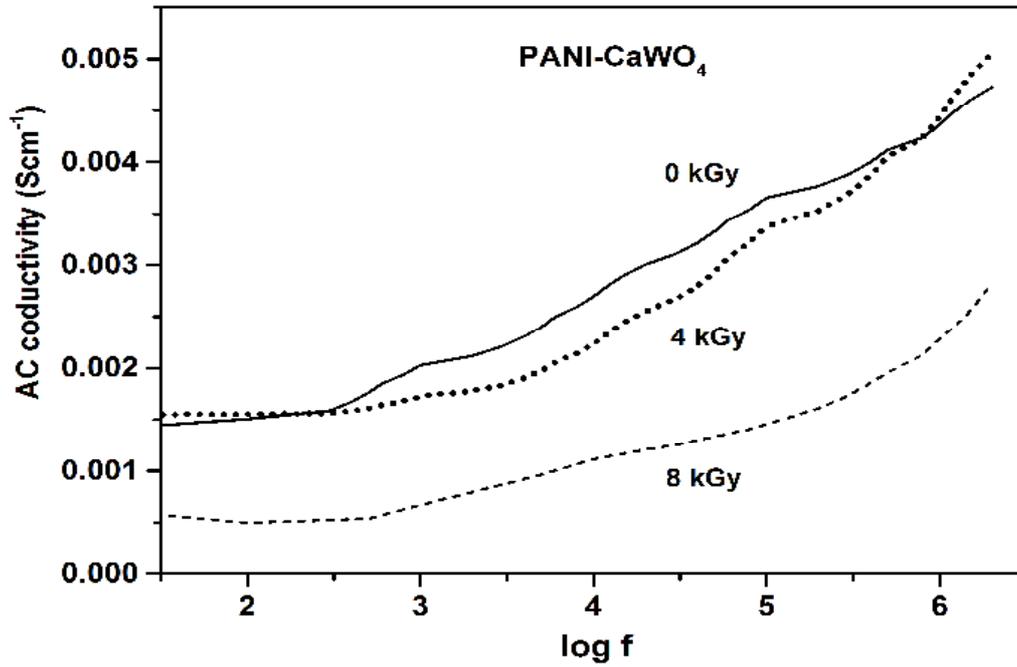
Fig. 5.34 Variation in the AC conductivity of PANI-CaWO$_4$

composite as a function of frequency

Equation	y = a + b*x	
0 kGy	Intercept	-3.14079
	Slope	0.11702
4 kGy	Intercept	-3.21911
	Slope	0.12478
8kGy	Intercept	-3.70113
	Slope	0.15321
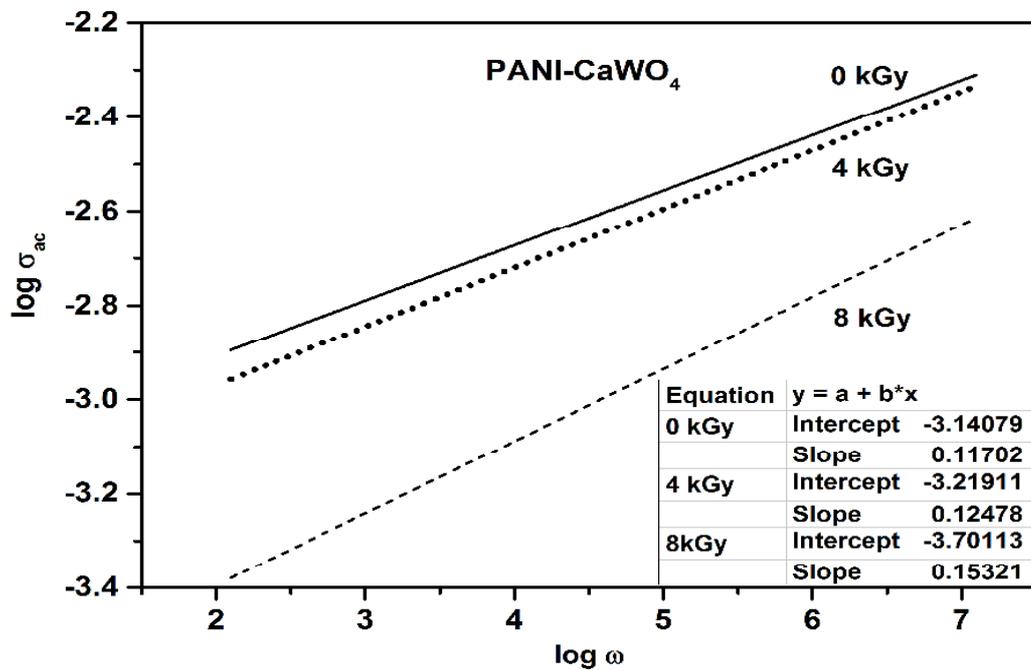
Fig. 5.35 Linear fits of log ω versus log [σ_{ac}] plots

The power law dependence of AC conductivity can be checked using the plot of log ω versus log [σ_{ac}] curve in Fig. 5.35. The values of n obtained from the slopes are 0.12, 0.12 and 0.15 respectively for 0, 4 and 8 kGy irradiated samples. These values lie between 0 and 1, which means conduction is by hopping process.

5.6 Potential applications of PANI-MnWO$_4$ and PANI-CaWO$_4$ nanocomposites-a comparison

Both PANI-MnWO$_4$ and PANI-CaWO$_4$ nanocomposites have high dielectric constants and low loss tangents. This indicates their potential in microwave applications. In the electron beam irradiated sample a 10-fold increase in DC conductivity is measured for PANI-MnWO$_4$. This shows its potential for the use in applications like antistatic coatings and electromagnetic interference shielding. PANI-MnWO$_4$ is thermally more stable compared to PANI-CaWO$_4$ nanocomposite.

5.7 Conclusion

➢ Polyaniline composites of MnWO$_4$ and CaWO$_4$ are readily synthesized by *in situ* chemical oxidative polymerization of aniline monomer.

➢ TGA/DTA analysis shows that PANI-ES composites of tungstates are not thermally stable above 250 ℃. Above 250 ℃, de-protonation followed by decomposition of PANI occurs. However, thermal analysis shows evidence for some cross-linking of PANI chains in the composite centred on 425 ℃.

➢ XRD studies confirm the presence of local crystalline centres of PANI in PANI-MnWO$_4$/CaWO$_4$ composites. The average crystallite size of PANI-MnWO$_4$/CaWO$_4$ composites is lower compared to the crystallite size of the nanocrystalline MnWO$_4$/CaWO$_4$ before the composite formation. Electron beam irradiation of PANI-MnWO$_4$ shows crystallite size reduction with increasing electron doses. In PANI-CaWO$_4$, the crystallite size first decreases and then increases with increase in electron dose.

➢ All chemical bonds present in PANI-ES and MnWO$_4$/CaWO$_4$ are revealed in the FTIR studies of PANI-MnWO$_4$/CaWO$_4$ composites. Moreover slight changes in certain peak positions confirm interaction between PANI and tungstates in the composites. The FTIR spectrum shows a new weak absorption peak centred on 1066 cm^{-1} in PANI-MnWO$_4$. In the electron irradiated PANI-MnWO$_4$ sample this peak shifts to 1107 cm^{-1}. A similar event is observed in PANI-CaWO$_4$ composite at 1101 cm^{-1}and the peak shifts to 1126 cm^{-1}in the electron irradiated samples. The shift in peak positions is due to the cross linking and charge delocalization in PANI.

➢ Fibre clew-like morphology is seen in the SEM images of PANI-ES and PANI-MnWO$_4$ composites. Very long rod shaped structures along with irregular shaped clusters are seen in the SEM images of PANI-CaWO$_4$ composite. Magnified FE-SEM shows an average diameter of the fibres less than 100 nm. The EDS analysis confirms the presence

of all elements those are expected in the PANI-MnWO$_4$/CaWO$_4$ composites.

➤ TEM images show bead shaped PANI connected together as a long chain. The presence of crystalline centres in PANI is visible from the HRTEM images. Crystallinity of PANI is also supported by the SAED pattern obtained. TEM images of PANI-MnWO$_4$/CaWO$_4$ composites contained nanostructures of different shapes with a majority of PANI fibres.

➤ UV-Visible absorption studies reveal two absorption centres in PANI-MnWO$_4$/CaWO$_4$ composites which correspond to π-π* electronic transition and the inter band charge transfer associated with excitation of the benzenoid to the quinoid moieties. The first absorption peak centres on 340 nm and the second one on 665 nm in PANI-MnWO$_4$. The corresponding peaks in the case of PANI-CaWO$_4$ are seen centred at 430 and 685 nm, respectively. These peak positions are shifted from those of PANI differently due to the difference in the interaction between PANI and the two tungstates. The optical bandgap of PANI-ES is found to be 1.5 eV and it decreased to 1.48 and 1.16 eV in PANI-MnWO$_4$ and PANI-CaWO$_4$ composites, respectively. It is interesting that a decrease in the bandgap of PANI occurs upon composite formation. However, electron beam irradiated samples show only a slight variation in the bandgap.

➤ The DC conductivity of both PANI-MnWO$_4$ and PANI-CaWO$_4$ nanocomposite varies in the range of 10^{-4} to 10^{-3} Scm^{-1} as the

temperature is raised from the room temperature to about 450 K. DC conductivity of PANI increases upon composite formation. This might be due to the positive synergistic effect between the polymer and the tungstates that improves the polaron hopping. In the electron beam irradiated sample a 10-fold increase in DC conductivity is measured for PANI-MnWO$_4$. This shows its potential for the use in applications like antistatic coatings and electromagnetic interference shielding. PANI-CaWO$_4$ exhibits only a slight increase in DC conductivity in the irradiated samples.

➤ In PANI-MnWO$_4$/CaWO$_4$ composites slight and random variations in dielectric constant and loss tangent are seen after electron beam irradiation. But high dielectric constant and low loss tangents in these materials indicate their potential in microwave applications. AC studies show that both the composites obeyed the power law and that the conduction is due to polaron hopping.

References

1   I. Y. Sapurina and M. A. Shishov, *Oxidative Polymerization of Aniline: Molecular Synthesis of Polyaniline and the Formation of Supramolecular Structures*. (2012).

2   A. G. MacDiarmid, Angewandte Chemie International Edition **40** (14), 2581 (2001).

3   J. P. Pouget, M. E. Jozefowicz, A. J. Epstein, X. Tang, and A. G. MacDiarmid, Macromolecules **24** (3), 779 (1991).

4   M. M. Nobrega, C. H. Silva, V. R. Constantino, and M. L. Temperini, The journal of physical chemistry. B **116** (48), 14191 (2012).

5   J. Yue, A. J. Epstein, Z. Zhong, P. K. Gallagher, and A. G. Macdiarmid, Synthetic Metals **41** (1), 765 (1991).

6   Y. Wei and K. F. Hsueh, Journal of Polymer Science Part A: Polymer Chemistry **27** (13), 4351 (1989).

7   S. Bhadra and D. Khastgir, Polymer Degradation and Stability **93** (6), 1094 (2008).

8   A. N. Begum, N. Dhachanamoorthi, M. E. Saravanan, P. Jayamurugan, D. Manoharan, and V. Ponnuswamy, Optik **124** (3), 238 (2013).

9   R. Mathew, D. Yang, B. R. Mattes, and M. P. Espe, Macromolecules **35** (20), 7575 (2002).

10   L. Ding, X. Wang, and R. V. Gregory, Synthetic Metals **104** (2), 73 (1999).

11   S. Cho, M. Kim, J. S. Lee, and J. Jang, ACS applied materials & interfaces **7** (40), 22301 (2015).

12   K. Lee, S. Cho, S. Heum Park, A. J. Heeger, C.-W. Lee, and S.-H. Lee, Nature **441** (7089), 65 (2006).

13   S. Banerjee, S. Sarmah, and A. Kumar, Journal of Optics **38** (2), 124 (2009).

14   N. Aloysius Sabu, X. Francis, J. Anjaly, S. Sankararaman, and T. Varghese, The European Physical Journal Plus **132** (6), 290 (2017).

15   B. Prasanna, D. Avadhani, and H. Muralidhara, (2014).

16   I. C. Amaechi, A. C. Nwanya, A. B. C. Ekwealor, P. U. Asogwa, R. U. Osuji, M. Maaza, and F. I. Ezema, Eur. Phys. J. Appl. Phys. **69** (3), 30901 (2015).

17   F. Muhammad and K. Syed, Bulletin of the Korean Chemical Society **34** (1), 99 (2013).

18   N. Joseph, J. Varghese, and M. T. Sebastian, RSC Adv. **5** (26), 20459 (2015).

19   J.-C. Chiang and A. G. MacDiarmid, Synthetic Metals **13** (1), 193 (1986).

20   E. A. Sanches, J. M. S. da Silva, J. M. de O. Ferreira, J. C. Soares, A. L. dos Santos, G. Trovati, E. G. R. Fernandes, and Y. P. Mascarenhas, Journal of Molecular Structure **1074**, 732 (2014).

21   M. Trchová, I. Šeděnková, E. Tobolková, and J. Stejskal, Polymer Degradation and Stability **86** (1), 179 (2004).

22   A. S. Roy, K. R. Anilkumar, and M. V. N. Ambika Prasad, Ferroelectrics **413** (1), 279 (2011).

23   W. S. Huang and A. G. MacDiarmid, Polymer **34** (9), 1833 (1993).

24   M. Canales, J. Torras, G. Fabregat, A. Meneguzzi, and C. Alemán, The Journal of Physical Chemistry B **118** (39), 11552 (2014).

25   K. Deb, A. Bera, and B. Saha, RSC Advances **6** (97), 94795 (2016).

26   O. Kwon and M. L. McKee, The Journal of Physical Chemistry B **104** (8), 1686 (2000).

27   R. P. McCall, J. M. Ginder, J. M. Leng, H. J. Ye, S. K. Manohar, J. G. Masters, G. E. Asturias, A. G. MacDiarmid, and A. J. Epstein, Physical Review B **41** (8), 5202 (1990).

28   S. Stafström, J. L. Brédas, A. J. Epstein, H. S. Woo, D. B. Tanner, W. S. Huang, and A. G. MacDiarmid, Physical review letters **59** (13), 1464 (1987).

29   K. C. Sajjan, A. S. Roy, A. Parveen, and S. Khasim, Journal of Materials Science: Materials in Electronics **25** (3), 1237 (2014).

30   P. Ghosh, A. Sarkar, A. K. Meikap, S. K. Chattopadhyay, S. K. Chatterjee, and M. Ghosh, Journal of Physics D: Applied Physics **39** (14), 3047 (2006).

31   R. M. Hill and A. K. Jonscher, Journal of Non-Crystalline Solids **32** (1–3), 53 (1979).

32   M. O. Ansari, M. M. Khan, S. A. Ansari, and M. H. Cho, New J. Chem. **39** (11), 8381 (2015).

33   J. R. Laghari and A. N. Hammoud, IEEE Transactions on Nuclear Science **37** (2), 1076 (1990).

34   U. A. Sevil, O. Güven, A. Kovács, and I. Slezsák, Radiation Physics and Chemistry **67** (3–4), 575 (2003).

35   S. M. Reda and S. M. Al-Ghannam, Advances in Materials Physics and Chemistry **02** (02), 75 (2012).

36   Shumaila, G. B. V. S. Lakshmi, M. Alam, A. M. Siddiqui, M. Zulfequar, and M. Husain, Current Applied Physics **11** (2), 217 (2011).

37   A. K. Jonscher, *Dielectric Relaxation in Solids*. (Chelsea Dielectric Press, London, 1983).

38   A. K. Himanshu, R. Ray, S. El-Sayed, A. Hassen, S. K. Bandyopadhayay, and T. P. Sinha, Radiation Effects and Defects in Solids **169** (1), 73 (2013).

39   D. Mezdour, M. Tabellout, J. F. Bardeau, and S. Sahli, presented at the 2014 North African Workshop on Dielectic Materials for Photovoltaic Systems (NAWDMPV), 2014 (unpublished).

40   D. D. Chung, *Composite materials: science and applications*. (Springer Science & Business Media, 2010).

41   S. Tiptipakorn, P. Suwanmala, K. Hemvichian, and Y. Pornputtanakul, Advanced Materials Research **550-553**, 861 (2012).

42   J. Bhadra, N. J. Al-Thani, N. K. Madi, and M. A. Al-Maadeed, Arabian Journal of Chemistry (2015).

43   Y. Katsumi, H. Shigenori, and I. Yoshio, Japanese Journal of Applied Physics **21** (9A), L569 (1982).

44   A. Shakoor, T. Z. Rizvi, and A. Nawaz, Journal of Materials Science: Materials in Electronics **22** (8), 1076 (2011).

45   Y. T. Ravikiran, M. T. Lagare, M. Sairam, N. N. Mallikarjuna, B. Sreedhar, S. Manohar, A. G. MacDiarmid, and T. M. Aminabhavi, Synthetic Metals **156** (16–17), 1139 (2006).

46   B. M. Greenhoe, M. K. Hassan, J. S. Wiggins, and K. A. Mauritz, Journal of Polymer Science Part B: Polymer Physics **54** (19), 1918 (2016).

47   H. S. O. Chan, P. K. H. Ho, E. Khor, M. M. Tan, K. L. Tan, B. T. G. Tan, and Y. K. Lim, Synthetic Metals **31** (1), 95 (1989).

48   Z. Durmus, A. Baykal, H. Kavas, and H. Sözeri, Physica B: Condensed Matter **406** (5), 1114 (2011).

49   X. Lu, W. Zhang, C. Wang, T.-C. Wen, and Y. Wei, Progress in Polymer Science **36** (5), 671 (2011).

50   R. N. P. Choudhary, R. Palai, and S. Sharma, Journal of Materials Science: Materials in Electronics **11** (9), 685 (2000).

51   D. Ashis, D. Sukanta, D. Amitabha, and S. K. De, Nanotechnology **15** (9), 1277 (2004).

****൧✪ൽ****

Chapter - 6
SUMMARY

The main objective of the present investigation, as brought out in section 1.3, is to synthesize and characterize nanophase $MnWO_4$, $CaWO_4$ and their polyaniline composites (PANI-$MnWO_4$/$CaWO_4$). Nanocrystalline $MnWO_4$ and $CaWO_4$ are synthesized using simple chemical precipitation method and are characterized using various tools as mentioned in Chapter 2. The structural, optical and electrical characterizations of the synthesized nanocrystalline $MnWO_4$ and $CaWO_4$ before and after electron beam irradiation are presented in Chapter 3 and 4 respectively. Polyaniline composites of $MnWO_4$ and $CaWO_4$ are synthesized by *in situ* chemical oxidative polymerization of aniline and their properties are investigated using structural, optical and electrical characterization techniques. The synthesis method and characterization results along with discussion are presented in Chapter 5.

A summary of the synthesis, characterization and the effect of electron beam irradiation in nanocrystalline $MnWO_4$, $CaWO_4$ and their polyaniline composites (PANI-$MnWO_4$/$CaWO_4$) are presented in the current chapter.

The important outcomes, promising applications of the materials synthesized and the outlook of the research work are mentioned as closing remarks of this chapter.

6.1 Summary of research

Nanocrystalline $MnWO_4$ in the powder form is successfully prepared by simple chemical precipitation method. TGA/DTA analysis shows that the material is thermally stable in the temperature range 390-850 °C. XRD analysis confirms the monoclinic wolframite structure. The crystallite size is found to increase with increase in the calcination temperature which results in slight lattice contraction. The electron beam irradiated samples exhibit a decrease in crystallite size with lattice expansion. FTIR studies further confirm the formation of $MnWO_4$. Careful observation reveals eighteen Raman modes in the range 100 to 1200 cm^{-1}. The electron beam irradiation results in the broadening and slight blue shift of the Raman peaks. SEM analysis shows that the particles are aggregated to form micro-clusters and do not reveal any regular shape for the particles or clusters. There is more aggregation of particles due to electron beam irradiation. The EDS analysis confirms the presence of all the elements expected for $MnWO_4$. Bar-shaped morphology for the particles with a width of ~78 nm is found in TEM images.

The UV-Visible absorption maximum for the synthesized $MnWO_4$ nanoparticle is found to be in the ultraviolet region. Calculations show a bandgap of 2.63 eV for the sample calcined at 450 °C. In $MnWO_4$

nanoparticles, a slight decrease in bandgap is observed with the increase in calcination temperature. In the electron beam irradiated samples, increase in absorbance and bandgap is observed. Electron beam irradiated samples show slightly enhanced PL emission due to the creation of new defect states. These observations indicate its potential for photocatalytic applications.

Thermally activated polaronic DC conductivity is observed in both unirradiated and irradiated samples of $MnWO_4$. A ten-fold increase in DC conductivity in the electron irradiated sample is confirmed. AC studies show that the values of dielectric constant and loss tangent increase with the increase in temperature. The values decrease with the increase in grain size at lower frequencies. AC conductivity increases with the increase in frequency in accordance with the Jonscher's universal power law. The frequency independent part of the observed AC conductivity is lower in samples calcined at higher temperatures. But this DC component is elevated as the measurement temperature is increased. Compared to unirradiated sample the values of dielectric constant, tangent loss and AC conductivity are enhanced in the irradiated $MnWO_4$ samples. In brief, the optical and electrical properties of the $MnWO_4$ nanoparticles synthesized in this work can be tuned using calcination and electron beam irradiation. The $MnWO_4$ particles tailored in this manner have the potential for photocatalysis and to sense humidity.

Nanocrystalline $CaWO_4$ is synthesized by simple chemical precipitation. White powder form of the final product is found to be very

stable in the temperature range from 350 to 850 °C. XRD studies confirm the tetragonal scheelite structure of $CaWO_4$. Unlike $MnWO_4$, a lattice expansion is observed in this structure on increasing the calcination temperature. The average crystallite size also increases in the samples calcined at higher temperatures. But, the crystallite size first increases and then decreases on increasing the electron dose from 0-8 kGy in steps of 2 kGy. Formation of the various bonds in $CaWO_4$ is confirmed through FTIR spectrum analysis. Out of the 13 Raman bands predicted by theory only 10 peaks are observed in the product. SEM images display dumb-bell shaped nanoclusters. SEM images show that the sample irradiated with 6 kGy is the most affected. Compositional analysis using EDS confirms the presence of all the elements expected for $CaWO_4$. The aggregation of nanoparticles produces a thick contrast in the TEM image. Average size of the particles is ~82 nm.

UV-Visible absorption studies of calcined samples show red shift in the absorption edge because of the reduction in the bandgap due to calcination. A bandgap of 4.12 eV is calculated for $CaWO_4$ nanoparticles calcined at 350 °C. A variation in the bandgap in accordance with particle size variation is also observed in the electron beam irradiated samples. PL peak shifts from 350 to 430 nm as the calcination temperature varies from 350 to 650 °C. The PL intensity also decreases accordingly. Electron beam irradiation of $CaWO_4$ sample produces remarkable changes in its PL properties. PL emission peak in $CaWO_4$ calcined at 350 °C is found to be at ~357 nm in the ultraviolet region. For lower doses (2 to 4 kGy) of electron

beam irradiation, the PL emission in $CaWO_4$ is shifted to longer wavelength at ~430 nm. The emission peak returns to the initial position gradually with further increase in electron dose. These shift in PL emission peaks occur due to variations in the emission centres caused by different electron dose.

In $CaWO_4$, DC electrical conductivity increases exponentially with temperature. The low values of activation energy obtained for the sample support conduction by ionic hopping. The conductivity of the irradiated sample is higher than that of the bare sample. Dielectric study reveals the usual relaxation processes relating to the different types of polarizations. But in the irradiated samples, dielectric constant and losses are elevated at lower frequencies. But the loss is very low at higher frequencies. In nanocrystalline $CaWO_4$, AC conductivity shows power law dependence. In the irradiated sample, an enhanced AC conductivity is observed. In short, the electron beam irradiation in nanocrystalline $CaWO_4$ can modify its structural, optical and electrical properties. Electron beam irradiation creates interesting changes in the PL property of the material. Proper selection of calcination temperature as well as electron dose can produce intense PL emission and it can be tuned for specific applications.

PANI-$MnWO_4$/$CaWO_4$ nanocomposites are synthesized under normal conditions by adding $MnWO_4$/$CaWO_4$ during the *in situ* chemical oxidative polymerization of aniline monomer in the presence of hydrochloric acid using ammonium persulphate (APS) as oxidant. HCl doped form of polymer nanocomposite appears greenish-back. Thermal analysis shows a dedoping of PANI in the temperature range from 250 to 400 °C. But, there

is evidence for the cross-linking of PANI chains centred on 425 ℃. Decomposition of PANI occurs in the temperature range from 450 to 650 ℃ and is maximum at 541.16 ℃. From these observations, it may be concluded that PANI is not thermally stable above 150 ℃. PANI composite is found to be more stable.

XRD analysis of PANI-MnWO$_4$ composites confirms localized crystalline centres (PANI) other than the crystalline regions of tungstates. All major peaks found in the XRD spectrum of MnWO$_4$ are also present in the spectrum of the PANI- MnWO$_4$ composite. Due to the interaction between PANI and tungstate, the XRD peaks in the composite are slightly shifted to lower 2θ values. A further shift in 2θ occurs in the electron beam irradiated samples. Average crystallite size obtained for PANI-MnWO$_4$ is 11.5 nm. A comparison of the FTIR spectra of PANI-ES, MnWO$_4$ and PANI-MnWO$_4$ confirm the formation of the PANI composite. A new absorption peak (FTIR) appears in the electron irradiated sample at 1107 cm^{-1} which is related to cross linking and charge delocalization.

Fibre clew-like morphology is seen in the SEM images of PANI-ES and PANI-MnWO$_4$. Magnified FE-SEM shows an average fibre diameter of ~80 nm. In the EDS analysis of PANI-MnWO$_4$ composite, the elements carbon, oxygen, nitrogen, manganese, tungsten and chlorine are detected. Hydrogen being a very light element is not detected in the EDS. But the presence of hydrogen in the composite is confirmed from the presence of hydrogen containing functional groups in the FTIR spectrum of PANI-MnWO$_4$. TEM images show bead shaped PANI connected together as a

long chain. Semi-crystalline regions in PANI are visible in the HRTEM images. Crystallinity of PANI is also supported by the SAED pattern obtained. TEM images of PANI-MnWO$_4$ composite contain nanostructures of different shapes along with nanofibres.

Two major absorption centres are found in the UV-Visible spectrum of PANI composites with tungstates. In the PANI-ES synthesized, two absorption peaks are observed at 372 and 648 nm. In PANI-MnWO$_4$ composite the first absorption peak is shifted to 340 nm and the second to 665 nm. The shift in the peak positions are due to the interaction between PANI and MnWO$_4$ nanoparticles. The bandgap decreased from 1.50 to 1.48 eV in PANI-MnWO$_4$.

The DC conductivity of PANI-MnWO$_4$ nanocomposite varied in the range of 10^{-4} to 10^{-3} Scm^{-1} as the temperature is raised from room temperature to about 450 K. Semiconductor behaviour is reflected in this observation. But in electron beam irradiated sample, a 10-fold increase in DC conductivity is measured. There is an increase in DC conductivity of PANI upon composite formation due to the positive synergistic effect between the polyaniline and the tungstate that increases the polaron hopping. AC studies proved the Jonscher's power law dependence of AC conductivity in PANI-MnWO$_4$ composite and confirmed polaron hopping. Only slight and random variations in dielectric constant and loss tangent are caused by electron beam irradiation.

Decrease in crystallite size with increase in electron dose is also observed in PANI- $CaWO_4$ composite. The crystallite size in PANI-$CaWO_4$ composite also changes upon electron irradiation. The FTIR spectrum showed a new absorption peak in the electron irradiated PANI-$CaWO_4$ sample at 1126 cm^{-1}. This indicates that the doping of PANI is enhanced by electron irradiation. The SEM micrographs of PANI-$CaWO_4$ show very long rod shaped fibres along with irregular shaped clusters. In the EDS analysis of PANI- $CaWO_4$ composite, the elements carbon, oxygen, nitrogen, calcium, tungsten and chlorine are detected. TEM images of PANI-$CaWO_4$ composite also contain nanostructures of different shapes along with nanofibres.

UV-visible study of PANI-$CaWO_4$ shows absorption peaks centred on 430 and 685 nm. The bandgap of PANI changed from 1.5 to 1.16 eV after PANI-$CaWO_4$ formation. In PANI-$CaWO_4$ composite, electron irradiation caused only slight variation in the bandgap.

The DC conductivity of PANI-$CaWO_4$ nanocomposite is also found to increase with temperature. The DC conductivity of PANI increases when it forms a composite with $CaWO_4$. A positive synergistic effect between the polymer and the tungstate is also seen in PANI-$CaWO_4$ nanocomposite. There is only a slight increase in DC conductivity due to electron beam irradiation in PANI-$CaWO_4$ nanocomposite.

AC studies proved the Jonscher's power law dependence of the AC conductivity in PANI-$CaWO_4$ composite. Only slight and random variations

in dielectric constant and loss tangent are caused by electron beam irradiation. But the high dielectric constant and low loss tangents in these materials indicate their scope in microwave applications and electromagnetic interference shielding.

6.2 Important outcomes

➢ Nanocrystalline tungstate nanoparticles ($MnWO_4$ and $CaWO_4$) are synthesized through chemical precipitation method without using any capping agent. This simple method can also be extended for the synthesis of other tungstates.

➢ Novel polyaniline composites of $MnWO_4$ and $CaWO_4$ are successfully synthesized by *in situ* chemical oxidative polymerization of aniline.

➢ Changes in the vibrational properties of the materials synthesized are detected in the IR and Raman studies.

➢ Studies based on the effect of calcinations temperature confirm changes in the structural, optical and electrical properties of $MnWO_4$ and $CaWO_4$ nanoparticles.

➢ In $MnWO_4$, a lattice expansion occurs with crystallite size reduction upon electron beam irradiation. But in $CaWO_4$, a lattice contraction takes place on irradiation.

➢ The electron beam irradiation results in structural modifications of the materials synthesized ($MnWO_4$, $CaWO_4$ and PANI-$MnWO_4$/$CaWO_4$ composites), which in turn produces changes in their optical and electrical properties.

➢ Electron irradiation of a suitable dose can be applied for the tuning of bandgap and photoluminescence properties of nanocrystalline tungstates and their composite for specific applications.

➢ Electron beam irradiation can also be used to enhance the DC electrical conductivity of nanocrystalline tungstates and their composite.

➢ The high dielectric constant and low loss tangents found in PANI-$MnWO_4$/$CaWO_4$ composites indicate their scope in microwave applications and electromagnetic interference shielding.

Apart from the above mentioned physical outcomes, other qualitative outcomes such as getting acquainted with novel analytical tools, practicing the scientific methods and above all an inquisitive ambience in academic life are achieved.

6.3 Outlook

Future research could be conducted on the use of these materials in existing as well as novel applications. For specific applications, research has to be continued further to control the size and the effect of irradiation time. More extensive and systematic studies, on optimization of synthesis conditions of metal tungstates and their polyaniline composites, are needed to explore their unique properties for usage in photocatalysis, antistatic coating, EMI shielding and microwave applications.

****ഇ✪ఇ****